Research in Optoelectronics (A)

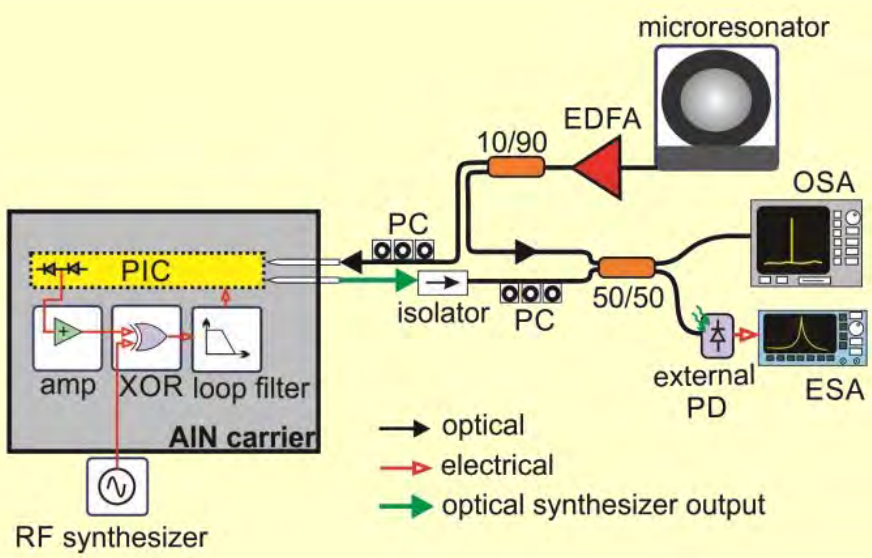

2017 Reprints of

Professor Larry A. Coldren

and Collaborators

ECE Technical Report 18-01

Department of Electrical & Computer Engineering

University of California, Santa Barbara

Research in Optoelectronics (A)

Reprints published in 2017

by

Professor Larry A. Coldren

and Collaborators

Published as

Technical Report # ECE 18-01

of

The Department of Electrical & Computer Engineering

The University of California

Santa Barbara, CA 93106

Phone: (805) 893-4486

Fax: (805) 893-4500

E-mail: coldren@ece.ucsb.edu

http://www.ece.ucsb.edu/Faculty/Coldren/

Introduction:

In 2017 Professor Coldren and collaborators published a dozen papers in a number of journals and conferences. All of work involves photonic devices and integrated circuits on III-V compound semiconductor materials as well as their integration into small sub-systems. The characterization of these devices and circuits within systems environments is also included in most cases.

As in the past, the reprints have been grouped into several areas. As in recent years, most of these are within **I. Photonic Integrated Circuits** (PICs): subcategories called out are *A. Reviews, B. Optical Phase Locked Loops, C. Optical Frequency Synthesis, D. Signal Processing, and E. PICs for LIDAR.* Within a second category, **II. Low-power Lasers**, there are two more papers.

The work was performed with funding from a couple of federal grants, some gift funds from industry, and support from the Kavli Endowed Chair in Optoelectronics and Sensors. Some of the PIC work was funded by the MTO Office of DARPA via subcontracts from Lockheed-Martin and UC-Davis. There was also a GOALI from NSF together with support from Freedom Photonics. The PIC fabrication was performed in the UCSB Nanofab facility partially supported by the NSF.

Sub-section (**I***A.*) contains a single invited Tutorial that reviews recent history and the state-of-the-art in InP-based photonic-integrated-circuits (PICs). Copies of the presentation slides are included. In (**I***B.*), three papers describe continued work on low-power integrated heterodyne optical phase-locked loop (OPLL) circuits. These might be used in 'Analog Coherent' communications, in frequency synthesis, or other sensor applications. Sub-section (**I***C.*) contains four papers which describe work using the OPLLs to lock widely-tunable lasers to stable reference sources, such as Kerr frequency combs from micro-resonators, for optical frequency synthesis. Prof. Yao continues to study our active micro-ring filters in sub-section **I***D*, this time operating them as tunable lasers. In **I***E*. the emission properties of sparse aperiodic arrays is studied as relevant to Lidar applications.

In the second major section **II**, a new compact, potentially efficient, integrable tunable laser is explored in two papers co-authored with Freedom Photonics researchers. The work involves an active coupled cavity structure, which employs one HR-coated facet mirror and two gratings, one intermediate between two gain sections, the other as the output mirror that may continue into an integrated waveguide. At least one passive phase section is also included in one cavity for tuning.

Professor Coldren's Group

I. *Researchers*

S. Arafin	Assistant Project Scientist, UCSB

III. *Staff*

A. Miller	Center Assistant, OTC

Collaborators

I. *Faculty*

J. Bowers	UCSB
M. Rodwell	UCSB
J. Klamkin	UCSB
J. Yao	University of Ottawa
M. Li	China Academy of Science

II. *Researchers*

M. Lu	Infinera (former Postdoctoral Scholar)
M. Mashanovitch	Freedom Photonics (former Associate Project Scientist)
L. Johansson	Freedom Photonics (former Associate Research Engineer)
Gordon Morrison	Freedom Photonics
E. Norberg	Member of Staff, Aurrion, Inc. (former Graduate Student)
J. Parker	Freedom Photonics (former Graduate Student)
R. Guzzon	Photonic Systems Engineer, Aurrion, Inc.

T. Komlijenovic	Research Scientist, UCSB
A. Simsek	Research Assistant, UCSB
S. Kim	Teledyne Scientific & Imaging
W. Liang	OEwaves, Inc.
D. Eliyahu	OEwaves, Inc.
A. Matsko	OEwaves, Inc.
L. Maleki	OEwaves, Inc.
R. Helkey	Associate Director, IEE & AIM Photonics, UCSB
Vladimir Ilchenko	OEwaves, Inc.
Anatoliy Savchenkov	OEwaves, Inc.

III. *Collaborating Students*

S. Dwivedi	UCSB, Klamkin

Table of Contents:

I. Photonic Integrated Circuits

A. Reviews

B. Optical Phase Locked Loops

C. Optical Frequency Synthesis

II. Low-power Lasers

Shamsul Arafin, Gordon Morrison, Milan Mashanovitch, Leif Johansson, and Larry A. Coldren, "Coupled-Cavity Lasers for a Low-Power Integrated Coherent Optical Receiver" *Proc. Conference on Lasers and Electro-Optics (CLEO)*, paper AM3A.5, San Jose, California (May 14-19, 2017)

Shamsul Arafin, Gordon B. Morrison, Milan L. Mashanovictch, Leif A. Johansson, and Larry A. Coldren, "Compact Low-Power Consumption Single-Mode Coupled Cavity Lasers," *IEEE Journal of Selected Topics in Quantum Electronics*, **23**, (6), 6000309 (Nov.-Dec., 2017)

I. Photonic Integrated Circuits

A. Reviews of Applications

Indium-phosphide photonic-Integrated-circuits –A Tutorial

Abstract:
A collection of slides from the author's conference presentation is given. Integration platforms; Historical overview; Motivation for photonic integration; Transceiver bracket history; InP technology; Choherent communicator motivated photonic integration; Tunable lasers; Commercial PIC examples; Research PIC examples; Analog coherent vs. digital for low power/cost; Hybrid integration; Take-aways.

Published in: Optical Fiber Communications Conference and Exhibition (OFC), 2017
Date of Conference: 19-23 March 2017

Indium-Phosphide Photonic-Integrated-Circuits

What's the problem?

OFC 2017

Size, Weight, Power, Cost, Performance, Reliability

Where?

- Communication
  - Long haul
  - Metro, campus
  - Data centers, Supercomputers
- Sensing/instrumentation
- Computing

Integration Platforms

OFC 2017

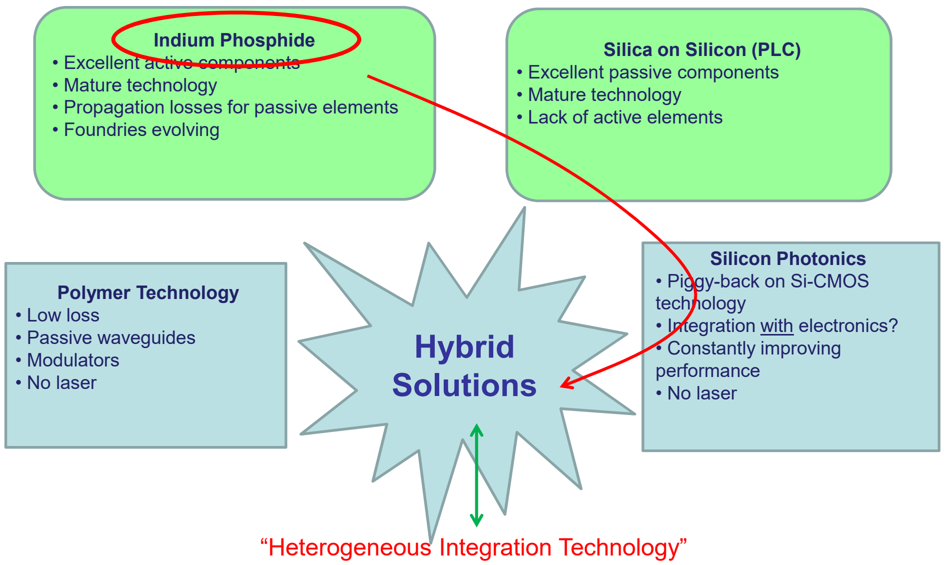

Introduction/Historical View—PICs

OFC 2017

- **1970's - OEICs on GaAs for high-speed computing**
- **1980's – InP photonics/fiber; integration & tunables for coherent → <u>Reach</u>**
- **1990's – Widely-tunables, laser-mods, small-scale int. for WDM and cost**
- **1990's – VCSELs for datacom and optical interconnection**
- **2000 - Bubble: Explosion of strange ideas, bandwidth-demand satisfied by DWDM → crash; but bandwidth needed by 2010.**
- **2000's – InP PICs & PLCs expanded and matured; increasing use of VCSELs in high-speed datacom and computing interconnects**
- **2006+ – Emergence of Si-PICs with several different goals: low-cost OEICs; high-performance PICs; or stop Moore's-Law saturation**
- **2008+ - Use of advanced modulation formats/coherent receivers for improved <u>Spectral Efficiency</u> —need for integration at both ends of links**
- **2010's – Increased InP-PIC use; maturity of Si-photonics solutions; improved VCSEL performance; heterogeneous integration approaches**
- **2017 – Some delineations; InP-PICs for long-haul/metro; Si-photonics beginning to emerge in high-volume short-data/metro**

Motivation

Communication Requires a Complex Network

OFC 2017

- The Ethernet ecosystem—it's nearly all optical (fiber)
- Need higher bandwidth & performance with lower SWAP-C

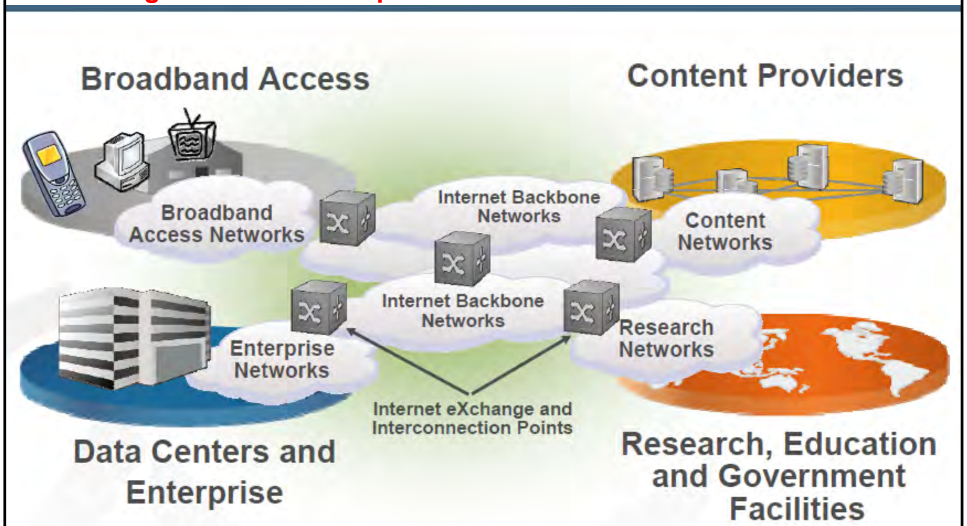

UCSB

Data is King

OFC 2017

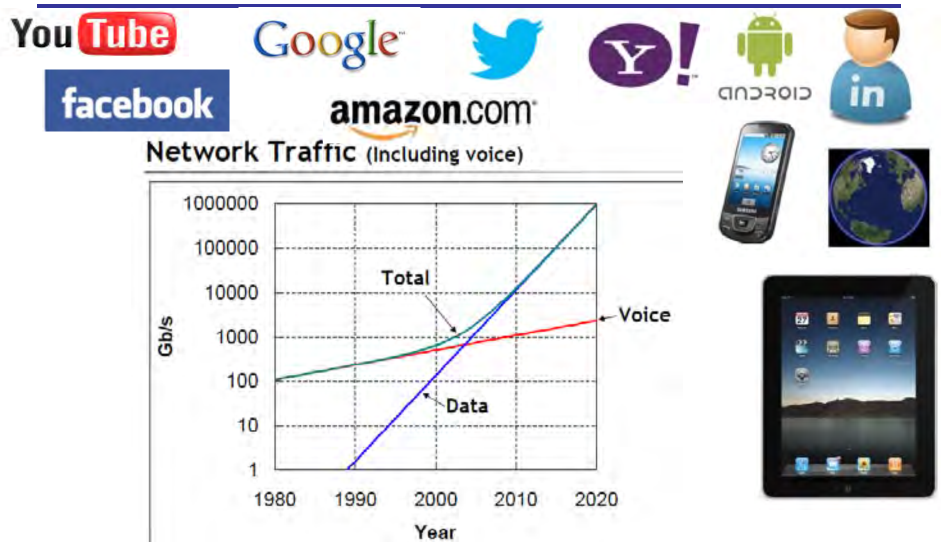

Exponential network traffic growth is driven by high-bandwidth digital applications

G4, Video-on-demand, HD-TV, wireless backhaul, cloud computing & services

UCSB

Scaling spectral efficiency through WDM, Coherent, ?

OFC 2017

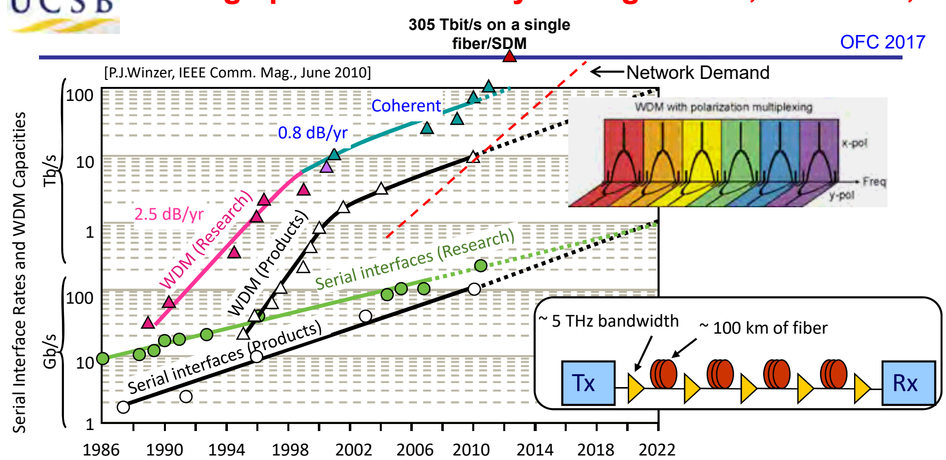

~10 Terabit/s WDM systems are now commercially available

~100+ Terabit/s WDM systems have been demonstrated in research (Coherent)

EDFA enabled WDM (wavelength division multiplexing)in 1990s

Growth of WDM system capacities has noticeably slowed down

Now “Space-Division-Multiplexing” (SDM) is being explored

Courtesy P. Winzer

Motivation for Photonic Integration

OFC 2017

- Reduced size, weight, power (SWAP)
- Improved performance (coupling losses, stability, etc.)
- Improved reliability (fewer pigtails, TECs, fiber alignment optics, etc…), although chip yield may not be highest
- Cost (in volume)

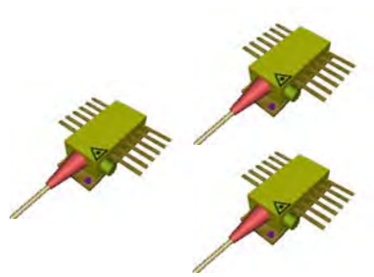

Horizontal and vertical integration possible
- multiple functionality and arrays of chips in one

After C. Joyner, infinera

InP vs Si vs PLC

	Performance		
Building block	InP	Si	TriPleX
Passive components	●	●●	●●●
Lasers	●●●	○	○
Modulators	●●●	●●	●
Switches	●●●	●●●	●
Optical amplifiers	●●●	○	○
Detectors	●●●	●●●	○

Footprint	●●	●●●	●
Chip cost	●	●●	●●
CMOS compatibility	○○	●●	●
Low cost packaging	○	○[1]/●●[2]	●●

[1] Endfire coupling (low refl.)

[2] Vertical coupling (med. refl.)

Performance	
●●●	Very good
●●	Good
●	Modest
○	Challenging

TU/e Technische Universiteit Eindhoven University of Technology

Transceiver market history and projection

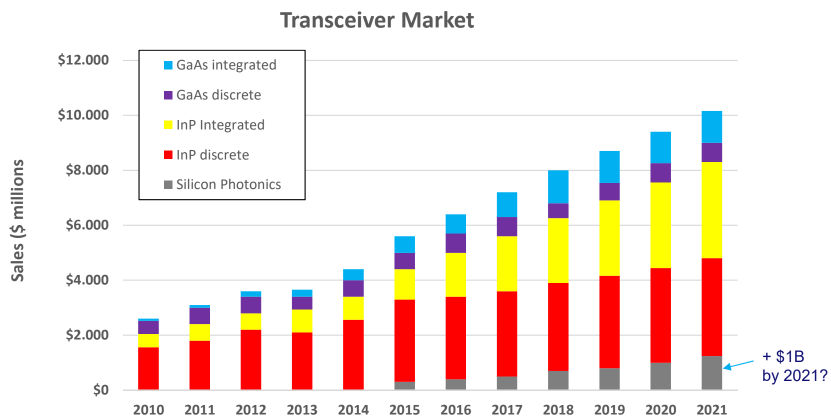

Source *LightCounting*

+ $1B Amplifiers and Passives

TU/e Technische Universiteit Eindhoven University of Technology

Update on Si-Photonics

UCSB

OFC 2017

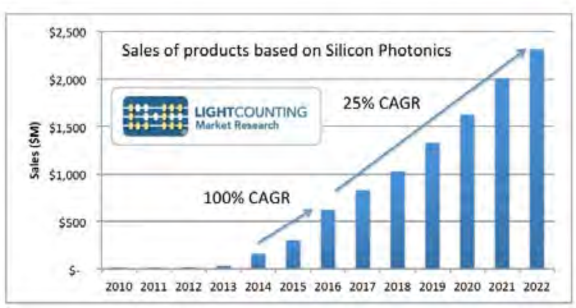

11/16

renee@lightcounting.com

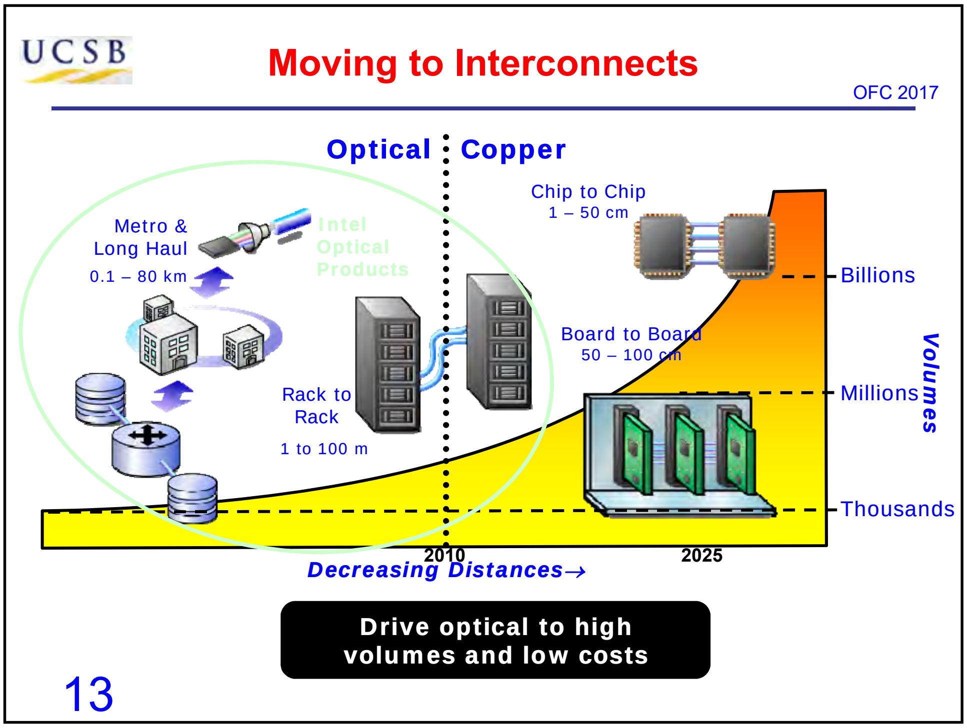
UCSB
Moving to Interconnects
OFC 2017
Optical
Copper
Metro & Long Haul
0.1 – 80 km
Intel Optical Products
Chip to Chip
1 – 50 cm
Billions
Board to Board
50 – 100 cm
Rack to Rack
1 to 100 m
Millions
Volumes
Thousands
2010
2025
Decreasing Distances→
Drive optical to high volumes and low costs
13

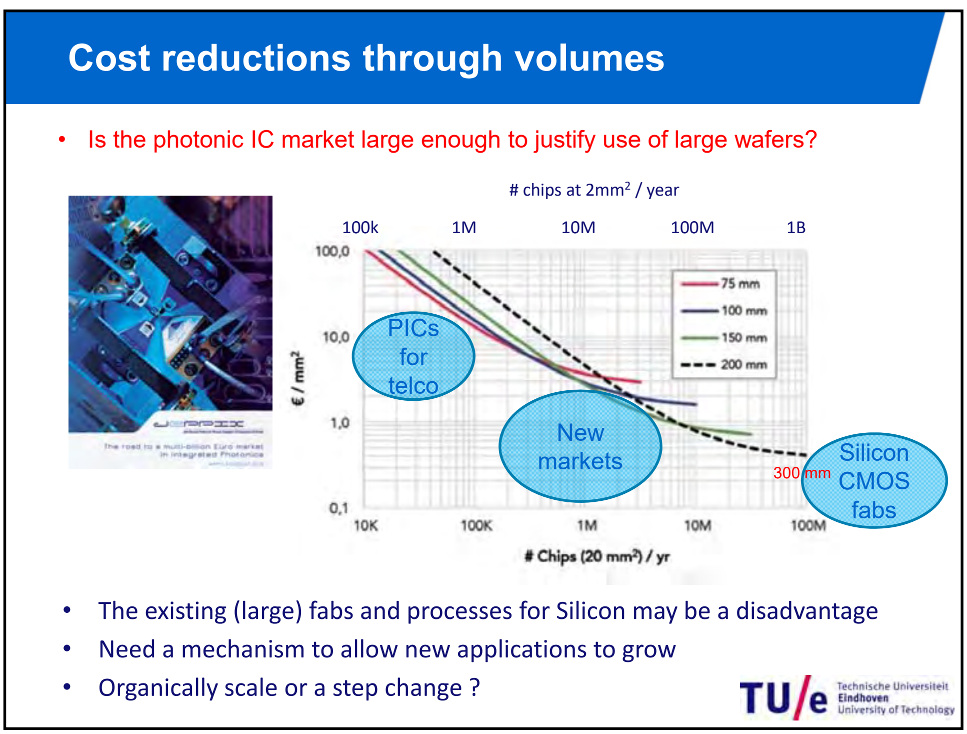
Cost reductions through volumes
• Is the photonic IC market large enough to justify use of large wafers?
chips at 2mm² / year
100k
1M
10M
100M
1B
100,0
10,0
1,0
0,1
€ / mm²
75 mm
100 mm
150 mm
200 mm
PICs for telco
New markets
300 mm
Silicon CMOS fabs
10K
100K
1M
10M
100M
Chips (20 mm²) / yr
• The existing (large) fabs and processes for Silicon may be a disadvantage
• Need a mechanism to allow new applications to grow
• Organically scale or a step change ?
TU/e Technische Universiteit Eindhoven University of Technology

Moore's Law for Photonics

Scaling in Photonic ICs

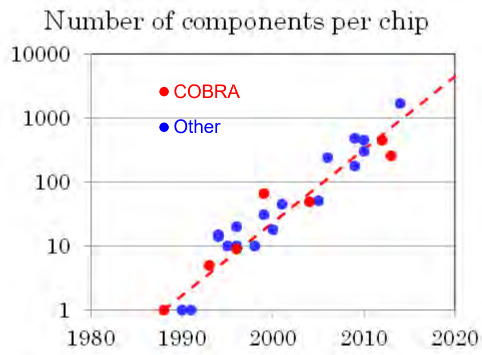

Photonics Research 3, 5, pp. B60-B68 (2015)

https://www.osapublishing.org/prj/abstract.cfm?uri=prj-3-5-b60

Technische Universiteit Eindhoven University of Technology

Indium Phosphide as the Materials Platform

Indium Phosphide

OFC 2017

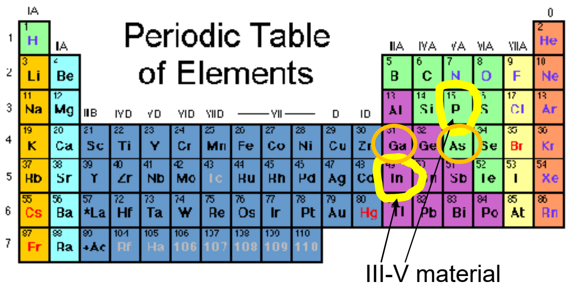

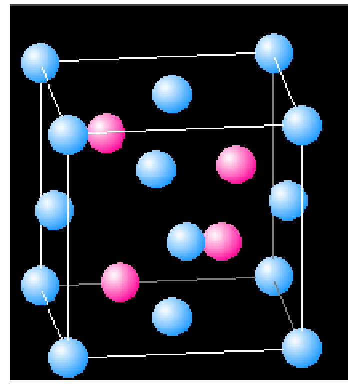

Zincblende structure

(two intersecting FCC lattices, one for In and one for P)

Lattice constant = 5.87 A at 300K

InGaAsP/InP lattice-matched alloys

OFC 2017

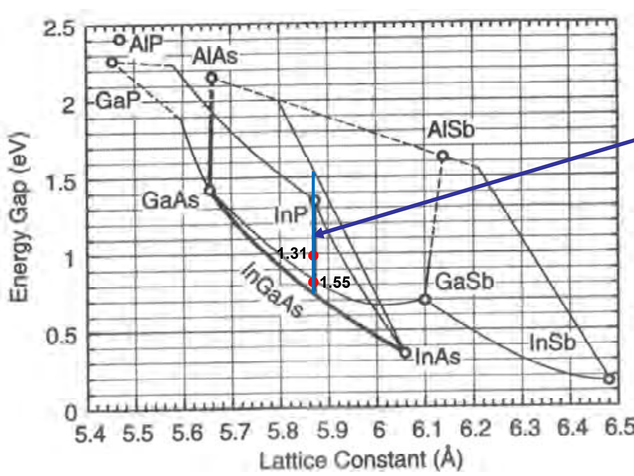

InGaAsP lattice-matched to InP

Also use InGaAlAs

$\lambda_g(\mu m) = 1.24/\ E_g(eV)$

Integration Technology:
Lateral waveguides/couplers

OFC 2017

Waveguide cross sections

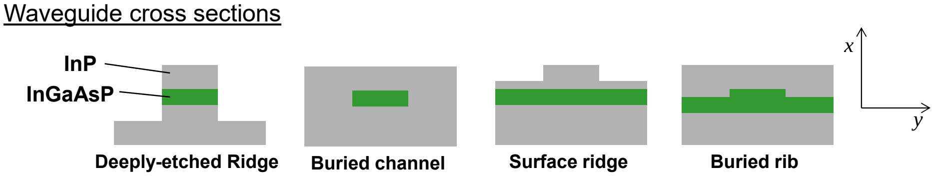

MMI coupler

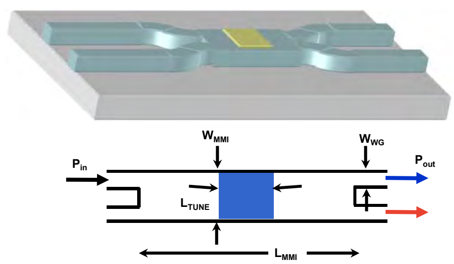

Integration Technology:
Active-Passive (axial) Integration

OFC 2017

Desire lossless, reflectionless transitions between sections

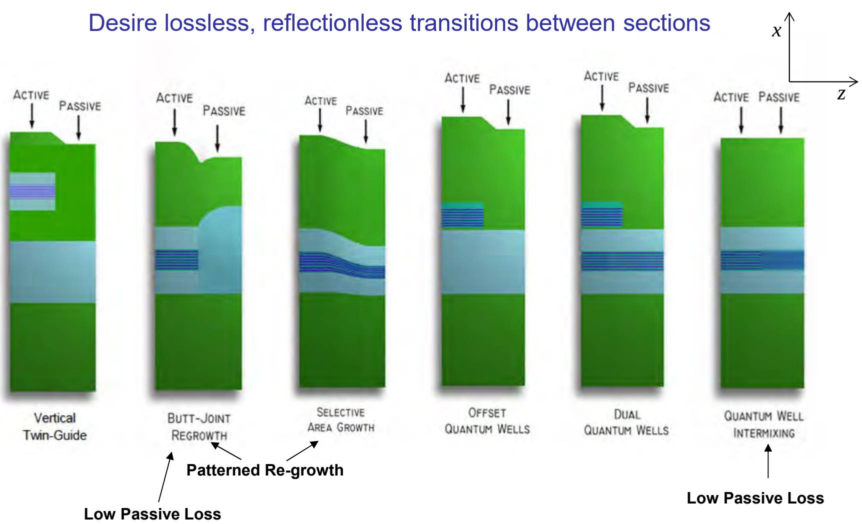

3 Bandgaps usually desired

Integration Technology: Offset Quantum Well Process (DBR)

UCSB

OFC 2017

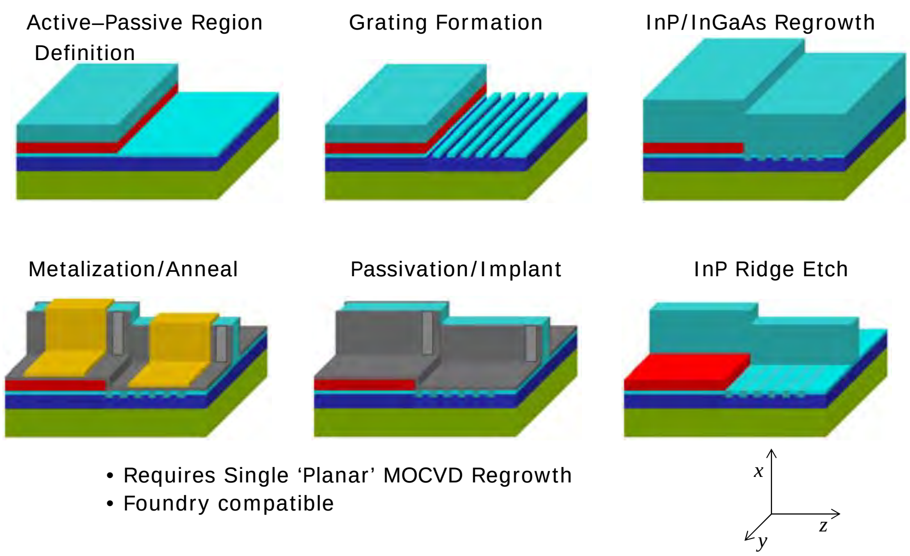

- Requires Single 'Planar' MOCVD Regrowth
- Foundry compatible

Integration Technology: QWI For Multiple-Band Edges/Single Growth

UCSB

OFC 2017

Simple/robust QWI process
- Ability to achieve multiple band edges with a single implant

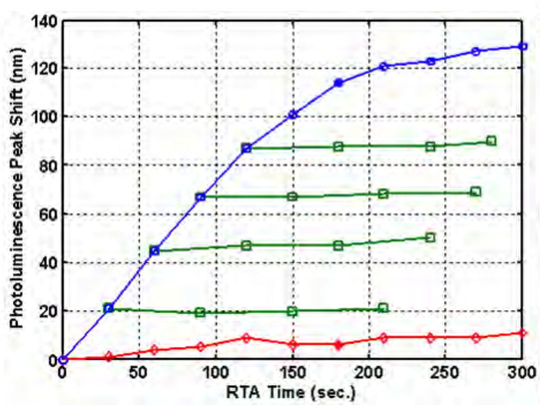

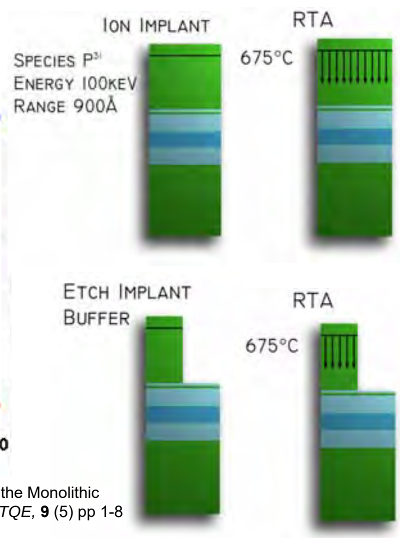

E. Skogen et al, "Post-Growth Control of the Quantum-Well Band Edge for the Monolithic Integration of Widely-Tunable Lasers and Electroabsorption Modulators," *JSTQE*, **9** (5) pp 1-8 (Sept, 2003).

InP integration platforms

Integration Technology		Design constraints	Other advantages/issues
Dual waveguides (offset quantum wells)	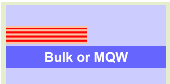 	Gain/mode overlap Carrier injection into the laser	Coupling loss
QW intermixing	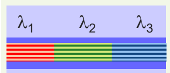 	Number of QWs and doping is shared between all functional sections	- QW width is not optimum for laser and/or modulator; - detuning control is difficult; - shape of the QWs is affected by intermixing => modulator efficiency degradation
Selective Area Growth (SAG)	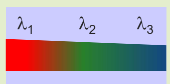 	Number of QWs and doping is shared between all functional sections	- QW width is not optimum for the laser/or modulator; - transition regions; - detuning control is difficult
Regrowth	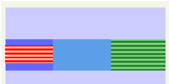	None	Regrowth can be combined with SAG to tailor waveguide thickness further (ex. spot size converter)

➢ Regrowth integration is robust integration platform with ultimate design flexibility:

✓ Optimization of material composition, number and width of the quantum wells, and doping

LUMENTUM 23

UCSB

Early Active PICs—InP

OFC 2017

Partially transmissive mirrors (couplers) and active-passive integration needed

→ DBR gratings and vertical couplers
- Tunable single frequency
- Combined integration technologies

Y. Tohmori, Y. Suematsu, Y. Tushima, and S. Arai, "Wavelength tuning of GaInAsP/InP integrated laser with butt-jointed built-in DBR," *Electron. Lett.*, 19 (17) 656-7 (1983).

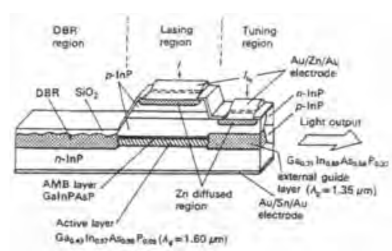

→**EML =** electroabsorption-modulated laser
- Still in production today

M. Suzuki, et al., *J. Lightwave Technol.*, **LT-5**, pp. 1277-1285, 1987.

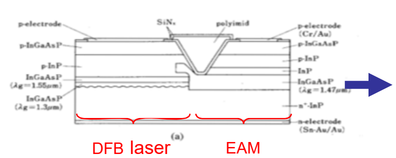

Coherent Communication Motivated Photonic Integration

OFC 2017

- In the 1980's coherent communication was widely investigated to increase <u>receiver sensitivity</u> and repeater spacing. It was also seen as a means of expanding WDM approaches because optical filters would not be so critical.

  Y. Yamamoto and T. Kimura, "Coherent optical fiber transmission systems," *IEEE J. Quantum Electron*, vol. 17, no. 6, pp. 919-925, Jun. 1981.

- This early coherent work drove early photonic integration efforts—<u>Stability</u>; enabled phase-locking

  T. L. Koch, U. Koren, R. P. Gnall, F. S. Choa, F. Hernandez-Gil, C. A. Burrus, M. G. Young, M. Oron, and B. I. Miller, "GaInAs/GaInAsP multiple-quantum-well integrated heterodyne receiver," *Electron. Lett.*, vol. 25, no. 24, pp. 1621-1623, Nov. 1989

Integrated Coherent Receiver
(Koch, et al)

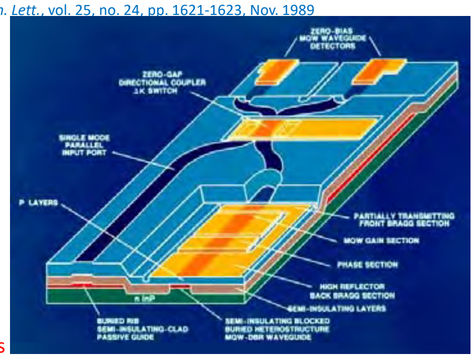

- The EDFA enabled simple WDM repeaters
- (just amplifiers) and coherent was put on the shelf
- But, some aspects of Photonic Integration continued → e.g., <u>Tunable Lasers</u>

Tunable Lasers

OFC 2017

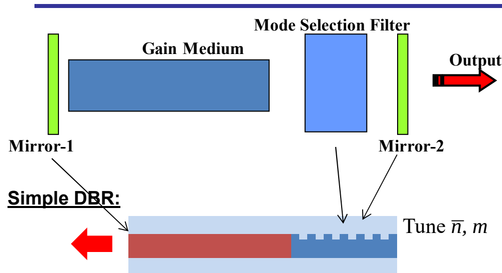

$$m\lambda/2 = \bar{n}L$$

Tunable DBR Lasers→ SGDBR

OFC 2017

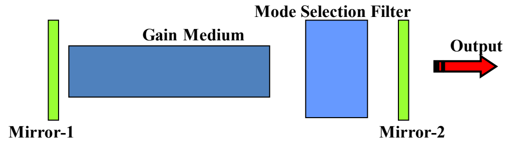

$m\lambda/2 = \bar{n}L$

Simple DBR:

SGDBR:

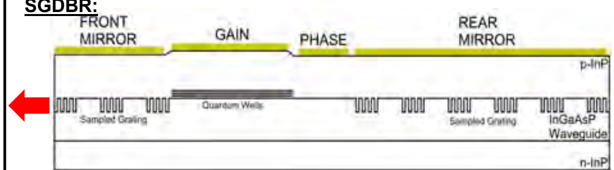

- **Uses vernier effect for multiband tuning**
- **$\Delta\lambda/\lambda$ = N x $\Delta n/n$ by differential mirror tuning**

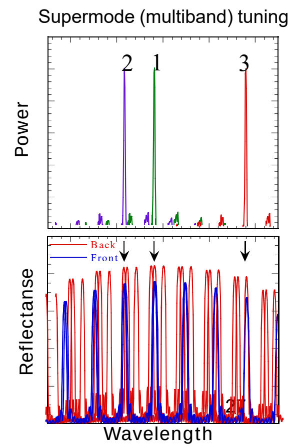

Tunable Lasers: Sampled-Grating DBR: Monolithic and Integrable

OFC 2017

SGDBR+X widely-tunable transmitter:
- Foundation of PIC work at UCSB

(UCSB'90-- → Agility'99-'05 → JDSU'05→ Lumentum'15)

"Multi-Section Tunable Laser with Differing Multi-Element Mirrors," US Patent # 4,896,325 (January 1990)

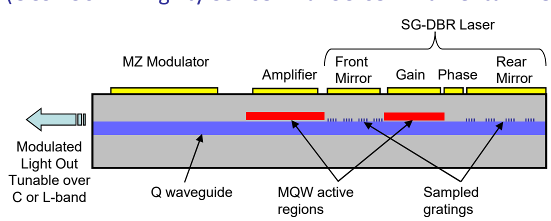

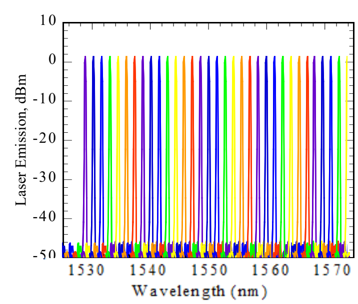

- Vernier tuning over 40+nm near 1550nm
- SOA external to cavity provides power control
- Currently used in many new DWDM systems (variations)
- <u>Integration technology for much more complex PICs</u>

<u>ILMZ TOSA (~ 18mm)</u>

JDSU 2008

6 section InP chip

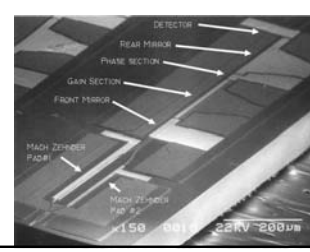

J. S. Barton, et al," *ISLC,* TuB3, Garmish, (Sept, 2002)

Commercial PIC Examples

Widely Deployed Commercial "WDM" PICs (~2009)

OFC 2017

EML's:

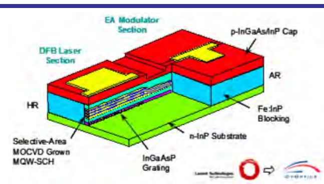

into XFP transceivers, etc.

Tunables & Selectable Arrays:

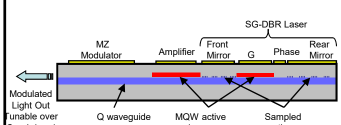

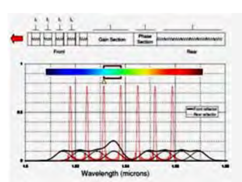

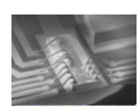

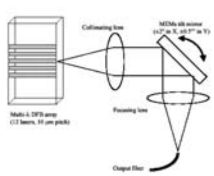

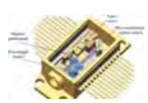

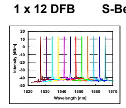

courtesy of T. Koch

InP PICs for datacenter transceivers

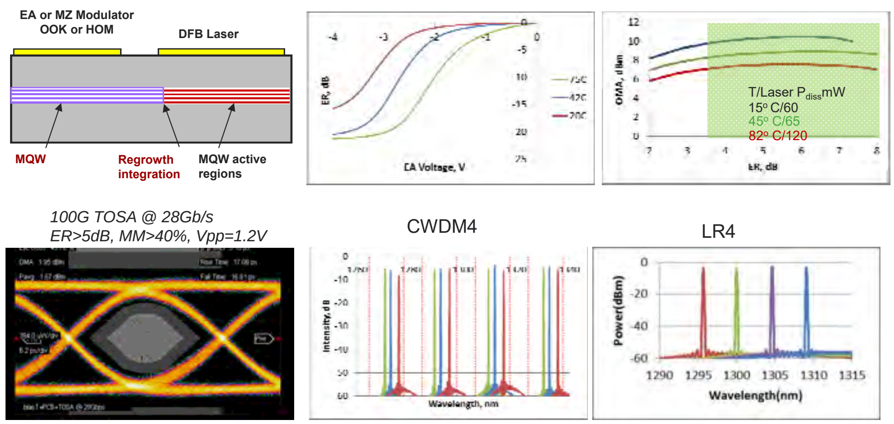

- InP PIC technology enabled 100Gb/s QSFP28 CWDM4 and LR4 transceivers
- Lossless integration of lasers with high efficiency modulators delivers high OMA and ER with low modulation voltage and low power dissipation
- => continues to be technology choice for 28 and 53Gbaud PAM4 400 Gb/s transceivers

2004: First Commercial Large-Scale InP-Based PICs
100 Gb/s (10 x 10Gb/s) Transmitter and Receiver PIC

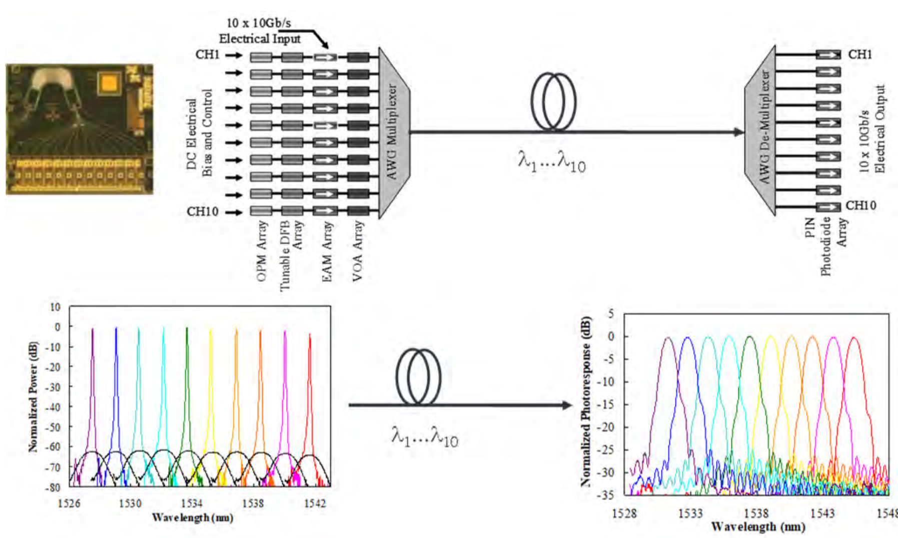

100Gb/s InP PIC-Based Systems Lead Market

2007 – 2011 Infinera PICs capture 45% of All LH 10G ports*

>1B Field Hours Without A Failure (100 Gb/s PIC Pairs: Tx+Rx)

100Gb/s (10 x 10Gb/s) PIC-Based Optical Transport System

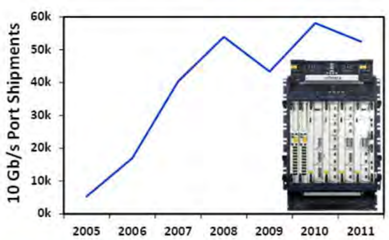

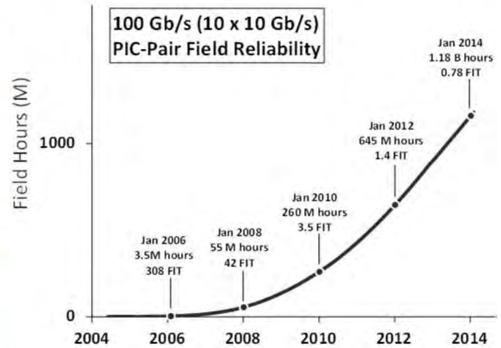

Large-Scale PICs Enable:
- 100 Gb/s per card (slot)
- Integrated Switching for digital bandwidth management

infinera

Data Capacity Scaling in The Network

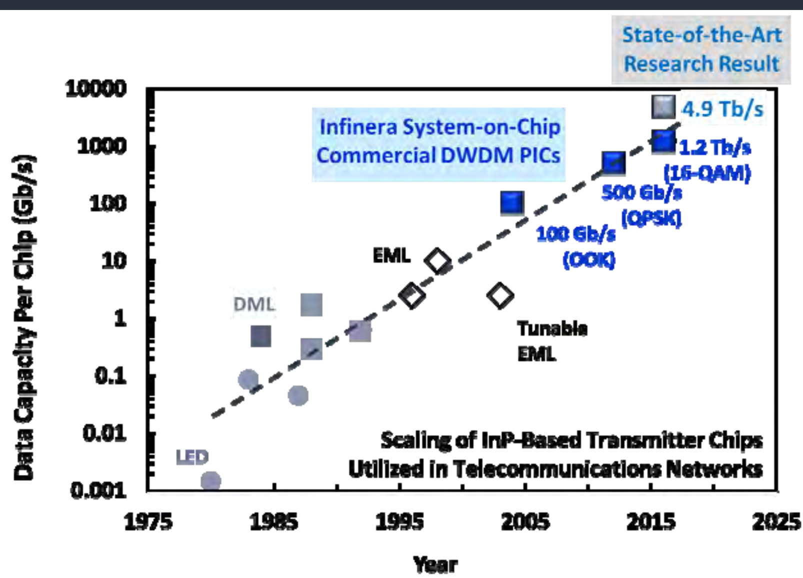

infinera

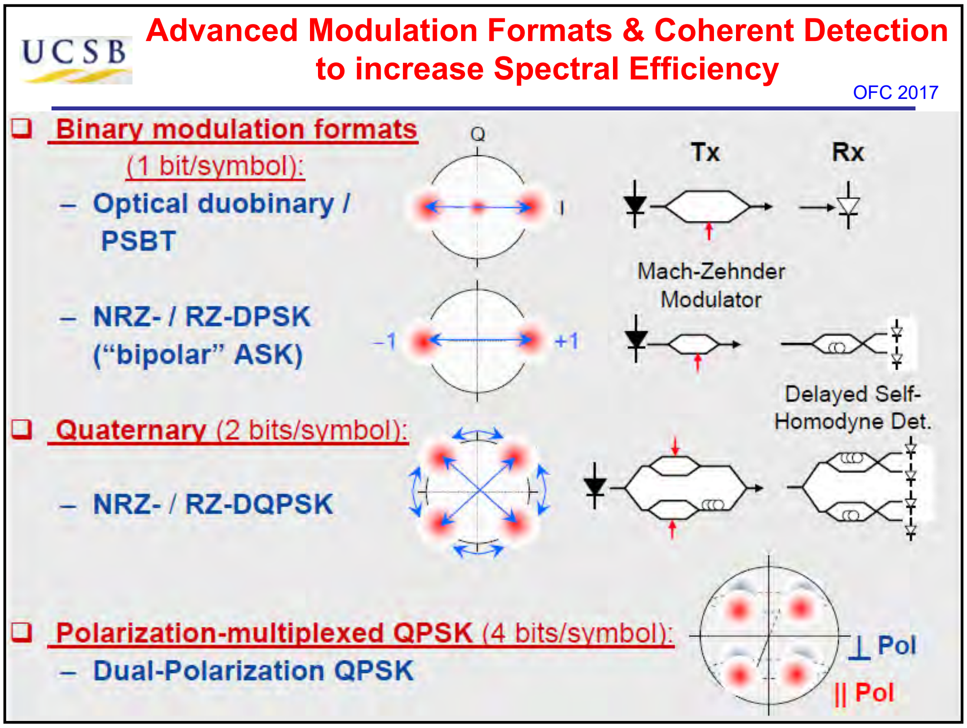
UCSB
Advanced Modulation Formats & Coherent Detection
to increase Spectral Efficiency
OFC 2017
Binary modulation formats
(1 bit/symbol):
– Optical duobinary / PSBT
– NRZ- / RZ-DPSK
("bipolar" ASK)
Quaternary (2 bits/symbol):
– NRZ- / RZ-DQPSK
Polarization-multiplexed QPSK (4 bits/symbol):
– Dual-Polarization QPSK
Q
I
−1
+1
Tx
Rx
Mach-Zehnder
Modulator
Delayed Self-
Homodyne Det.
⊥ Pol
|| Pol

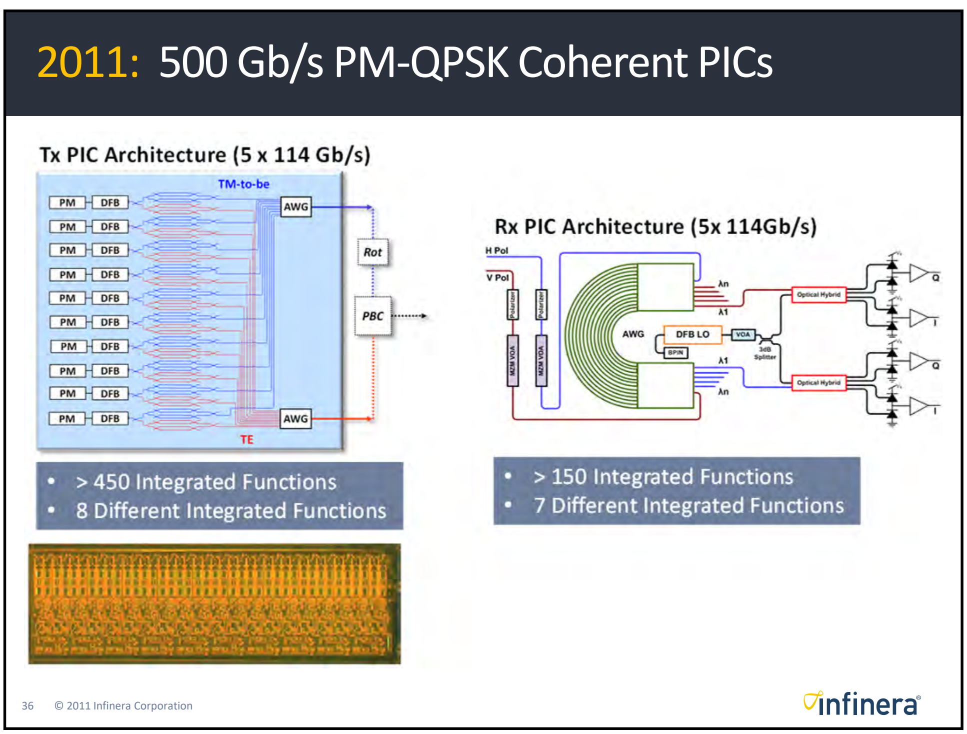
2011: 500 Gb/s PM-QPSK Coherent PICs
Tx PIC Architecture (5 x 114 Gb/s)
TM-to-be
TE
PM
DFB
AWG
Rot
PBC
• > 450 Integrated Functions
• 8 Different Integrated Functions
Rx PIC Architecture (5x 114Gb/s)
H Pol
V Pol
AWG
DFB LO
VOA
Optical Hybrid
• > 150 Integrated Functions
• 7 Different Integrated Functions
36
© 2011 Infinera Corporation
infinera

500 Gb/s PM-QPSK Coherent PICs

500 Gb/s Tx→Rx Contiguous Super-Channel

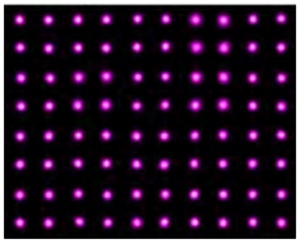

500Gb/s PIC-based Transport / Switching System

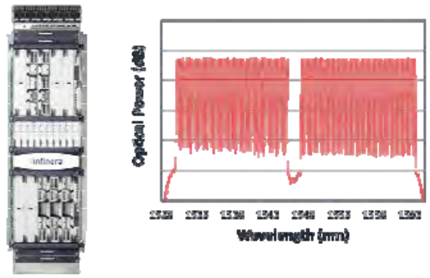

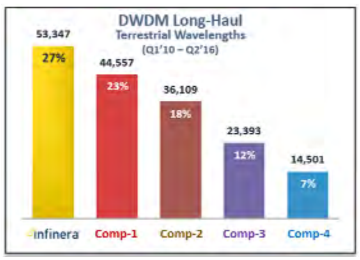

#1 in 100G Long-haul

Infinera has 28% of all 100G LH wavelengths sold since Q1-2010, excluding china

37 © 2011 Infinera Corporation

infinera

2016 : 1.2Tbps Extended C-Band tunable coherent 32GBaud/16-QAM coherent Transceiver

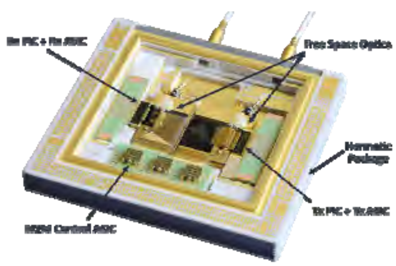

- 1.2 Tbps, 6-Channel transmitter and receiver PICs in single Module
- Independent extended C-Band tunable channels
- 200Gbps per channel (33GBaud/16QAM) capable to 1500km Reach.
- 44GBaud data rate demonstrated

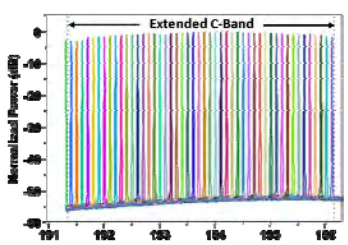

Typical laser output spectrum

33GBaud, 16-QAM   44GBaud, 16-QAM

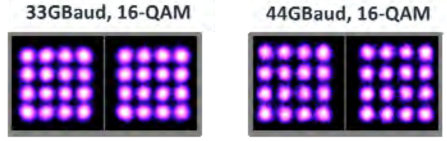

B2B Constellations

38 © 2011 Infinera Corporation

infinera

C-band Tunable Integrated Coherent Transmitter PIC

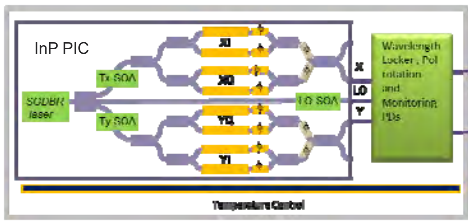

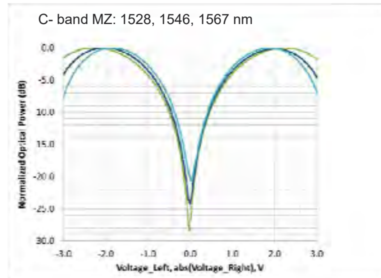

- Narrow Linewidth Sampled-Grating DBR laser
- Two quadrature Mach-Zehnder modulators
- High power LO output
- 3 SOAs
  - Independent power control for LO and each Tx polarization
  - VOAs
- InP PIC technology is employed for 32 Gbaud 100 and 200 Gb/s coherent pluggable modules

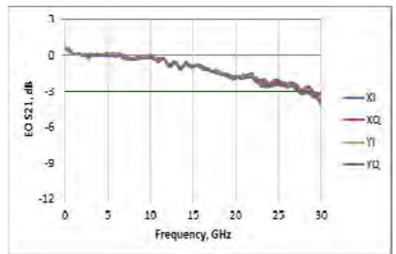

Narrow linewidth thermally-tuned SGDBR Laser

- 70kHz linewidth and 50dB SMSR at +17dBm fiber power over 41nm range in C-band

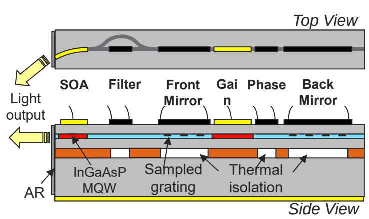

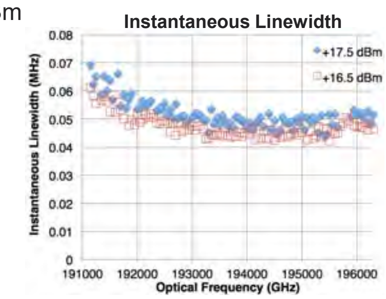

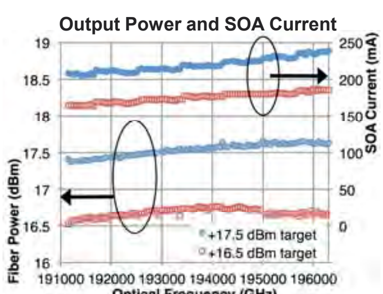

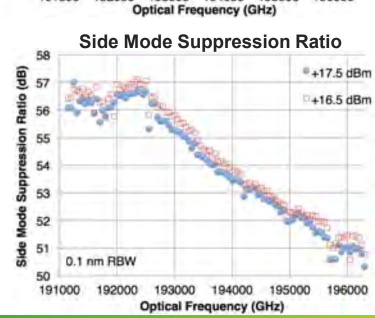

M.C. Larson et al., OFC 2015, M2D.1

Tunable Interferometric Transmitter

- Compact cavity (broadband HR back mirror used)
- Dual output laser – natural fit for interferometric modulation
- Lumped or traveling wave modulators
- (Optional) SOAs for power balancing

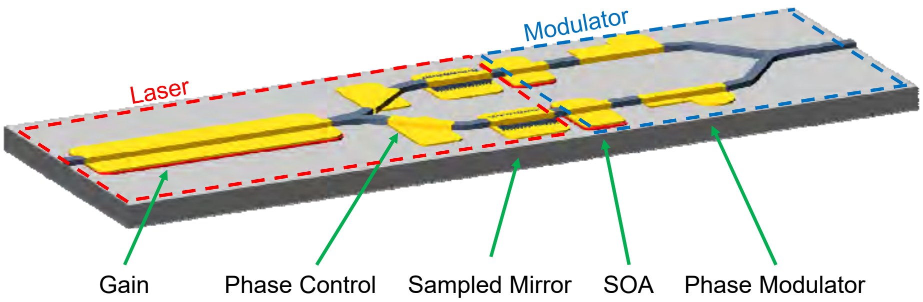

1550 nm Widely Tunable Interferometric Transmitter

- 50 dB SMSR
- 50 nm tuning range
- 12.5 Gbps operation
  - 25 Gbps in development
- Chirp control
- 80+ km reach in SMF-28 fiber

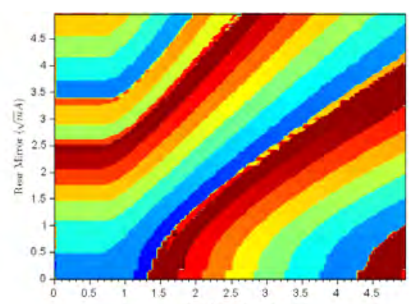

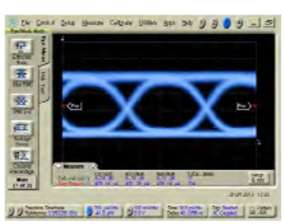

12.5 Gbps

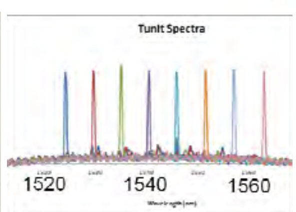

Quad Transmitter- Butt Joint Platform

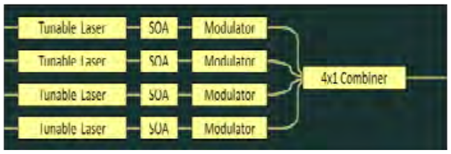

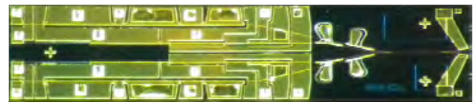

- Monolithic InP QUAD C-Band tunable Tx PIC with single output waveguide
- PIC operates at 55°C for reduced power consumption of TEC
- Individual SOAs amplify output power and enable VOA and blanking
- 12.5Gbps Electro-absorption modulators

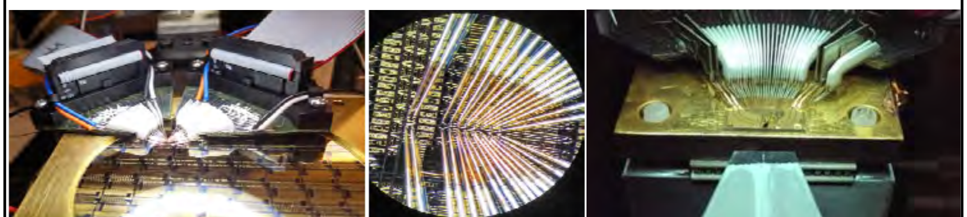

Wafer-Level Electrical and Optical Measurements

CoC CW and RF Testing

Quad Transmitter– RF Performance

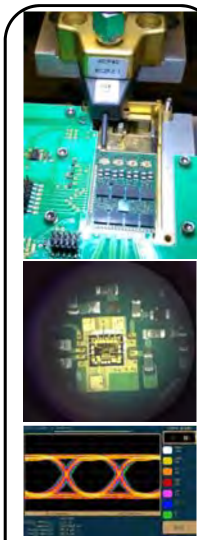

Driver E-E
12.5Gbps

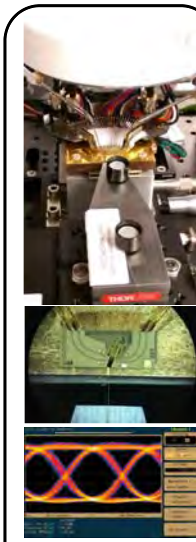

CoC E-O
12.5Gbps

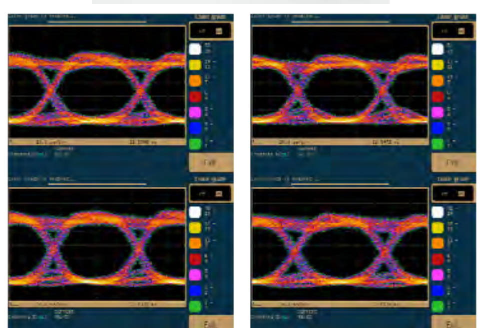

TOSA E-O, all Transmitters
(Non-optimized impedance of driver -> CoC transition) 10Gbps

Research Examples

Background:

DARPA-PhASER

Microwave Filtering - with Integrated Photonics

Demonstrated reconfigurable photonic filter - using an active <u>InGaAsP platform</u> and <u>deeply etched waveguides</u>

→ Novel filter characteristics – unmatched by electrical RF filters!

(Optimum NF @ SOA gains to give near zero net filter insertion loss)

Schematic

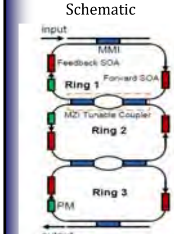

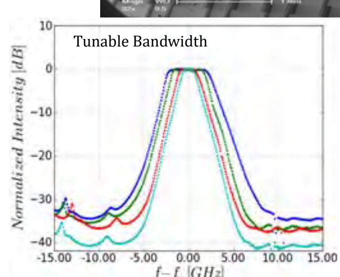

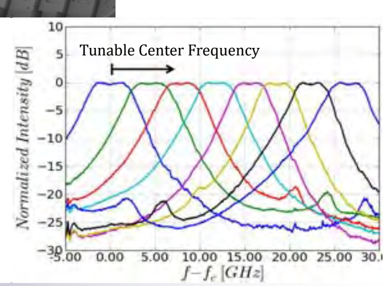

*E J. Norberg, R S. Guzzon, J S. Parker, L A. Johansson and L A. Coldren, "Programmable Photonic Microwave Filters Monolithically Integrated in InP/InGaAsP", J. Lightwave Technol, vol. 29, no. 11, 2011

Erik Norberg

Integration Platform – RF-linearity results

- RF-linearity improves with lower confinement material platform
  - Best RF-linearity reported for SOAs
- SOAs demonstate ~4 dB noise figure (w\o coupling loss)
- SOA demonstrates useful SFDR performance!
  - Design devices with short SOAs (G small)

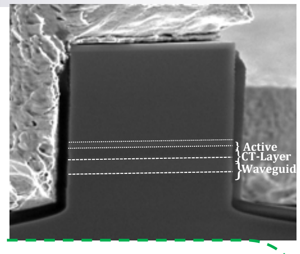

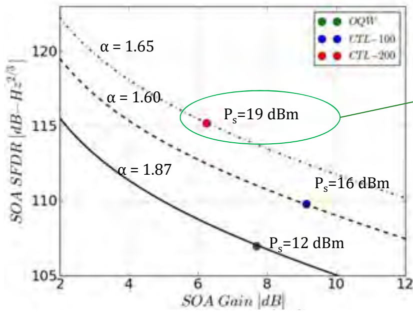

SFDR of integrated tunable filter can be optimized by using low gain SOAs!**

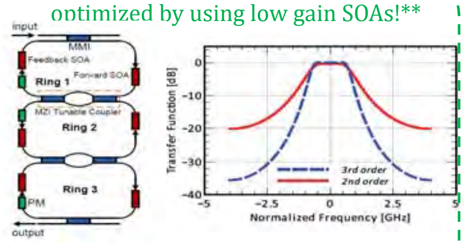

Device **SFDR >115dB-Hz$^{2/3}$** is predicted!**

Robert S. Guzzon, Erik J. Norberg, and Larry A. Coldren,"Spurious-Free Dynamic Range in Photonic Integrated Circuit Filters with Semiconductor Optical Amplifiers", *JQE*, **48 (2) p269-278 (2012)

UCSB *Erik Norberg*

UCSB

3654 JOURNAL OF LIGHTWAVE TECHNOLOGY, VOL. 32, NO. 20, OCTOBER 15, 2014

A Photonic Temporal Integrator With an Ultra-Long Integration Time Window Based on an InP-InGaAsP Integrated Ring Resonator

OFC 2017

Weilin Liu, *Student Member, IEEE*, Ming Li, *Member, IEEE*, Robert S. Guzzon, Erik J. Norberg, John S. Parker, Larry A. Coldren, *Life Fellow, IEEE, Fellow, OSA*, and Jianping Yao, *Fellow, IEEE, Fellow, OSA*

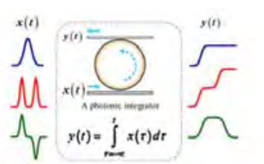

Fig. 1. The schematic diagram of a photonic temporal integrator based on a microring resonator.

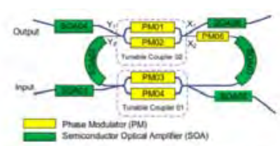

Fig. 2. The schematic of the proposed on-chip photonic temporal integrator based on a microring resonator.

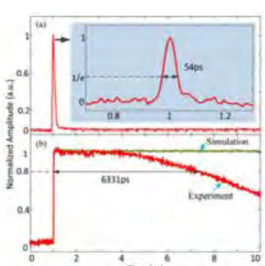

Fig. 7. The experimental results. (a) The input Gaussian pulse with a temporal width of 54 ps. (b) The integral of the Gaussian pulse with an integration time window of 6331 ps.

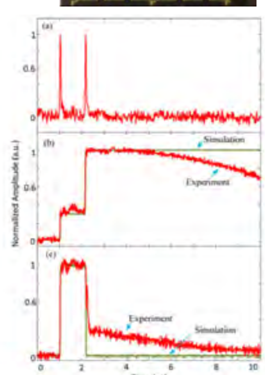

Fig. 8. The experimental results. (a) The input in-phase doublet pulse, (b) the integral of the in-phase doublet pulse, and (c) the integral of the out-of-phase doublet pulse.

1 THz, 100×10 GHz monolithically integrated InP OAWG with Built-in Adaptive RF-Photonic Passband Engineering

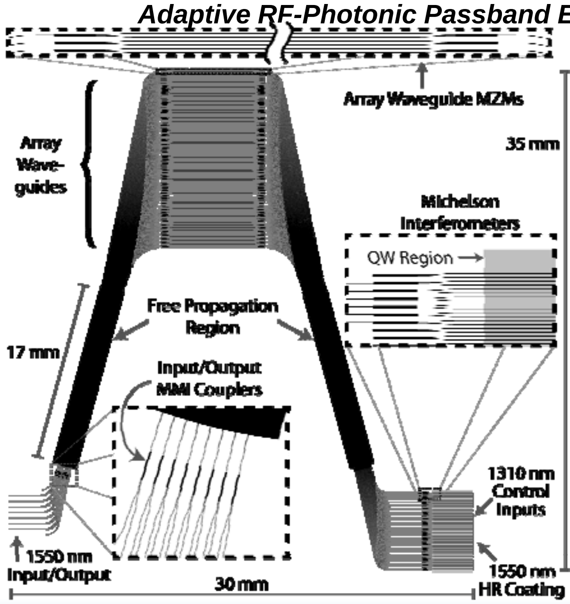

F. M. Soares et al., IEEE PJ, **3**, p 975 (2011)

100ch x 10 GHz AWG Output Spectrum After Phase-Error Correction

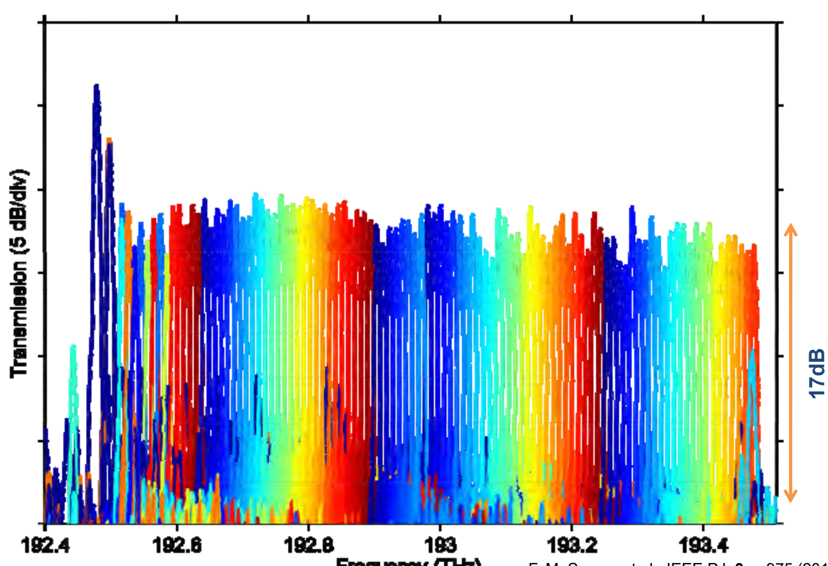

F. M. Soares et al., IEEE PJ, 3, p 975 (2011)

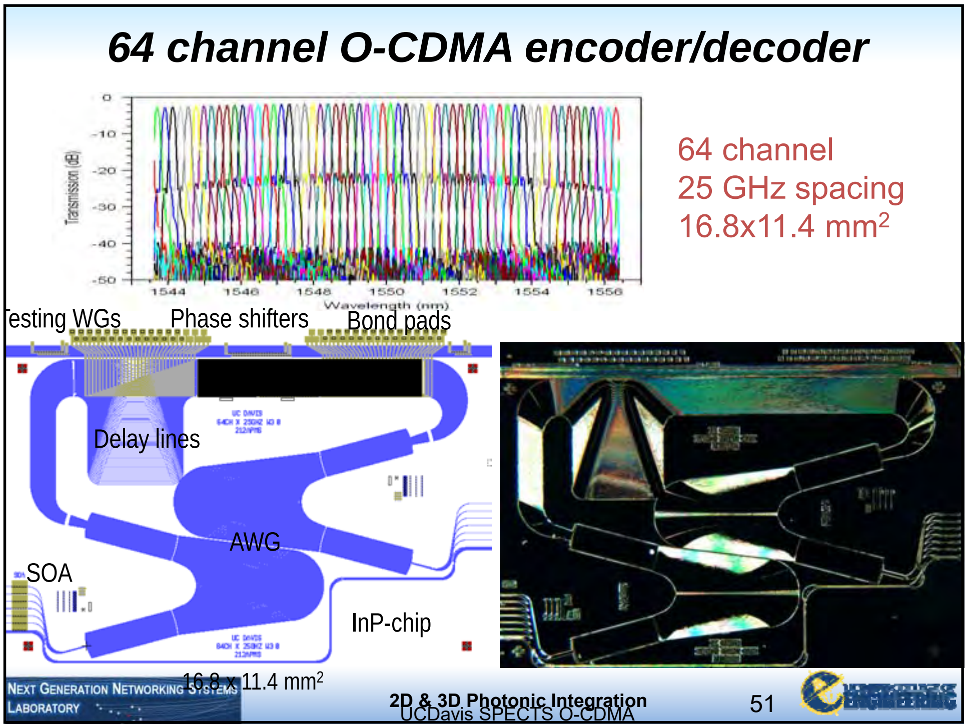
64 channel O-CDMA encoder/decoder
Transmission (dB)
Wavelength (nm)
64 channel
25 GHz spacing
16.8x11.4 mm2
Testing WGs
Phase shifters
Bond pads
Delay lines
AWG
SOA
InP-chip
16.8 x 11.4 mm2
Next Generation Networking Systems Laboratory
2D & 3D Photonic Integration
UCDavis SPECTS O-CDMA
51

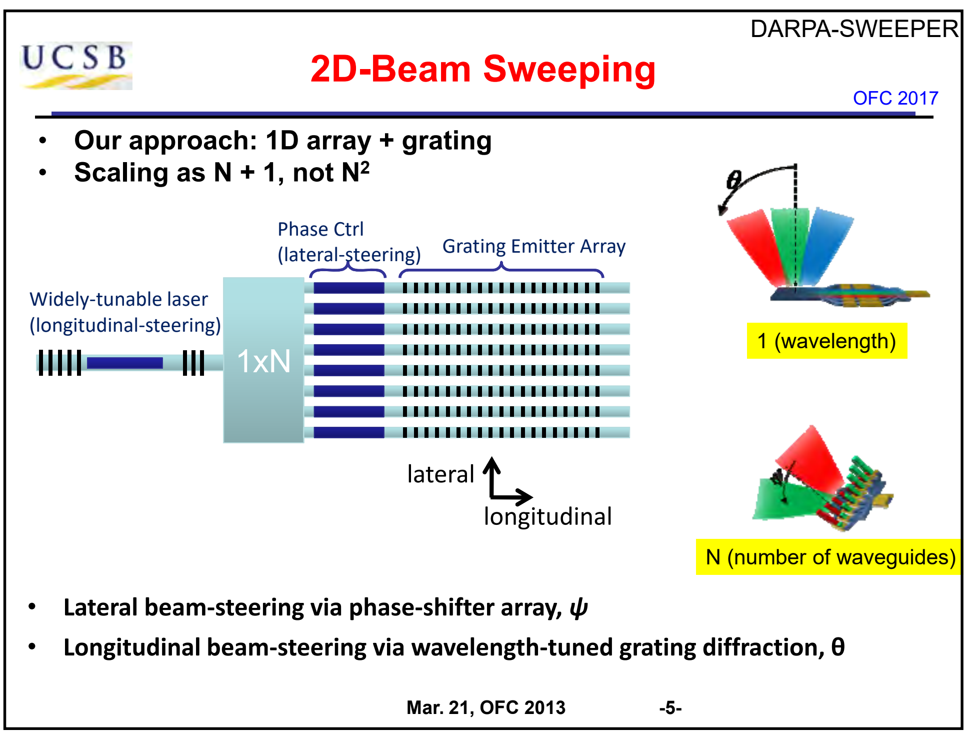
DARPA-SWEEPER
UCSB
2D-Beam Sweeping
OFC 2017
Our approach: 1D array + grating
Scaling as N + 1, not N2
Phase Ctrl
(lateral-steering)
Grating Emitter Array
Widely-tunable laser
(longitudinal-steering)
1xN
lateral
longitudinal
θ
1 (wavelength)
N (number of waveguides)
Lateral beam-steering via phase-shifter array, ψ
Longitudinal beam-steering via wavelength-tuned grating diffraction, θ
Mar. 21, OFC 2013
-5-

32 x N: Surface-emitting grating phased-array Optical Beam SWEEPER—PIC

OFC 2017

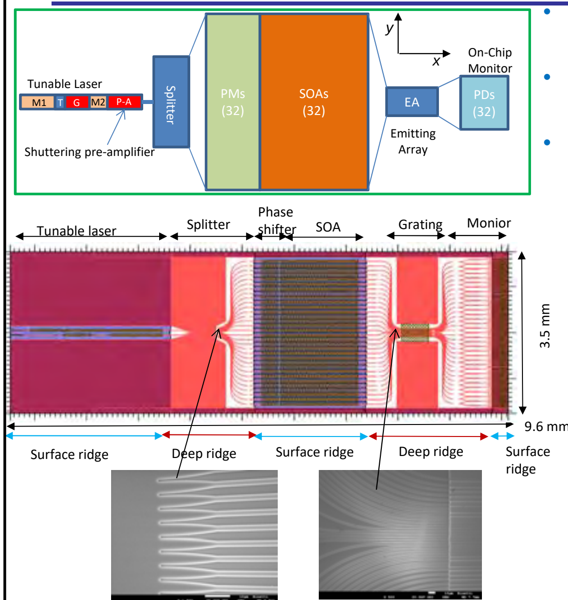

- Waveguide spacing varied to suppress lateral side lobes.
- Grating duty-factor weighted to extend effective length
- Nearly Gaussian shape

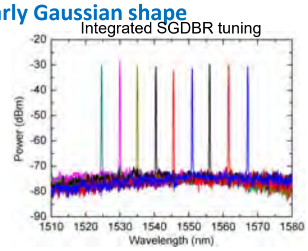

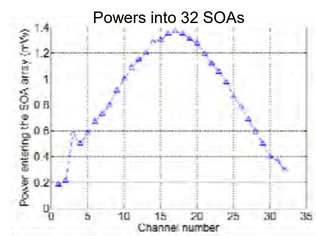

2D Beam Sweeping results (32 x N)

OFC 2017

Flip-chipped PIC-on-carrier

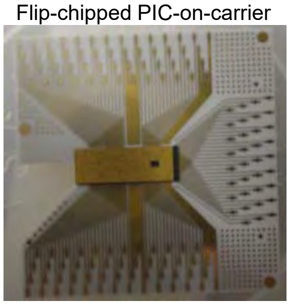

110 good contacts

- 2D beam steering demonstrated

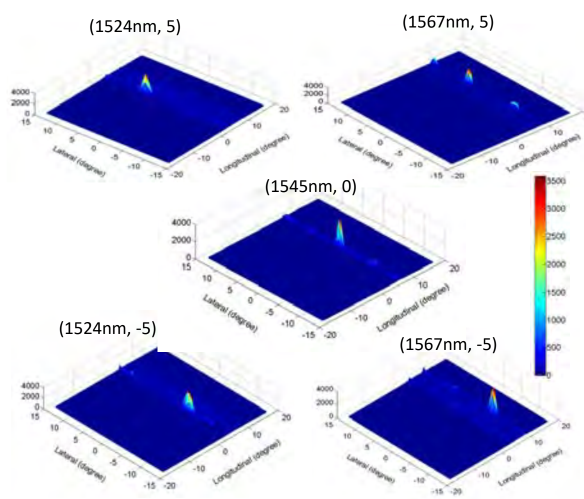

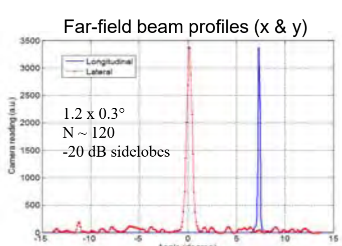

MOABB LIDAR Project (2016→)

Similar sweeping concept, but wider angles & larger arrays + LIDAR

Phase 1 Cell

Demonstrates all key building blocks
Demonstrates full operation of 1x10 mm emission aperture cell

Phase 2 Tile

Demonstrates ability to generate arrays of cells operating as coherent apertures
Demonstrates 16 independant sensing channels
Demonstrates Phase 1 cell operation as lidar

Phase 3 Multi-Tile

Demonstrates large aperture scalability
Stacks PIC layers 2-4 vertically
Integrates PICs, ASICS in 3D
Demonstrates Phase 2 tile as lidar

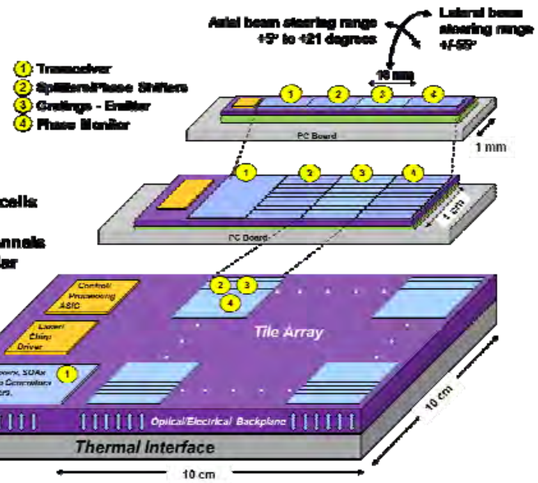

Phase 1 PIC Layout--MOABB

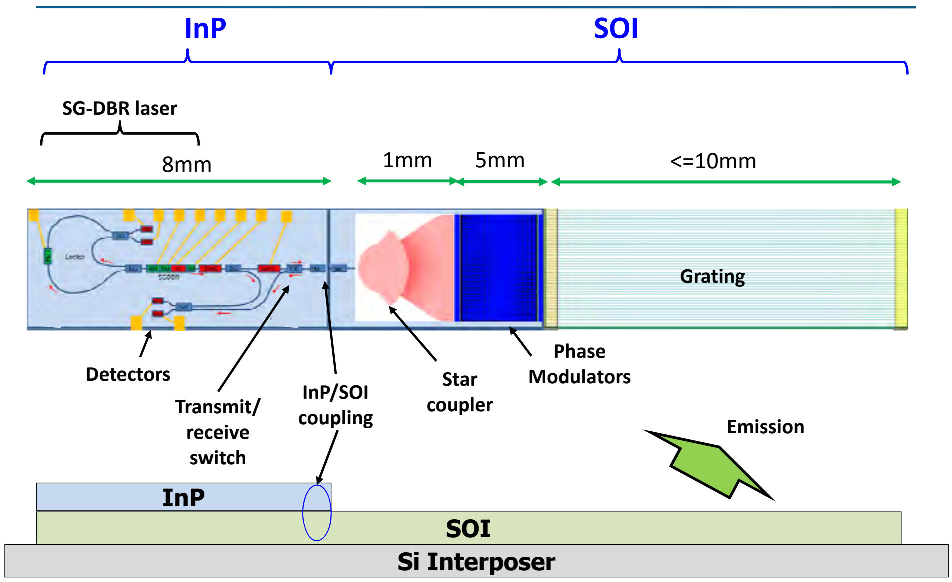

Reduced-Linewidth Rapidly-Tunable Laser

Optical Frequency Locked Loop

UCSB

OFC 2017

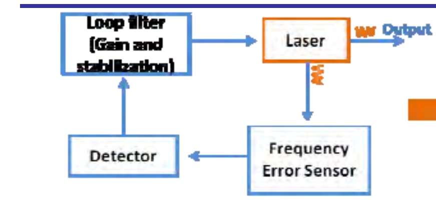

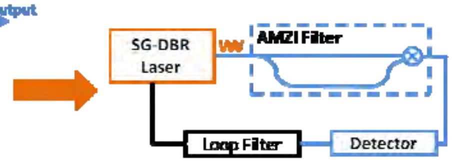

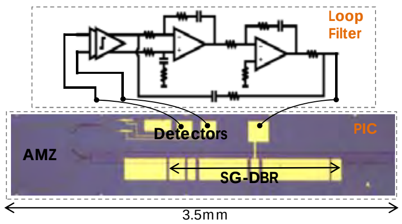

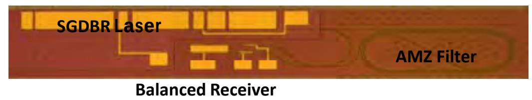

- Laser – SGDBR (40 nm tunability)
- Frequency Error Sensor – Asymmetric MZI
- Filter FSR = 10 GHz
- Open loop tuning-to-lock in 30 ns

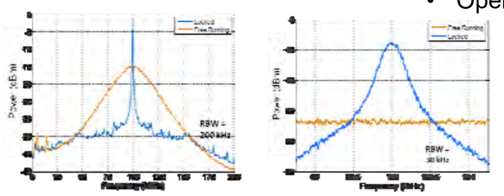

- Open loop→ > 5MHz linewidth
- Closed loop →150 kHz linewidth

A. Sivananthan, et al, OFC, 2013

3D Hybrid Integration for Silicon Photonics

3D Hybrid Integration (Klamkin group)

UCSB

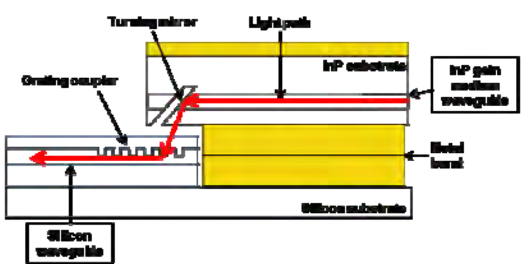

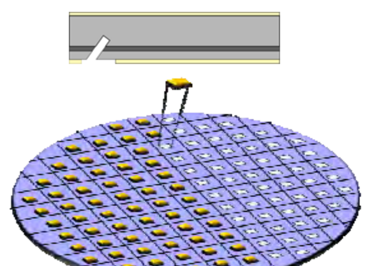

- InP laser or PIC with integrated total internal reflection (TIR) turning mirror coupled to Si with grating coupler
- Chips attached with standard IC bonding
- Could be carried out at wafer level in backend step
- P-side down bond to Si substrate for heat removal

B. Song, et al., ECOC 2015
B. Song, et al., Optics Express 2016

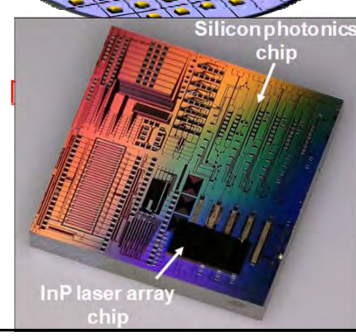

InP Widely-tunable Coherent Receiver PIC

(Phase-locked or Intradyne—also for Optical Synthesis)

OFC 2017

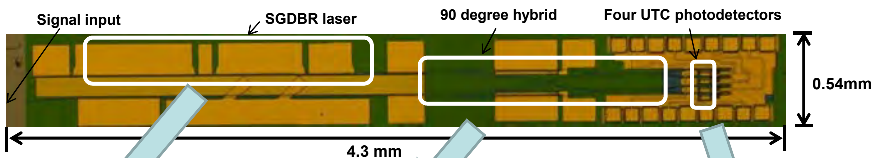

- **SG-DBR laser**

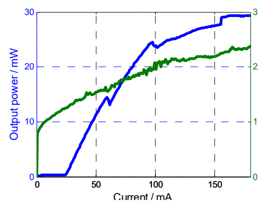

- **30 mW output power**
- **40 nm tuning range**
- **25 mA threshold current**

- **90 deg hybrid**
  - ***1x2 MMI couplers***
  - ***Directional couplers***
  - ***Phase shifters***

No phase error
4% power imbalance

- **UTC photodetectors**

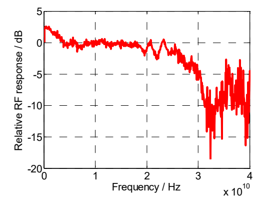

- ***29 GHz 3-dB bandwidth with -2V bias***
- ***18 mA saturation current at -5V bias.***

Mingzhi Lu, et. al., Optics Express, Vol. 20, Issue 9, pp. 9736-9741 (2012)

Intradyne or Phase-locked Receivers for generic sensor, instrumentation, or short-reach communication application?

OFC 2017

Intradyne Coherent Detection

- Phase and polarization diversity
- Frequency-locked local oscillator
- Digital signal processing of received electrical signals
  - Electronic CD compensation
  - Electronic polarization demultiplex
  - Adaptive PMD compensation

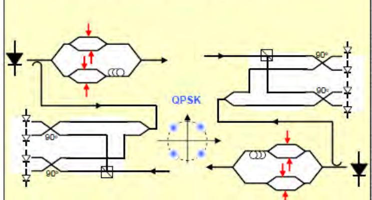

Typical Intradyne receiver architecture

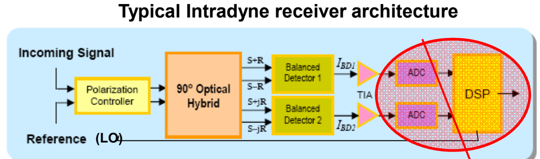

But for short-modest reach:

"Analog Coherent"

Homodyne receiver architecture

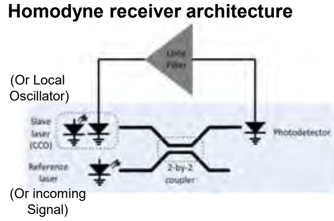

❖ **Use Phase-locked detection instead of power-hungry and costly Intradyne/ADC-DSP?**

- **Integrated Costa's loop receivers with widely-tunable LOs have been explored**
- **High-speed A/Ds & DSPs require lots of power and are expensive to design, especially as data rate increases**
- **Short feedback loops narrow LO linewidth and enable rapid and robust phase locking.**
- **Some impairments can be removed with much slower, lower-power, lower-cost signal-processing.**

UCSB

Phase Locked Coherent BPSK Receiver "Analog Coherent"

OFC 2017

OPLL + Costas Loop → 1 cm^2 footprint

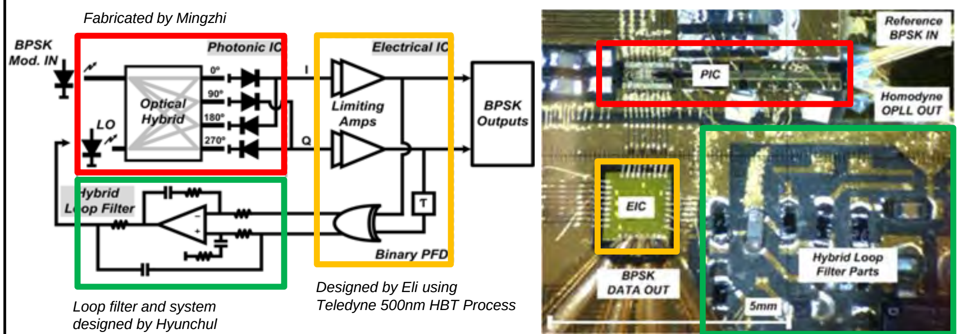

Photonic IC: SGDBR laser, optical hybrid, and un-balanced PDs

Electronic IC: limiting amplifiers and phase & frequency detector (PFD)

Hybrid loop filter: Feed-forward technique, op-amplifier and 0603 SMDs

Mingzhi Lu, et. al., Optics Express, Vol. 20, Issue 9, pp. 9736-9741 (2012)

UCSB

BPSK Data Reception—BERs "Analog Coherent"

OFC 2017

BER vs. OSNR (20Gb/s to 40Gb/s)

Error-free up to 35Gb/s , < 1.0E-7 @ 40Gb/s

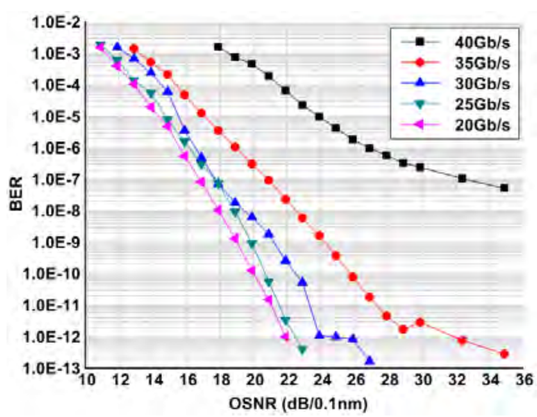

- **1.1GHz** closed loop bandwidth
- **120ps** loop propagation delay
- **100kHz** SGDBR-linewidth *(as ref. laser)*
- **-100dBc/Hz@above 50kHz** phase noise
- **600ns** frequency pull-in time
- **<10ns** phase lock time

40Gb/s Back-to-back

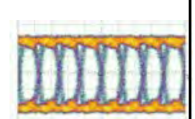

10Gb/s

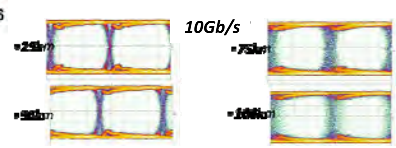

Mingzhi Lu, et. al., Optics Express, Vol. 20, Issue 9, pp. 9736-9741 (2012)

Electronic-Photonic Integration

- **Single-chip vs 2.5 or 3-D integration?**

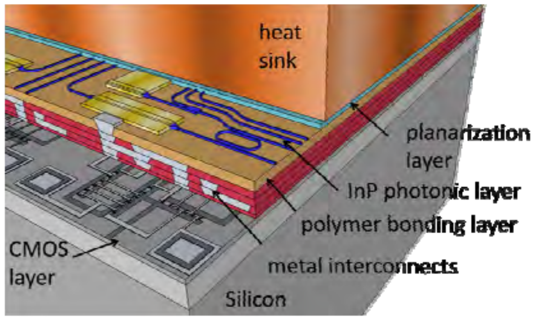

Horizon 2020
2016-2018
wipe.jeppix.eu

Connecting high performance foundry Silicon Electronics to high performance foundry InP photonic ICs

Minimizing interconnects for speed and energy efficiency

Simplifying assembly

TU/e Technische Universiteit Eindhoven University of Technology

Hybrid integration technology

VLSI chip

Photonic chip

Hybrids

Assembled test vehicle

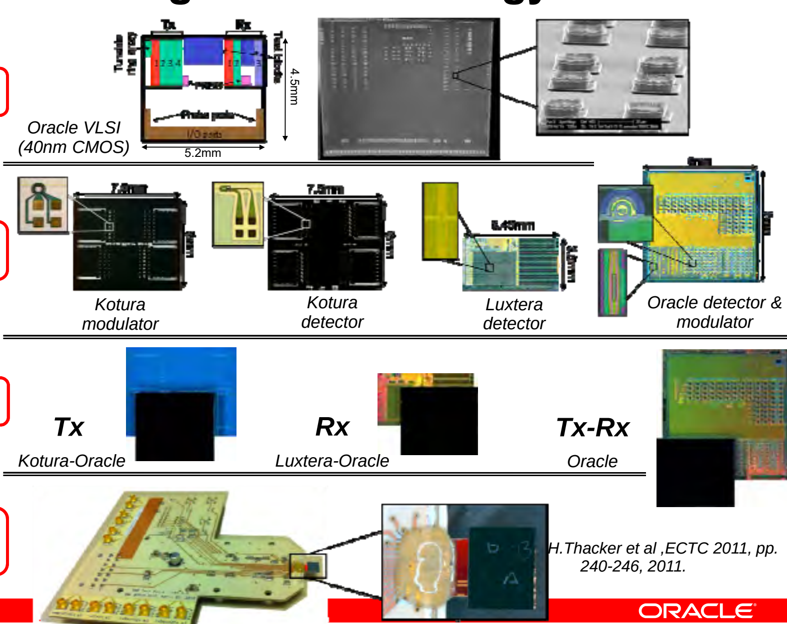

H.Thacker et al ,ECTC 2011, pp. 240-246, 2011.

ORACLE

Hybrid integration scaling

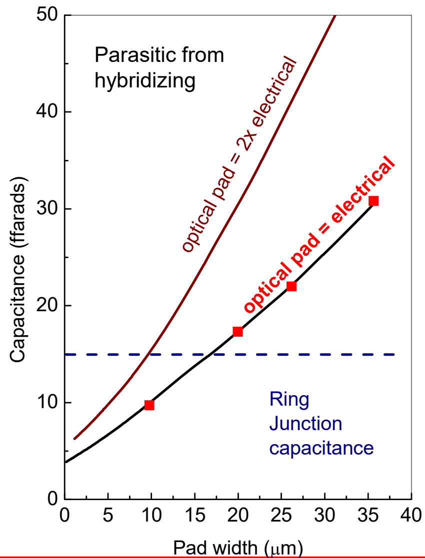

Hybrid approach parasitics become smaller than device junction as pad shrinks

Hybrid can outperform (monolithic) in speed, power, density, and TTM

Optimization enables/requires electronics-photonics co-design

3D (or Heterogeneous) integration → Integration

ORACLE

Foundry/Fabrication Services

Example InP-PIC Foundry/Fabrication Orgs.

OFC 2017

Foundries/PDK (generic)

- JePPIX* (broker: www.jeppix.eu)
  - HHI
  - Tyndall
  - Smart Photonics
  - Linkra
  - LioniX

  Bright Photonics (design only)
  PhoeniX Software (design only)
- AIM Photonics (via Infinera—available 2018—RF only)

Contract Manufacturing/no PDK (custom)

- Canadian Photonics Fabrication Centre
- Global Communications Semiconductors
- Leti
- Freedom Photonics (research—design/fab)

*For more information, see:
http://iopscience.iop.org/article/10.1088/0268-1242/29/8/083001

Generic Integration

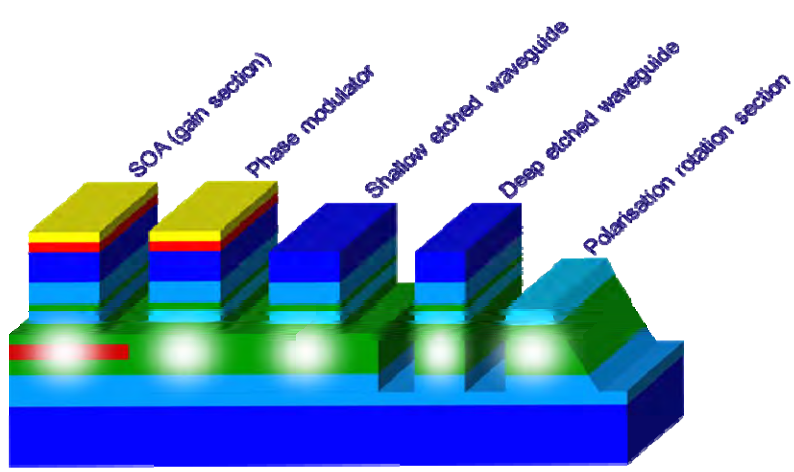

Technische Universiteit Eindhoven University of Technology

Application Specific Photonic ICs—JePPIX

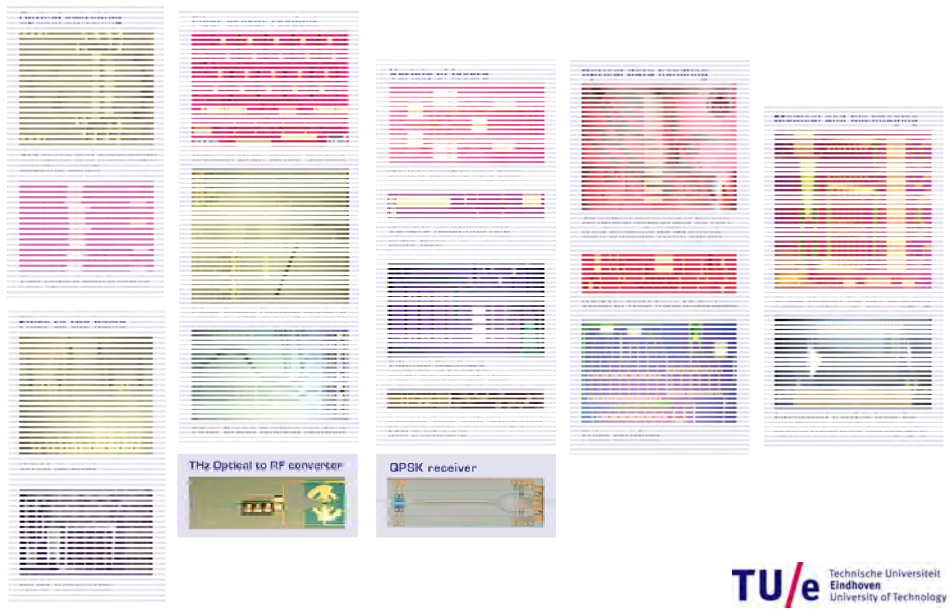

TU/e Technische Universiteit Eindhoven University of Technology

UCSB

Take-Aways

OFC 2017

- PICs are desirable for modest to high volume communication, sensing and instrumentation functions, where size, weight, power and cost (SWAP-C) reductions are desired.
- PICs are important because of the inherently stable phase relationships and possibly seamless interfaces between elements.
- PICs generally bring better reliability once properly designed; yield and some aspects of performance may be compromised.
- InP-PICs currently lead the market for Long-Haul and Metro communications; 'heterogeneous integration' & Si-photonics expanding in datacom and metro.
- For Electronic-Photonic integration, single-crystal (e.g. CMOS) integration may not be as desirable as heterogeneous (3D, 2.5D) integration (unless very high volume).

I. Photonic Integrated Circuits

B. Optical Phase Locked Loops

A Chip-Scale Heterodyne Optical Phase-Locked Loop with Low-Power Consumption

Arda Simsek[1], Shamsul Arafin[1], Seong-Kyun Kim[1], Gordon Morrison[2], Leif A. Johansson[2], Milan Mashanovitch[2], Larry A. Coldren[1], and Mark J. Rodwell[1]

[1]*Department of Electrical and Computer Engineering, University of California, Santa Barbara, CA, 93106, USA.*
[2]*Freedom Photonics LLC, Santa Barbara, CA, 93117, USA*
ardasimsek@ece.ucsb.edu

Abstract: A chip-scale heterodyne optical phase-locked loop, consuming only 1.3 W of electrical power, with a maximum offset locking frequency of 17.4 GHz is demonstrated. The InP-based photonic integrated receiver circuit consumes only 166 mW.

OCIS codes: (250.5300) Photonic integrated circuits; (060.2840) Heterodyne; Optical phase-locked loop; (060.5625) Radio Frequency Photonics

1. Introduction and Design of the Heterodyne OPLL

There has been significant effort for realizing highly-integrated chip-scale optical phase-locked loops (OPLLs) in the last decade along with the development in the photonic integration. Traditional free space optics creates loop delays in the order of tens of nanoseconds, which makes the loop bandwidth small. However, with the improvement in photonic integration, OPLLs can be realized with loop bandwidths in the order of hundreds of MHz [1] or even more than 1 GHz [2]. This makes OPLLs attractive and they can be used in a wide range of applications including coherent receivers, high sensitivity detection, laser linewidth narrowing, millimeter and THz wave generation and optical frequency synthesis [3-5]. In previous works, offset locking ranges up to 25 GHz [6], large loop bandwidth exceeding 1 GHz [2] and residual OPLL phase noise variance as low as 0.03 rad^2 [1] were demonstrated for the chip-scale OPLLs. However, these OPLLs consume almost 3 W of electrical power [2], being unsuitable for the real life applications. In this work, a chip-scale heterodyne OPLL with a total power consumption of 1.3 W is designed and demonstrated utilizing a novel indium phosphide (InP)-based photonic integrated circuit (PIC) and commercial-off-the-shelf (COTS) electronic ICs. The PIC receiver contains a widely-tunable (50 nm) compact Y-branch laser, a 180° hybrid (MMI) and two photodiodes. This is offset locked to narrow-linewidth (100 kHz) external-cavity laser (ECL) up to a range of 17.4 GHz with an RF synthesizer.

The low power consumption PIC is integrated with COTS electronic ICs in order to realize the highly-integrated OPLL. An optical microscope image and the schematic of the receiver PIC is shown in Fig. 1(a) and (b), respectively. The PIC incorporates a compact Y-branch laser formed between a high-reflectivity coated back mirror and a pair of Vernier tuned front mirrors. The output from one mirror leads to the coherent receiver used for offset locking, while the other output forms the optical output signal from the backend integrated system. The Y-branch laser has a compact cavity with short gain and mirror sections, requiring low current and therefore low drive power. It is tuned via Vernier effect and has been designed for high efficiency at 30º C ambient. The measured tuning range exceeds 50 nm with >50 dB side-mode suppression ratio.

The low power receiver PIC is connected with SiGe-based COTS ICs including a limiting amplifier and digital XOR as a mixer/phase detector. The limiting amplifier has a 3-dB bandwidth of 17 GHz with 30 dB of differential gain. The digital XOR operates up to at least 12.5 GHz input RF frequencies. The limiting amplifier limits the signal coming from photodiode pair to logic levels, which enables the system to be insensitive to any optical intensity fluctuations. A second order dual-path loop filter was used to get high loop bandwidth. This was achieved by employing a fast feedforward path which increases the system frequency acquisition range. Fig. 1(b) and (c) displays the architecture and a microscope image of the whole OPLL system, respectively. The PIC, electronic ICs and the loop filter are all integrated on an aluminum nitride (AlN) carrier, and wire-bonded. The system size is approximately 1.8 cm by 1.6 cm. Total delay is less than 300 ps, and the loop bandwidth is approximately 500 MHz.

2. Results and Discussion

Total power consumption of the OPLL system excluding the thermoelectric controller power is measured to be 1.318 W, which is the lowest power consumption for an OPLL to the best of authors' knowledge. In this system, the PIC consumes only 166 mW, and the COTS control electronics consume 1.152 W. Table 1 demonstrates the power consumption of every component and the total power consumption. This result is considerably better than the previous result reported in [2].

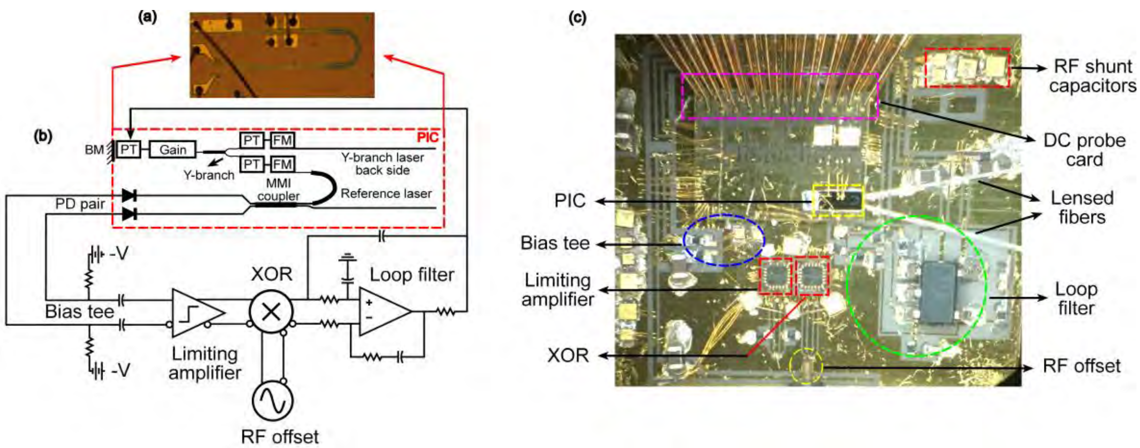

Figure 1. (a) An optical microscope picture of the PIC, (b) the schematic of the receiver PIC with the architecture of the OPLL system, and (c) a microscope picture of the OPLL system (PT: phase tuner, FM: Front mirror, BM: Back mirror, PIC: photonic integrated circuit, PD: photodiode)

Table 1. Power consumption of individual components and the total OPLL system

Photonic Integrated Circuit (Component / Power (W))	Gain	Phase tuner	Photodiodes	Total
	0.154 W	0.008 W	0.004 W	0.166 W
Electronic Integrated Circuits (Component / Power (W))	**Limiting Amplifier**	**XOR**	**Op-amp**	**Total**
	0.594 W	0.462 W	0.096 W	1.152 W
Total Power Consumption				**1.318 W**

Experimental setup shown in Fig. 2 was prepared in order to demonstrate the offset locking. The reference ECL was coupled into the PIC using lensed fiber and added to the tunable laser output from the lower Y-branch arm in the MMI coupler. Light from the top arm of the Y-branch laser was coupled out of the PIC for monitoring purposes. The optical spectrum of the reference laser together with that from the Y-branch laser were measured by an optical spectrum analyzer (OSA). At the same time their beat-note was measured by an electrical spectrum analyzer (ESA) through a high speed photodiode.

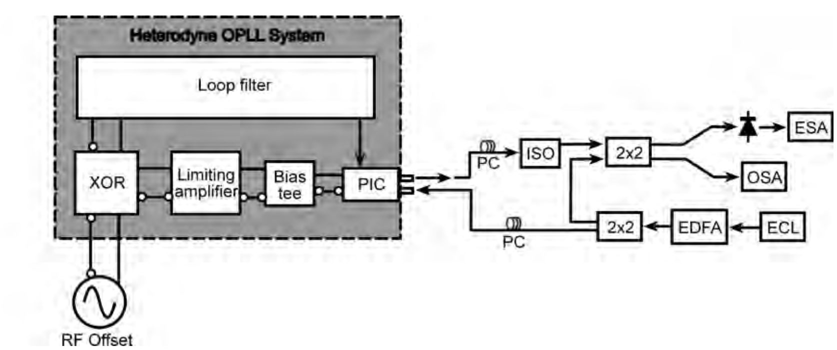

Figure 2. The test setup of the OPLL system. (ECL: external cavity laser, ESA: electrical spectrum analyzer, OSA: optical spectrum analyzer, PC: polarization controller, ISO: isolator)

The experiment demonstrates phase locking between the Y-branch laser and the reference laser. Fig. 3(a) shows the optical spectrum when the Y-branch laser and the reference laser are offset locked at 11 GHz, as determined by the RF frequency synthesizer. The OSA spectral separation between the lasers is ~ 0.09 nm which corresponds to 11 GHz. The beating tone of the locked lasers is shown in Fig. 3(b) both before and after the locking circuit is activated. The relative linewidth of the locked beat note at 11 GHz is in the order of sub-Hz, which is limited by the resolution bandwidth of the ESA. The beat note has a linewidth in the order of a MHz before the locking—that of the unlocked Y-branch laser. (With 20 km of fiber between the upper and lower external 2x2 couplers to de-correlate the ECL from the PIC output in time, the locked PIC linewidth becomes ~ 100 kHz—that of the ECL.) Fig. 3(c) shows a series of electrical spectra for the different offset locking conditions up to 17.4 GHz. Observed noise peaks are 400-500 MHz away from the main peak, and this suggests that the loop bandwidth of the system is approximately 400-500 MHz.

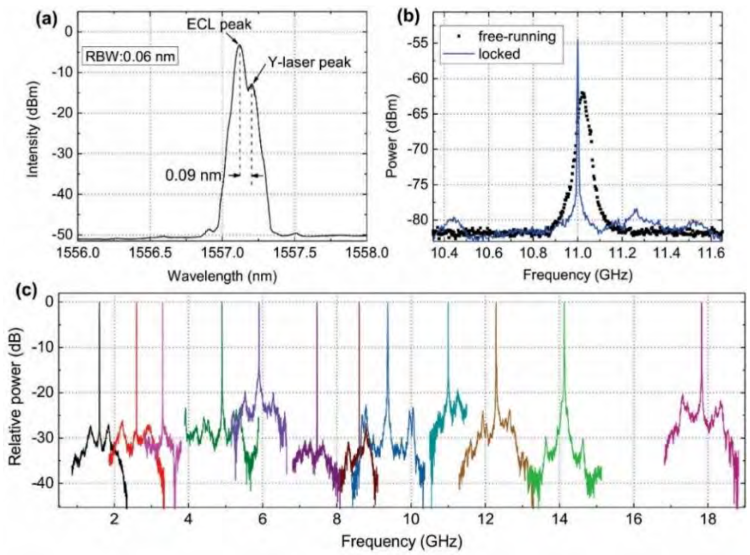

Figure 3. (a) The optical spectrum when the Y-branch laser and the ECL are offset locked at 11 GHz with a wavelength separation of 0.09 nm; (b) corresponding RF spectra measured at a 100 kHz resolution bandwidth (RBW), showing the locked beat note together with the unlocked case at 11 GHz, and (c) offset locking at multiple frequencies at a RBW of 3 MHz

3. Conclusion and Future Work

In this paper, a highly integrated heterodyne OPLL with a record power consumption of 1.3 W is demonstrated and on-chip widely-tunable Y-branch laser is offset locked to ECL up to a range of 17.4 GHz. This OPLL can be used in coherent receivers and optical frequency synthesizers. Without using any complicated digital signal processors (DSP) and high-speed analog-to-digital converters (ADC); low cost, low power short to modest distance communication systems can be realized using this kind of OPLL. In addition, this OPLL can create an opportunity to create chip level optical frequency synthesis with low power consumption.

With some straight-forward improvements in the COTS electronics, we expect to reduce the power consumption to below a Watt. Furthermore, application specific ICs consuming a few hundreds of mW power levels can be designed by using lower node CMOS processes, and this should enable such an OPLL with less than half a Watt of power consumption. If this system were to be interfaced with a self-referenced micro-resonator based optical frequency comb generator, a wide-band optical frequency synthesizer with a total volume of less than a cubic centimeter and a total power consumption of less than a Watt should be possible. This will create a new era in optical communication, sensing and imaging.

Acknowledgement

This work was supported by DARPA-MTO under the DODOS Project. A portion of this work was carried out in the UCSB nanofabrication facility, part of the NSF funded NNIN network.

4. References

[1] S. Ristic, A. Bhardwaj, M. J. Rodwell, L. A. Coldren, and L. A. Johansson, “An optical phase-locked loop photonic integrated circuit,” J. Lightwave Technol. **28**, 526–538 (2010).

[2] H. Park, M. Lu, E. Bloch, T. Reed, Z. Griffith, L. A. Johansson, L. A. Coldren, and M. J. Rodwell, "40Gbit/s coherent optical receiver using a Costas loop," Opt. Express **20**, B197-B203 (2012).

[3] K. Balakier, M. J. Fice, L. Ponnampalan, A. J. Seeds, and C. C. Renaud, “Monolithically integrated optical phase lock loop for microwave photonics,” J. Lightwave Technol. **32**, 3893-3900 (2014).

[4] R. J. Steed, L. Ponnampalam, M. J. Fice, C. C. Renaud, D. C. Rogers, D. G. Moodie, G. D. Maxwell, I. F. Lealman, M. J. Robertson, L. Pavlovic, L. Naglic, M. Vidmar, and A. J. Seeds, “Hybrid integrated optical phase-lock loops for photonic terahertz sources,”, J. Sel. Topics Quantum Electron. **17**, 210-217 (2011).

[5] M. Lu, H. Park, E. Bloch, L. A. Johansson, M. J. Rodwell, and L. A. Coldren, “A highly-integrated optical frequency synthesizer based on phase-locked loops,” in *Optical Fiber Communication Conference*, OSA Technical Digest (online) (Optical Society of America, 2014), paper W1G.4

[6] M. Lu, H. Park, E. Bloch, L. A. Johansson, M. J. Rodwell, and L. A. Coldren, "An integrated heterodyne optical phase-locked loop with record offset locking frequency," in *Optical Fiber Communication Conference*, OSA Technical Digest (online) (Optical Society of America, 2014), paper Tu2H.4.

Optics Letters

Heterodyne locking of a fully integrated optical phase-locked loop with on-chip modulators

Shamsul Arafin,[1,*] Arda Simsek,[1] Mingzhi Lu,[1,2] Mark J. Rodwell,[1] and Larry A. Coldren[1,3]

[1]*Department of Electrical and Computer Engineering, University of California, Santa Barbara, California 93106, USA*
[2]*Currently at Infinera Corp., Sunnyvale, California 94089, USA*
[3]*e-mail: coldren@ece.ucsb.edu*
**Corresponding author: sarafin@ucsb.edu*

Received 7 July 2017; revised 24 August 2017; accepted 28 August 2017; posted 29 August 2017 (Doc. ID 301996); published 19 September 2017

We design and experimentally demonstrate a highly integrated heterodyne optical phase-locked loop (OPLL) consisting of an InP-based coherent photonic receiver, high-speed feedback electronics, and an RF synthesizer. Such coherent photonic integrated circuits contain two widely tunable lasers, semiconductor optical amplifiers, phase modulators, and a pair of balanced photodetectors. Offset phase-locking of the two lasers is achieved by applying an RF signal to an on-chip optical phase modulator following one of the lasers and locking the other one to a resulting optical sideband. Offset locking frequency range >16 GHz is achieved for such a highly sensitive OPLL system which can employ up to the third-order-harmonic optical sidebands for locking. Furthermore, the rms phase error between the two lasers is measured to be 8°.

OCIS codes: (250.5300) Photonic integrated circuits; (060.5625) Radio frequency photonics; (060.2840) Heterodyne; (140.0140) Lasers and laser optics; (140.3600) Lasers, tunable; (140.3945) Microcavities.

https://doi.org/10.1364/OL.42.003745

There has been a great deal of interest in millimeter/micro/terahertz-wave photonic link technology to enable a number of applications including broadband wireless communication [1] and optically fed phased-array antenna beamformers [2]. As a counterpart of noncoherent direct detection in these fiber-optic links [3], coherent remote heterodyne detection (RHD) technique offers a number of advantages, such as higher link gain and carrier to noise ratio, as well as lower sensitivity to chromatic dispersion [4]. Most importantly, one of the major building blocks in such RHD-based photonic links is the highly integrated and low-power photonic transmitter at the base station [5]. According to the RHD principle, two phase-correlated laser signals with a certain frequency offset are generated by a dual-frequency laser transmitter. Both laser signals are transmitted through the fiber link, and finally, they are mixed in a photodetector at the receiver end.

A heterodyne optical phase-locked loop (OPLL) [6] is one of the most attractive and effective techniques for achieving offset phase-locking between these two lasers of the transmitter. This suggests that a successful realization of the highly integrated OPLL is a prime requirement for developing an efficient photonic transmitter. Highly integrated heterodyne OPLLs, consisting of coherent photonic integrated receiver circuits with two widely tunable lasers, optical couplers, and a pair of balanced photodetectors—all monolithically integrated together with short delay, high-speed feedback electronics, and a tunable RF synthesizer—have been explored previously [7].

There are two techniques that could be adopted for such heterodyne locking [8]. As a first technique, the RF signal can be applied to an electronic mixer following optical detection in the feedback electronics and the RF difference frequency used for offset locking. Another technique is to apply the RF to an on-chip optical modulator monolithically integrated on the photonic receiver following one of the tunable lasers and to achieve the offset locking using an optical sideband.

There are a number of reports [6,9] that employ the former technique for demonstrating the offset locking, paving for the way to energy-efficient photonic transmitter. Due to the electronic mixer used in the first technique, the OPLL system, however, requires roughly ~0.5 W more electrical power and extra space compared to a system based on the latter technique. In contrast, the small-area on-chip optical phase modulator operated in reverse bias requires considerably less power. Ristic *et al.* have already employed the second technique as a proof of principle demonstration of locking two sampled-grating distributed Bragg reflector (SG-DBR) lasers in InP-based photonic integrated circuits [10]. However, the OPLL system presented there suffered from small loop bandwidth, a narrow offset-locking range of 5 GHz, and slow feedback electronics with a single-ended signal coming from a photodetector.

In this Letter, we report the second technique using refined InP-based photonic integrated circuits by properly positioning the on-chip modulators for applying the RF. Agile and highly sensitive feedback electronics with a unity-gain open-loop bandwidth of 500 MHz was used [11], which utilize two photodetectors as a balanced pair. Offset locking frequency range on the order of >16 GHz is achieved in the system which can employ up to the third-order-harmonic optical sidebands for locking. A reduced phase noise of the OPLL is also obtained.

0146-9592/17/193745-04 Journal © 2017 Optical Society of America

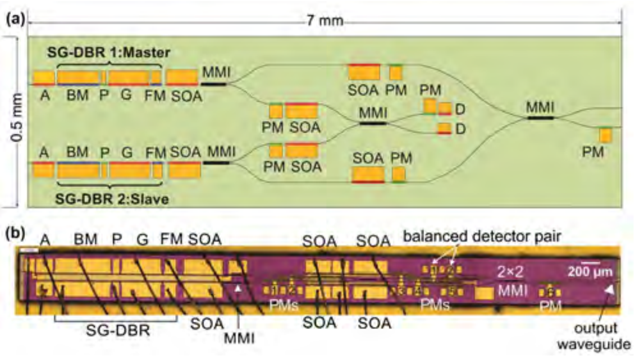

Fig. 1. Functional schematic of the coherent photonic integrated receiver circuit composed of two SG-DBR lasers, MMI couplers/splitters, SOAs, phase modulators, and a balanced photodetector pair, and (b) microscope image of the fully processed PIC mounted on a separate AlN carrier and wirebonded. (A, absorber; BM, back mirror; D, photodetector; FM, front mirror; G, gain; MMI, multimode interference; P, phase tuner; PM, phase modulators; SOA, semiconductor optical amplifier.)

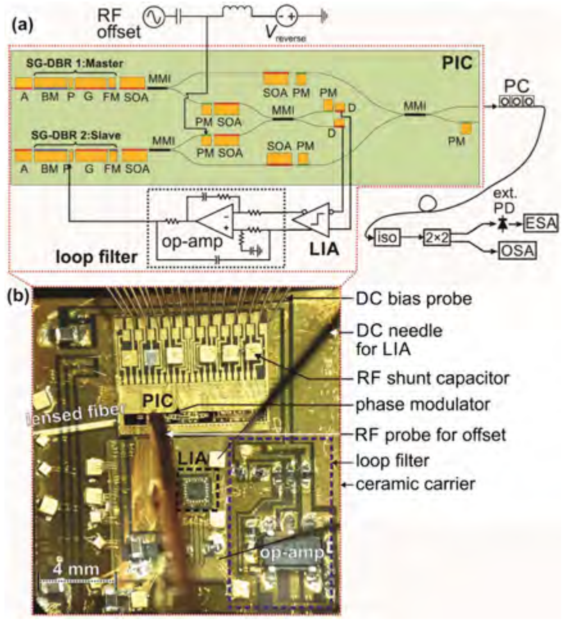

Fig. 2. (a) Test setup of the heterodyne OPLL system for confirming the phase-locking between two SG-DBR lasers. (ESA, electrical spectrum analyzer; OSA, optical spectrum analyzer; PC, polarization controller; iso, isolator; ext. PD, external photodetector; LIA, limiting amplifier; PIC, photonic integrated circuit.) (b) Optical microscope image of the OPLL system including PIC, limiting amplifier (LIA), and loop filter on a separate AlN carrier.

Figure 1(a) shows a schematic of the coherent optical receiver photonic integrated circuit (PIC) used for OPLL. It includes two widely tunable SG-DBR lasers that are to be offset locked, multimode interference (MMI) couplers, semiconductor optical amplifiers (SOAs), photodetectors, and six optical modulators. Given the wide tuning range, exceeding 40 nm in both on-chip lasers, laser outputs with frequency offsets from DC to 5 THz are possible. Among the modulators in the chip, two are for offset locking, one is for adding phase adjustments in the feedback loop, and the remaining three are for possible imposition of data on one of the two carriers that exit the chip on the right. The chip size is 7 mm × 0.5 mm.

As can be seen, light from each laser is first equally divided into two portions using 1 × 2 MMIs. One half from each laser is guided into a central 2 × 2 MMI, which is a part of the feedback loop. Each input arm of the 2 × 2 MMI contains a phase modulator that is used for applying the RF to generate optical sidebands. After combining these two lasers in the MMI coupler, light signals are detected in a pair of photodetectors (D) with a balanced receiver configuration. The other half from each laser is directed through a power boosting SOA and an optional RF signal encoding phase modulator into a 2 × 2 MMI at the far right side of the OPLL-PIC, where there are also outputs to fibers. In these experiments, these outputs are useful for monitoring the interference resulting from the beating of the two SG-DBR lasers. In practical use, these would be the outputs that would be used for RF signal remoting.

An optical microscope photo of the fully processed PIC on an InGaAsP/InP material platform is shown in Fig. 1(b). The process used to fabricate the devices is quantum-well intermixing (QWI) that creates self-aligned passive regions by intermixing the quantum-wells with their barriers and surrounding waveguide material by a patterned diffusion of implanted phosphorus ions after a first growth. Details of the processing steps for the well-established QWI-based material structure can be found elsewhere [12].

In these heterodyne OPLL experiments, one of the integrated SG-DBR lasers was used as a master, with the other as a slave to be offset phase-locked to the former. Prior to combining the outputs of these two lasers using the central 2 × 2 optical coupler, the output of the slave SG-DBR laser was intensity-modulated for offset locking using an RF offset frequency applied to its integrated on-chip modulator to create sidebands. The on-chip photodetectors generated a current response proportional to the difference frequency between the master laser and the selected sideband to which the slave laser was open-loop tuned. This current was amplified and filtered through the feedback electronics and fed back to the phase tuning section (P) of the slave laser, as schematically illustrated in Fig. 2(a). With sufficient gain in the limiting amplifier and proper integration in the loop filter, the difference frequency was driven to zero, and the phase difference between the master and slave laser fields was minimized.

Figure 2(b) shows an optical image of the assembled heterodyne OPLL system, including the PIC and the feedback electronic circuits. The electronic circuits were built by integrating a SiGe-based limiting amplifier (LIA) manufactured by ADSANTEC [13] and discrete loop filter components. These three parts were tightly integrated on a patterned aluminum-nitride (AlN) carrier by wirebonding. A DC-coupled system was prepared, since the photodetectors require reverse biasing by 2 V, which was provided from the electronic circuits. In fact, due to current mode logic (CML)-type inputs of LIA, together with the 50 Ω loads and off-chip level-shifting diodes, the LIA develops −2 V input voltage through self-biasing. In other words, the LIA directly interfaces to the PIC by reverse biasing the photodetectors by 2 V.

To summarize, the random phase variation between the two lasers translates into intensity-modulated error signals at the outputs of the 2 × 2 MMI in the PIC and finally into current error signals at the output of the photodetectors. The error signals generated by these reverse biased photodetectors were amplified by the LIA and filtered by the loop filter. Finally, the filtered output is converted into current signals needed to control the injection of carriers into the forward-biased phase section of the slave SG-DBR laser.

To demonstrate offset locking of the slave laser to the master laser, the inner optical modulator after the 1 × 2 MMI following the slave laser was reverse biased using a bias tee. Based on the Franz–Keldysh effect through reverse bias modulation, this electro-absorption modulator generates multiple optical sidebands after applying the RF signal into it. The amount of reverse bias and magnitude of the RF determines what intensity modulation is obtained versus phase modulation. Mixing the slave laser and its associated sidebands with the master laser occurs in the photodetectors, which generate corresponding current error signals to the feedback electronics. Since the loop bandwidth of the OPLL is ∼500 MHz, only the nearest sideband(s) is amplified and fed to the phase section of the slave laser as an error signal. When the frequency separation between the two SG-DBR lasers equals the modulation frequency, the detected photocurrent will contain a phase-dependent DC component, and sideband locking of the slave laser to the master becomes possible. It should be noted that the power in the sidebands is smaller in comparison to the power at the center frequencies of the slave laser.

The combined beat signal of the slave and master lasers was coupled out from the output waveguide of the PIC using a lensed fiber for monitoring purposes. An optical isolator was used at the combined output to reduce back reflections. To measure the OPLL tone, the combined optical output passes through an off-chip 2 × 2 coupler. One output was detected via an external high-speed photodetector and measured on the electrical spectrum analyzer (ESA). The other output of this coupler was connected to the optical spectrum analyzer (OSA) to measure the optical spectra of the lasers.

Prior to performing the phase-locking between these lasers, it is important to know the optimum bias point of the on-chip modulator in order to obtain maximum modulation efficiency. Figure 3(a) shows the slave SG-DBR laser output power versus reverse bias voltage applied to the on-chip modulators located at the inner output part of the 1 × 2 MMI followed by the slave laser. Based on the characteristics shown here, approximately −3.5 V is found to be the optimum bias point of significant absorption at which the modulator was driven with strong RF signal to obtain strong sidebands beside the optical carrier and a reasonably good extinction ratio. In this case, both intensity (I) and phase modulation (PM) result. However, intensity modulation (IM) generates better sidebands than PM, considering that the on-chip modulator is driven by a strong RF tone that cannot be done without the large reverse bias. Hence, this of necessity puts our modulator in the IM regime.

Figure 3(b) shows the optical spectra of the same laser modulated at two different modulation frequencies, when the RF power of the modulation signal is kept at 17 dBm. At a modulation frequency of 10 GHz, a number of sidebands are generated with intensity comparable to that of the optical carrier. The ratio of 5 dB for the optical carrier to the first-order sideband is enough for our offset locking experiments. On the other hand, when the laser is modulated at 20 GHz, a fewer number of sidebands with reduced intensity can be observed, that is, the ratio of −8.5 dB of the first-order sideband with respect to the optical carrier is obtained. Please note that a customized GSG RF probe with a 50 Ω terminating resistor and a copper heat sink was used to launch the high-power RF signal into the reverse-biased modulator.

Figure 4(a) shows the optical spectrum when the two on-chip lasers are offset locked at ∼3.1 GHz, as determined by the RF frequency synthesizer. The OSA spectral separation between the lasers is ∼0.03 nm, which corresponds to ∼3.1 GHz. The beating tone of the locked lasers is shown in Fig. 4(b) both before and after the locking circuit is activated. The beat note has a linewidth on the order of MHz before the phase-locking. After offset phase-locking, the differential linewidth is reduced significantly, indicating strong phase-correlation between the two lasers.

Figure 5 shows a series of electrical spectra for the different offset locking conditions up to the fundamental RF frequency of 16.3 GHz. By changing the RF reference frequency to the on-chip optical modulator, these heterodyne locking conditions were obtained. The higher the offset locking range, the easier it becomes for the OPLL to track the reference signal over a broad range of frequencies. The offset locking range, pull-in range, and hold-in range of our heterodyne OPLL are measured to be ∼16 GHz, 1.2 GHz, and 1.4 GHz, respectively.

With deep phase modulation of the integrated modulator, it is possible to generate a number of side bands, and such modulators can be made with bandwidths up to ∼100 GHz [14,15], so it is anticipated that such offset locking might be possible up to the THz range without having to generate RF higher than 100 GHz. Using our heterodyne OPLL system, offset phase-locking of the lasers up to the third-order harmonic optical sidebands is obtained, as shown in Fig. 6.

The locked beat note at 2.3 GHz produced between the on-chip lasers was connected to the ESA, and the residual phase

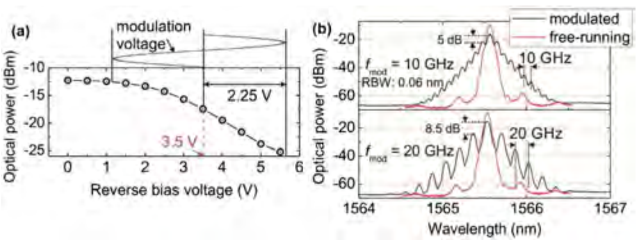

Fig. 3. Optical output power of the slave laser against reverse bias voltage applied into electro-absorption phase modulators in the PIC, and (b) optical spectra of the same laser at two different modulation frequencies applied into modulator biased at a voltage of −3.5 V.

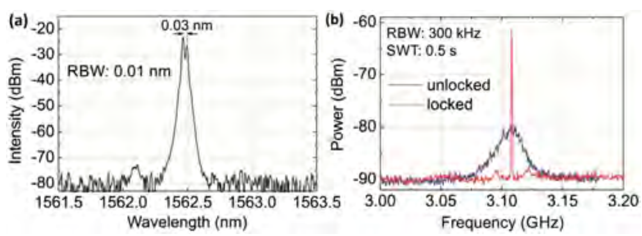

Fig. 4. (a) Optical spectrum when the two on-chip lasers that are offset locked to each other, and (b) RF spectrum of the locked beatnote between these lasers at 3.1 GHz. RBW, resolution bandwidth; SWT, sweeping time.

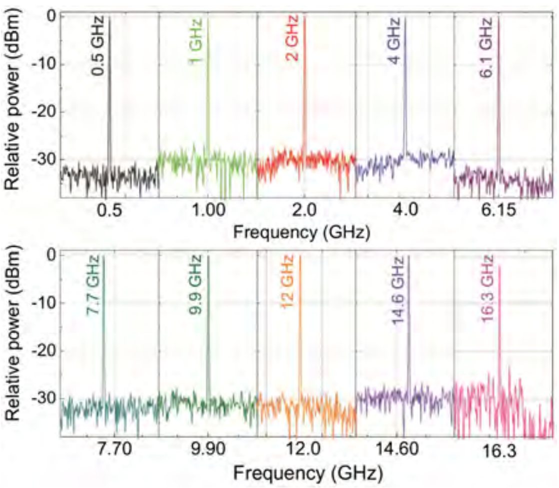

Fig. 5. Offset locking demonstrated at different offset frequencies.

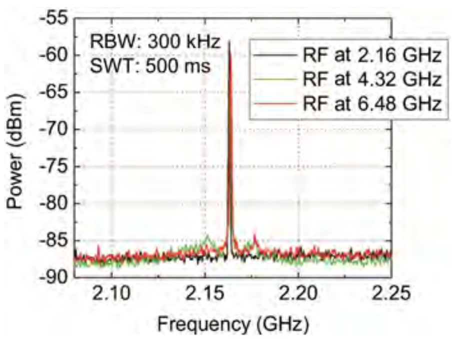

Fig. 6. Offset locking demonstrated at a fundamental RF offset frequency and up to the third harmonics.

noise spectral density (PNSD) was measured from 10 Hz to 1 GHz, as shown in Fig. 7. With a balanced photodetector pair on the chip, as well as their utilization through differential limiting amplifier based electronics, reduced noise in the feedback loop was observed. This is evidenced by the phase noise variance from 10 Hz to 1 GHz, which is calculated to be 0.02 rad^2, corresponding to 8° standard deviation from the locking point. The OPLL phase noise at low frequencies exhibits more

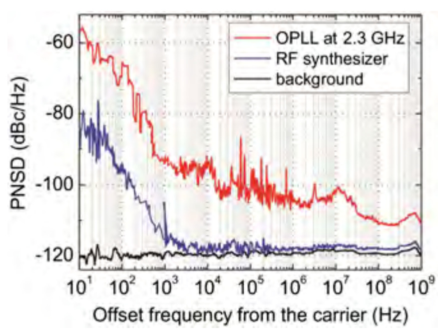

Fig. 7. Single-sideband residual phase noise of the heterodyne OPLL. Phase noise of the RF synthesizer and background are also shown here for comparison.

noise compared to the RF source. This low frequency noise component is believed to be introduced by the measurement setup, such as fiber vibration and AM-to-PM conversion in the ESA, rather than the OPLL system itself [12]. The phase noise at high frequencies might be caused by the relative intensity noise of the laser.

In this work, we have successfully demonstrated a highly integrated OPLL by employing PICs with all optical master and slave SG-DBR lasers, high-speed modulators, high-speed photo detectors, MMI couplers, and interconnecting optical waveguides. An experiment to demonstrate offset (up to ~16 GHz) locking of the master and slave SG-DBR lasers is performed. Future works involve the use of high bandwidth on-chip phase modulators and high-gain limiting amplifier in order to achieve offset locking with higher-order-harmonic optical sidebands. Hence, our OPLL is expected to generate phase stable optical beat at very high frequencies.

Funding. GOALI project, National Science Foundation (NSF) (1402935).

REFERENCES

1. T. Nagatsuma, S. Horiguchi, Y. Minamikata, Y. Yoshimizu, S. Hisatake, S. Kuwano, N. Yoshimoto, J. Terada, and H. Takahashi, Opt. Express **21**, 23736 (2013).
2. L. N. Langley, M. D. Elkin, C. Edge, M. J. Wale, U. Gliese, X. Huang, and A. J. Seeds, IEEE Trans. Microwave Theory Tech. **47**, 1257 (1999).
3. Z. Qiang, X. Changsong, N. Stojanovic, G. Goeger, S. Chun, F. Yuanyuan, Z. Enbo, L. Gordon Ning, and X. Xiaogeng, in *Opto-Electronics and Communications Conference* (IEEE, 2015), paper JTuA.41.
4. U. Gliese, T. N. Nielsen, S. Nørskov, and K. E. Stubkjær, IEEE Trans. Microwave Theory Tech. **46**, 458 (1998).
5. Y. Shoji, IEICE Trans. Electron. **E88-C**, 1465 (2005).
6. S. Arafin, A. Simsek, S. K. Kim, S. Dwivedi, W. Liang, D. Eliyahu, J. Klamkin, A. Matsko, L. Johansson, L. Maleki, M. Rodwell, and L. A. Coldren, Opt. Express **25**, 681 (2017).
7. K. Balakier, L. Ponnampalam, M. J. Fice, C. C. Renaud, and A. J. Seeds, IEEE J. Sel. Top. Quantum Electron. **24**, 1 (2017).
8. L. A. Coldren, M. Lu, J. Parker, L. Johansson, S. Arafin, D. Dadic, and M. J. Rodwell, *Advanced Photonics Congress* (Optical Society of America, 2016), paper JM1A.2.
9. S. Arafin, A. Simsek, S. K. Kim, W. Liang, D. Eliyahu, G. Morrison, M. Mashanovitch, A. Matsko, L. Johansson, L. Maleki, M. J. Rodwell, and L. A. Coldren, IEEE Photon. J. **9**, 1 (2017).
10. S. Ristic, A. Bhardwaj, M. J. Rodwell, L. A. Coldren, and L. A. Johansson, J. Lightwave Technol. **28**, 526 (2010).
11. A. Simsek, S. Arafin, S.-K. Kim, G. Morrison, L. A. Johansson, M. Mashanovitch, L. A. Coldren, and M. J. Rodwell, *Optical Fiber Communication Conference* (Optical Society of America, 2017), paper W4G.3.
12. M. Lu, "Electrical and computer engineering," Ph.D. dissertation (University of California Santa Barbara, 2013).
13. http://www.adsantec.com/344-asnt5020-bd.html.
14. Y. Ogiso, J. Ozaki, Y. Ueda, N. Kashio, N. Kikuchi, E. Yamada, H. Tanobe, S. Kanazawa, H. Yamazaki, Y. Ohiso, T. Fujii, and M. Kohtoku, J. Lightwave Technol. **35**, 1450 (2017).
15. P. Evans, M. Fisher, R. Malendevich, A. James, G. Goldfarb, T. Vallaitis, M. Kato, P. Samra, S. Corzine, E. Strzelecka, P. Studenkov, R. Salvatore, F. Sedgwick, M. Kuntz, V. Lal, D. Lambert, A. Dentai, D. Pavinski, J. Zhang, J. Cornelius, T. Tsai, B. Behnia, J. Bostak, V. Dominic, A. Nilsson, B. Taylor, J. Rahn, S. Sanders, H. Sun, K.-T. Wu, J. Pleumeekers, R. Muthiah, M. Missey, R. Schneider, J. Stewart, M. Reffle, T. Butrie, R. Nagarajan, M. Ziari, F. Kish, and D. Welch, Opt. Express **19**, B154 (2011).

This article has been accepted for publication in a future issue of this journal, but has not been fully edited. Content may change prior to final publication. Citation information: DOI 10.1109/JLT.2017.2758744, Journal of Lightwave Technology

Evolution of Chip-Scale Heterodyne Optical Phase-Locked Loops towards Watt Level Power Consumption

Arda Simsek, *Student Member, IEEE,* Shamsul Arafin, *Senior Member, IEEE,* Seong-Kyun Kim, Gordon Morrison, Leif A. Johansson, Milan Mashanovitch, Larry A. Coldren, *Life Fellow, IEEE,* and Mark J. Rodwell, *Fellow, IEEE*

***Abstract*—We design and experimentally demonstrate two chip-scale and agile heterodyne optical phase-locked loops (OPLLs) based on two types of InP-based photonic integrated coherent receiver circuits. The system performance of the first generation OPLL was improved in terms of offset-locking range, and power consumption with the use of a power-efficient and compact photonic integrated circuit (PIC). The second generation PIC consists of a 60 nm widely-tunable Y-branch laser as a local oscillator with a 2×2 MMI coupler and a pair of balanced photodetectors. This PIC consumes only 184 mW power in full operation, which is a factor of 3 less compared to the first generation PIC. In addition, the sensitivity of these OPLLs was experimentally measured to be as low as 20 µw. A possible solution to increase the sensitivity of these OPLLs is also suggested.**

***Index Terms*—Photonic integrated circuits, optical phase-locked loop, heterodyne, integrated optics**

I. Introduction

Optical phase-locked loops (OPLLs) have been of great interest for the last couple of decades due to the promising applications in the areas of communications, sensing and frequency control [1, 2]. These applications include short to medium range coherent optical communications [3], laser linewidth narrowing [4-6], terahertz signal generation [6, 7] and optical frequency synthesis [8-11]. With the improvements in the photonic integration, OPLLs became more attractive since they can offer small loop delay, which allows having OPLLs with loop bandwidths as large as 1.1 GHz [3]. However, these prior OPLLs consume almost 3 Watts of electrical power [3]. This high-power consumption makes the use of OPLLs in practical applications questionable.

Manuscript received July 1, 2017; revised August 23, 2017; accepted September 25, 2017. This work was supported by DARPA-MTO under the DODOS Project, and National Science Foundation under Grant No. 1402935.

A. Simsek, S. Arafin, L. A. Coldren and M. J. Rodwell are with the Department of Electrical and Computer Engineering, University of California, Santa Barbara, CA 93106 USA (email: ardasimsek@ece.ucsb.edu).

S. K. Kim is with Teledyne Scientific and Imaging Company, Thousand Oaks, 1049 Camino Dos Rios, CA, 91360 USA.

G. Morrison, L. A. Johansson, and M. Mashanovitch are with Freedom Photonics, LLC, Santa Barbara, CA 93117 USA.

Therefore, realizing a low-power consumption OPLL is important to take advantage of recent advances in photonic integration. A chip-scale, compact, low power consumption OPLL can push the technology in the aforementioned application areas further forward. With the proper design of compact photonic integrated circuits (PICs), power consumption in such PICs, therefore OPLLs, can be lowered [12]. In this work, two chip-scale, highly-integrated OPLLs are designed and experimentally demonstrated using two different InP-based photonic integrated coherent receiver circuits.

After successfully achieving OPLLs with reasonable offset locking range and power consumption, a detailed sensitivity analysis and some relevant experiments were performed. A minimum input optical power to demonstrate the phase-locking using our OPLLs was measured as 20 µw both theoretically and experimentally. A novel solution is proposed that can be implemented in such OPLLs in order to lock input power levels as low as nanowatts.

This paper is organized as follows. This paper begins with a short summary of OPLL system design together with the PIC design. We then present the experimental results for the first, and second generation OPLL. After this, the power budget for both OPLLs is given. Finally, the sensitivity analysis and a proposed solution for high sensitivity OPLL is provided.

II. Optical Phase-Locked Loop System Design

A. PIC Design

Since two different types of PICs are used in this study for demonstrating heterodyne OPLLs, we have named them as gen-1 and gen-2 PICs for clarity. All active/passive components in these PICs are monolithically integrated on an InGaAsP/InP material platform. Details of the fabrication of such PICs can be found in [13, 14]. Microscope images of both PICs are shown in Fig. 1(a) and (b).

Out of two PICs, gen-1 PIC (see Fig. 1(a)) consists of 40 nm widely-tunable sampled-grating distributed-Bragg-reflector (SG-DBR) laser, 2×2 MMI coupler, a balanced photodetector pair and a couple of semiconductor optical amplifiers (SOAs) on reference and local-oscillator (LO) optical paths. Reference optical signal was coupled into this PIC using the upper arm and amplified by two SOAs. SG-

This article has been accepted for publication in a future issue of this journal, but has not been fully edited. Content may change prior to final publication. Citation information: DOI 10.1109/JLT.2017.2758744, Journal of Lightwave Technology

DBR laser output propagated in the lower arm. These two optical signals were combined in a 2×2 MMI coupler and mixed in a balanced photodetector pair to produce the beat note for the electronics part. The SG-DBR laser also has a second output from its backside for monitoring purposes.

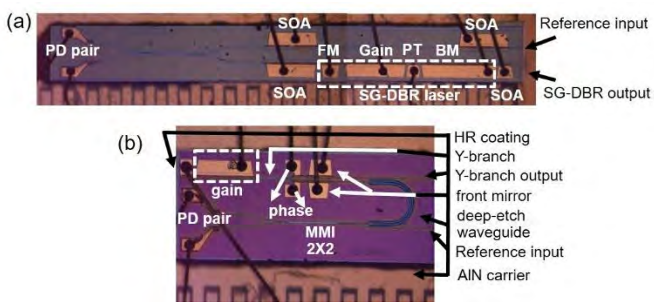

Fig. 1. (a) Microscope image of the gen-1 InP based PIC. (b) Microscope image of low power consumption gen-2 InP based PIC. (BM: back mirror, FM: front mirror, PD: photodiode, PT: phase tuner, SG-DBR: sampled-grating distributed-Bragg-reflector, and SOA: semiconductor optical amplifier)

Gen-2 PIC (see Fig. 1(b)) was designed for low power consumption. This PIC incorporates a widely tunable, compact Y-branch laser, formed between a high-reflectivity coated back cleaved mirror and a pair of Vernier tuned sampled-grating front mirrors, as well as a 2×2 MMI coupler and a balanced photodetector pair. The optical output from one of the front mirrors was connected to the MMI coupler, while the other output from another front mirror was used externally for monitoring the OPLL operation. The Y-branch laser has a compact cavity with short gain and mirror sections, requiring low current and therefore low drive power. It is tuned via Vernier effect and has been designed for high efficiency at 30º C. The measured tuning range exceeds 60 nm with >50 dB side-mode suppression ratio [15].

B. Feedback Electronics Design and OPLL Assembly

Both OPLLs use SiGe-based commercial-off-the-shelf (COTS) electronic ICs and loop filters built from discrete components as the control electronics. Figure 2 shows an exemplary OPLL system assembled by mounting gen-1 PIC and electronic components on a patterned AlN carrier.

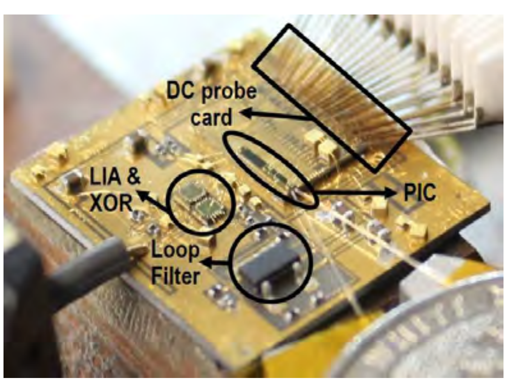

Fig. 2. OPLL system under measurement setup integrated on an AlN carrier including gen-1 PIC and control electronics

In this study, both OPLLs are designed to be heterodyne-type, which takes input offset frequency from external RF synthesizer and locks LO laser to the reference oscillator at this offset frequency. The second order loop filter with fast feedforward path was used in feedback electronics in order to get a high loop bandwidth. The circuit schematics of both OPLL systems can be seen in Fig. 3(a) and (b).

A limiting amplifier with 30 dB differential gain and 17 GHz 3-dB bandwidth, and a digital XOR gate functioning as a phase detector [16], together with an op-amp-based loop filter were used in the feedback electronics. The on-chip LO laser of the PIC was mixed via the external reference laser through the 2×2 MMI coupler and the PD pair to produce the beat note. This beat note then feeds the electronic ICs. First, it is amplified to logic levels through limiting amplifier and then mixed via external RF frequency synthesizer in order to produce an error signal. This error signal goes through the loop filter and feeds back to the phase-tuning section (PT) of on-chip LO laser. With sufficient feedback gain, this error signal becomes zero and LO laser is locked to external reference laser at given RF offset frequency.

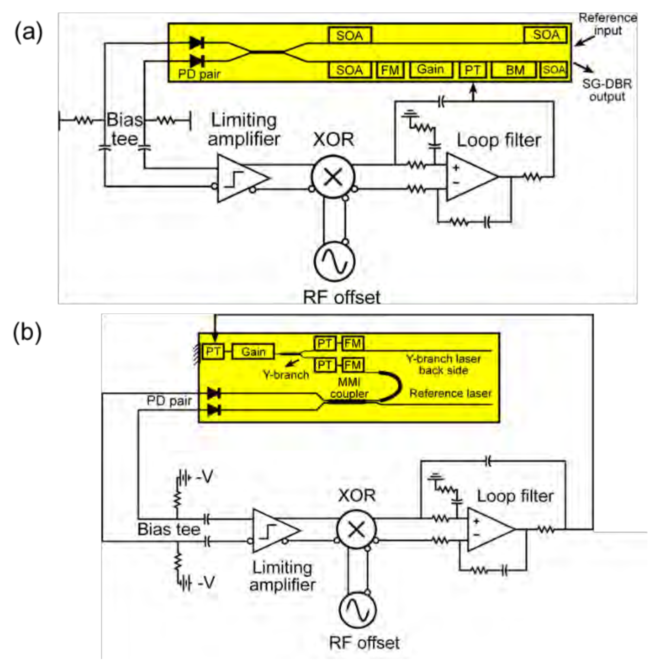

Fig. 3. (a) Circuit diagram of the first generation OPLL including gen-1 PIC in yellow and the control electronics. (b) Circuit diagram of the second generation OPLL including gen-2 PIC in yellow, and the control electronics. (BM: back mirror, FM: front mirror, PD: photodiode, PT: phase tuner, SG-DBR: sampled-grating distributed-Bragg-reflector, SOA: semiconductor optical amplifier)

Open loop transfer function of an OPLL can be written as a product of gain, and the time constants of the loop [17]. Therefore, open loop transfer function of both OPLLs in this work can be expressed as follows:

$$T(s) = K_{\mathrm{PD}} K_{\mathrm{CCO}} \frac{1}{(\tau_{\mathrm{laser}} s + 1)} e^{-\tau_{\mathrm{d}} s} \times \left(\frac{\tau_2 s + 1}{\tau_1 s} \frac{1/R_{out}}{\tau_{\mathrm{op}} s + 1} e^{-\tau_{\mathrm{dop}} s} + \frac{C_{\mathrm{FF}}}{2} \right)$$

This article has been accepted for publication in a future issue of this journal, but has not been fully edited. Content may change prior to final publication. Citation information: DOI 10.1109/JLT.2017.2758744, Journal of Lightwave Technology

where K_{PD} is the phase detection gain, K_{CCO} is the laser tuning sensitivity, τ_{laser} is the laser tuning frequency responsivity, τ_1 is the loop filter pole, τ_2 is the loop filter zero, τ_{OP} is the op-amp parasitic pole, R_{out} is the voltage to current conversion resistance at the output, C_{FF} is the feed-forward capacitor and τ_{dop} is the op-amp delay, and τ_{d} is the total loop delay. Here K_{PD} is a constant value $\left(2 * V_{\mathrm{log}ic} / \pi\right)$ due to the limiting amplifier, which makes the system loop bandwidth insensitive to the optical power level variations. This loop was designed to have a safe phase margin of around 50-60° at unity gain crossover frequency for both OPLLs in order to realize a robust and stable system.

III. First Generation OPLL Experimental Results

The experimental setup, as shown in Fig. 4, was used in order to demonstrate the offset locking with the OPLL using the gen-1 PIC. The reference external cavity laser (ECL) was coupled into the PIC using lensed fiber from the back side of the PIC. It was then combined with the tunable on-chip SG-DBR laser output in the MMI coupler and mixed to form the desired beat note in the PDs. Light from the SG-DBR laser was coupled out from the lower arm for monitoring purposes. The superimposed optical spectra of the reference laser together with on chip SG-DBR laser were measured by an optical spectrum analyzer (OSA). At the same time, the resulting RF beat-note was measured by an electrical spectrum analyzer (ESA) through a high speed photodiode.

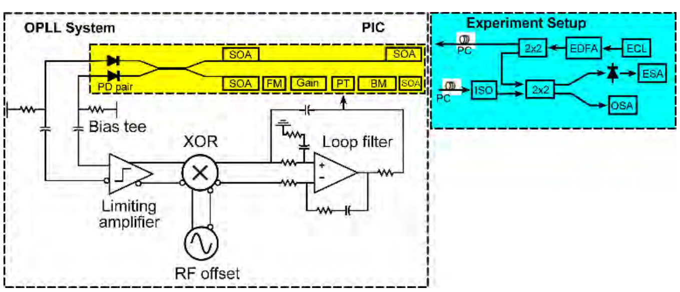

Fig. 4. (a) Experimental setup for the first generation OPLL system. (ECL: external cavity laser, ESA: electrical spectrum analyzer, OSA: optical spectrum analyzer, PC: polarization controller, ISO: isolator)

This experiment shows offset-phase locking between the on chip SG-DBR laser and the external cavity laser (ECL) as the reference. ECL used in this study has the optical linewidth of 100 kHz. Figure 5(a) demonstrates the optical spectrum when the reference laser and the on chip SG-DBR are offset locked at 6 GHz, which is determined by the RF frequency synthesizer. As can be seen in the figure, the separation between the two peaks are about 0.05 nm, which corresponds to 6 GHz frequency separation. In Fig. 5(b), the RF beat-note of the reference laser and the on chip SG-DBR laser is presented both in locked and unlocked cases. The relative linewidth of the locked beat note at 6 GHz is in the order of sub-Hz, which is limited by the resolution bandwidth of the ESA. It should be noted that the optical linewidth of our free-running on-chip laser is 10 MHz.

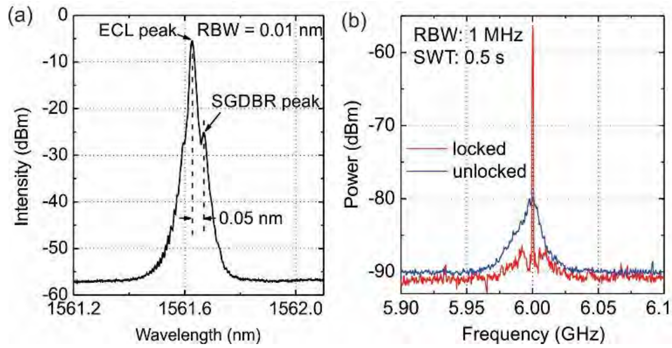

Fig. 5. (a) OSA spectrum when SGDBR is offset locked to the reference laser at 6 GHz offset, which corresponds 0.05 nm separation in optical domain. (b) Corresponding ESA spectrum when SGDBR is offset locked to the reference laser at 6 GHz offset, blue is before locking and red is after locking.

In order to measure the absolute linewidth of the locked beat note, the measurement was performed after adding 20 km of fiber between the upper and lower external 2x2 couplers to de-correlate the ECL from the SG-DBR. In this case, one would expect to get a linewidth of the RF beat note equal to the optical linewidth of the ECL. Figure 6 demonstrates this result. On chip SG-DBR is offset locked at 4.4 GHz, but this time long fiber is added to de-correlate the ECL from the SG-DBR. In this case, the absolute linewidth of the locked beat tone was measured as 100 kHz, indicating the linewidth cloning of the SG-DBR to the ECL.

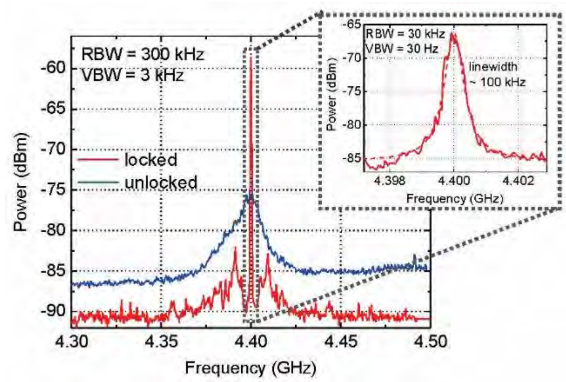

Fig. 6. (a) ESA spectrum when SG-DBR is offset locked to the reference laser at 4.4 GHz offset. In this case, ECL and SG-DBR are de-correlated using a long fiber. Therefore, relative linewidth of the beat note is equal to 100 kHz, which is the linewidth of the ECL (reference laser).

After proving the phase locking, the offset-locking range was demonstrated for different offset frequencies from 1.14 GHz up to 15.2 GHz as can be seen in Fig. 7. The higher the offset locking range, the easier it became for the OPLL to track the reference signal over a broad range of frequencies [18, 19].

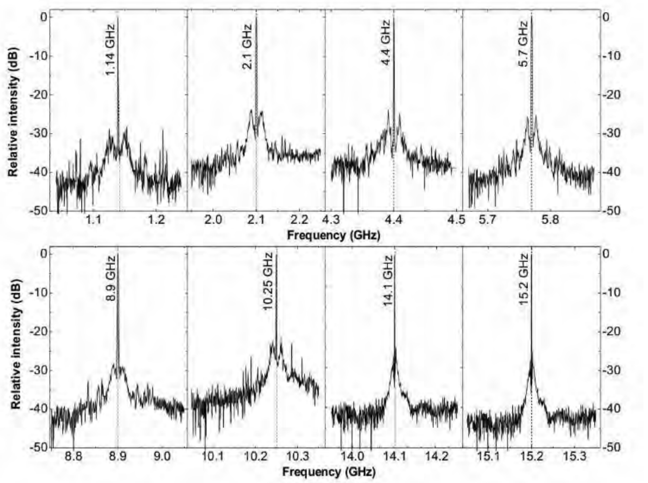

Fig. 7. (a) Offset locking at multiple frequencies with the first generation OPLL at a RBW of 3 MHz

IV. Second generation OPLL experimental results

Similar to the first generation OPLL, the experimental setup shown in Fig. 4 was used to demonstrate phase locking for the second generation OPLL. In this case, gen-1 PIC was replaced with the gen-2 PIC.

This experiment demonstrates phase locking between the on-chip Y-branch laser and the reference laser. Fig. 8(a) shows the optical spectrum when the reference laser and the on chip Y-branch laser are offset locked at 8.6 GHz, which is determined by the RF frequency synthesizer. As can be seen in the figure, the separation between the two peaks are about 0.07 nm, which corresponds to 8.6 GHz frequency separation. In Fig. 8(b), the RF beat-note between the reference laser and the on chip Y-branch laser is displayed both before the locking and after the locking. The relative linewidth of the locked beat note at 8.6 GHz is in the order of sub-Hz, which is limited by the resolution bandwidth of the ESA. The beat note has a relative linewidth in the order of a MHz before the locking, which is the unlocked Y-branch laser's linewidth [12].

With similar arguments presented for the first generation OPLL, one can add a long enough fiber at the output between the upper and lower external 2×2 couplers to de-correlate the ECL from the Y-branch laser and measure the actual linewidth of the beat note, which is equal to the linewidth of the ECL ~ 100 kHz.

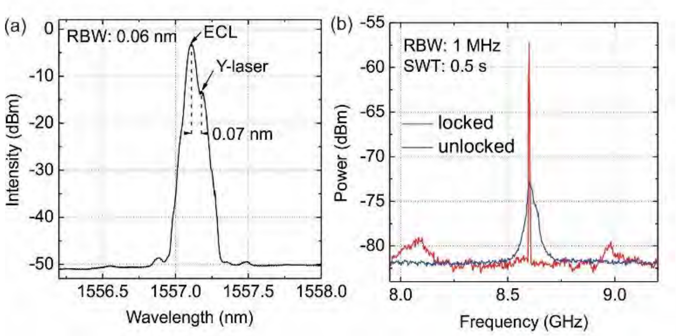

Fig. 8. (a) OSA spectrum when on chip Y-branch laser is offset locked to the reference laser at 8.6 GHz offset, which corresponds 0.07 nm separation in optical domain. (b) Corresponding ESA spectrum when Y-branch laser is offset locked to the reference laser at 8.6 GHz offset.

As the next experiment, several offset frequencies from 1 GHz to 20 GHz were applied from the RF frequency synthesizer, and the same phase locking experiment was performed. Figure 9 presents offset locking at several offset frequencies ranging from 1.6 GHz to 17.8 GHz.

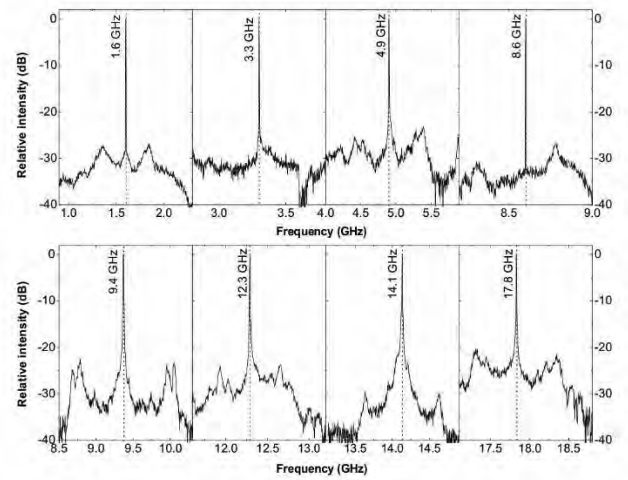

Fig. 9. Offset locking at multiple frequencies with the second generation OPLL at a RBW of 3 MHz

In addition to the phase locking experiments, the residual phase noise spectral density of the OPLL system was measured when on chip local oscillator is offset locked to the reference laser. Since the loop parameters and order were not changed from the OPLL with gen-1 PIC to the gen-2 based OPLL, we only provide phase noise spectrum of the former one. Figure 10 shows phase noise spectrum when on chip SG-DBR laser is offset locked to reference ECL at 2.5 GHz. This figure also demonstrates the ESA background and RF synthesizer phase noise spectrum at 2.5 GHz. The phase noise variance is calculated to be 0.067 rad^2 from 1 kHz to 10 GHz offset interval. This corresponds to 14.8° standard deviation from the locking point. This OPLL achieves -100 dBc/Hz phase noise at offset of 5 kHz. These results are comparable with the state of the art results in [20, 21].

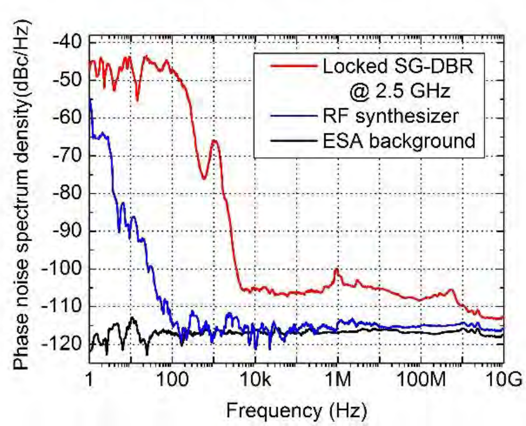

Fig. 10. Single-sideband residual phase noise of the heterodyne OPLL at 2.5 GHz offset locking. Phase noise results of the RF synthesizer at 2.5 GHz, and background is also shown here.

This article has been accepted for publication in a future issue of this journal, but has not been fully edited. Content may change prior to final publication. Citation information: DOI 10.1109/JLT.2017.2758744, Journal of Lightwave Technology

For our OPLL system, the time domain equivalent of the phase error variance is equal to the timing jitter in the frequency range from 1 kHz to 10 GHz [22], which can be calculated as:

$$\text{Jitter} = \frac{\sqrt{0.067}}{2\pi \times 2.5\times 10^{9}} = 16.48\text{ps}$$

This study is a proof-of-principle demonstration of optical phase locking to a reference laser with low power consumption. This system can be integrated with a better reference sources such as microresonator based optical frequency combs to synthesize arbitrary pure optical frequencies [10, 15]. Also, such narrow RF beat tones generated by beating on-chip laser with the comb lines can be used in wide range of applications, including short to medium range optical communications, as well as broadband wireless communication in microwave photonic link technology.

V. Power budget of both OPLLs

As mentioned, one of the primary objectives for this work was to realize a compact, chip-scale OPLL with Watt-level power consumption. In order to do this, one can improve the control electronics, PIC or both. In this work we proposed a novel, compact, low power consumption PIC as a possible solution to realize a chip scale, a Watt level OPLL. Table 1 and 2 provides the power consumption of gen-1 PIC, gen-2 PIC, control electronics and overall OPLL systems. (Numbers in the parentheses for each section in the PIC part tell how many of them are integrated in the PIC, BM: back mirror, FM: front mirror, LIA: limiting amplifier, PD: photodiode, PT: phase tuner, SOA: semiconductor optical amplifier)

TABLE I
Power budget for first generation PIC Providing 10 mW Optical Power and overall OPLL system

	Section	Current (mA)	Voltage (V)	Power (mW)
Gen-1 PIC	Gain(1)	73	1.5	109.5
	FM (1)	30	1.5	45
	PT (1)	7	1.3	9.1
	PD (2)	1	2	4
	BM (1)	120	1.5	180
	SOA (3)	70	1.5	315
PIC-1 TOTAL				**662.6**
	LIA	180	3.3	594
	XOR	130	3.3	429
	Op-amp	16	6	96
Electronic ICs TOTAL				**1119**
Total Power Consumption Gen-1 OPLL				**1.78 (W)**

TABLE II
Power budget for second generation PIC Providing 10 mW Optical Power and overall OPLL system

	Section	Current (mA)	Voltage (V)	Power (mW)
Gen-2 PIC	Gain(1)	73	1.5	109.5
	FM (2)	20	1.3	52
	PT (2)	7	1.3	18.2
	PD (2)	1	2	4
PIC-2 TOTAL				**184**
	LIA	180	3.3	594
	XOR	130	3.3	429
	Op-amp	16	6	96
Electronic ICs TOTAL				**1119**
Total Power Consumption Gen-2 OPLL				**1.3 (W)**

As can be seen from these tables gen-1 PIC consumes 660 mW, whereas gen-2 PIC consumes only 184 mW. Together with the control electronics, the OPLL with gen-2 PIC only consumes record-low 1.3 Watts of electrical power.

IV. Sensitivity of the OPLL system

For practical applications including coherent optical communications and optical frequency synthesis, OPLLs should be able to lock to input reference power levels in the order of µWs or even 10s of nWs. In this section, sensitivity analysis of the OPLL is given and experimental sensitivity results are reported. In addition to these results, a novel high gain trans-impedance amplifier (TIA) is presented and possible OPLL is proposed using this TIA, which can lock to input power levels as low as 25 pW.

Both OPLLs in this work employs SiGe based COTS limiting amplifier, which has 30 dB differential gain. InP based PICs have on chip tunable lasers, which produces reasonable amount of optical power. This is mixed with the reference input power through 2×2 MMI coupler and the PDs. The detected electrical signal is then fed into the limiting amplifier having a 50 Ohms common mode logic interface. In this system, the minimum required input current level from the balanced PD pair can be found as follows, where $V_{INPUT,MIN}$ represents the minimum required voltage level just before the limiting amplifier and $I_{BEAT,MIN}$ represents the minimum required beat current produced by the photodiodes:

$$Gain_{LIA} = 30dB = 31.6$$

$$V_{INPUT,MIN} = \frac{300mV}{31.6} = 9.5mV$$

$$I_{BEAT,MIN} = \frac{9.5mV}{50} = 0.19mA$$

This article has been accepted for publication in a future issue of this journal, but has not been fully edited. Content may change prior to final publication. Citation information: DOI 10.1109/JLT.2017.2758744, Journal of Lightwave Technology

From the above equations, we found out that the minimum input current level for offset locking with the designed OPLLs is around 0.19 mA. Given the responsivity of the on-chip PDs is around 1 A/W, the minimum input beat power is around 0.19 mW. If we use this in the coherent detection equation, we can get the minimum required input power level from the reference laser as follows, where I_{BEAT} represents the beat current produced by the PDs, I_{LO} is the current produced by LO laser and I_{INPUT} is the current produced by the reference laser.

$$I_{BEAT} = 2\sqrt{I_{LO} I_{INPUT}}$$

$$I_{INPUT,MIN} = \frac{I_{BEAT,MIN}{}^2}{4 I_{LO}}$$

$$I_{INPUT,MIN} = 9\mu A$$

Therefore, the minimum input power required to offset lock this OPLL is theoretically about 9 µW, which is close to the experimental results demonstrated in Fig. 11(b), in which the minimum input power level required to operate the OPLL system was found to be 20 µW.

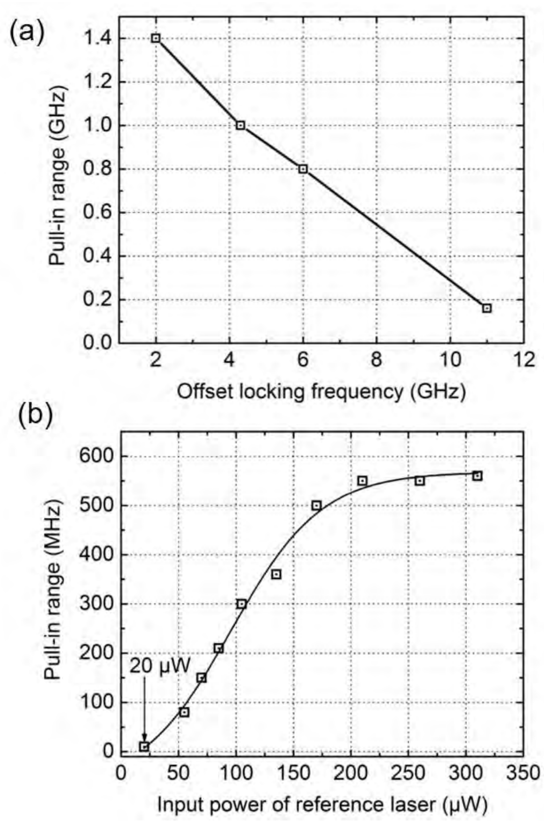

Fig. 11. (a) Pull-in range vs. offset locking frequency (b) Pull in range vs. input power of the reference external cavity laser. Minimum input power required for locking was found 20 µW experimentally.

Fig. 11(a) and (b) demonstrates the pull-in range of the OPLL system with respect to offset locking frequency and input power levels respectively. Pull-in range varies from 1.4 GHz to 200 MHz depending on the offset frequency range. As expected, the pull-in range decreases with increasing offset frequencies, since the gain of the overall loop reduces. Similarly, decreasing input power levels reduces the pull-in range, and eventually at some point OPLL stops working with the certain input power levels. This minimum input power level was found to be 20 µW, as can be seen in Fig. 11(b).

In order to improve the sensitivity of the OPLL further, an application specific trans-impedance amplifier (TIA) with low noise, high gain and wide bandwidth using 130 nm SiGe HBT process was designed. This chip was designed for 80 dB voltage gain and 120 dB ohm trans-impedance gain with 30GHz 3-dB bandwidth. It has less than 10 pA/$\sqrt{Hz}$ input referred noise current density up to 20 GHz with respect to 50 fF photodiode capacitance according to the circuit level simulations. With this TIA minimum input power level of reference signal can be reduced to as low as 22.5 pW as follows, where each symbol is used the same way as explained previously:

$$Gain_{TIA} = 120 dB\Omega = 1M\Omega$$

$$I_{BEAT,MIN} = \frac{300mV}{10^6\Omega} = 0.3\mu A$$

$$I_{BEAT} = 2\sqrt{I_{LO} I_{INPUT}}$$

$$I_{INPUT,MIN} = \frac{I_{BEAT,MIN}{}^2}{4 I_{LO}}$$

$$I_{INPUT,MIN} = 22.5 pA$$

Using this TIA, one can make a highly sensitive OPLL, which can be used in optical communications and optical frequency synthesis systems. Figure 12 shows the proposed OPLL system using this novel TIA. The COTS SiGe limiting amplifier is replaced by this TIA in the proposed OPLL system. Please note that TIA gain was measured functionally to be 60 dB without DC restoration loop. With a proper DC restoration loop, one can get the simulated gain of 80 dB from the TIA. The study relating to the sensitive OPLL system with these high-performance TIAs is ongoing and will be reported in the future.

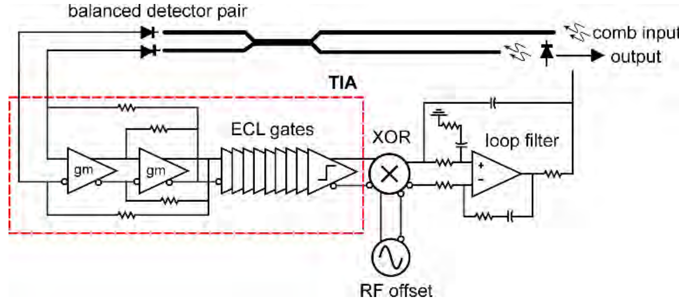

Fig. 12: Schematic of the sensitive OPLL with low noise, high gain trans-impedance amplifier.

V. CONCLUSIONS

In this paper, two chip-scale OPLLs were designed and demonstrated. By designing a novel, low power consumption InP-based photonic integrated receiver circuit, overall power consumption of the first generation OPLL was significantly reduced. The second generation OPLL consumes only 1.35 Watts of electrical power, which is the lowest power consumption reported for an OPLL to the best of author's knowledge. Both OPLLs have 500 MHz loop bandwidth, with 0.067 rad^2 phase noise variance, integrating from 1 kHz to 10 GHz. Offset locking ranges are 15.2 GHz and 17.8 GHz respectively. Minimum input power level required from the reference side for phase locking was measured to be 20 µW. Novel, application specific electrical IC was proposed for lowering the sensitivity of such OPLLs to as low as 25 pW.

REFERENCES

[1] L. G. Kazovsky, "Balanced phase-locked loops for optical homodyne receivers: performance analysis, design considerations, and laser linewidth requirements," *J. Lightw. Technol.*, vol. 4, pp. 182–195, Feb. 1986.

[2] V. Ferrero and S. Camatel, "Optical phase locking techniques: an overview and a novel method based on single side sub-carrier modulation," *Opt. Express*, vol. 16, no. 2, pp. 818–828, Jan. 2008.

[3] H. C. Park, M. Lu, E. Bloch, T. Reed, Z. Griffith, L. Johansson, L. Coldren, and M. Rodwell, "40Gbit/s coherent optical receiver using a Costas loop," *Opt. Express*, vol. 20, no. 26, pp. B197-B203, Dec. 2012.

[4] S. Camatel, V. Ferrero, "Narrow linewidth CW laser phase noise characterization methods for coherent transmission system applications", *J. Lightw. Technol.*, vol. 26, no. 17, pp. 3048-3055, Sep. 2008.

[5] S. Ristic, A. Bhardwaj, M. J. Rodwell, L. A. Coldren and L. A. Johansson, "An optical phase-locked loop photonic integrated circuit," in *J. Lightw. Technol.*, vol. 28, no. 4, pp. 526-538, Feb. 2010.

[6] K. Balakier, M. J. Fice, L. Ponnampalan, A. J. Seeds, and C. C. Renaud, "Monolithically integrated optical phase lock loop for microwave photonics," *J. Lightw. Technol.*, vol. 29, pp. 3893-3900, Oct. 2014.

[7] R. J. Steed, L. Ponnampalam, M. J. Fice, C. C. Renaud, D. C. Rogers, D. G. Moodie, G. D. Maxwell, I. F. Lealman, M. J. Robertson, L. Pavlovic, L. Naglic, M. Vidmar, and A. J. Seeds, "Hybrid integrated optical phase-lock loops for photonic terahertz sources,", *IEEE J. Sel. Topics Quantum Electron.*, vol. 17, pp. 210-217, Feb. 2011.

[8] D. T. Spencer, A. Bluestone, J. E. Bowers, T. C. Briles, S. Diddams, T. Drake, R. Ilic, T. Kippenberg, T. Komljenovic, S. H. Lee, Q. Li, N. Newbury, E. Norberg, D. Y. Oh, S. Papp, P. M. H. Peter, L. Sinclair, K. Srinivasan, J. Stone, M. G. Suh, L. Theogarajan, K. Vahala, N. Volet, D. Westly, and K. Yang, "Towards an integrated-photonics optical-frequency synthesizer with <1 Hz residual frequency noise," *in Proc. Opt. Fiber Commun. Conf*, 2017, pp. 1-3.

[9] C. C. Renaud, C. F. C. Silva, M. Dueser, P. Bayvel and A. J. Seeds, "Exact, agile, optical frequency synthesis using an optical comb generator and optical injection phase lock loop," *in Proc. of IEEE/LEOS Summer Topical Meeting*, 2003, pp. WC1.3/67-WC1.3/68.

[10] S. Arafin, A. Simsek, S. K. Kim, S. Dwivedi, W. Liang, D. Eliyahu, J. Klamkin, A. Matsko, L. Johansson, L. Maleki, M. J. Rodwell, and L. A. Coldren, "Towards chip-scale optical frequency synthesis based on optical heterodyne phase-locked loop," *Opt. Express*, vol. 25, no. 2, pp. 681-695, Jan. 2017.

[11] M. Lu, H. C. Park, E. Bloch, L. A. Johansson, M. J. Rodwell, and L. A. Coldren, "A highly-integrated optical frequency synthesizer based on phase-locked loops," *in Proc. Opt. Fiber Commun. Conf*, 2014, pp. 1-3.

[12] A. Simsek, S. Arafin, S. Kim, G. Morrison, L. Johansson, M. Mashanovitch, L. A. Coldren, and M. Rodwell, "A chip-scale heterodyne optical phase-locked loop with low-power consumption," *in Proc. Opt. Fiber Commun. Conf.*, 2017, pp. 1-3.

[13] L. A. Coldren, S. C. Nicholes, L. Johansson, S. Ristic, R. S. Guzzon, E. J. Norberg, and U. Krishnamachari, "High performance InP-based photonic ICs-A tutorial," *J. Lightw. Technol.*, vol. 29, no. 4, pp. 554-570, Feb. 2011.

[14] M. Lu, "Integrated optical phase-locked loops," Ph.D. Dissertation, Electrical and Computer Engineering, University of California, Santa Barbara, 2013.

[15] S. Arafin, A. Simsek, S.-K. Kim, W. Liang, D. Eliyahu, G. Morrison, M. Mashanovitch, A. Matsko, L. Johansson, L. Maleki, M. J. Rodwell, and L. A. Coldren, "Power-efficient Kerr frequency comb based tunable optical source," *IEEE Photonics Journal*, vol. 9, no. 3, pp. 1-14, June 2017

[16] http://www.adsantec.com/200-asnt5020-pqc.html http://www.adsantec.com/83-asnt5040-kmc.html

[17] F. G. Agis, L. K. Oxenløwe, S. Kurimura, C. Ware, H. C. H. Mulvad, M. Galili, and D. Erasme, "Ultrafast phase comparator for phase-locked loop-based optoelectronic clock recovery systems," *J. Lightw. Technol.*, vol. 27, no. 13, pp. 2439-2448, Jul. 2009.

[18] K. Balakier, L. Ponnampalam, M. J. Fice, C. C. Renaud, and A. J. Seeds, "Integrated semiconductor laser optical phase lock loops (Invited Paper)," in *IEEE J. Sel. Topics Quantum Electron.* , vol.24, no.1, pp.1-1, Jan. 2018.

[19] M. Lu, H. C. Park, E. Bloch, A. Sivananthan, A. Bhardwaj, Z. Griffith, L. A. Johansson, M. J. Rodwell, and L. A. Coldren, "Highly integrated optical heterodyne phase-locked loop with phase/frequency detection," *Opt. Express*, vol. 20, no. 9, pp. 9736-9741, April 2012.

[20] R. J. Steed, F. Pozzi, M. J. Fice, C. C. Renaud, D. C. Rogers, I. F. Lealman, D. G. Moodie, P. J. Cannard, C. Lynch, L. Johnston, M. J. Robertson, R. Cronin, L. Pavlovic, L. Naglic, M. Vidmar, and A. J. Seeds, "Monolithically integrated heterodyne optical phase-lock loop with RF XOR phase detector," *Opt. Express*, vol. 19, no. 21, pp. 20048-20053, Oct. 2011.

[21] M. Lu, H. C. Park, E. Bloch, A. Sivananthan, J. S. Parker, Z. Griffith, L. A. Johansson, M. J. Rodwell, and L. A. Coldern, "An integrated 40 Gbit/s optical costas receiver," *in J. Lightw. Technol.*, vol. 31, no. 13, pp. 2244-2253, July 2013.

[22] T. R. Clark, T. F. Carruthers, P. J. Matthews and I. N. D. III, "Phase noise measurements of ultrastable 10-GHz harmonically modelocked fibre laser," Electron. Lett., vol. 35, no. 9, pp. 720-721, Apr. 1999.

Arda Simsek received the B.S. degree in electrical engineering from Bilkent University, Turkey, in 2014, and the M.S. degree in electrical and computer engineering from the University of California, Santa Barbara (UCSB) in 2015. He is currently working towards the Ph.D. degree in electrical and computer engineering at UCSB. His main research interests are RF and millimeter wave integrated circuits in silicon and III-V technologies for phased-array systems and optical phase locked-loops.

Shamsul Arafin (S'08–M'12–SM'17) received the B.Sc. degree in electrical and electronics engineering from Bangladesh University of Engineering and Technology, Dhaka, Bangladesh, in 2005, the M.Sc. degree in communication technology from Universitat Ulm, Ulm, Germany, in 2008, and the Ph.D. degree from the Walter Schottky Institut, Technische Universitat Munchen, Munich, Germany, in 2012. He is currently an Assistant Project Scientist at the University of California, Santa Barbara (UCSB), Santa Barbara, CA, USA. Prior to joining UCSB, he was a Postdoctoral Research Scholar in Device Research Laboratory, University of California, Los Angeles, CA, USA. He has authored and coauthored more than 80 papers in leading technical journals and international conferences.

Seong-Kyun Kim received the B.S., M.S., and Ph.D. degrees from the College of Information and Communication Engineering, Sungkyunkwan University, Suwon, South Korea, in 2007, 2009, and 2013, respectively. He is currently a Post-Doctoral Research Fellow with the Department of Electrical and Computer Engineering, University of California, Santa Barbara, CA, USA. His current research interests include RF and millimeter-wave integrated circuits for wireless communications and phased-array.

Gordon B. Morrison received the B.A.Sc. degree (Hons.) from the Simon Fraser University, Vancouver, BC, Canada, in 1997, and the Ph.D. degree from McMaster University, Hamilton, ON, Canada, in 2002, both in engineering physics. His doctoral work, under Prof. D. T. Cassidy, focused on modeling and characterization of gain-coupled DFB lasers. From 1998 to 2002, he spent more than a year at Nortel Networks, ON, Canada, as a Graduate Student Researcher. From 2002 to 2003, he was a Post-Doctoral Fellow with McMaster University, where he was involved in development of a model for asymmetric-multiple-quantum-well gain and worked on process

This article has been accepted for publication in a future issue of this journal, but has not been fully edited. Content may change prior to final publication. Citation information: DOI 10.1109/JLT.2017.2758744, Journal of Lightwave Technology

development for quantum-well intermixing. In June 2003, he joined the Department of Electrical and Computer Engineering, University of California, Santa Barbara, as a Visiting Assistant Research Engineer in Prof. L. Coldren's group, where he participated in the design, fabrication, and characterization of small footprint DBR EMLs using quantum-well-intermixing technology, and used photocurrent spectroscopy to characterize and optimize photonic integrated circuits. In 2005, he joined ASIP (formally III-V Photonics), Houten, The Netherlands, and in 2006 joined Apogee Photonics (formerly ASIP/T-Networks), Allentown, PA, where he worked on uncooled 1310 EML technology, 40G EA modulators, and monolithically integrated SOA/EA products. Apogee photonics was acquired by CyOptics Inc, Breinigsville PA, and subsequently was acquired by Avago technologies. At CyOptics/Avago, he continued work on EML development while additionally focusing on design, characterization, calibration, and qualification of liquid crystal external cavity tunable lasers for coherent applications. In 2014, he joined Freedom Photonics LLC, Santa Barbara, CA, USA, as the Director of Engineering. He is the author or co-author of more than 30 peer-reviewed journal papers.

Leif A. Johansson (M'04) received the Ph.D. degree in engineering from the University College London, London, U.K., in 2002. He has been a Research Scientist with the University of California at Santa Barbara, Santa Barbara, CA, USA, and is the Founder of Freedom Photonics, Santa Barbara, CA, USA. His current research interests include design and characterization of integrated photonic devices for analog and digital applications and analog photonic systems and subsystems.

Milan L. Mashanovitch (M'99–SM'13) received the Dipl.Ing. degree in electrical engineering from the University of Belgrade, Belgrade, Serbia, in 1998, and the Ph.D. degree in electrical engineering from the University of California, Santa Barbara, CA, USA, in 2004. He co-founded Freedom Photonics LLC, Santa Barbara, CA, USA, in 2005, and he has been in many technical roles related to product development and program management since. In addition to Freedom Photonics, he has worked for the University of California Santa Barbara, both as a Researcher on photonic integrated circuits, and as an Adjunct Professor teaching graduate level classes on semiconductor lasers and photonic ICs. He has co-authored nearly 130 papers, many invited, on photonic integrated circuits and various photonic devices. He is one of the authors of the second edition of the Diode Lasers and Photonic Integrated Circuits (Wiley, 2012). He has chaired, serves or has served on technical committees for IEEE Avionics, Fiber Optics and Photonics Conference, IEEE Microwave Photonics Conference, OSA's Integrated Photonics Research Conference, International Semiconductor Laser Conference, and Indium Phosphide and Related Materials Conference.

Larry A. Coldren (S'67–M'72–SM'77–F'82-LF'12) received the Ph.D degree in electrical engineering from Stanford University, Stanford, CA, USA, in 1972. After 13 years in the research area with Bell Laboratories, he joined the University of California at Santa Barbara (UCSB) in 1984. He is currently the Fred Kavli Professor of optoelectronics and sensors and holds appointments with the Department of Materials and the Department of Electrical and Computer Engineering. From 2009 to 2011, he was acting Dean of the College of Engineering. In 1990, he cofounded Optical Concepts, later acquired as Gore Photonics, to develop novel VCSEL technology, and, in 1998, he cofounded Agility Communications, later acquired by JDSU (now Lumentum), to develop widely tunable integrated transmitters. At UCSB, he worked on multiple-section widely tunable lasers and efficient vertical-cavity surface-emitting lasers (VCSELs). More recently, his group has developed high-performance InP-based photonic integrated circuits and high-speed, high-efficiency VCSELs. He has authored or coauthored more than a thousand journal and conference papers, eight book chapters, a widely used textbook, and 63 issued patents. He is a Fellow of OSA, IEE, and the National Academy of Inventors, as well as a member of the National Academy of Engineering. He received the 2004 John Tyndall Award, the 2009 Aron Kressel Award, the 2014 David Sarnoff Award, the 2015 IPRM Award, and the 2017 Nick Holonyak, Jr. Award.

Mark Rodwell (Ph.D. Stanford University 1988) holds the Doluca Family Endowed Chair in Electrical and Computer Engineering at UCSB. He also manages the UCSB Nanofabrication Lab. His research group develops nm and THz transistors, and millimeter-wave and sub-mm-wave integrated circuits. The work of his group and collaborators has been recognized by the 2010 IEEE Sarnoff Award, the 2012 IEEE Marconi Prize Paper Award, the 1997 IEEE Microwave Prize, the 1998 European Microwave Conference Microwave Prize, and the 2009 IEEE IPRM Conference Award.

I. Photonic Integrated Circuits

C. Optical Frequency Synthesis

Research Article
Optics EXPRESS

Towards chip-scale optical frequency synthesis based on optical heterodyne phase-locked loop

SHAMSUL ARAFIN,[1,4] ARDA SIMSEK,[1] SEONG-KYUN KIM,[1] SARVAGYA DWIVEDI,[1] WEI LIANG,[2] DANNY ELIYAHU,[2] JONATHAN KLAMKIN,[1] ANDREY MATSKO,[2] LEIF JOHANSSON,[3] LUTE MALEKI,[2] MARK RODWELL,[1] AND LARRY COLDREN[1,5]

[1]*Department of Electrical and Computer Engineering, University of California at Santa Barbara, Santa Barbara, CA 93106, USA*
[2]*2OEwaves Inc., Pasadena, CA 91107, USA*
[3]*Freedom Photonics LLC, Santa Barbara, CA 93117, USA*
[4]*sarafin@ece.ucsb.edu*
[5]*coldren@ece.ucsb.edu*

Abstract: An integrated heterodyne optical phase-locked loop was designed and demonstrated with an indium phosphide based photonic integrated circuit and commercial off-the-shelf electronic components. As an input reference, a stable microresonator-based optical frequency comb with a 50-dB span of 25 nm (~3 THz) around 1550 nm, having a spacing of ~26 GHz, was used. A widely-tunable on-chip sampled-grating distributed-Bragg-reflector laser is offset locked across multiple comb lines. An arbitrary frequency synthesis between the comb lines is demonstrated by tuning the RF offset source, and better than 100Hz tuning resolution with ± 5 Hz accuracy is obtained. Frequency switching of the on-chip laser to a point more than two dozen comb lines away (~5.6 nm) and simultaneous locking to the corresponding nearest comb line is also achieved in a time ~200 ns. A low residual phase noise of the optical phase-locking system is successfully achieved, as experimentally verified by the value of −80 dBc/Hz at an offset of as low as 200 Hz.

OCIS codes: (250.5300) Photonic integrated circuits; (060.5625) Radio frequency photonics; (060.2840) Heterodyne; (140.0140) Lasers and laser optics; (140.3600) Lasers, tunable; (140.3945) Microcavities; (230.5750) Resonators

References and links

1. D. J. Jones, S. A. Diddams, J. K. Ranka, A. Stentz, R. S. Windeler, J. L. Hall, and S. T. Cundiff, “Carrier-envelope phase control of femtosecond mode-locked lasers and direct optical frequency synthesis,” Science **288**(5466), 635–639 (2000).
2. J. Castillega, D. Livingston, A. Sanders, and D. Shiner, “Precise measurement of the J = 1 to J = 2 fine structure interval in the 2(3)P state of helium,” Phys. Rev. Lett. **84**(19), 4321–4324 (2000).
3. M. J. Thorpe, K. D. Moll, R. J. Jones, B. Safdi, and J. Ye, “Broadband cavity ringdown spectroscopy for sensitive and rapid molecular detection,” Science **311**(5767), 1595–1599 (2006).
4. W. C. Swann and N. R. Newbury, “Frequency-resolved coherent lidar using a femtosecond fiber laser,” Opt. Lett. **31**(6), 826–828 (2006).
5. T. Udem, J. Reichert, R. Holzwarth, and T. W. Hänsch, “Absolute optical frequency measurement of the Cesium D_1 line with a mode-locked laser,” Phys. Rev. Lett. **82**(18), 3568–3571 (1999).
6. A. A. Madej, L. Marmet, and J. E. Bernard, “Rb atomic absorption line reference for single Sr^+ laser cooling systems,” Appl. Phys. B **67**(2), 229–234 (1998).
7. H. S. Moon, E. B. Kim, S. E. Park, and C. Y. Park, “Selection and amplification of modes of an optical frequency comb using a femtosecond laser injection-locking technique,” Appl. Phys. Lett. **89**(18), 181110 (2006).
8. L.-S. Ma, Z. Bi, A. Bartels, L. Robertsson, M. Zucco, R. S. Windeler, G. Wilpers, C. Oates, L. Hollberg, and S. A. Diddams, “Optical frequency synthesis and comparison with uncertainty at the $10^{(-19)}$ level,” Science **303**(5665), 1843–1845 (2004).
9. Y.-J. Kim, J. Jin, Y. Kim, S. Hyun, and S.-W. Kim, “A wide-range optical frequency generator based on the frequency comb of a femtosecond laser,” Opt. Express **16**(1), 258–264 (2008).

10. H. Y. Ryu, S. H. Lee, W. K. Lee, H. S. Moon, and H. S. Suh, "Absolute frequency measurement of an acetylene stabilized laser using a selected single mode from a femtosecond fiber laser comb," Opt. Express **16**(5), 2867–2873 (2008).
11. http://www.menlosystems.com/assets/documents-2/FC1500-ProductBrochure.pdf
12. K. J. Vahala, "Optical microcavities," Nature **424**(6950), 839–846 (2003).
13. P. Del'Haye, A. Schliesser, O. Arcizet, T. Wilken, R. Holzwarth, and T. J. Kippenberg, "Optical frequency comb generation from a monolithic microresonator," Nature **450**(7173), 1214–1217 (2007).
14. T. J. Kippenberg, R. Holzwarth, and S. A. Diddams, "Microresonator-based optical frequency combs," Science **332**(6029), 555–559 (2011).
15. K. Saha, Y. Okawachi, B. Shim, J. S. Levy, R. Salem, A. R. Johnson, M. A. Foster, M. R. E. Lamont, M. Lipson, and A. L. Gaeta, "Mode locking and femtosecond pulse generation in chip-based frequency combs," Opt. Express **21**(1), 1335–1343 (2013).
16. V. B. Braginsky, M. L. Gorodetsky, and V. S. Ilchenko, "Quality-factor and nonlinear properties of optical whispering-gallery modes," Phys. Lett. A **137**(7–8), 393–397 (1989).
17. A. A. Savchenkov, A. B. Matsko, V. S. Ilchenko, and L. Maleki, "Optical resonators with ten million finesse," Opt. Express **15**(11), 6768–6773 (2007).
18. W. Liang, D. Eliyahu, V. S. Ilchenko, A. A. Savchenkov, A. B. Matsko, D. Seidel, and L. Maleki, "High spectral purity Kerr frequency comb radio frequency photonic oscillator," Nat. Commun. **6**, 7957 (2015).
19. V. S. Ilchenko, A. A. Savchenkov, A. B. Matsko, and L. Maleki, "Generation of Kerr frequency combs in a sapphire whispering gallery mode microresonator," Opt. Eng. **53**(12), 122607 (2014).
20. I. M. White, J. D. Suter, H. Oveys, X. Fan, T. L. Smith, J. Zhang, B. J. Koch, and M. A. Haase, "Universal coupling between metal-clad waveguides and optical ring resonators," Opt. Express **15**(2), 646–651 (2007).
21. X. Zhang and A. M. Armani, "Silica microtoroid resonator sensor with monolithically integrated waveguides," Opt. Express **21**(20), 23592–23603 (2013).
22. T. J. Kippenberg, S. M. Spillane, and K. J. Vahala, "Kerr-nonlinearity optical parametric oscillation in an ultrahigh-Q toroid microcavity," Phys. Rev. Lett. **93**(8), 083904 (2004).
23. T. Herr, V. Brasch, J. D. Jost, I. Mirgorodskiy, G. Lihachev, M. L. Gorodetsky, and T. J. Kippenberg, "Mode spectrum and temporal soliton formation in optical microresonators," Phys. Rev. Lett. **113**(12), 123901 (2014).
24. M. Erkintalo and S. Coen, "Coherence properties of Kerr frequency combs," Opt. Lett. **39**(2), 283–286 (2014).
25. W. Liang, V. S. Ilchenko, D. Eliyahu, A. A. Savchenkov, A. B. Matsko, D. Seidel, and L. Maleki, "Ultralow noise miniature external cavity semiconductor laser," Nat. Commun. **6**, 7371 (2015).
26. A. B. Matsko and L. Maleki, "On timing jitter of mode-locked Kerr frequency combs," Opt. Express **21**(23), 28862–28876 (2013).
27. A. A. Savchenkov, D. Eliyahu, W. Liang, V. S. Ilchenko, J. Byrd, A. B. Matsko, D. Seidel, and L. Maleki, "Stabilization of a Kerr frequency comb oscillator," Opt. Lett. **38**(15), 2636–2639 (2013).
28. A. C. Bordonalli, C. Walton, and A. J. Seeds, "High-performance homodyne optical injection phase-lock loop using wide-linewidth semiconductor lasers," IEEE Photonics Technol. Lett. **8**(9), 1217–1219 (1996).
29. K. Balakier, M. J. Fice, L. Ponnampalam, A. J. Seeds, and C. C. Renaud, "Monolithically integrated optical phase-lock loop for microwave photonics," J. Lightwave Technol. **32**(20), 3893–3900 (2014).
30. C. C. Renaud, M. Duser, C. F. C. Silva, B. Puttnam, T. Lovell, P. Bayvel, and A. J. Seeds, "Nanosecond channel-switching exact optical frequency synthesizer using an optical injection phase-locked loop (OIPLL)," IEEE Photonics Technol. Lett. **16**(3), 903–905 (2004).
31. C. C. Renaud, C. F. C. Silva, M. Dueser, P. Bayvel, and A. J. Seeds, "Exact, agile, optical frequency synthesis using an optical comb generator and optical injection phase-lock loop," in *Digest of the LEOS Summer Topical Meetings* (2003), paper WC1.3/67.
32. H. Inaba, T. Ikegami, H. Feng-Lei, A. Onae, Y. Koga, T. R. Schibli, K. Minoshima, H. Matsumoto, S. Yamadori, O. Tohyama, and S. I. Yamaguchi, "Phase locking of a continuous-wave optical parametric oscillator to an optical frequency comb for optical frequency synthesis," IEEE J. Quantum Electron. **40**(7), 929–936 (2004).
33. T. R. Schibli, K. Minoshima, E. L. Hong, H. Inaba, Y. Bitou, A. Onae, and H. Matsumoto, "Phase-locked widely tunable optical single-frequency generator based on a femtosecond comb," Opt. Lett. **30**(17), 2323–2325 (2005).
34. J. E. Bowers, A. Beling, A. Bluestone, S. M. Bowers, L. Chang, S. Diddams, G. Fish, T. Kippenberg, T. Komljenovic, E. Norberg, S. Papp, K. Srinivasan, L. Theogarajan, K. Vahala, and N. Volet, "Chip-scale optical resonator enabled synthesizer (CORES): Miniature systems for optical frequency synthesis," in *IEEE International Frequency Control Symposium (IFCS)* (2016), pp. 1–5.
35. L. Mingzhi, P. Hyun-chul, E. Bloch, A. Sivananthan, J. S. Parker, Z. Griffith, L. A. Johansson, M. J. W. Rodwell, and L. A. Coldren, "An integrated 40 gbit/s optical costas receiver," J. Lightwave Technol. **31**(13), 2244–2253 (2013).
36. S. Ristic, A. Bhardwaj, M. J. Rodwell, L. A. Coldren, and L. A. Johansson, "An optical phase-locked loop photonic integrated circuit," J. Lightwave Technol. **28**(4), 526–538 (2010).
37. M. Lu, H.-C. Park, E. Bloch, L. A. Johansson, M. J. Rodwell, and L. A. Coldren, "A highly-integrated optical frequency synthesizer based on phase-locked loops," *Optical Fiber Communication Conference 2014* (2014).
38. J. Parker, M. Lu, H. Park, E. Bloch, A. Sivananthan, Z. Griffith, L. A. Johansson, M. J. Rodwell, and L. A. Coldren, "Offset locking of an SG-DBR to an InGaAsP/InP mode-locked laser," in *IEEE Photonics Conference (IPC)* (2012).

39. J. Parker, A. Sivananthan, M. Lu, L. Johansson, and L. Coldren, "Integrated phase-locked multi-THz comb for broadband offset locking," in OSA Technical Digest, *Optical Fiber Communication Conference* (2012), paper OM3E.5.
40. M. Lu, "Integrated optical phase-locked loops," in *Electrical and Computer Engineering*, University of California, Santa Barbara (2013) p. 252.
41. http://www.adsantec.com/200-asnt5020-pqc.html http://www.adsantec.com/83-asnt5040-kmc.html
42. R. J. Steed, F. Pozzi, M. J. Fice, C. C. Renaud, D. C. Rogers, I. F. Lealman, D. G. Moodie, P. J. Cannard, C. Lynch, L. Johnston, M. J. Robertson, R. Cronin, L. Pavlovic, L. Naglic, M. Vidmar, and A. J. Seeds, "Monolithically integrated heterodyne optical phase-lock loop with RF XOR phase detector," Opt. Express **19**(21), 20048–20053 (2011).

1. Introduction

There has been recent and extensive research in the development of optical frequency synthesizers (OFSs) with applications including absolute optical frequency measurements [1], optical spectroscopy [2], gas sensing [3], light detection and ranging (LiDAR) [4], and optical frequency metrology [5, 6]. Despite their widespread potential applications, at present optical frequency synthesizers have found only limited use due to their cost, size, weight, and dc power requirements.

Considering this, realization of a compact, inexpensive, and low-power OFS is a key requirement. These goals suggest highly-integrated chip scale designs. However, it is challenging to integrate various optical and electronic devices on the same chip. Low power consumption is especially important because thermal cross-talk and associated thermal management may prevent the tight integration of the optical components.

An OFS includes several key elements. An optical frequency comb must be locked to an optical clock. This comb defines the frequency of the generated optical signal. Also required is a broadly tunable laser or bank of lasers that are referenced to the optical frequency comb. Finally, efficient and agile electronic circuits are needed to offset lock the laser to the frequency comb.

Despite being fully-locked and referenced, commercially-available optical frequency synthesizers involve bulk optics and electronics consuming power on the order of kW. This power is primarily consumed by the optical frequency comb generators. Mode-locked femtosecond optical frequency combs lay in the core of the OFS approaches [7–10]. Commercially available systems based on titanium sapphire or fiber laser based femtosecond mode-locked lasers are 0.14 m^3 in volume and consume 0.5 kW power [11].

The problem of the power-efficient optical frequency comb generator can be solved using optical microresonators [12]. Microresonator-based Kerr frequency combs belong to the class of frequency comb generators that lend themselves for on-chip integration [13]. An added advantage is that compared to traditional mode-locked or femtosecond laser-based optical frequency comb (OFC), a microresonator-based comb uses few hundreds of mW power, and provides ultralow noise and phase-coherent output with spectral linewidths on the order of sub-Hz. While monolithic planar resonators integrated on various platforms and producing the frequency combs were demonstrated [14, 15], none of them were integrated with the pump laser, and hence none of them represent complete chip-scale devices. The reason is that the power required to produce the frequency combs is usually in hundreds of mW range, which makes the chip integration impractical. The large power consumption by the laser as well as significant attenuation of the pump light in the microresonator complicates the thermal management of the system as the whole. To reduce the power consumption, one needs high quality (Q-) factor microresonators.

The frequency comb generator is based on the crystalline whispering gallery mode (WGM) resonator that has the following salient advantages over other devices of this kind [16, 17]. Firstly, it has low intrinsic loss (if overloaded) and high intrinsic Q-factor [17]. As the result, it is possible to reduce absorption of the light in the resonator. Secondly, the resonator has outstanding thermo-mechanical properties that allow realizing ultranarrow linewidth lasers on a chip using self-injection locking of the laser to the resonator. The optical frequency comb oscillator benefits from the laser and, as the result, the relative optical stability of each comb harmonic does not exceed 10^{-10} at 1 sec [18]. Thirdly, high optical Q allows reducing fundamental noises of the Kerr comb oscillator. The noises are further reduced since proper design of the resonator morphology results in increase of the volume of the optical mode need for reduction of the thermodynamic noise associated with the resonator. Fourthly, the resonator has small mass and large mechanical Q that reduces its acceleration and vibration sensitivity [19]. This feature is supported by the low acceleration sensitivity of the whole oscillator platform. Despite the fact that WGM resonators were created on a chip, the efficient planar couplers are yet to be developed for them. Preliminary studies show that it is possible [20, 21].

The Kerr frequency comb generated in the microresonator results from the process of four-wave mixing [22]. The comb emerges when the pump power, produced by the continuous-wave laser self-injection locked to a mode of the resonator, exceeds a certain threshold. The resonator is characterized with the ultimate anomalous group velocity dispersion and supports formation of the intracavity dissipative solitons [23]. The frequency comb stability is defined by the stability of the pump light, on one hand, and the repetition rate of the soliton train, on the other. Both values are extremely good. As the result, the whole oscillator represents an ultimate reference for creation of the OFS.

The OFC coherence can change through its spectrum, resulting a broader spectral linewidth for comb components that are away from the pump wavelength [24]. However, for a practically realizable spectrally narrow mode-locked Kerr frequency comb, this is not the case as the phase noise of the comb repetition rate is low [18], if compared with the properly normalized noise of the pump laser [25]. Moreover, in an ideal case, the repetition-rate noise of the Kerr frequency comb does not depend on the pump laser noise and can be extremely low [26, 27]. It means that for the narrow OFC reported here, we can neglect repetition rate induced phase noise and assume that all the optical harmonics have sub-Hz linewidth corresponding to the pump laser.

An optical frequency comb generates a series of discrete optical frequency harmonics, whereas an OFS has to provide a continuous tuning of the optical frequency. To realize this functionality, one needs a widely tunable laser that can be frequency locked to the optical frequency comb. There are several locking approaches such as optical injection locking (OIL), optical injection phase-lock loop (OIPLL) and optical phase-lock loop (OPLL) to achieve this functionality. Optical frequency synthesis with a wide tuning range is not possible using OIL approach alone due to the system instability above critical injection levels [28, 29]. Moreover, OIL is purely a homodyne technique, which does not allow for continuous tuning of an offset between the slave laser and the comb. Continuous tuning over a wide range of frequencies was achieved through the combination of OIL and OPLL technologies [30, 31]. However, such a hybrid system increases the system complicacy and the issue of offset tunability still remains.

Phase locking a tunable local oscillator to the OFC using chip scale OPLLs is, therefore, considered as the most popular ways of achieving OFSs [32–34]. With the developments in PIC and electronic IC integration, small loop delays and large loop bandwidths; realization of OPLLs is a more appealing solution compared to OIL, and OIPLL [35]. OFSs with accurate and stable optical output phase-locked to a phase-coherent and ultra-low linewidth optical reference with feedback control in the radio frequency (RF) domain can be utilized in the devices. The so-called heterodyne OPLL [36] is the concept by which chip scale and highly integrated OFSs were demonstrated, where the OFC with spectral span ~3 nm was generated with a modest linewidth of 100 kHz external-cavity laser and two cascaded modulators [37]. In addition, similar type of frequency synthesis was shown by offset locking a widely tunable on-chip laser to mode-locked laser comb, which also needs to be stabilized by second phase locking to a narrow-linewidth reference laser [38, 39], introducing more complexity. All of these solutions are power hungry, difficult to integrate and complex unlike the work reported here.

In this paper, we report on the experimental demonstration of a chip scale optical frequency synthesizer achieved by offset-locking an on-chip widely tunable sampled-grating distributed-Bragg-reflector (SG-DBR) laser to a magnesium fluoride (MgF_2) microresonator-based optical frequency comb with a 50-dB span of 25 nm (~3 THz) around 1550 nm and ~26 GHz repetition rate. The reference frequency comb generator used in the chip-scale OFS represent an example of fully heterogeneously integrated Kerr frequency comb generator. The physical package of the device, that includes the pump laser, the optical coupling element, the high-*Q* microresonator, and support electronics and thermal control has volume less than 0.2 cm^3 and total electric power consumption of 400 mW. This study also reports the demonstration of tuning between comb lines with a tunable RF synthesizer for offset locking. Tuning resolution better than 100 Hz within ± 5 Hz accuracy is also accomplished. As a further evaluation of our OFS, the frequency switching time with a wavelength separation >5 nm by jumping over 28 comb lines is also experimentally measured. The total power consumption of the entire OFS system is roughly 2 W (excluding EDFA). To the best of our knowledge, this is the first demonstration of a chip scale OFS with fastest switching time between the comb lines, highest tuning resolution and lowest power consumption.

This paper is organized as follows. This paper begins with a discussion on the concept of the OFS, design of highly integrated heterodyne OPLL and operation of Kerr frequency comb generation. We then describe the experimental setup used for offset locking to OFC and the corresponding results. Finally, the measured metrics of the chip-scale OFS are introduced.

2. Concept and design of frequency synthesis

The basic idea of a compact and chip-scale OFS is illustrated in Fig. 1. A microresonator-based OFC is used as the ultra stable and narrow linewidth source, serving as a master laser. The comb lines are then used as the reference for the heterodyne OPLL. A RF frequency f_{RF} from a tunable RF synthesizer is applied to feedback electronic circuits of the OPLL to introduce a frequency offset. By tuning the phase section current of the slave laser as well as f_{RF}, the slave laser is phase-locked to the comb lines. The two basic requirements to be met in order for an OFS to cover all the frequencies between comb lines are: (i) the heterodyne OPLL offset frequency range must be at least half of the comb's free-spectral-range (FSR), and (ii) the FSR of the comb must be less than the slave laser's mode-hop free tuning range. In such a way, continuous tuning is achieved.

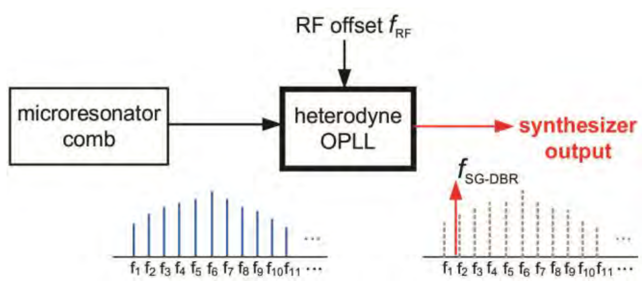

Fig. 1. Optical frequency synthesizer system, showing two main building blocks – a comb source and a heterodyne OPLL. The optical spectra are also plotted at the output of each block.

From the two building blocks of the OFS shown in Fig. 1, a more detailed view of the thick-lined rectangle block, labelled as heterodyne OPLL, is displayed in Fig. 2. The heterodyne OPLL system consists of a photonic integrated circuit (PIC) and feedback electronic circuits. The latter is composed of electronic ICs (EICs) and a loop filter. The master (injected single comb line in this case) and slave lasers in a PIC oscillate at different frequencies, producing a beat signal at this offset frequency on the balanced photodetector pair. The beat signal is then amplified by the limiting amplifier (LIA) to make the system insensitive to intensity fluctuation from the PIC. In other words, LIA limits the optical beat note signal to logic values so that system is unresponsive to any changes in optical intensity. A phase detector (logic XOR gate in this case) compares the phase of the beat signal with a reference signal from a tunable RF synthesizer, thus generating the baseband phase error signal. This is then fed back through the loop filter to control the slave laser phase and hence lock the phase of the slave laser to a single comb line.

Figure 3 shows an optical microscope photo of the heterodyne OPLL system board where PIC, EIC and LF were assembled closely together by wirebonding. The inset shows the picture of the test bench. The PIC consists of a widely tunable sampled-grating distributed Bragg reflector (SG-DBR) laser, a 2 × 2 multi-mode interference (MMI) coupler, a couple of semiconductor optical amplifiers (SOAs) to preamplify the input comb lines, two high-speed quantum well (QW)-based waveguide photodetectors (PDs), all integrated on an InGaAsP/InP platform. The on-chip SG-DBR laser has a wavelength tuning range of 40 nm.

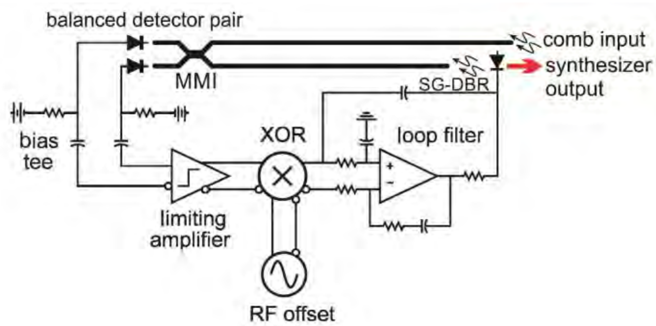

Fig. 2. System architecture of the heterodyne OPLL-based widely tunable OFS.

With a −3 V bias, the 3-dB RF bandwidth of the QW PDs can be as high as 14 GHz [40]. For the high-speed LIA and logic XOR gate, commercial-off-the-shelf (COTS) SiGe elements were employed for the electronics part, whereas discrete surface-mount device (SMD) components were used to build up the loop filter circuit whose loop bandwidth is designed to be ~400 MHz. LIA has a differential gain about 30 dB with a 3-dB bandwidth of 17 GHz. XOR can work at least up to 13 GHz input clock frequencies. The details of these COTS ICs can be found in [41]. The OPLL system size is around 1.8 × 1.6 cm^2. A 24-pin dc probe card was used to power up the OPLL system, and two 2signal-line GSGSG RF probes were used to monitor the device performance and supply the RF offset reference signal to the XOR. The maximum offset frequency our OPLL can lock the tunable laser to a reference laser at was verified to be as high as 15.6 GHz, clearly allowing the OFS to be continuously tuned.

3. Kerr frequency comb generation

To create the Kerr frequency comb generator, we fabricated a high-*Q* MgF2 whispering gallery mode resonator (WGMR) out of a cylindrical crystalline preform using mechanical grinding and polishing. The resonator is approximately 2.7 mm in diameter and 0.1 mm in thickness. The intrinsic optical *Q*-factor of the resonator exceeded 5×10^9. The resonator was characterized with a FSR of 25.7 GHz and anomalous group velocity dispersion resulting in 3 kHz difference between two adjacent FSRs.

The resonator was integrated with two coupling prisms and the loaded *Q*-factor was reduced to 5×10^8. The over coupling of the WGMR is useful for reduction of the thermal instabilities of the resonator occurring because of the light attenuation in the resonator host material.

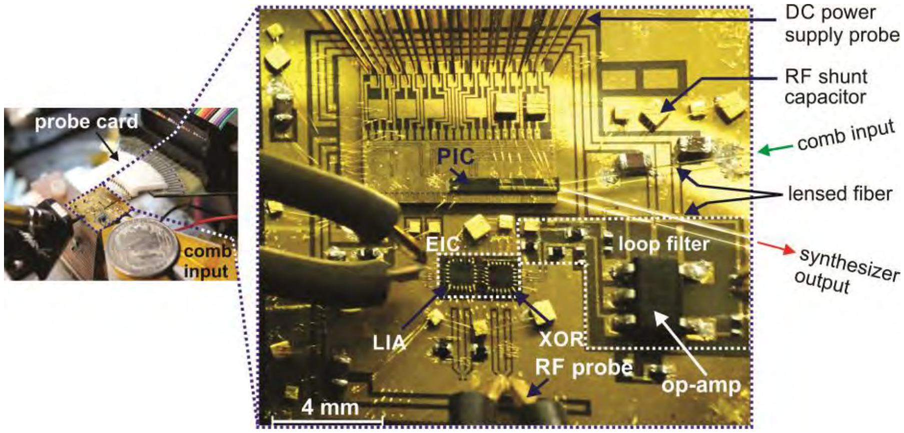

Fig. 3. The heterodyne OPLL on the test bench where the US quarter shown as a scale (right). A close-up view of the heterodyne OPLL board (left). The PIC, EIC and loop filter are labeled.

Light emitted by a semiconductor distributed feedback (DFB) laser was collimated and send to the resonator. When the light hit a WGM, the laser frequency was locked to the mode due to the optical feedback from the mode occurring because of resonant Rayleigh scattering. As the result of the locking the linewidth of the laser reduced to a sub-kHz level. As illustrated in Fig. 4(a), the light exiting the resonator through add and drop prism couplers was sent to a fast RF photodiode and an output optical coupler, respectively.

When the laser power exceeded a certain threshold (approximately 3 mW laser power corresponding to 1 mW in the mode) the unit produced a coherent frequency comb operating in the self-injection locked regime. The demodulating the frequency combs on a fast photodiode results in spectrally pure RF signal. Figure 4(d) shows the measured optical spectrum of the generated comb in the C-band under 20 mW laser power. The total power output from the fiber is ~335 μW and the comb envelope is 15 dB lower than the carrier.

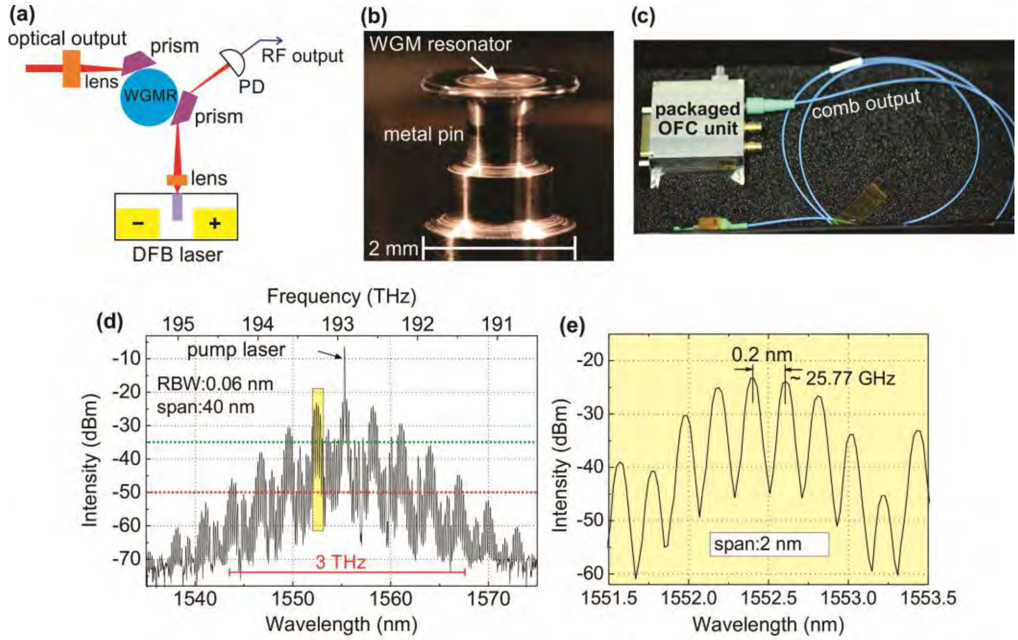

Fig. 4. (a) Schematic diagram of the set-up of the optical frequency comb (OFC) in a MgF_2 crystalline whispering gallery mode (WGM) resonator. The distributed feedback (DFB) laser pumps the resonator using an evanescent wave prism coupler. The generated frequency comb leaves the resonator through prism couplers. The light exiting one of the prism couplers was sent to a fast RF photodiode and optical output was obtained from the other coupler, (b) optical microscope image of the MgF_2 crystal forming optical WGM resonators, (c) packaged OFC unit with green fiber pigtail, (d) optical spectrum of a stabilized Kerr frequency combs (left) generated in the unit (right). The comb spans 3 THz defined as the width where the intensity ≥ 50 dBm (red dotted line) and has a line spacing of 25.7 GHz, yielding more than 115 lines. The optical output comb power exiting the fiber (greenjacketed) is 100 µW obtained after subtracting from the pump laser power, meaning only ~0.5 µW per comb line is achieved in the wavelength range of 1535 nm-1575 nm. The horizontal (green) dashed line denotes the 0.5 µW per comb line power level. (e) Clearly observed lines of a multi-soliton Kerr frequency comb with a spacing of 0.2 nm.

4. Experimental setup

The comb output from the packaged and fiber-pigtailed OFC unit goes through an erbium-doped fiber amplifier (EDFA) and finally coupled into the OPLL PIC using lensed fiber. The power requirement per comb line for stable offset-locking is measured to be 20 µW (17 dBm) in the fiber near 1550 nm operating wavelength. As the comb output is only 10 dBm in the fiber and divided over several comb lines, the EDFA is necessary to provide adequate power levels. The SG-DBR laser signal was coupled out from the back mirror and through a short semiconductor optical amplifier (SOA) using similar lensed fiber for monitoring purposes. To measure the OPLL tone, the output from the SGDBR was mixed with the comb in a 2 × 2 coupler, detected via an external high speed photodetector, and measured on an electrical signal analyzer (ESA), as shown in Fig. 5. The other output of this coupler is connected to the optical spectrum analyzer (OSA) to measure the optical spectra of SG-DBR laser and the comb output. Note that the linewidth of the unlocked SG-DBR is on the order of 10 MHz. A signal with a frequency equal to the beat note frequency, f_{RF} as frequency offset is applied from the RF synthesizer to XOR within the EIC.

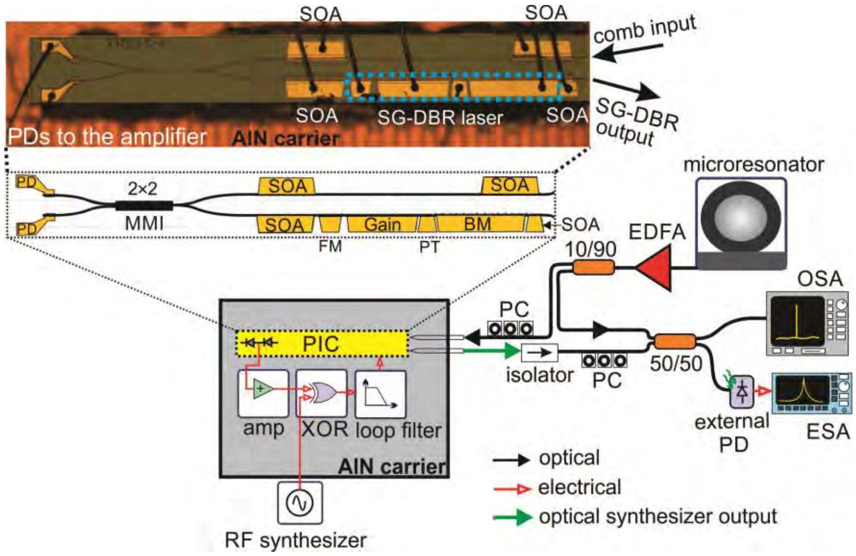

Fig. 5. The test setup of the optical synthesizer using heterodyne OPLL locking scheme. A microscope picture of the fully fabricated PIC mounted on AlN carrier with wirebonding shown at the top. (amp: amplifier, BM: back mirror, ESA: electrical spectrum analyzer, EDFA: erbium doped fiber amplifier, FM: front mirror, MMI: multimode interference, OSA: optical spectrum analyzer, PC: polarization controller, PT: phase tuner, PD: photodetector, PIC: photonic integrated circuit, SOA: semiconductor optical amplifier).

5. Results and discussion

5.1 Offset locking to comb lines

The phase-locking of the SG-DBR laser to the comb lines is achieved. Figure 6 shows the optical and electrical spectra when two lasers are phase-locked with an offset frequency of 11 GHz. The combined optical spectra of the SG-DBR and the comb lines are shown in Fig. 6(a) where both light source peaks around 1562 nm with a wavelength separation of 0.09 nm are seen. Since the OFC lines are uneven in amplitude, and they are roughly equally amplified by EDFA, some of the lines are buried by the amplified spontaneous emission (ASE) noise floor. The RF spectra of the beat note at an offset frequency of 11 GHz, in cases of locked and free running, are shown in Fig. 6(b). In the locked case, the RF linewidth is reduced significantly, indicating the coherence between the SG-DBR laser and comb. The beat tone generated between the locked SG-DBR and the adjacent comb line is seen at 14.7 GHz (i.e. 25.7 ± 11 GHz). This is expected, since comb lines are stable in phase with respect to each other and the OPLL is phase-locked to the central comb line, hence the OPLL is phase-locked to the adjacent comb line. Also, the RF beat tone produced between comb lines is observed at 25.7 GHz (not shown).

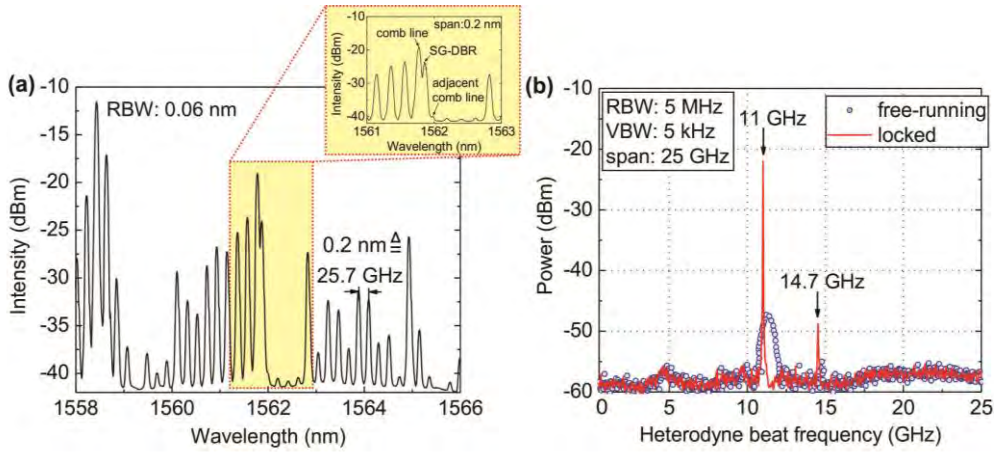

Fig. 6. (a) Optical spectrum when SG-DBR laser and comb are phase locked with a frequency difference of 11 GHz. The locking is to the comb line at 1561.77 nm. The zoom-in spectrum with a span of 2 nm is shown as inset, and (b) the RF spectrum, showing the locked beat note between SG-DBR and comb at 11 GHz is recorded. The beat note generated between SG-DBR and adjacent comb line is also visible. Both the phase-locked and free-running cases are shown to illustrate the improved relative spectral coherence between the on-chip tunable laser and comb.

5.2 Tuning resolution of OFS

The RF signal generated by beating between comb lines on a fast PD was measured. An exceptionally high spectrally pure RF line, as shown in Fig. 7(b), is observed. The 3-dB beat width of the RF tone at 25.7 GHz is <100 Hz, limited by the resolution bandwidth (RBW) of the ESA. This clearly suggests that this ultra-narrow linewidth and frequency stabilized OFC itself could be used as a reference light source for measuring the tuning resolution of our developed OFS. As a part of the experiment, the OFS output from our integrated OPLL system was mixed with the phase-coherent OFC output. As can be seen in Fig. 7(a), the mixed optical outputs are then beat down to a RF frequency by detecting that light on a high-speed external PD for precise measurement. The RF synthesizer connected to the XOR of our OPLL system was tuned in by a number of 100 Hz steps. The RF spectra were then recorded using ESA when the optical beat note is offset-locked at 2.5 GHz, as displayed in Fig. 7(c). The output optical beat note frequency shift $\Delta f_{\text{optical}}$ was then plotted as a function of change in RF frequency Δf_{RF} (Fig. 7(d)). Deviation from 100 Hz is observed to be on the order of ± 5 Hz. In such a way, our optical synthesizer achieves sub-100 Hz tuning resolution, which is the highest resolution so far reported for a chip-scale OFS. It should be noted that the optical beat note, shown in Fig. 7(c), is formed by beating the locked laser to the reference laser, indicating relative linewidth between these two light sources.

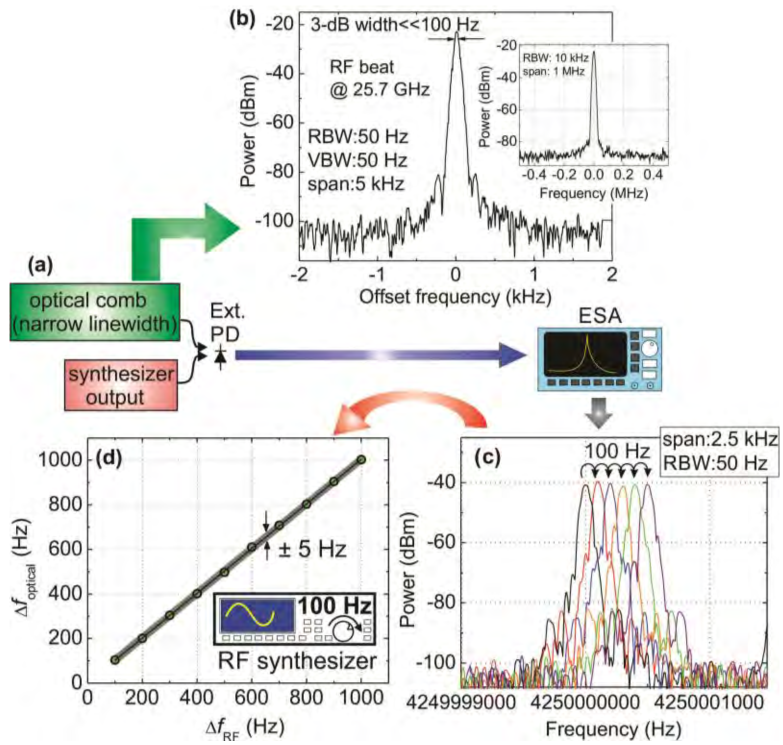

Fig. 7. (a) The measurement setup for the tuning resolution of our OFS, (b) Power spectra of an RF frequency signal at 25.7 GHz generated by beating between comb lines on a high-speed PD integrated in the packaged unit measured with different resolution bandwidth. The smaller peaks are of 60 Hz and its harmonics, appearing from the power source, (c) locked beat signal between reference comb line and the SG-DBR laser and its movement by 100 Hz, and (d) plot of change in the optical beat note with respect to change in the RF offset frequency.

5.3 Switching speed of OFS

Figure 8(a) shows how switching speed measurements of our OFS were performed. The front mirror section of the SG-DBR laser was modulated by square wave signal with a frequency of 800 kHz and 50% duty cycle from a function generator; whereas the back mirror remained open. A bias tee was used to add such a time-varying signal upon the dc bias. The square-wave signal into the front mirror modulates the lasing wavelength between two values with a separation of 5.6 nm. The peak-to-peak amplitude of modulation current applied into the front mirror was 1.6 mA measured using current probe. Laser output was then passed onto manually tunable bandpass optical filter with a 3dB bandwidth 0.95 nm, which allows only one wavelength component to pass through. Optical signals were then detected by an external high-speed photodetector and the traces on the real-time oscilloscope were analyzed. When the modulation is on, the wavelength is switched between two values separated by 5.6 nm at 800 kHz speed, which is much faster than spectrum capturing rate the optical spectrum analyzer (OSA). Therefore, both wavelength values on the OSA are observed simultaneously, as shown in Fig. 8(b). The dc offset and amplitude of the square wave are carefully selected in a way so that two output wavelengths of SG-DBR lasers can beat against two comb lines with a reasonably good optical intensity and generate a RF beat note with the same frequency. The superimposed optical spectra of comb output and laser at these two specific states are shown in Fig. 8(c). Note that the oscilloscope was triggered with the sync. output signal of the function generator. The wavelength separation between the two peaks of SG-DBR laser and comb output in two different spectral regions is 0.024 nm, corresponding to an offset frequency ~2.5 GHz, when they beat with each other.

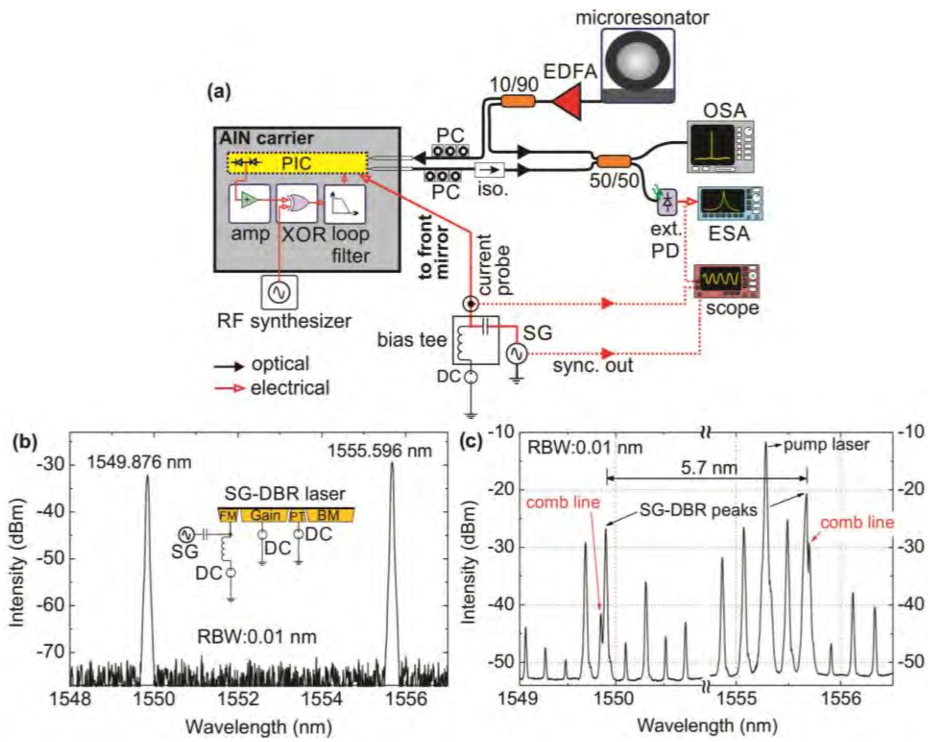

Fig. 8. (a) The test setup for measuring the switching speed of our OFS, (b) the optical spectrum of SG-DBR laser when the front mirror is modulated by a 800 kHz square-wave from a signal generator and gain current is set to a constant value of 130 mA, resulting wavelength switching between $\lambda_{1,SG\text{-}DBR}$ = 1549.876 nm and $\lambda_{2,SGDBR}$ = 1555.596 nm, and (c) superimposed optical spectra of comb output and SG-DBR laser, where both comb peaks separated by 0.024 nm from their corresponding SG-DBR laser peaks can be resolved. (BM = back mirror, DC = direct current, EDFA = erbium doped fiber amplifier, ext. PD = external photodetector, FM = front mirror, PIC = photonic integrated circuit, PC = polarization controller, PT = phase tuner, RBW = resolution bandwidth)

During the wavelength switching of SG-DBR laser, the electrical spectrum measured in ESA is shown in Fig. 9. The sharp single peak at an offset frequency of 2.5 GHz generated between SG-DBR and comb lines around 1550 nm and 1555 nm is the clear evidence for phase locking of on-chip noise lasers to comb output. The beating tone between the SG-DBR laser and the adjacent comb lines at 23.2 GHz as well as the tone at 25.7 GHz between comb lines are also seen here.

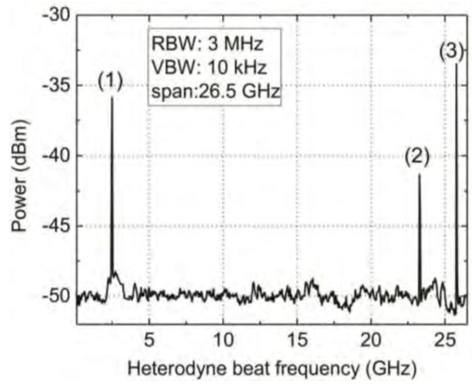

Fig. 9. RF spectrum measured at the ESA of modulated SG-DBR laser beating with the comb output during dynamic wavelength switching of SG-DBR. Three peaks are seen, (1) the locked beat note is at 2.5 GHz, produced by beating between both SGDBR peaks and the corresponding comb lines, (2) The beat note generated between both SG-DBR peak and adjacent corresponding comb line is at 23.3 GHz, and (3) the beat note produced between comb lines is at 25.7 GHz.

The OPLL will lock the on-chip SG-DBR laser to comb when the whole system including the right offset frequency from the RF synthesizer is on. This is clearly evidenced by Fig. 8(c) and 9 where one can see that two wavelengths of SG-DBR line up with two lines of the comb, generating single sharp RF beat note at 2.5 GHz. This time the output of the external PD is monitored on a wide-bandwidth real-time oscilloscope instead of connecting with ESA, illustrated by the dotted electrical path shown in Fig. 8(a). The oscilloscope trace, displayed in Fig. 10, is showing that the SG-DBR laser is phase-locked most of the time except for a short period of OPLL transient time. Importantly, this is happening periodically at a modulation frequency 800 kHz. The time interval in between two high states of such a trace can be considered as wavelength switching of SG-DBR and OPLL locking time, which is extracted as 200 ns. In the time interval of phase locking, a sinusoidal signal at 2.5 GHz, representing the locked beat note, is observed, which is shown in Fig. 10(b). Hence, our synthesizer achieves sub-µs switching and locking time.

5.4 Phase noise measurement

To evaluate the performance of our OPLL system using COTS ICs, residual phase noise of the OPLL was measured from 10 Hz to 1 GHz using the setup shown in Fig. 5. The locked beat note at 2.9 GHz produced between SG-DBR and comb was connected to the ESA and the single-sideband (SSB) phase-noise spectral density (PNSD) was then measured. The signal power level of this measurement was 42 dBm. Figure 11 shows the residual OPLL phase noise at offsets from 10 Hz to 1 GHz. For the comparison, PNSD of the background, RF synthesizer at 2.9 GHz, and comb source (through the RF beat note generated between comb lines) are superimposed in Fig. 11. The output signal power levels were kept the same during the measurement in order to obtain consistency.

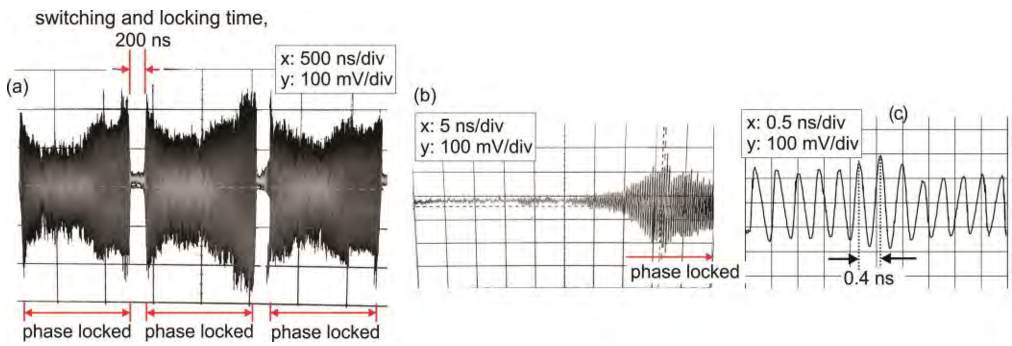

Fig. 10. (a) A real-time oscilloscope trace of the external photodiode output of both wavelength component of SG-DBR laser during wavelength switching in order to measure the locking time of the OPLL system. Three periods are shown here which corresponds to the modulation frequency of front mirror, i.e. 800 kHz, (b) trace with a smaller span, showing the transition to phase-locking, and (c) trace with smallest span to show 2.5 GHz signal during phase-locking.

The phase noise variance from 1 kHz to 10 GHz is calculated to be 0.08 rad^2, corresponding to 14° standard deviation from the locking point. This result is better than the one reported in [39]. As can be seen in Fig. 11, low frequency noise with a value less than 80 dBc/Hz at an offset above 200 Hz for PNSD was achieved., whereas the same value at an offset above 10 kHz was achieved in [29, 42]. Lu et al. also reported better than 80 dBc/Hz at offsets above 5 kHz which is again worse than the performance reported here [35]. However, the phase variance of our results is comparable with [29, 42] which could be attributed to the pedestal after 1 kHz which may be caused by a fiber path length mismatch between the comb and OPLL laser paths (see Fig. 5). Thus, after 1 kHz some additional noise from the slave laser is observed and contributes to the overall phase variance. Matched path length will be used in the future work.

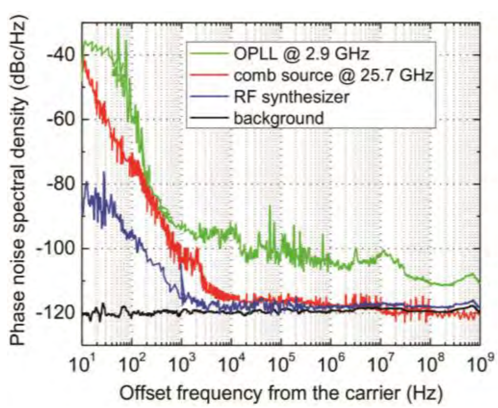

Fig. 11. Single-sideband residual phase noise of the heterodyne OPLL at 2.9 GHz. Phase noise results of the RF signal at 25.7 GHz generated between comb lines, RF synthesizer, and background is also shown here for comparison.

6. Summary and outlook

In this work, a chip-scale optical frequency synthesis spanning 25 nm is demonstrated. A stable heterogeneously integrated Kerr frequency comb characterized with 26 GHz repetition rate is used as a reference. Better than 100 Hz resolution within an accuracy of 5 Hz, which is the highest resolution reported for chip-scale optical frequency synthesis, is obtained. Both switching between two adjacent comb lines as well as multiple comb lines (i.e. 28 lines) separated by 5.6 nm and phase locking at the same time are achieved. As a future work, our main goal is to develop a fully chip scale synthesizer which requires to replace the EDFA used in this study with on-chip SOAs. Instead of amplifying the power in the optical domain, we can increase the sensitivity of our electronic ICs as an alternative so that the weak error signal generated by beating on-chip laser and low-power comb line at the balanced photodiodes can be handled by the feedback electronics. Specifically, the sensitivity of our OPLL system can be increased by using ultrahigh-gain amplifiers with low noise figure or designing an application specific IC so that on-chip lasers can be phase locked to a comb line without an EDFA. This will open a new era for optical communications and sensing. This work will allow OPLL systems to be as useful as traditional RF phase-locked loops. In addition to this, another important goal is to achieve a 2/3 octave spanning optical frequency comb and use this as a reference source. This will allow us to have a broader synthesizer.

Funding

This work was supported by the GOALI project funded by the National Science Foundation (NSF) under Grant No. 1402935.

Acknowledgment

A portion of this work was carried out in the UCSB nanofabrication facility, part of the NSF funded NNIN network.

Optical Frequency Synthesis by Offset-Locking to a Microresonator Comb

Shamsul Arafin[1,*], Arda Simsek[1], Seong-Kyun Kim[1], Sarvagya Dwivedi[1], Wei Liang[2], Danny Eliyahu[2], Jonathan Klamkin[1], Andrey Matsko[2], Leif Johansson[3], Lute Maleki[2], Mark J. Rodwell[1], and Larry A. Coldren[1,*]

[1]Department of Electrical and Computer Engineering, University of California Santa Barbara, Santa Barbara, CA 93106, USA
[2]OEwaves Inc., Pasadena, CA 91107, USA
[3]Freedom Photonics LLC, Santa Barbara, CA 93117, USA
**Email: sarafin@ece.ucsb.edu*

Abstract: We report on the experimental demonstration of a chip-scale microresonator comb enabled optical frequency synthesizer using an agile and highly-integrated heterodyne optical phase-locked loop with InP-based photonic integrated circuit and commercial-off-the-shelf electronic components.

OCIS codes: (250.5300) Photonic integrated circuits; (060.5625) Radio frequency photonics; (060.2840) Heterodyne (140.0140) Lasers and laser optics; (140.3600) Lasers, tunable; (140.3945) Microcavities; (230.5750) Resonators

In recent years, chip-scale and low-power optical frequency synthesizers (OFSs) based on self-stabilization of full-octave microresonator combs are being increasingly investigated for various ultra-high-precision applications in which micro-Hertz levels of stability are sought [1]. However, for many practical applications, including optical spectroscopy [2], optical communication [3], light detection and ranging (LiDAR) [4], and some types of frequency metrology, stabilities in the few Hertz range would be very attractive. In this work, we report on the experimental demonstration of a continuously-tunable, microresonator-enabled, ultra-compact OFS near 1550 nm achieved by using a heterodyne optical phase-locked loop (OPLL) [5].

Figure 1(a) illustrates the basic concept of a compact and chip-scale OFS. A microresonator-based optical frequency comb (OFC) was used as an ultra-stable and narrow linewidth source, serving as a master oscillator (MO) [6]. The comb lines are then used as the reference for the heterodyne OPLL. A RF frequency from a tunable RF synthesizer is applied to feedback electronic circuits of the OPLL to introduce a frequency offset, defined by the frequency difference between the master laser and the local oscillator (LO) laser. By tuning the phase section current of the LO laser as well as f_{RF}, the LO is phase-locked to the comb lines. In order for an OFS to synthesize any arbitrary frequency between comb lines, the heterodyne OPLL offset frequency range must be at least half of the comb's free spectra range (FSR). Also for such continuous tuning, the FSR of the comb must be less than the slave laser's mode-hop free tuning range.

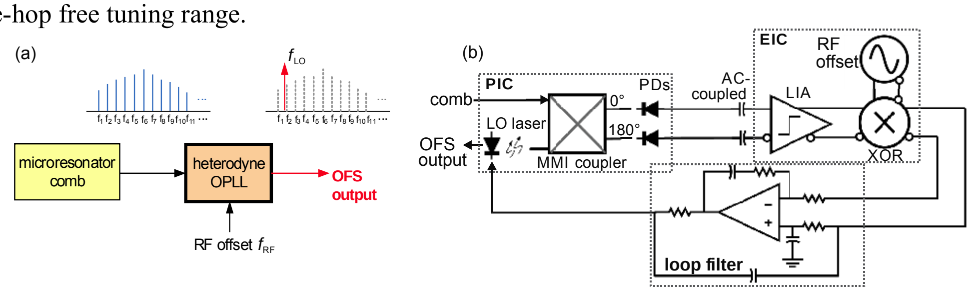

Fig. 1. (a) Optical frequency synthesizer (OFS) system, showing two main building blocks – a comb source and a heterodyne OPLL. The optical spectra are also plotted at the output of each block, and (b) system architecture of the heterodyne OPLL. (MMI: multimode interference, LIA: limiting amplifier, PIC: photonic integrated circuit, EIC: electronic integrated circuit, and PDs: photodiodes)

The heterodyne OPLL, serving as a core building block of an OFS is displayed in Fig. 1(b). This system is composed of a photonic integrated circuit (PIC) and feedback electronic circuits. The latter is composed of electronic ICs (EICs) and a loop filter. Injected single comb line as a MO and sampled-grating distributed Bragg reflector (SG-DBR) as a LO in a PIC oscillate at different frequencies, producing a RF beatnote at this offset frequency on the balanced photodetector pair. The beat signal is then amplified by the limiting amplifier (LIA) to make the system insensitive to intensity fluctuation from the PIC. A phase detector (logic XOR gate in this case) compares the phase of the beat signal with a reference signal from a tunable RF synthesizer, thus generating the baseband phase error signal. This is then fed back through the loop filter to control the LO laser's phase and hence lock the phase of the LO to a single comb line.

The heterodyne OPLL board was assembled by soldering both PIC and EIC on top of the AlN carriers. The loop filter as a part of the feedback electronic circuits was also built on the same carrier using discreet components and an operational amplifier. The PIC, EIC, and loop filter were placed together closely using wirebonds. The carriers were carefully designed to decrease the loop delay as much as possible. A photograph of such an OPLL system and its zoomed-in version are shown in Fig. 2(a) and (b), respectively. The experimental setup is shown in Fig. 2(c). Using lensed fibers, the microresonator comb output was coupled into the PIC for offset locking. The SG-DBR laser was coupled out from the back mirror to beat with the comb off-chip for verifying phase-locking.

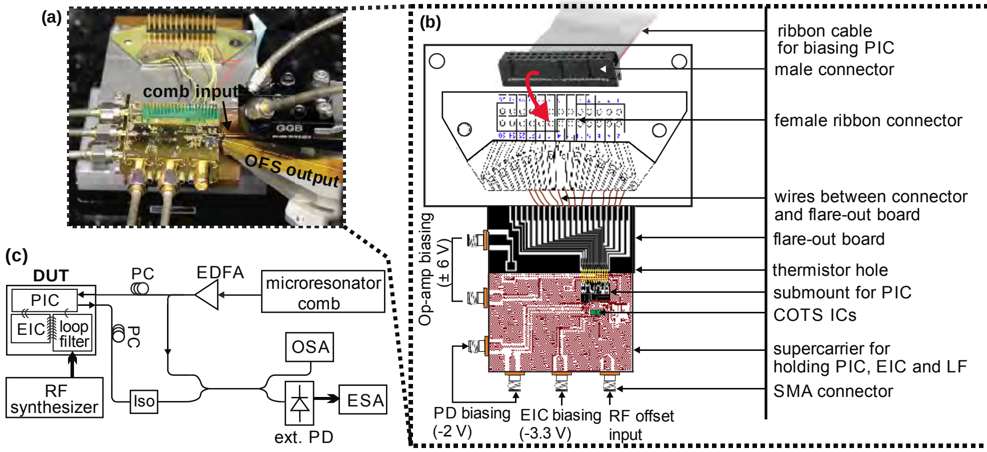

Fig. 2. (a) A photograph of the OPLL system, and its (b) zoomed-in version (lensed fibers and XYZ stages are not shown), and (c) the schematic of the test setup for monitoring the performance of the optical frequency synthesizer. Thinner lines show fiber connection and thicker lines show the RF cable connection. (ESA: electrical spectrum analyzer, EDFA: erbium doped fiber amplifier, OSA: optical spectrum analyzer, PC: polarization controller, ext. PD: external photodetector, iso: isolator)

We successfully phase-locked the SG-DBR laser to the optical frequency comb (OFC) using our heterodyne OPLL system. Under this locked condition, the superimposed optical spectra of comb output and laser are shown in Fig. 3(a) where the wavelength difference between comb peak and the nearest SG-DBR laser peak is 0.02 nm. The RF spectra of the beatnote at an offset frequency of 2.5 GHz, in cases of free-running and phase-locked, are shown in Fig. 3(b). In the locked case, the RF linewidth is reduced significantly, indicating the improved relative spectral coherence between the LO laser and the comb. Figure 3(c) shows the RF spectrum acquired with a higher span. Thus the on-chip SG-DBR laser is offset-locked across multiple comb lines by changing the current in mirror and phase sections of the SG-DBR laser and by applying the right RF offset frequency. Synthesizing an arbitrary optical frequency between two adjacent comb lines is achieved by tuning the RF offset source and the phase section current. In other words, an arbitrary optical frequency synthesis in the range from 1543 nm to 1568 nm (mainly limited by the output power level of the comb) is demonstrated using our presented OFS. Frequency switching of the on-chip laser to a point more than two dozen comb lines away (~5.6 nm) and simultaneous locking to the corresponding nearest comb line is also achieved in a time of ~200 ns. The synthesizer's performance characteristics relating to frequency switching and tuning resolution will be shown at the conference.

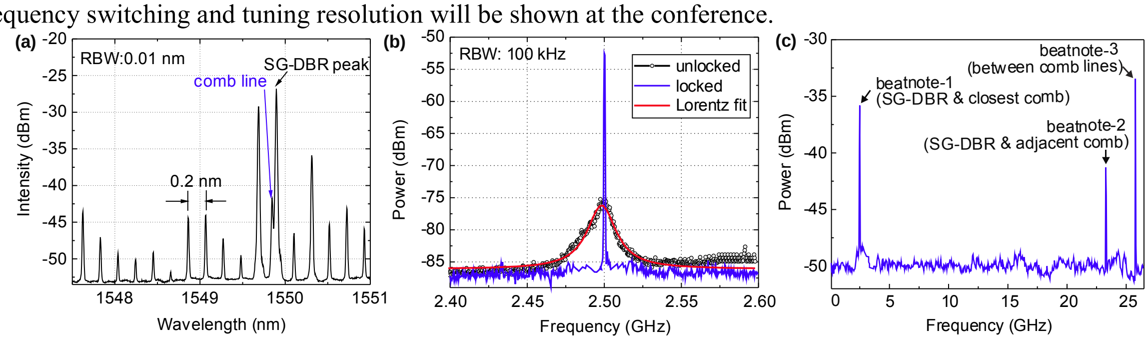

Fig. 3. (a) Optical spectra of comb at 1549.848 nm and LO laser when offset-locked to the comb, (b) the corresponding RF spectra, showing the measured linewidth of the free-running SG-DBR (LO) laser and phase-locked SG-DBR laser, and (c) RF spectrum of the locked beatnote between LO laser and comb at 2.5 GHz acquired with a higher span. The beatnote generated between LO laser and adjacent comb line at 23.2 GHz and the beatnote produced between comb lines at 25.7 GHz are also visible. The resolution bandwidth is 3 MHz.

[1] M. Martin, et al., "Testing ultrafast mode-locking at microhertz relative optical linewidth," Opt. Express 17, 558-568 (2009).
[2] A. A. Madej, et al., "Rb atomic absorption line reference for single Sr+ laser cooling systems," Appl. Phys. B **67**, 229–234 (1998).
[3] J. Castillega, et al., "Precise measurement of the J = 1 to J = 2 fine structure interval in the 2(3)P state of helium," Phys. Rev. Lett. **84**, 4321-4324 (2000).
[4] W. C. Swann, and N. R. Newbury, "Frequency-resolved coherent lidar using a femtosecond fiber laser," Opt. Lett. **31**, 826-828 (2006).
[5] S. Ristic, et al., "An Optical Phase-Locked Loop Photonic Integrated Circuit," J. Lightwave Technol. **28**, 526-538 (2010).
[6] W. Liang, et al., "High spectral purity Kerr frequency comb radio frequency photonic oscillator," Nature Communications **6**, 7957 (2015).

IEEE Photonics Journal
An IEEE Photonics Society Publication

Open Access

Power-Efficient Kerr Frequency Comb Based Tunable Optical Source

Volume 9, Number 3, June 2017

S. Arafin, *Member, IEEE*
A. Simsek, *Student Member, IEEE*
S.-K. Kim
W. Liang
D. Eliyahu
G. Morrison
M. Mashanovitch, *Senior Member, IEEE*
A. Matsko, *Senior Member, IEEE*
L. Johansson, *Member, IEEE*
L. Maleki, *Fellow, IEEE*
M. J. Rodwell, *Fellow, IEEE*
L. A. Coldren, *Life Fellow, IEEE*

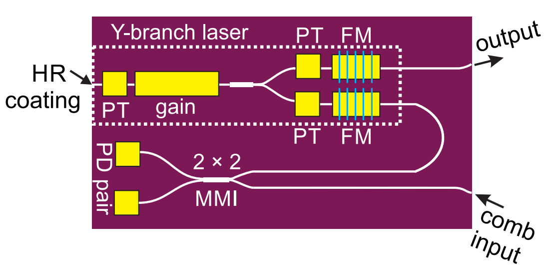

(a)

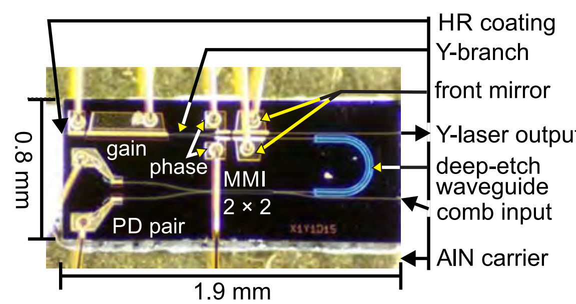

(b)

DOI: 10.1109/JPHOT.2017.2696858

Power-Efficient Kerr Frequency Comb Based Tunable Optical Source

S. Arafin,[1] *Member, IEEE*, A. Simsek,[1] *Student Member, IEEE*, S.-K. Kim,[1] W. Liang,[2] D. Eliyahu,[2] G. Morrison,[3] M. Mashanovitch,[3] *Senior Member, IEEE*, A. Matsko,[2] *Senior Member, IEEE*, L. Johansson,[3] *Member, IEEE*, L. Maleki,[2] *Fellow, IEEE*, M. J. Rodwell,[1] *Fellow, IEEE*, and L. A. Coldren,[1] *Life Fellow, IEEE*

[1]Department of Electrical and Computer Engineering, University of California, Santa Barbara, CA 93106 USA
[2]OEwaves Inc., Pasadena, CA 91107 USA
[3]Freedom Photonics LLC, Goleta, CA 93117 USA

DOI:10.1109/JPHOT.2017.2696858

Manuscript received February 27, 2017; revised April 5, 2017; accepted April 18, 2017. Date of publication April 24, 2017; date of current version May 3, 2017. This work was supported in part by DARPA-MTO under the DODOS project and in part by the National Science Foundation (NSF) under Grant 1402935. A portion of this work was carried out at the UCSB Nanofabrication facility, part of the NSF funded NNIN network. Corresponding author: S. Arafin (e-mail: sarafin@ece.ucsb.edu).

Abstract: We designed and demonstrated a power-efficient highly integrated photonic system, requiring a total power consumption of 1.7 W and producing a spectrally pure coherent optical signal with a wavelength range of 23 nm in the C-band. The system consists of a compact, low-power InP-based photonic integrated coherent receiver, microresonator-based Kerr frequency comb, and agile electronic circuits. The photonic coherent receiver contains a 60-nm widely tunable Y-branch local oscillator (LO) diode laser, a coupler, and a pair of photodetectors. It consumes record-low (approximately 184 mW) electrical power. The optical frequency comb reference has excellent spectral purity, $<$4 kHz optical linewidth, and good frequency stability. The spectrally pure tunable optical source was produced by offset locking the on-chip LO laser of the integrated receiver to this frequency comb source. A possibility of further stabilization of the frequency comb repetition rate by locking to an external radio frequency synthesizer was demonstrated.

Index Terms: Photonic integrated circuits, integrated optics, optical phase-locked loop, heterodyne, optical frequency comb, optical microresonator.

1. Introduction

Over the past couple of decades, numerous research efforts have been devoted to the area of photonic integrated circuits (PICs) [1]–[5]. This is mainly because the cost, size, weight, and combined insertion loss of the on-chip optical components can be significantly reduced through integration, while the stability and performance of the photonic integrated systems can be drastically enhanced. In addition to these obvious advantages, low-power-consumption is also an important motivating factor for photonic integration. The device reliability increases with decreasing power levels, and therefore, PICs contribute to the system reliability to a great extent by reducing its operating electrical power [3]. The associated total thermoelectric cooler (TEC) power consumption also decreases significantly.

Recently, highly integrated optical phase-locked loops (OPLLs) have been found to be one of the most attractive technologies for a number of emerging applications, including optical sensing and frequency synthesis [6]. Many novel compact optical systems in these areas can be developed by using such integrated OPLLs. In this work, we demonstrate the OPLL-based offset locking of an on-chip widely-tunable local oscillator (LO)-laser within the coherent receiver PIC to a microresonator-based optical frequency comb (OFC). This is a major step towards an eventual demonstration of the chip-scale, low-power, ultrastable optical frequency synthesizer. An integrated optical synthesizer is a device that is able to produce a narrow-linewidth optical signal at a desired wavelength. Such a synthesizer can be created by offset locking of a broadly tunable LO laser to an OFC master oscillator (MO).

In addition to the LO and MO, the synthesizer includes a photonic integrated coherent receiver and feedback electronics to realize an OPLL. The photonic receiver receives the mixed output of LO and MO signals and produces an error signal fed into the electronic circuits that tune the phase of the LO in order to match that of the MO. Therefore, high-performance, low-power and compact coherent receiver PICs with an integrated widely-tunable LO are of significant research interest due to their use in optical coherent communication, possibly employing OPLL systems in relatively short links [7].

Researchers have already demonstrated prototype PIC receivers for OPLLs [8], [9]. Very recently, we have shown a highly integrated heterodyne OPLL with an InP-based receiver PIC and commercial-off-the-shelf electronic components [10]. However, the PICs used in these studies consumed 0.5 W of power and their footprint exceeded 2.3 mm^2 [9]–[11]. A significant improvement of these parameters is still needed in designing compact and low-power systems. In this paper, we report on the development of a compact, low-power, coherent receiver PIC and its use in OPLLs for frequency synthesis. Compared to the state-of-the-art results reported in [10]–[12], our photonic receiver circuit is 1.5 times smaller in size, it consumes 2.7 times less electrical power and it exhibits 10 nm wider wavelength tuning. We found that the geometrical size and the electrical power consumption for the PICs can be reduced significantly by careful design. Also, inherent advantages of integration were obtained by making the system much smaller. This is attractive since small PICs enable a short OPLL loop delay which results in a high loop bandwidth.

The coherent receiver PIC in an OPLL system usually consists of a widely-tunable LO laser, optical couplers, and a balanced photodetector pair integrated monolithically. Due to the characteristics of the heterodyne OPLL, the noisy LO laser can be forced to clone the low phase noise of the reference laser within its loop bandwidth. With a good RF offset source, this feature can be maintained while tuning the optical frequency away from the reference with Hz level accuracy. To completely take advantage of the heterodyne OPLL, a spectrally pure OFC source with many stable lines, should serve as the reference. This configuration enables tuning across a wide optical frequency range.

In our experiment, we utilized an OFC oscillator [13] developed specifically for the OPLL. The device involves a high quality factor (Q) crystalline whispering gallery mode resonator (WGMR) heterogeneously integrated on a microphotonic bench with a pump laser. This entire oscillator can be easily integrated on an optical microbench and eventually reproducibly integrated on a PIC [14].

The nonlinear WGMR pumped with continuous-wave (CW) light produces an OFC when the power of the pump exceeds a certain threshold [15]. The process results from an optical phenomenon relying upon both self- and cross-phase modulation in the reonator host material, and it is similar to the modulation instability in optical fiber. The high Q-factor of the WGMR ensures that the pump power required to produce an OFC spanning a few THz does not exceed a few tens of mW. Thus, the low power consumption of the comb reference also contributes to minimizing overall system power. Our OFC spans approximately 23 nm, and it is produced by pumping the WGMR with 20 mW of light at 1550 nm.

Further stabilization of such an integrated OFC using external radio frequency (RF) oscillators is also reported. It was demonstrated previously by means of thermal, thermo-optical, as well as mechanical actuation. However, the microresonator OFC devices were not packaged and the actuation bandwidth was comparably narrow. Here, we use a completely packaged microphotonic

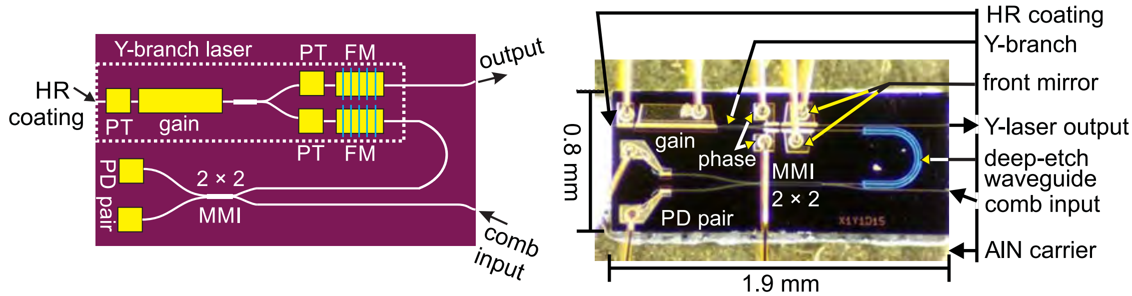

(a) (b)

Fig. 1. (a) Functional schematic of the photonic integrated receiver circuit composed of a Y-branch laser, two MMI couplers, and a balanced photodetector pair, as well as (b) microscope image of the PIC mounted on a separate aluminium-nitride (AlN) carrier and wirebonded. (FM: front mirror, HR: high reflection, MMI: multimode interference, PD: photodetector, and PT: phase tuner.)

structure that includes a high-Q WGMR with laminated piezo element (PZT) enabling locking the repetition rate of the OFC to an external source within 100 kHz bandwidth. The demonstrated relative stability of the locking is better than 10^{-14} per hour integration time.

This paper is organized as follows. Section 2 is devoted to a discussion on the newly developed photonic coherent receiver used in this study. The electronic-photonic integration details are described in Section 3. The spectral characteristics of the comb device, as well as heterodyne OPLL results, are presented in Section 4. Operation of the Kerr OFC unit and its stabilization is elucidated in Section 5.

2. Receiver Details

2.1 Design and Fabrication

A widely tunable compact Y-branch laser, a 2 $\times$ 2 multimode interference (MMI) coupler, a balanced photodetector pair and input waveguide are monolithically integrated on an InGaAsP/InP material platform. A schematic of the coherent receiver PIC is shown in Fig. 1(a). The device size is 1.9 mm $\times$ 0.8 mm. For the integration, the offset quantum well (OQW) platform was employed, where the active-region quantum-wells are first grown on top of a common waveguide, and then removed in the regions that are to become passive prior to the regrowth of the top cladding and contact layers. Details of the processing steps for the well-established OQW-based material structure can be found elsewhere [16]. A microscope image of the processed chip is shown in Fig. 1(b), where two output ports after a 1 $\times$ 2 MMI coupler can be seen. For the Y-branch laser design, front grating mirrors on both ports are incorporated. One port is coupled to the integrated coherent receiver, while the second port provides the output signal.

One of the key components in this integrated chip is the Y-branch laser which consumes most of the power. Similar to the sampled-grating distributed Bragg reflector(SG-DBR) laser, the Y-branch laser uses Vernier tuning to reach a wide tuning range. Our design was optimized with a shorter cavity and a highly-reflecting back cleaved/HR-coated mirror for low-power consumption. The high-reflection (HR) coating with a reflectivity of $>$95% at back facet enables a short gain section further shortening the overall length. The front sampled-grating mirrors select wavelength through Vernier tuning but have lower reflection for better efficiency and higher output power. Phase sections are included for continuous tuning. No long absorber section or integrated booster preamplifier was included in this design so that the power consumption and chip-size could be reduced further. The output and input waveguide cleaved facets were coated with antireflection (AR) coating to suppress parasitic reflections.

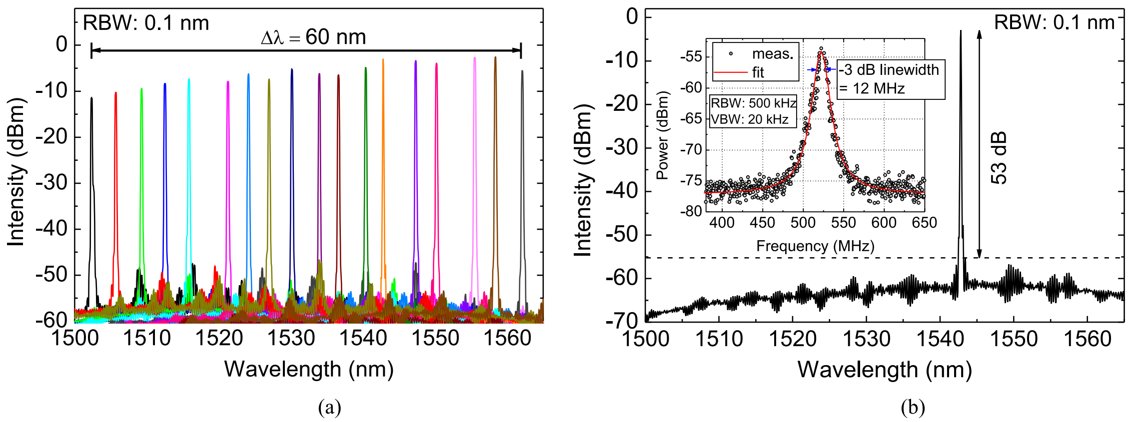

Fig. 2. (a) Superimposed measured lasing spectra of the Y-branch laser with an emission wavelength, ranging from 1502 to 1562 nm, and (b) typical single-mode lasing spectrum at a wavelength of 1543 nm with a side-mode suppression ratio of 53 dB. Beat spectrum of the laser obtained using a heterodyne technique is shown as the inset.

2.2 Spectral Characterization of Y-Branch Lasers

Fig. 2(a) shows the superimposed measured lasing spectra from 1502 nm to 1562 nm. Electrical current in both front mirrors is tweaked to obtain such wide tuning. As can be seen, the tuning range of such a laser is about 60 nm, covering the entire C-band. Any and all wavelengths can be obtained in this range by setting a combination of these mirror currents to set the approximate wavelength window, and then fine tuning of the cavity mode with the phase section, which is controlled by the OPLL in the phase-locked source. Tuning to a particular wavelength is, thus, not done by continuously tuning across the spectrum, but by digitally tuning to the desired wavelength in these two steps. Spurious outputs could be avoided by blanking the output during this process. The peak gain wavelength of the device being tested is blue-shifted. This induces the tuning range of the laser to be shifted towards the shorter wavelength. Fig. 2(b) shows a typical single-mode lasing spectrum of the Y-branch laser at the emission wavelength of 1543 nm. The laser shows good single-mode working performance with a side-mode suppression ratio (SMSR) of 53 dB. SMSRs above 45 dB across the whole tuning range with typical values greater than 48 dB are observed. The linewidths of the Y-branch lasers were also measured, using a heterodyne technique. First, we beat this laser with a narrow linewidth external-cavity laser (ECL) and the beatnote is detected to an external fast photodetector (PD) which converts it into an electrical tone. The RF signal was then measured with an electrical spectrum analyzer (ESA). Thus, before phase-locking, the 3-dB linewidth is measured to be 12 MHz, as shown in the inset of Fig. 2(b).

2.3 Balanced Photodiode Characterization

High bandwidth, low dark current, and high saturation power are the desired characteristics of on-chip photodiodes (PDs). The coherent receiver PIC was characterized by measuring the dark current and bandwidth of the balanced PD pair. The current-voltage ($I-V$) characteristics at room-temperature are shown in Fig. 3(a) for both PDs. For the quantum-well (QW) PD with the size of $3.3 \times 50\ \mu\text{m}^2$, the dark current is 10 μA at -3 V. The bandwidth of these PDs was measured using a lightwave network analyzer. By sweeping the modulation frequency from the network analyzer, the relative RF response of the photodetectors (PDs) biased at a -3 V was measured. The response, as shown in Fig. 3(b), is normalized at 1 GHz due to the low-frequency noise from the measurement system. In addition to the noise, gain ripples with $\pm$ 3 dB were observed at frequencies below 1 GHz, possibly due to the impedance mismatch between devices under study and the system. The modulation characteristics of these PDs were measured with the device wirebonded. By direct

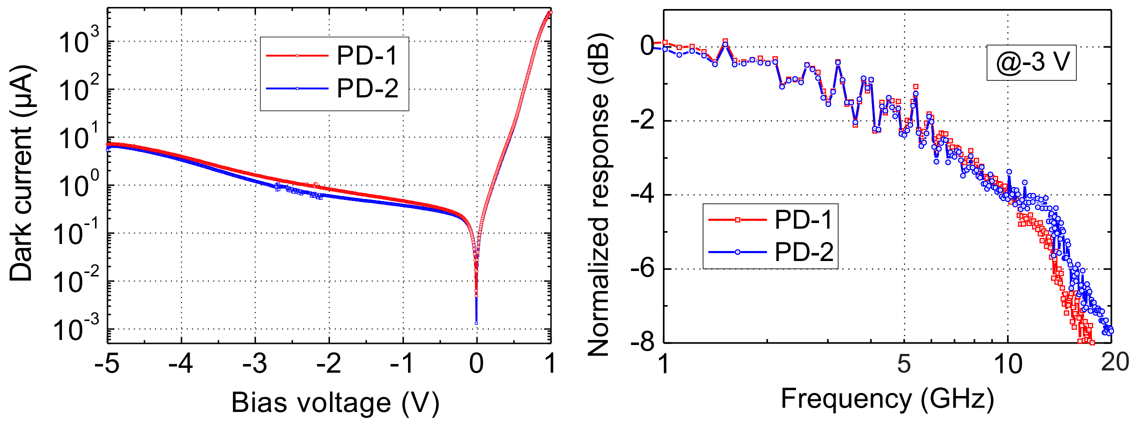

(a) (b)

Fig. 3. (a) Dark currents and (b) modulation characteristics of the two on-chip photodiodes in InP monolithic coherent receiver PIC shown in Fig. 1.

TABLE 1

Total Power Consumption of the Optical Frequency Synthesis System Using Photonic Coherent Receiver Based on Y-Branch Lasers

Element	Section	Number	Current (mA)	Voltage (V)	Power (mW)
PIC	gain	1	73	1.5	109.5
	FM	2	20	1.3	52
	PT	2	7	1.3	18.2
	PD	2	−1	−2	4
EIC	LIA	1	180	3.3	594
	XOR	1	130	3.3	429
	op-amp	1	16	6	96
OFC	pump laser	1	165	2.4	396
	Total		**616**		**1699**

EIC = electronic integrated circuits, FM = front mirror, LIA = limiting amplifier, OFC = optical frequency comb, PD = photodetector, PIC = photonic integrated circuits, and PT = phase tuner. Please note that Erbium-doped fiber amplifier (EDFA) and thermo-electric cooler (TEC) power are not included here.

probing on chip, a better performance is expected. Importantly, the bandwidth of the PDs is large enough that our OPLL system with the sensitive feedback electronic circuits can exhibit the offset locking range as high as 18 GHz [17].

2.4 Power Budget Calculation

Table 1 presents the total maximum power consumption of our photonic coherent receiver based on Y-branch lasers during the full operation, enabling 60 nm wavelength tuning. There are three phase

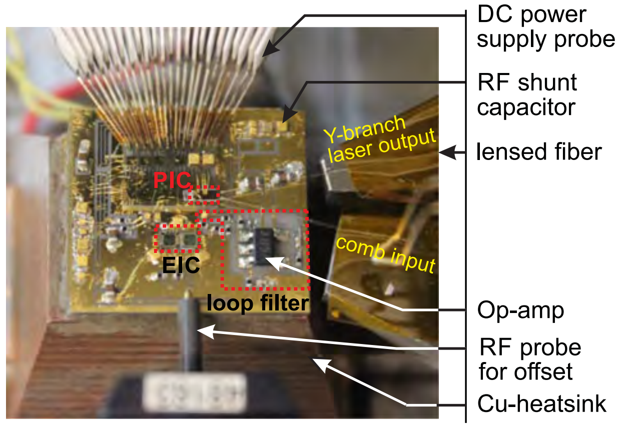

Fig. 4. Microscope image of the entire heterodyne OPLL system where PIC, COTS ICs and loop filter are highly integrated on a separate AlN supercarrier. Finally, it rests on a copper heatsink for the measurement. Two lensed fibers at the right are butt-coupled to the waveguide endface of the photonic chip.

tuning sections integrated in the receiver circuit. The ones, located after the Y-branch and next to the front mirror, are responsible for supermode jumping. In other words, those two phase sections allow us to tune the reflection envelope unlike the one which is located at the far left in Fig. 1. The phase section at the left side of the gain section is responsible for fine emission wavelength tuning, i.e., cavity mode tuning, which was connected to the feedback electronic circuits. It should be noted that it is possible to achieve full wavelength coverage using only two phase sections of the Y-branch laser. One of the phase sections next to the front mirrors can be considered as a redundant. Table 1 also reports the power consumption of other elements, including the packaged OFC unit, EICs, and loop filter components in the overall OPLL.

3. Electronic-Photonic Integration

Fig. 4 shows an image of the heterodyne OPLL system board on the test stage, where PIC, EIC and loop filter (LF) were assembled closely together by wirebonding. This assembly was done by mounting all these three parts on a patterned ceramic supercarrier in close proximity to minimize loop delay. An AC-coupled system was prepared by forming an on-chip bias tee in order to continuously remove DC offsets from the balanced-PD signals. The balanced-PDs reduce the influence of relative intensity noise (RIN) from the LO laser since this noise is common to both detectors.

As a part of the feedback electronics, SiGe-based limiting amplifier (LIA) and logic XOR gate, both manufactured by ADSANTEC [18], were employed. A high-speed emitter coupled logic differential amplifier with a 30 dB differential gain was used as a LIA. It is connected to the balanced PD pair in order to limit and square-up the input PD signals. This helps to make the OPLL system insensitive to PD power fluctuations. This LIA was followed by a high-speed digital XOR gate to obtain the phase difference between the RF beatnote resulting from the beating of the two lasers and a reference signal from a tunable RF synthesizer. Both are commercial-off-the-shelf (COTS) SiGe elements whose details can be found in [18]. A commercial LMH6609 op-amp and discrete surface-mount device (SMD) components were used to build up the LF circuit and its design details are listed in [19]. An additional fast feedforward path was also included in the LF to increase the loop bandwidth to 500 MHz. The output from the XOR gate is smoothed out by the LF to control the LO laser's phase and hence lock the phase of the LO to a single comb line. The OPLL system size is approximately 1.8 $\times$ 1.6 cm^2. The system could be made as compact as 1 cm^2 easily by optimizing the supercarrier design.

4. Offset Locking to Microresonator Comb

4.1 Spectral Characterization of Optical Frequency Combs

An OFC generated using a semiconductor laser pumping a crystalline MgF_2 resonator with a mode spacing of 25.7 GHz was used in this study [15]. The unit was packaged in ∼1 inch cubed form factor and its fiber-coupled output was sent to an OSA. The measured optical spectrum with a 50-dB span of 23 nm is shown in Fig. 5(a). The strongest central line at 1555.27 nm originates from residual light of the pump laser. The RF signal generated by beating between comb lines on a fast PD integrated in the packaged unit was measured to distinguish between chaotic and coherent regimes of the frequency comb. An exceptionally high spectrally pure RF line with the coherent comb is observed. The 3-dB beat width of the RF tone at 25.7 GHz is <100 Hz, limited by the resolution bandwidth (RBW) of the ESA [10]. The phase noise of this RF tone is shown in Fig. 5(b). The noise was measured using OEwaves' phase noise test system.

Depending on the initial conditions, the OFC unit produces frequency combs with envelopes varying in shape. The variations can be linked to the generation of a different number of optical pulses within the WGMR. While all the realized coherent states are intrinsically stable and suitable for LO stabilization, the state corresponding to the single pulse localized in the resonator is advantageous as it does not have any envelope structure. Changing of the power of the comb lines makes the offset locking to some of the modes of the OFC a hard task. We tried to utilize the frequency combs with the smoothest envelope.

Fig. 5(b) shows the measured single sideband (SSB) phase noise of the beat of two self-injection locked pump lasers. One of the pump lasers is integrated in our packaged OFC unit. The optical phase noise corresponds to less than 100 Hz instantaneous linewidth of the pump laser is shown in the inset. To determine an effective linewidth, the frequency noise spectrum is derived from the phase noise spectrum by the following relation [20]:

$$S_\nu(f) = 2f^2\mathcal{L}(f) \tag{1}$$

where $\mathcal{L}(f)$ [Hz^{-1}] is the SSB power density of the phase noise, and $S_\nu(f)$ [Hz^2/Hz] the corresponding frequency power noise. The effective instantaneous linewidth $\Delta\nu_{\mathrm{instant}}$ is then given by the minimum of frequency noise multiplied by π [20]

$$\Delta\nu_{\mathrm{instant}} = \pi * \min{}^{\mathrm{m}}[S_\nu(f)]. \tag{2}$$

To measure the phase noise, two packaged OFC units were used. We tuned them in a way that the combs were produced and then changed the frequencies of the lasers (by changing the frequencies of the resonators) so that the beat note of the lasers did not exceed a few GHz, and measured separately the phase noise of the RF signals produced by the units (by the combs) as well as RF signal produced by the two lasers emitted by the units. Assuming that the lasers are nearly identical, the laser beat phase noise should be reduced by 3 dB with respect to the shown noise to reflect the noise of the single laser. We also studied the spectral purity of the optical comb lines using the heterodyne-technique. The 3 dB linewidth of the RF beatnote created on a fast photodiode by beating a comb frequency harmonic, centered at 1553 nm, and a low noise local oscillator does not exceed 4 kHz, as shown in Fig. 5(c). Measurement with smaller RBW was hindered because of the jitter of the beat note frequency. This clearly suggests that comb lines can be considered as an ultra-narrow linewidth light source.

4.2 Experimental Setup

The comb output from the packaged and fiber-pigtailed OFC unit is optically amplified by an erbium-doped fiber amplifier (EDFA) and finally coupled into the photonic coherent receiver PIC using a tapered lensed fiber. The Y-branch laser output through front mirror was coupled out from the front side of the PIC using a similar lensed fiber for monitoring purposes. An optical isolator was used at the laser output to reduce back reflections. To measure the OPLL tone, the output from the laser was mixed with the comb in an off-chip 2 × 2 coupler, detected via an external high speed

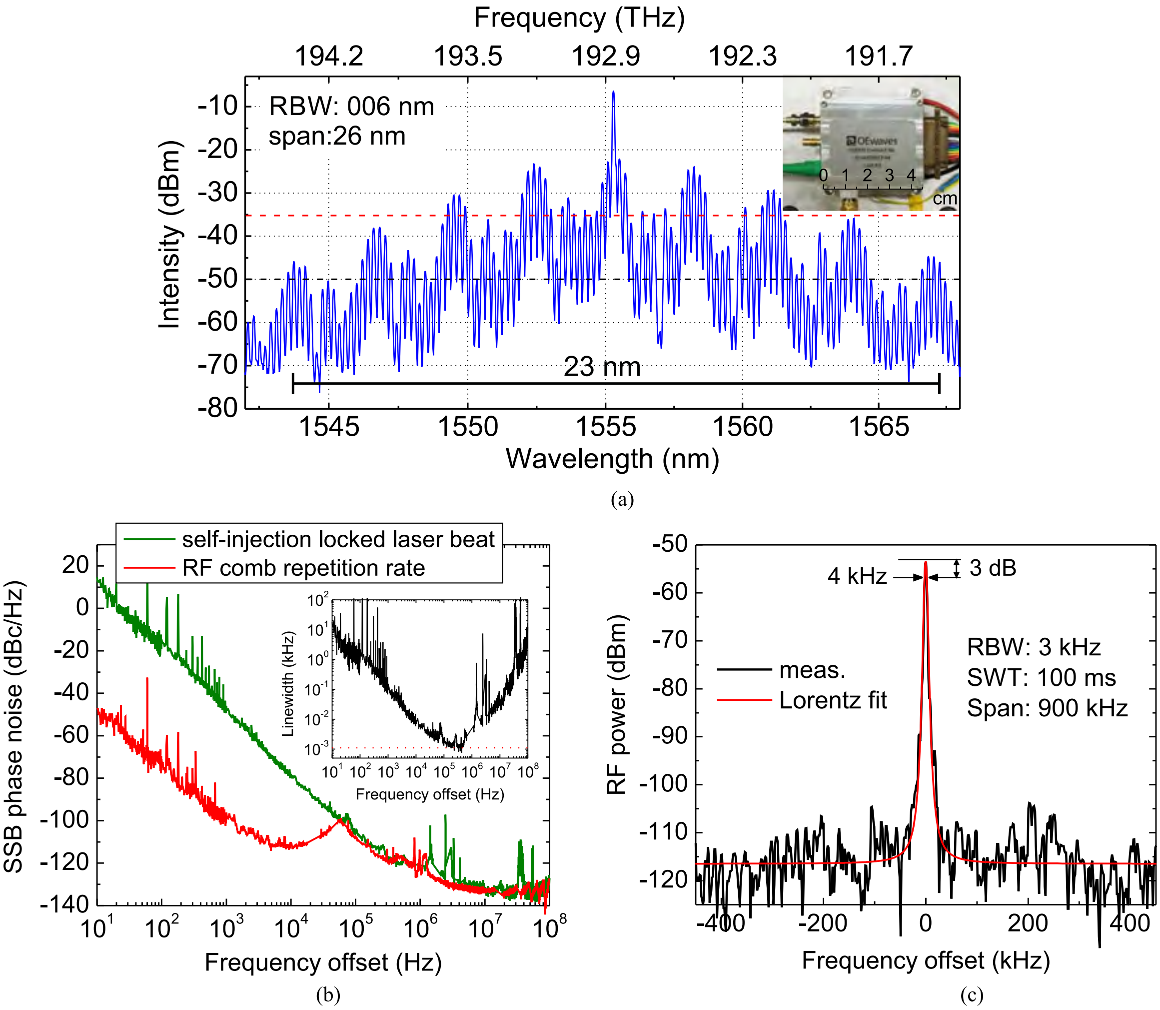

Fig. 5. (a) Optical spectrum of a stabilized Kerr frequency combs generated in the unit, shown in the inset. The comb spans 23 nm, which is defined as the spectral region in which the frequency comb envelope power exceeds −50 dBm (black dotted line) and has a line spacing of 0.2 nm, yielding more than 115 lines. The optical output comb power exiting the fiber obtained after subtracting from the pump laser power is 100 μW, meaning only ~0.5 μW per comb line is accumulated in the wavelength range of 1542 nm-1568 nm. The horizontal (red) dashed line denotes the ~0.5 μW per comb line power level, (b) single sideband (SSB) phase noise of the injection-locked DFB laser, used as a pump laser, integrated in the packaged OFC unit and the RF signal generated by the Kerr comb repetition rate. The instantaneous linewidth of the pump laser is extracted from its phase noise, as shown in the inset. The linewidth of a laser is ill-defined because of flickering and drifting frequency. Various techniques [20], [21] were proposed to circumvent the problem. It is known that frequency noise spectrum is a more relevant entity to characterize the laser performance. To resolve the issue, we utilized the formula $\Delta\nu_{\text{instant}} = \pi * [S_\nu(f)]$, where $S_\nu(f)$ is the corresponding frequency power noise, and $\Delta\nu_{\text{instant}}$ is the effective instantaneous linewidth. Hence, the linewidth is uniquely defined at the particular spectral frequency using the frequency noise values measured experimentally, and (c) RF beatnote, resulting from beating one of the comb lines with ultra-narrow linewidth lasers [22] to measure the optical linewidth of the comb line.

photodetector and measured on the ESA, as shown in Fig. 6. The other output of this coupler was connected to the optical spectrum analyzer (OSA) to measure the optical spectra of Y-branch laser and the comb output. A signal with a frequency equal to the beatnote frequency as a frequency offset was applied from the RF synthesizer to the XOR gate within the EIC.

In order to achieve heterodyne-locking our tunable LO to the comb, the LO wavelength is tuned with respect a comb line to get any random beatnote frequencies, i.e., ≤ half of the comb FSR. After

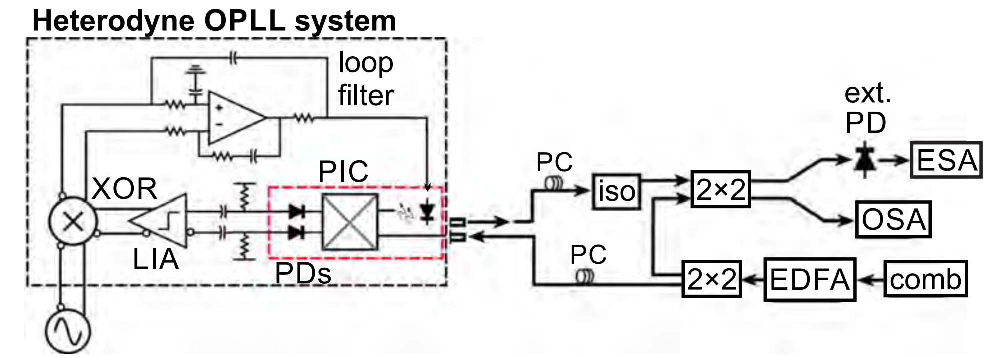

Fig. 6. Test setup of the heterodyne OPLL system for monitoring the performance of the Y-branch laser. (ECL: external cavity laser, EDFA: erbium-doped fiber amplifier, ESA: electrical spectrum analyzer, ext. PD: external photodiode, iso: isolator, LIA: limiting amplifier, OSA: optical spectrum analyzer, PC: polarization controller, and PIC: photonic integrated circuit).

differential PD signals are amplified by the LIA, the RF synthesizer then applies a signal close to the beatnote frequency to the XOR gate. With all feedback electronics is turned on, the XOR gate outputs a signal that becomes zero when the beatnote and RF signal have the same frequency and phase. In other words, the loop filter keeps tuning the LO's phase so that the beatnote signal with a constant offset frequency and phase matches the RF offset. This means that the LO and comb are at a constant phase and frequency offset, i.e., they are phase-locked to each other.

4.3 Locking Results

Our heterodyne OPLL successfully phase locks the Y-branch laser to a comb line up to an offset frequency of 18 GHz with an RF synthesizer. Such maximum offset locking frequency is mainly limited by the operational frequency range of the XOR [18] and on-chip balanced PDs. Since the Y-laser has a tuning range of 60 nm, the whole frequency spectrum within the comb span with a FSR of 25.7 GHz can be utilized for such offset locking. Fig. 7(a) shows the optical spectrum of the Y-branch laser with its emission wavelength 0.046 nm offset from the nearest comb line while the phase locking to this comb line is achieved. This is evidenced by the RF spectrum measured by the ESA at the resolution bandwidth (RBW) of 3 MHz, as shown in Fig. 7(b). The RF beating tones show that the offset frequency is at 5.6 GHz, corresponding to the 0.046 nm. The beat tone generated between the locked Y-laser and the adjacent comb line is also seen at 20.1 GHz. This is expected, since comb lines are stable in phase with respect to each other and the OPLL is phase-locked to the central comb line, hence the OPLL is phase-locked to the adjacent comb line as well. Also, the RF beat tone produced between comb lines is observed at 25.7 GHz, as indicated in Fig. 7(b). Thus, the 23 nm wavelength span of OFC can be covered by tuning the wavelength of our receiver's tunable LO laser. The free running laser has 12 MHz instantaneous linewidth, whereas the relative linewidth of the locked beatnote is less than 100 Hz, revealing excellent relative spectral coherence between the on-chip LO laser and comb. Such a dramatic narrowing of the heterodyne linewidth occurred when the LO laser was phase-locked to the reference OFC. Figs. 7(c)–(e) show the clear coherent peaks of the locked beat note at various RBWs. Sweeping time of each measurement is also shown.

To evaluate the performance of our OPLL system, residual SSB phase noise of the OPLL was measured from 10 Hz to 10 GHz using the setup shown in Fig. 6. The measurement was performed by directly connecting the locked beatnote to a Rohde & Schwarz FSU spectrum analyzer system and using its application firmware (R&S FS-K4). The locked beat note at 3.1 GHz produced between the locked LO laser and the comb was used in this case. The measurement result is shown in Fig. 8. The phase noise variance from 10 Hz to 10 GHz is calculated to be 0.04 rad^2 corresponding to 11.4° standard deviation from the locking point.

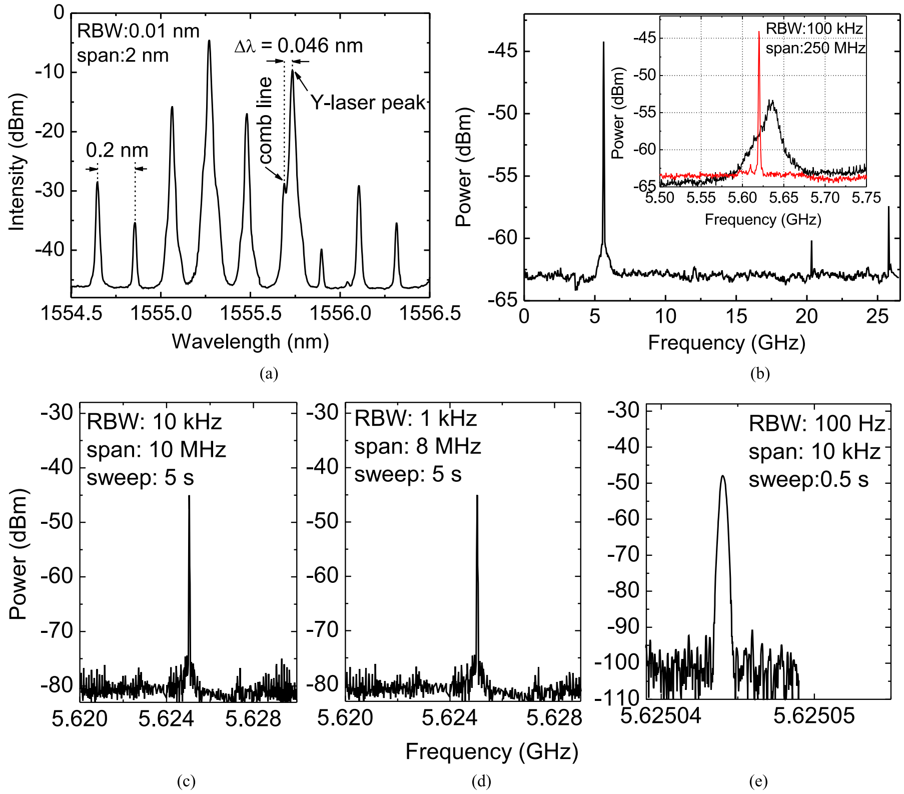

Fig. 7. (a) Optical spectrum when Y-branch laser is offset-locked to the comb at 1555.69 nm with a wavelength difference of 0.046 nm. (b) RF spectrum of the locked beatnote between Y-branch laser and comb at 5.6 GHz is recorded. The beatnote generated between on-chip laser and adjacent comb line at 20.1 GHz and the beatnote produced between comb lines at 25.7 GHz are also visible. The resolution bandwidth is 3 MHz. The zoom-in spectra with a span of 250 MHz is shown as the inset, where the phase-locked (red) and free-running (black) cases can be seen and (c)–(e) measured RF beatnotes at various RBWs.

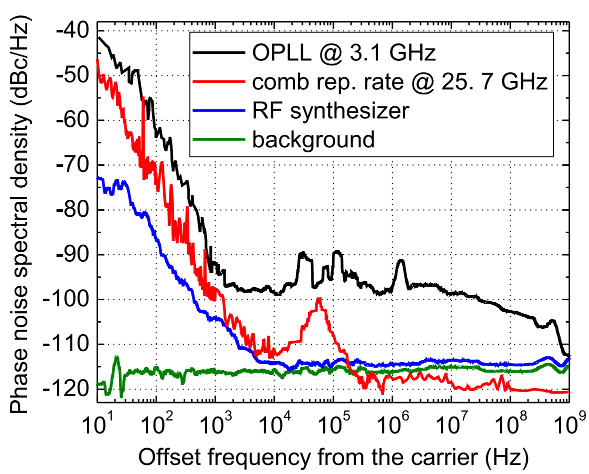

Fig. 8. Single-sideband residual phase noise of the heterodyne OPLL. Phase noise of the RF signal at 25.7 GHz generated by the comb repetition rate, RF synthesizer, and background is also shown here for comparison.

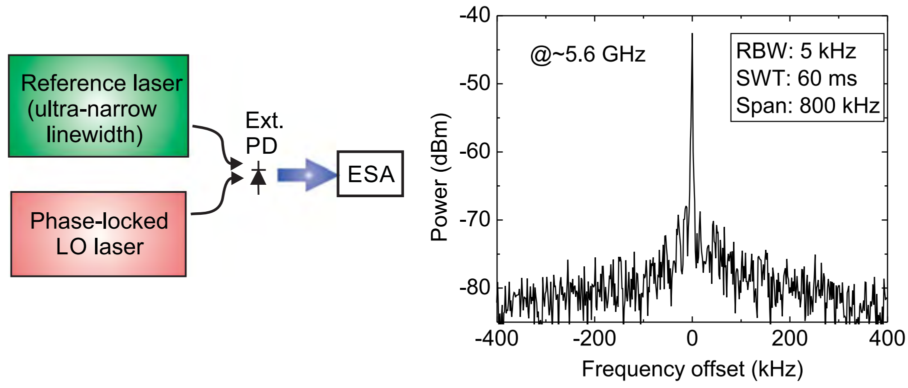

Fig. 9. (a) Out-of-loop measurement setup and (b) optical beatnote resulting from beating the phase-locked LO with other reference ultra-narrow linewidth lasers [22].

In order to measure the linewidth of the locked on-chip laser, an out-of-loop measurement was performed by beating the locked LO with another ultra-narrow linewidth reference laser [22]. Fig. 9 shows the corresponding optical out-of-loop beatnote, showing the linewidth of the laser is approximately the same as the linewidth of the comb harmonic and is <5 kHz. Measurement with smaller RBW was hindered because of the jitter of the beat note frequency, as observed earlier. In-loop measurement by mixing the LO laser back with the comb to which we are referencing cannot be used in this regard since a bound phase error which translates in zero frequency error between LO laser and the comb is obtained, once they are phase-locked. In other words, near zero linewidth can then be obtained in the RF spectrum analyzer with the LO offset phase-locked to the comb. Since the LO laser is being forced to instantaneously track the comb line (plus the RF offset) in order to be truly phase locked, common mode noise will not show up in the in-loop beat measurement.

So far, our on-chip tunable lasers are phase-locked to self-referenced and naturally stable OFC lines using heterodyne OPLL. However, further stabilization of OFCs is important for a range of scientific and technological applications, including frequency metrology at high precision, and high-purity optical as well as terahertz frequency synthesis. This stabilization is expected to be a key prerequisite for broadband and low-noise microcomb generation for metrology applications, as well as for integrated micro- and nanophotonic devices. In the next section, we present an effective scheme to achieve a good stability in the OFC, enabling all of these applications.

5. Stabilization of Kerr Frequency Comb

To completely stabilize a coherent mode-locked OFC, one needs to stabilize two of its dissimilar frequencies. Usually, it is desirable to create an octave spanning frequency comb, realize f-2f self-referenced frequency locking, and then either lock the repetition rate or an optical harmonic of the comb to a reference. A single-point locking usually does not reduce frequency drifts of the oscillator significantly. In the case of the Kerr frequency comb oscillator, a single point frequency lock can be instrumental because, unlike conventional mode-locked lasers used for frequency comb production, the microresonator OFC has fewer degrees of freedom: one of its harmonics always coincides with the frequency of the pump light. The pump light is locked to a mode of the WGMR to ensure stable operation of the device. The repetition rate of the frequency comb is partially decoupled from the parameters of the pump light because of the salient properties of the comb oscillator and is impacted mostly by the resonator. Hence, stabilization of the WGMR can stabilize both the pump light and the repetition frequency of the comb oscillator. To achieve the stabilization one needs to actuate the WGMR.

Multiple attempts for stabilization of the Kerr frequency comb oscillator were made [23]–[28]. In some experiments, the comb was locked to a reference femtosecond OFC [23], [24]. The frequency

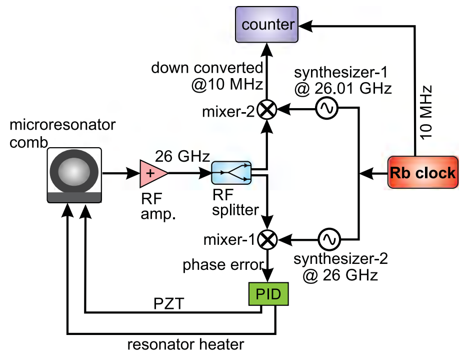

Fig. 10. The experimental setup used for locking Kerr frequency comb to a RF synthesizer. The two RF synthesizers used for phase locking and testing of the OFC are phase locked to a rubidium clock.

and power of the pump light were utilized to achieve the stabilization. Locking the repetition rate of a Kerr comb to a reference RF signal also has been demonstrated [28]. A PZT actuator was used in this case. We here report on stabilizing the repetition rate of the frequency comb using a similar physical principle, but with a heterogeneously integrated OFC.

We created a frequency comb oscillator with a MgF_2 WGM resonator laminated with a PZT actuator. The actuator allows for changing the WGMR radius and stress within the mode localization area. In other words, the frequency of the WGM resonator was altered by changing its temperature as well as by applying stress with a PZT actuator [29]. As a result, the frequency comb repetition rate can be actuated. The actuation bandwidth exceeds 100 kHz.

To lock the repetition rate of the frequency comb to the frequency of an RF synthesizer stabilized to a Rb atomic clock we utilized the PZT actuation. We took a signal from the synthesizer, mixed it with the signal of the comb oscillator and fed it back to the WGM resonator. The locking with PZT worked well, however, the locking range was too narrow with respect to the ambient frequency fluctuations and drifts. The oscillator jumped out of the lock in several minutes after its engagement. We introduced an additional, slow, locking loop utilizing thermal actuation of the resonator. The comb with this approach for stabilization was stable for tens of hours.

The experiment is described by Fig. 10. The 25.7 GHz RF signal coming out of the comb oscillator unit is amplified and split to mix with two synthesizers separately. The frequency of synthesizer #1 is set at 25.71 GHz so the down-converted 10 MHz beat signal can be recorded with a fast counter. The frequency of synthesizer #2 is set to 25.7 GHz. The signal at the output of mixer #2 is processed by a PID controller to lock the RF frequency of the OFC unit through the PZT actuator and a slow actuator (resonator heater). When the frequency difference between the frequency comb oscillator and synthesizer #2 is brought to within the locking range, the feedback loop locked the oscillator to synthesizer #2.

Fig. 11(a) illustrates the measurement of the relative frequency stability of the locked comb frequency measured over 60,000 seconds (blue line) and the calibration measurement (red line). This measurement was performed by Keysight 53152A microwave frequency counter, i.e. not a gapless one. A constant value is subtracted from the data, and therefore, the locked frequency is almost at zero. The comb frequency is locked to a synthesizer according to the previous schematic diagram. In Fig. 11(b), the blue (red) dots show the Allan deviation (AD) of the locked comb (calibration) frequency. For calibration, we measured the AD of the 10 MHz signal created by two RF synthesizers locked to the same Rb clocks.

The absolute stability of the locked comb oscillator is shown in Fig. 12. We locked the comb repetition rate to a Rb clock and compared it to an independent ultrastable quartz oscillator. The data shows that the stability of the locked frequency comb follows the worse of the stability of the clock and the quartz oscillator. Therefore, the developed locking technique allows outstanding locking efficiency for the repetition rate of the OFC. The AD of the self-injection locked pump-laser is also superimposed here. To measure its noise, we used two identical units, beat the lasers on a

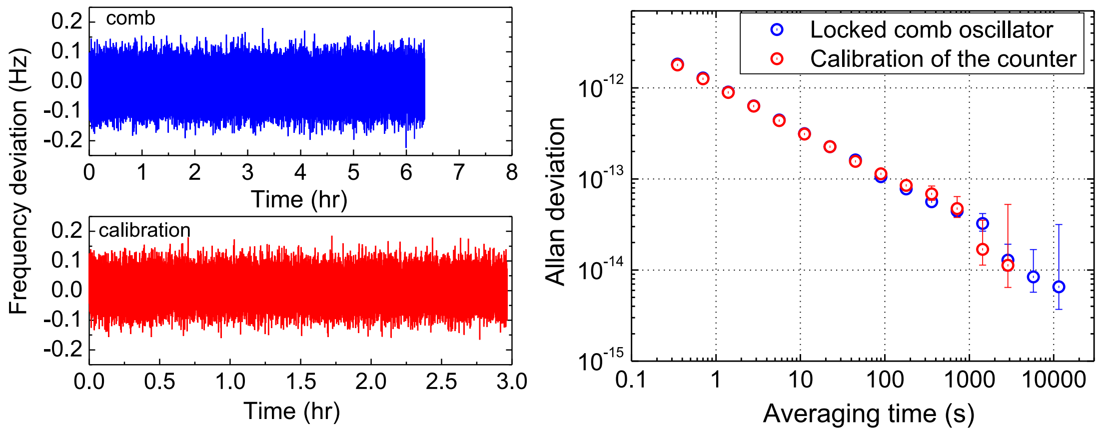

(a) (b)

Fig. 11. (a) Relative frequency stability of the locked comb frequency over 60,000 seconds (blue line) and the calibration measurement (red line). A constant value is subtracted from the data so that the locked frequency is almost at zero. (b) Allan deviation measured of the comb frequency after phase locking the comb to a RF synthesizer. As a calibration, the comb was replaced with a synthesizer locked to the same Rb.

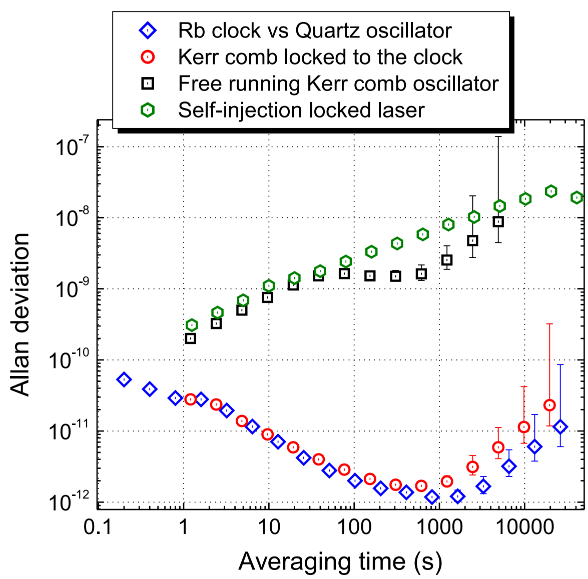

Fig. 12. Absolute stability of the locked Kerr frequency comb after locking the comb repetition rate to the Rb clock. For clarity, the result is compared to an independent ultrastable quartz oscillator. Allan deviation of the self-injection locked pump-laser (not locked to the external RF source) is also superimposed.

PD, measured AD, and then divided the result by $\sqrt{2}$, exhibiting a reasonably good estimation of the laser noise. The AD slighlty increases with integration times.

6. Conclusion

Optical frequency synthesis is realized by means of a highly-integrated heterodyne OPLL with record-low power consumption. Two novel components, including a small and a low power photonic coherent receiver with an integrated broadly tunable laser and an actuatable integrated Kerr frequency comb oscillator are developed and utilized. The demonstrated PIC receiver is promising for reduction of the total power consumption to watt-level in a highly integrated heterodyne OPLL system, enabling chip-scale optical frequency synthesis across the entire C-band with significant reductions in cost, size, weight, and power. Future work includes designing of the application-specific ICs, consuming only a few hundreds of mW of power. This will enable an OPLL with less than half of a watt of power consumption. An optical frequency synthesizer with a total volume of less than a cubic centimeter and a total power consumption of less than a watt should be possible by interfacing this system with a compact and self-referenced microresonator-based OFC. Such a development is attractive for optical communication, sensing, and imaging.

References

[1] T. L. Koch *et al.*, "GaInAs/GaInAsP multiple-quantum-well integrated heterodyne receiver," *Electron. Lett.*, vol. 25, no. 24, pp. 1621–1623, 1989.
[2] L. A. Coldren *et al.*, "High performance InP-based photonic ICs-A tutorial," *J. Lightw. Technol.*, vol. 29, no. 4, pp. 554–570, Feb. 2011.
[3] D. F. Welch *et al.*, "The realization of large-scale photonic integrated circuits and the associated impact on fiber-optic communication systems," *J. Lightw. Technol.*, vol. 24, no. 12, pp. 4674–4683, Dec. 2006.
[4] J. E. Bowers *et al.*, "Linear coherent receiver based on a broadband and sampling optical phase-locked loop," in *Proc. IEEE Int. Topical Meeting Microw. Photon.*, Victoria, BC, USA, 2007, pp. 225–228.
[5] W. Guo *et al.*, "Two-dimensional optical beam steering with InP-based photonic integrated circuits," *IEEE J. Sel. Topics Quantum Electron.*, vol. 19, no. 4, pp. 6100212(1–12), Aug. 2013.
[6] J. E. Bowers *et al.*, "Chip-scale optical resonator enabled synthesizer (CORES) miniature systems for optical frequency synthesis," in *Proc. IEEE Int. Frequency Control Symp.*, New Orleans, LA, USA, 2016, pp. 1–5.
[7] M. Lu *et al.*, "An integrated 40 Gbit/s optical costas receiver," *J. Lightw. Technol.*, vol. 31, no. 13, pp. 2244–2253, Jul. 2013.
[8] S. Ristic, A. Bhardwaj, M. J. Rodwell, L. A. Coldren, and L. A. Johansson, "An optical phase-locked loop photonic integrated circuit," *J. Lightw. Technol.*, vol. 28, no. 4, pp. 526–538, Feb. 2010.
[9] R. J. Steed *et al.*, "Monolithically integrated heterodyne optical phase-lock loop with RF XOR phase detector," *Opt. Exp.*, vol. 19, no. 21, pp. 20048–20053, 2011.
[10] S. Arafin *et al.*, "Towards chip-scale optical frequency synthesis based on optical heterodyne phase-locked loop," *Opt. Exp.*, vol. 25, no. 2, pp. 681–695, 2017.
[11] M. Lu *et al.*, "Monolithic integration of a high-speed widely tunable optical coherent receiver," *IEEE Photon. Technol. Lett.*, vol. 25, no. 11, pp. 1077–1080, Jun. 2013.
[12] H.-C. Park *et al.*, "40 Gbit/s coherent optical receiver using a Costas loop," *Opt. Exp.*, vol. 20, no. 26, pp. B197–B203, 2012.
[13] W. Liang *et al.*, "High spectral purity Kerr frequency comb radio frequency photonic oscillator," *Nature Commun.*, vol. 6, 2015, Art. no. 7957.
[14] L. Maleki, "Sources: The optoelectronic oscillator," *Nature Photon.*, vol. 5, pp. 728–730, 2011.
[15] A. A. Savchenkov, A. B. Matsko, and L. Maleki, "On frequency combs in monolithic resonators," *Nanophotonics*, vol. 5, no. 2, pp. 363–391, 2016.
[16] J. W. Raring *et al.*, "Advanced integration schemes for high-functionality/high-performance photonic integrated circuits," in *Proc. SPIE*, 2006, vol. 6126, pp. 167–186.
[17] A. Simsek *et al.*, "A chip-scale heterodyne optical phase-locked loop with low-power consumption," in *Proc. Opt. Fiber Commun. Conf.*, Los Angeles, CA, USA, 2017, Paper W4G.3.
[18] [Online]. Available: http://www.adsantec.com/
[19] M. Lu, "Integrated optical phase-locked loops," Ph.D. Dissertation, Dept. Electr. Comput. Eng., Univ. California, Santa Barbara, CA, USA, 2013.
[20] W. Liang, V. S. Ilchenko, A. A. Savchenkov, A. B. Matsko, D. Seidel, and L. Maleki, "Whispering-gallery-mode-resonator-based ultranarrow linewidth external-cavity semiconductor laser," *Opt. Lett.*, vol. 35, no. 16, pp. 2822–2824, 2010.
[21] G. D. Domenico, S. Schilt, and P. Thomann, "Simple approach to the relation between laser frequency noise and laser line shape," *App. Opt.*, vol. 49, no. 25, pp. 4801–4807, 2010.
[22] W. Liang *et al.*, "Ultralow noise miniature external cavity semiconductor laser," *Nature Commun.*, vol. 6, 2015, Art. no. 7371.
[23] P. Del'Haye, O. Arcizet, A. Schliesser, R. Holzwarth, and T. J. Kippenberg, "Full stabilization of a microresonator-based optical frequency comb," *Phys. Rev. Lett.*, vol. 101, no. 5, pp. 053903(1–4), 2008.
[24] P. Del'Haye, S. B. Papp, and S. A. Diddams, "Hybrid electro-optically modulated microcombs," *Phys. Rev. Lett.*, vol. 109, no. 26, pp. 263901(1–5), 2012.
[25] A. A. Savchenkov *et al.*, "Stabilization of a Kerr frequency comb oscillator," *Opt. Lett.*, vol. 38, no. 15, pp. 2636–2639, 2013.
[26] J. D. Jost *et al.*, "All-optical stabilization of a soliton frequency comb in a crystalline microresonator," *Opt. Lett.*, vol. 40, no. 20, pp. 4723–4726, 2015.
[27] J. Lim *et al.*, "Stabilized chip-scale Kerr frequency comb via a high-Q reference photonic microresonator," *Opt. Lett.*, vol. 41, no. 16, pp. 3706–3709, 2016.
[28] S. B. Papp, P. Del'Haye, and S. A. Diddams, "Mechanical control of a microrod-resonator optical frequency comb," *Phys. Rev. X*, vol. 3, no. 3, pp. 031003(1–7), 2013.
[29] W. Liang *et al.*, "Compact stabilized semiconductor laser for frequency metrology," *Appl. Opt.*, vol. 54, no. 11, pp. 3353–3359, 2015.

Optical Synthesis Using Kerr Frequency Combs

Shamsul Arafin, Arda Simsek, Seong-Kyun Kim, Mark J. Rodwell and Larry A. Coldren

Department of Electrical and Computer Engineering, University of California, Santa Barbara, CA, 93106, U.S.A.
e-mail: sarafin@ece.ucsb.edu

Lute Maleki, Wei Liang, Vladimir Ilchenko, Anatoliy Savchenkov, Danny Eliyahu, and Andrey Matsko

OEwaves Inc., 465 N Halstead St. Pasadena, CA 91107, U.S.A.
e-mail: andrey.matsko@oewaves.com

Gordon Morrison, Milan Mashanovitch, and Leif Johansson

Freedom Photonics LLC, 41 Aero Camino, Santa Barbara, CA 93117, U.S.A.

***Abstract*— An InP-based photonic integrated circuit was demonstrated for offset locking an on-chip broadly tunable laser to a heterogeneously integrated optical frequency comb oscillator based on a crystalline whispering gallery mode resonator. Optical tuning within 60nm band is demonstrated. The locked laser has excellent spectral purity, sub-kHz linewidth, and good frequency stability.**

Keywords*— *photonic integrated circuits, integrated optics, optical phase-locked loop, heterodyne, optical frequency comb, optical microresonator, whispering gallery mode, self-injection locked semiconductor laser

I. Introduction

Synthesizers are key capabilities in time and frequency applications. The advent of optical techniques in these fields has made a number of important applications possible, so optical synthesis supporting optical frequency control is under intense development in several laboratories around the world. Many coherent optical systems can be realized by using optical phase lock loops (OPLLs) as key elements of optical synthesis. These include optical atomic clocks, light detection and ranging (LiDAR), fiber optic sensing, optical tomography and terahertz wave generation. High-performance, low-power and compact photonic integrated circuits (PICs) -based OPLLs are important for enabling these applications and have been actively studied recently [1,2]. These demonstrated PICs consumed as high as ≥0.5 W [3] of power and their footprint exceeded 2.3 mm^2 [4]. Further improvement of these parameters is needed in designing compact and low-power systems.

In this paper we report on an experimental realization of an OPLL-based optical synthesizer. The device includes a compact, low-power coherent optical system involving a 60-nm-tunable LO laser, couplers and photodetectors monolithically integrated on a standard InP/InGaAsP material platform, as well as an integrated Kerr optical frequency comb (OFC) generator operating as a frequency reference. The heterodyne OPLL transfers the phase noise of a reference frequency comb to the generally noisy LO laser, within the loop bandwidth. Therefore, having an excellent LO is a prerequisite for success in realization of a high performance OPLL. We demonstrate the offset locking of an on-chip Y-branch laser to the OFC unit, making this an important step forward towards the future demonstration of a chip-scale, low-power, ultra-stable optical frequency synthesizer.

We found that the geometrical size and the electrical power consumption for the PICs can be improved significantly with a careful design [5,6]. The inherent advantages of chip integration can be enhanced in this way, and the system can be made much smaller. This is attractive since the small-sized PICs enable a short OPLL loop delay, which results in a larger loop bandwidth.

To create the optical synthesizer we utilized an OPLL involving commercial-off-the-shelf parts. This loop required usage of an optical amplifier to achieve locking to low power frequency comb lines. To show that the entire system can be placed on a chip we designed an OPLL with a trans-impedance amplifier (TIA) increasing the sensitivity of the system significantly. No optical amplification is needed when TIAs provides high electrical gain with minimal noise.

II. Experiment

Schematic of the experimental setup is shown in Fig. 1. It included two separate integrated components: an optical receiver chip and a frequency comb.

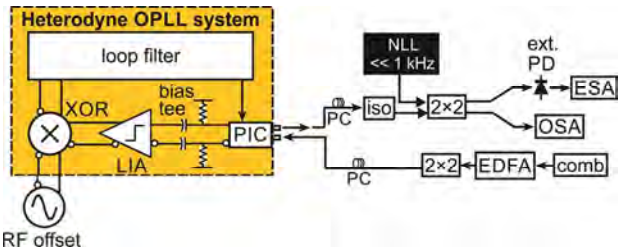

Figure 1: Experimental setup. The heterodyne OPLL system monitors the performance of the Y-branch laser. (ESA: electrical spectrum analyzer, OSA: optical spectrum analyzer, PC: polarization controller, iso: isolator and ext. PD: external photodiode, and EDFA: erbium-doped fiber amplifier, LIA: limiting amplifier, PIC: photonic integrated circuit

A. Broadly tunable laser and the receiver

This work was supported in part by DARPA MTO

The Y-branch laser in the full back-end PIC has a three times smaller cavity compared to standard sampled-grating distributed Bragg reflector. With short gain and mirror sections as well as a highly reflective back cleaved/HR-coated mirror, the device requires low current, and therefore lower drive power. The short cavity design was made by shortening the gain section and introducing zero-length back mirror through high-reflection coating, replacing the standard long back mirror. The emission wavelength is tuned via Vernier effect and was designed for high efficiency at 30º C ambient. The tuning range of the laser is measured to be 60 nm without changing the temperature, covering the entire C-band of optical communication. The laser shows good single-mode working performance with a side-mode suppression ratio of > 45 dB across the entire tuning range. No long absorber section or integrated booster preamplifier was included in this design so that the power consumption and chip-size could be reduced further. The output and input waveguide cleaved facets were coated with anti-reflection coating to suppress parasitic reflection. The laser is integrated into the receiver depicted in Figure 2.

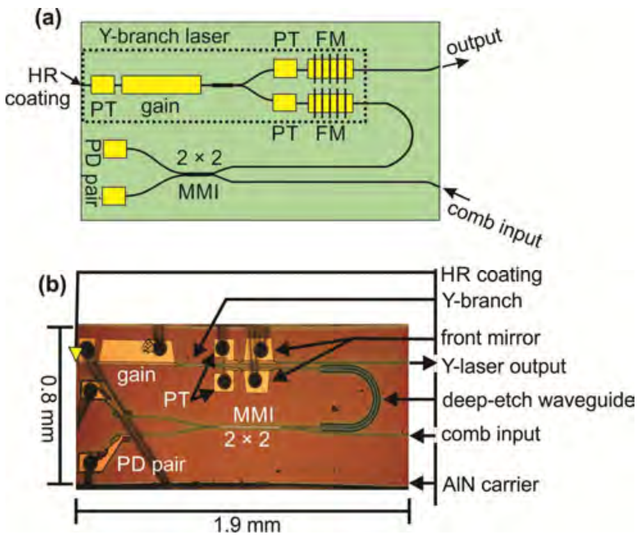

Figure 2: (a) Functional schematic of the photonic integrated receiver circuit composed of a Y-branch laser, two MMI couplers, and a balanced photodetector pair, (b) microscope image of the PIC mounted on a separate aluminium-nitride (AlN) carrier and wirebonded. (HR: high reflection, MMI: multimode interference, PT: phase tuner, FM: front mirror, PD: photodetector), (c) Schematic of the Kerr frequency comb generator.

B. Kerr frequency comb oscillator

We used an OFC generator consisting of a semiconductor laser pumping a crystalline MgF_2 resonator with a mode spacing of 25.5 GHz. The unit was packaged in a 12 cc form factor and its fiber-coupled output was sent to an optical spectrum analyzer (OSA). The measured optical spectrum with a 50-dB span of 23nm is shown in Fig. 3(a). The strongest central line at 1555.27nm is the residual light from the pump laser. The RF signal generated by the beat frequency of the comb lines on a fast PD integrated in the packaged unit was measured to distinguish between chaotic and coherent regimes of the frequency comb. An exceptionally high spectrally pure RF line was observed. The 3-dB bandwidth of the RF beat tone at 25.7 GHz is <100 Hz, limited by the resolution bandwidth (RBW) of the electronic spectrum analyzer, ESA. The phase noise of the repetition rate of the OFC, as well as the pump light, is shown at Fig. 3d.

Depending on the initial conditions, the OFC unit produces frequency combs varying in shape (see Fig. 4). The variations can be linked to the different number of optical pulses within the WGMR. While all the realized solutions are intrinsically stable and suitable for LO stabilization, the solution corresponding to the single pulse localized in the resonator is advantageous, as it does not have any envelope structure. Changing of the power of the comb lines makes the offset locking to some of the modes of the OFC a difficult task. We utilized the frequency combs with the smoothest envelope.

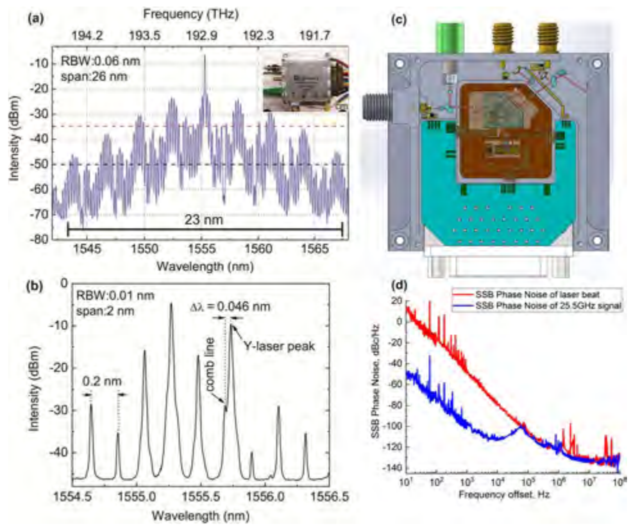

Figure 3: (a) Optical spectrum of a stabilized Kerr frequency comb generated by the OFC generator, as shown as inset. The comb spans 23 nm defined as the width where the intensity ≥ -50 dBm (black dotted line) and has a line spacing of 0.2 nm, yielding more than 115 lines. The optical output comb power exiting the fiber is 100 µW obtained after subtracting the pump laser power, meaning only ~0.5 µW per comb line is achieved in the wavelength range of 1542 nm-1568 nm. The horizontal (red) dashed line denotes the 0.5 µW per comb line power level, and (b) optical spectrum when Y-branch laser is offset--locked to the comb at 1555.69 nm with a wavelength difference of 0.046 nm. (c) Schematic of the frequency comb unit. (d) Single sideband phase noise of the laser and the comb repetition rate of the comb unit. The laser phase noise is measured by beating the laser with a similar device at a fast photodiode.

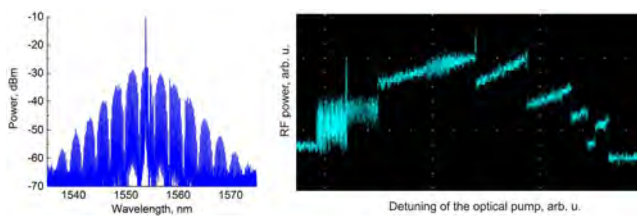

Figure 4: Illustration of the multi-stability of the Kerr frequency comb (compare with the spectrum in Fig. 3a). Left: Another type of Kerr comb frequency spectrum emitted by the oscillator. Right: An oscilloscope trace illustrating the RF power generated by the frequency combs emitted by the oscillator on a fast photodiode. The observed power jumps correspond to different comb regimes.

C. Heterodyne OPLL System

In the OPLL system reported here, a SiGe based commercial-off-the-shelf (COTS) limiting amplifier with 30-dB differential gain was used (Fig. 5). This gain is equal to 31.6 in linear units, indicating that offset phase-locking can be achieved using error signals with a peak to peak magnitude of approximately 10 mV. This corresponds to 0.2 mA required beat current in 50 Ω common mode logic system. In fact, this beat current is produced by beating optical comb-line power of 10 µW with the given 1 mW LO power. Please note that the responsivity of the on-chip PDs is assumed to be 1 A/W. The beat current I_{beat} can be calculated by the following expression:

$$I_{beat} = 2\sqrt{I_{\mathrm{REF}} I_{\mathrm{LO}}}$$
$$I_{beat} = 2\sqrt{0.01(mA)\times 1(mA)}$$
$$I_{beat} = 0.2mA$$

.

where, I_{REF} and I_{LO} are the photocurrents in the on-chip PD resulting from the optical power of the reference comb line and on-chip LO, respectively.

Hence, the minimum input optical comb line power required for the offset locking is experimentally measured to be about 10 µW.

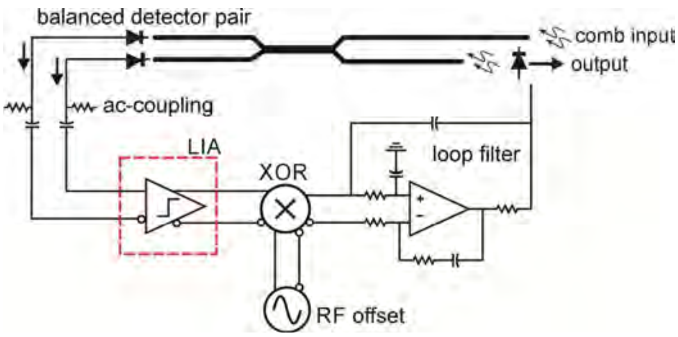

Figure 5: Schematic of the OPLL utilized in the optical synthesizer.

D. OPLL with improved sensitivity

Since the comb output power is not high for offset locking, an amplifier (the EDFA) is necessary to obtain adequate optical power levels in our presented OFS (see Fig. 1). For a fully chip-scale OFS, however, it is important to eliminate the EDFA and replace it with an on-chip semiconductor optical amplifiers. Furthermore, there is also an alternative way by which we could get rid of the EDFA. Instead of amplifying the power in the optical domain, we can increase the sensitivity of our electronic ICs so that the weak error signal generated by beating of the on-chip laser and low-power comb line on the balanced photodiodes can be handled by the feedback electronics. Specifically, the sensitivity of our OPLL system will be increased by using high-gain amplifiers with low noise figure so that on-chip lasers can be phase locked to a comb line without an EDFA. This also helps in reducing the OFS system power consumption further.

For this, we have designed a TIA with low noise, high gain and wide bandwidth using 130 nm SiGe HBT process (Fig. 6). This chip is designed for 80 dB voltage gain and 120 dBohm transimpedance gain with 30GHz bandwidth. It has less than 10 pA/Hz$^{1/2}$ input referred noise current up to 20 GHz with respect to 50 fF photodiode capacitance. These are the features that makes this application specific IC suitable for the frequency synthesis system.

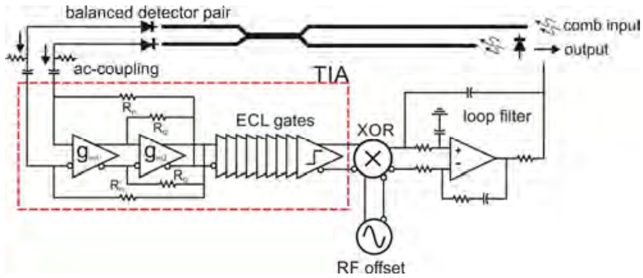

Figure 6: Schematic of the sensitive OPLL with low noise transimpedance amplifier.

As mentioned previously, each single harmonic of the optical frequency comb has only 0.5 µW of power. After considering the fiber coupling loss of 6 dB and optical power splitting by 2 x 2 MMI, the on-chip comb power available for beating is about 60 nW, whereas the local oscillator's power is about 1 mW. Given the responsivity of the on-chip PDs is 1 A/W, the beat current resulting from between on-chip-laser and one of the comb lines is approximately 15 µA in each PD, as shown in the following:

$$I_{beat} = 2\sqrt{I_{LO} I_{REF}}$$
$$I_{beat} = 2\sqrt{60(nA)\times 1(mA)}$$
$$I_{beat} = 15\mu A$$

This current needs to be amplified by the TIA and produce a logic output of 300 mV, which will drive the digital XOR gate. Thus, TIA should have at least the following gain.

$$Gain = \frac{300mV}{15\mu A} = 20k\Omega$$

$$Gain(dB\Omega) = 20\log_{10} 20000 = 86$$

Our TIA has more than enough gain to lock the local oscillator to the optical frequency comb lines. Functional test of the TIA demonstrates 60 dB differential gain, with a proper DC restoration loop this gain can be as high as 80 dB as simulated.

This sensitivity can be improved to as low as 60 nW using the novel TIA design discussed here. When this is achieved, EDFA is no longer needed and the OFS system total power consumption will be much lower as well as it will be more compact and will be closer to a true chip scale OFS system with much less than 2 Watts of power consumption. Implementation of the compact structure is our current goal.

III. Conclusion

A miniature and low power photonic coherent synthesizer with an integrated broadly tunable laser and an integrated Kerr frequency comb oscillator are developed. Low noise optical tone is produced on demand by tuning the laser across the comb span and phase locking it to any of the comb lines. In this way, the higher power laser reproduces the high spectral purity of the frequency comb. The demonstrated PIC synthesizer is promising for reduction of the total power consumption to watt-level in a highly integrated package.

REFERENCES

[1] S. Ristic, A. Bhardwaj, M. J. Rodwell, L. A. Coldren, and L. A. Johansson, "An Optical Phase-Locked Loop Photonic Integrated Circuit," *Journal of Lightwave Technology,* vol. 28, no. 4, pp. 526-538, 2010

[2] R. J. Steed, F. Pozzi, M. J. Fice, C. C. Renaud, D. C. Rogers, I. F. Lealman, D. G. Moodie, P. J. Cannard, C. Lynch, L. Johnston, M. J. Robertson, R. Cronin, L. Pavlovic, L. Naglic, M. Vidmar, and A. J. Seeds, "Monolithically integrated heterodyne optical phase-lock loop with RF XOR phase detector " *Optics Express* vol. 19, no. 21, pp. 20048-20053, 2011.

[3] H.-C. Park, M. Lu, E. Bloch, T. Reed, Z. Griffith, L. Johansson, L. Coldren, and M. Rodwell, "40Gbit/s coherent optical receiver using a Costas loop," *Optics Express,* vol. 20, no. 26, pp. B197-B203, 2012.

[4] M. Lu, H.-C. Park, A. Sivananthan, J. S. Parker, E. Bloch, L. A. Johansson, M. J. W. Rodwell, and L. A. Coldren, "Monolithic Integration of a High-Speed Widely Tunable Optical Coherent Receiver," *IEEE Photonics Technology Letters,* vol. 25, no. 11, pp. 1077-1080, 2013.

[5] Shamsul Arafin, Arda Simsek, Seong-Kyun Kim, Sarvagya Dwivedi, Wei Liang, Danny Eliyahu, Jonathan Klamkin, Andrey Matsko, Leif Johansson, Lute Maleki, Mark Rodwell, and Larry Coldren, "Towards chip-scale optical frequency synthesis based on optical heterodyne phase-locked loop," Opt. Express vol. 25, no. 2, pp. 681-695, 2017.

[6] S. Arafin, A. Simsek, S.-K. Kim, W. Liang, D. Eliyahu, G. Morrison, M. Mashanovitch, A. Matsko, L. Johansson, L. Maleki, M. J. Rodwell, and L. A. Coldren, "Power-efficient Kerr frequency comb based tunable optical source," IEEE Photonics Journal vol. 9, no. 3, art. no. 6600814, 2017.

I. Photonic Integrated Circuits

D. Signal Processing

nature COMMUNICATIONS

ARTICLE

Received 5 Jul 2016 | Accepted 24 Mar 2017 | Published 12 May 2017

DOI: 10.1038/ncomms15389

OPEN

An integrated parity-time symmetric wavelength-tunable single-mode microring laser

Weilin Liu[1,*], Ming Li[1,*,†], Robert S. Guzzon[2,*], Erik J. Norberg[2], John S. Parker[2], Mingzhi Lu[2], Larry A. Coldren[2] & Jianping Yao[1]

Mode control in a laser cavity is critical for a stable single-mode operation of a ring laser. In this study we propose and experimentally demonstrate an electrically pumped parity-time (PT)-symmetric microring laser with precise mode control, to achieve wavelength-tunable single-mode lasing with an improved mode suppression ratio. The proposed PT-symmetric laser is implemented based on a photonic integrated circuit consisting of two mutually coupled active microring resonators. By incorporating multiple semiconductor optical amplifiers in the microring resonators, the PT-symmetry condition can be achieved by a precise manipulation of the interplay between the gain and loss in the two microring resonators, and the incorporation of phase modulators in the microring resonators enables continuous wavelength tuning. Single-mode lasing at 1,554.148 nm with a sidemode suppression ratio exceeding 36 dB is demonstrated and the lasing wavelength is continuously tunable from 1,553.800 to 1,554.020 nm.

[1] Microwave Photonics Research Laboratory, University of Ottawa, 25 Templeton Street, Ottawa, Ontario, Canada K1N 6N5. [2] Department of Electrical and Computer Engineering, University of California Santa Barbara, Santa Barbara, California 93116, USA. † Present address: State Key Laboratory on Integrated Optoelectronics, Institute of Semiconductors, Chinese Academy of Sciences, Beijing 100083, China. * These authors contributed equally to this work. Correspondence and requests for materials should be addressed to J.Y. (email: jpyao@eecs.uottawa.ca).

Mode management in a laser cavity is an important topic in laser physics and has been extensively investigated[1,2]. Owing to the broad gain bandwidth of a laser cavity, mode management is required to select the desired mode and to suppress other modes to achieve single-mode operation, which is required for applications such as in optical communications systems[2] and nonlinear optical systems[3]. At present, there are four major approaches that have been extensively studied for mode management in a laser cavity. The first approach is to use optical feedback in a cavity to achieve single-mode operation[4–6]; the second is to enhance mode confinement by reducing the mode size in a laser cavity to achieve single-mode operation[7–9]; the third is to shape the spatial profile of a pump light to a laser cavity to achieve mode selection[10]; and the fourth approach is to use parity-time (PT) symmetry[11–16] to implement mode selection. The last approach has been an active topic and has been heavily researched recently[17–21].

Specifically, in the first approach, an optical cavity is incorporated into the active region of a laser structure for mode selection[4,5]. A strong feedback for a mode that is determined by the optical cavity would lead to a strong optical oscillation or lasing at that mode. The optical feedback can be achieved, for example, using an ultrashort cavity implemented by a pair of reflective mirrors[4] or a distributed feedback (DFB) grating[5]. An ultrashort cavity ($\sim$5.5 μm) with a large free spectral range (FSR) offers strong mode selectivity for single-mode lasing[4]. A DFB laser has an active region containing a periodically structured grating to provide a strong optical feedback for a single longitudinal mode operation, in which tunable operating wavelength is possible by thermal tuning[6]. However, the cavity feedback structure in a DFB laser is complicated and the use of such a structure would increase the fabrication complexity.

In the second approach, a metallic cavity is used to reduce mode size and enhance mode confinement for mode selection based on plasmonics. In a metallic cavity, surface plasmon polaritons excited at the metal-dielectric interfaces can provide an extremely strong light confinement, which enable intense, coherent and directional optical emission that is below the diffraction barrier[7,8]. With light waves confined in a volume structure in subwavelength dimensions, plasmon lasers can have a very small footprint on the nanoscale. However, very high gain is needed to enable lasing due to very high losses in metals[9].

In the third approach, lasing mode selection is achieved by shaping the spatial profile of the optical pump to the laser cavity. In a laser cavity, possible high-Q lasing modes exhibit distinct emission patterns, which can be selected by adaptively controlling the spatial profile of the pump light to achieve single-mode lasing[10]. To select a desired mode while suppressing other modes, the optical pump with a specific spatial profile is needed. The spatial profile of the optical pump for a desired lasing mode can be obtained by a genetic algorithm and specific optical pump can be realized by using a spatial light modulator[10]. This approach provides flexible mode selection but a time-consuming genetic algorithm is needed to search for the optimum pump profile for a desired lasing mode.

In the fourth approach, mode selection is achieved based on PT symmetry by manipulating the interplay between gain and loss in a laser cavity[17–21]. In a coupled arrangement with two identical microring resonators one is experiencing gain, whereas the other is experiencing an equal-magnitude loss, to form a PT-symmetry situation. By changing the relationship between the gain and loss, and the coupling between the two microring resonators, one can selectively break the PT-symmetry condition for a desired mode, which can be used to improve the maximum achievable gain for this mode. Therefore, the desired mode can be controlled for single-mode operation in an inherently multi-mode microring laser[18]. The breaking of the PT-symmetry condition provides a simple and effective solution to achieve single-mode lasing by allowing the desired mode to have a higher gain, while suppressing other modes[17–21]. In refs 18,19, a single-mode lasing was demonstrated with an enhanced mode discrimination by using the exceptional points in a PT-symmetric coupled ring resonator structure[20]. However, the lasing wavelength was not tunable and the sidemode suppression ratio was only 21 dB.

In this study, we propose and experimentally demonstrate an electrically pumped integrated microring laser that supports single-mode operation based on PT symmetry with an improved mode suppression ratio. The microring laser has a coupled arrangement in which two structurally identical microring resonators are mutually coupled via a tunable coupler, to enable truly PT-symmetric operation. By incorporating two semiconductor optical amplifiers (SOAs) in each of the two microring resonators, the gain–loss can be controlled by changing the injection currents to the SOAs. As the coupling between the two microring resonators is achieved by a tunable coupler, the coupling coefficient can be precisely controlled, to maintain or break the PT-symmetry condition for mode selection. In addition, the resonance wavelength can be controlled by changing the injection currents to the phase modulators (PMs) in the two microrings. Thus, the proposed PT-symmetric single-mode laser has the following advantages. First, compared with the biased PT-symmetric system in ref. 18, the proposed coupled ring system is truly PT symmetric. Second, the proposed laser is electrically pumped, whereas in refs 17,18 the lasers were optically pumped. Finally, the operating wavelength of the proposed laser can be continuously tuned by tuning the injection current to the PM in the ring resonator, which can also be used for compensating the phase mismatch between the two ring resonators almost in real time. Compared with a previously reported mode suppression ratio of 21 dB in a PT-symmetric

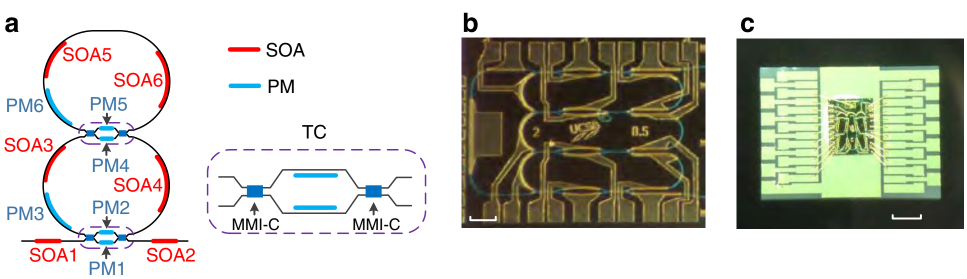

Figure 1 | The schematics of the proposed single-mode microring laser. (**a**) The schematic diagram of the microring laser consisting of two coupled rings and a bypass waveguide. (**b**) A photograph of the fabricated microring laser prototype with a scale bar of 200 μm. (**c**) A photograph of the laser wire bonded to a customized carrier for experimental test with a scale bar of 1 mm. MMI-C, multimode interference coupler; PM, phase modulator; SOA, semiconductor optical amplifier; TC, tunable coupler.

single-mode laser[18], the proposed laser presents an increased mode suppression ratio of 36.07 dB and the lasing wavelength is electronically tunable with a tuning range of 0.22 nm.

Results

Basic principle. The schematic of the proposed wavelength-tunable single-mode microring laser is shown in Fig. 1a. It consists of two structurally identical ring resonators that are mutually coupled by a tunable coupler. Within each microring resonator, there are two SOAs to enable gain control and a PM to enable wavelength tunability. By changing the injection currents to the SOAs, the gain or loss in each microring resonator can be controlled. A bus waveguide is also coupled to the bottom ring resonator for lasing output. The tunable coupling between the two coupled microring resonators and between the bottom ring and the bus waveguide is realized using two tunable couplers, each consisting of two multi-mode interference (MMI) couplers and two PMs, as shown in the inset in Fig. 1a. The coupling ratio of each tunable coupler can be continuously tuned by adjusting the injection currents to the two PMs. Under the PT-symmetry condition, the gain and loss are identical in the two microring resonators[18], which can be achieved by controlling the injection currents to the SOAs in the two ring resonators. In this case, a mode with a gain smaller than the total coupling coefficient of the two ring resonators will not lase. If the gain exceeds the total coupling coefficient, the PT-symmetry condition will be broken and a lasing mode will appear. With such a mode selection mechanism, the cavity resonance modes in a coupled ring resonator can be efficiently controlled without the need of additional filters.

In the time domain, the interplay between the nth longitudinal modes in the two microrings obeys two coupled differential equations for their respective modal amplitudes, a_n, b_n (ref. 12), given by

$$\frac{\mathrm{d}a_n}{\mathrm{d}t} = -j\omega_n a_n + j\kappa b_n + \gamma_{a_n} a_n \quad (1)$$

$$\frac{\mathrm{d}b_n}{\mathrm{d}t} = -j\omega_n b_n + j\kappa a_n + \gamma_{b_n} b_n \quad (2)$$

where γ_{a_n} and γ_{b_n} represent the net gain or loss in each microring resonator, ω_n is the angular frequency of the nth longitudinal mode and κ is the coupling coefficient between the two microring resonators. According to equations (1) and (2), the eigen frequencies, $\omega_n^{(1,2)}$, of the two supermodes of this system are given by

$$\omega_n^{(1,2)} = \omega_n + j\frac{\gamma_{a_n} + \gamma_{b_n}}{2} \pm \sqrt{\kappa_n^2 - \left(\frac{\gamma_{a_n} - \gamma_{b_n}}{2}\right)^2} \quad (3)$$

In the PT-symmetry situation, we have $\gamma_{a_n} = -\gamma_{b_n}$ and equation (3) is simplified to

$$\omega_n^{(1,2)} = \omega_n \pm \sqrt{\kappa_n^2 - \gamma_{a_n}^2} \quad (4)$$

It can be seen from equation (4) that any pair of modes whose gain/loss remains below the coupling coefficient $(\gamma_{a_n}(\omega) < \kappa_n(\omega))$ will remain neutral. However, as soon as the gain/loss exceeds the coupling coefficient $(\gamma_{a_n}(\omega) > \kappa_n(\omega))$, the PT-symmetry condition will be broken and a conjugate pair of lasing or decaying modes will emerge.

Device design. As ring resonators are used in the design, low-radius waveguide bends with a low bend radiation loss are required. A deeply etched waveguide geometry is used due to its high optical confinement, which can reduce bending losses in a small-radius waveguide bend. Typically, it is desired that a waveguide in a photonic integrated circuit (PIC) supports only a single mode. In the transverse direction, the waveguide is able to support a single-mode by the proper epitaxial structure design. In the lateral direction, the number of modes is defined by the width of the waveguide. Owing to the highly confined nature of the deeply etched geometry, the cutoff for the first odd mode is at a very narrow width of about 1.1 µm. However, a narrow deeply etched waveguide has a high scattering loss and potentially high surface recombination current compared with a wider waveguide. For this reason, in our PIC, wider multi-mode waveguides were used. In particular, 2.8 µm-wide waveguides were used in the active, passive and PM propagation regions, and were tapered down to 1.8 µm at the inputs and outputs of the MMI couplers. This narrower waveguide allowed us to design short (100 µm) couplers. Despite the waveguide of both widths supporting multiple modes, the PIC operates in a single-mode manner, because the components in the PIC favour the fundamental mode. Higher-order modes have higher scattering loss over the fundamental mode. This is due to an increased optical power at the edges of the waveguide. In the active regions, the first odd mode has a reduced gain when compared with the fundamental mode, because the current density at the edges of the waveguide is

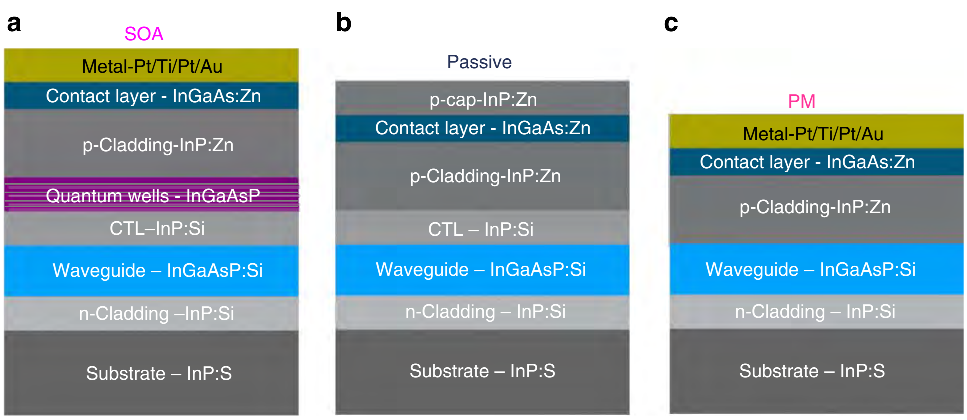

Figure 2 | The epitaxial structures of the components in the proposed microring laser. (**a**) The epitaxial structure of the SOA region, which has five QWs above the CTL. (**b**) The epitaxial structure of the passive waveguides without metal contacts, which are used for low-loss passive waveguide propagation sections. (**c**) The epitaxial structure of the phase modulator (PM) region, in which the CTL is removed to provide efficient current injection into the waveguide for high efficient phase tuning. Layer thickness: 150 nm contact layer, 1.7 µm p-cladding, 0–250 nm CTL, 300 nm waveguide and the QW layer contains 65 Å QWs and 80 Å barriers.

lower due to surface recombination. This is where the optical intensity is the highest for the first odd mode. Most importantly, MMI couplers are designed to be low loss for the fundamental mode. Owing to the decreased effective index, MMIs are highly lossy to high-order modes. For example, the MMI couplers theoretically show a 5 dB suppression for the first odd mode. This mode-filtering is crucial to achieve single-mode operation of the PIC. In fact, no multi-mode effects were witnessed in the fabricated PIC.

A prototype of the proposed microring laser is fabricated in an InP-InGaAsP material system, as shown in Fig. 1b, which is also wire bonded to a carrier for experimental demonstration, as shown in Fig. 1c. In the prototype, the length of the deeply etched waveguide ring is 3 mm. Two 400 μm SOAs with a confinement tuning layer (CTL) offset quantum well (QW) structure[22] are fabricated in the microring, to provide a peak gain of 9.6 dB per SOA. The epitaxial structure for the passive and active regions in the device is illustrated in Fig. 2 and discussed in Methods. With 3 mm of ring length and 1.7 cm^{-1} of passive waveguide loss, the total waveguide propagation loss is 1.6 dB. For a ring with 10% cross-coupling and 0.5 dB MMI insertion loss, the couplers add about 2 dB of loss. Thus, the total round-trip loss is 3.6 dB, which is compensated for by the two SOAs. Two additional active SOAs are incorporated in both input and output waveguides, to compensate for the fibre coupling losses. In addition, the waveguides are angled at 7° to minimize the reflections. Phase modulation in the ring and the tunable MMI Mach-Zehnder interferometer (MZI) coupler is accomplished by a forward bias current, to introduce free carrier absorption through the carrier plasma effect. A PM in the chip has a standard length of 300 μm.

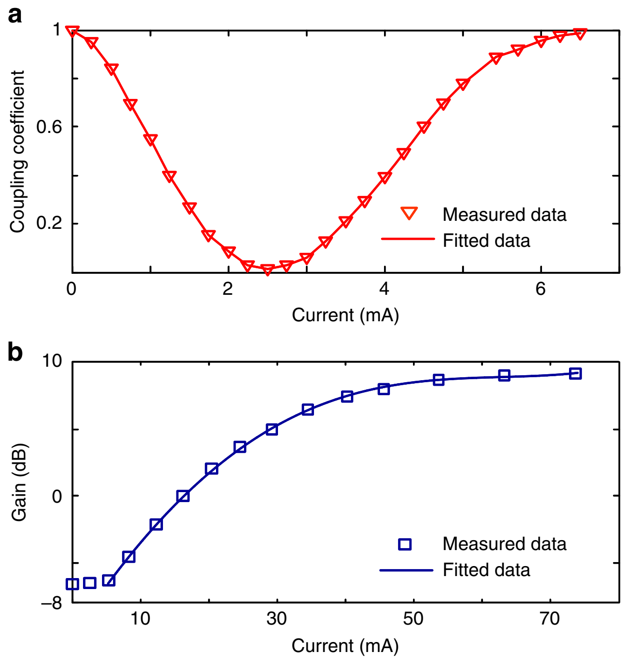

Figure 3 | Experimental results to show the component performance in the proposed laser. (**a**) Tunable coupling coefficients of an multimode interference Mach–Zehnder interferometer coupler at different injection currents ranging from 0 to 6.5 mA, to one PM in one of the two arms. A nonlinear cosine fitting is used in the fitted data. (**b**) The gain profile of a semiconductor optical optical amplifier as a function of the injection current from 0 to 75 mA. A quartic polynomial fitting is used in the fitted data.

Tunable coupler and SOA characterization. The coupling coefficient of a tunable coupler is measured at a different injection current to one of the two PMs, which can be controlled from 0 to 100% when the PM is injected with a current from 0 to 2.5 mA. Figure 3a shows the measured coupling coefficient as a function of the injection current to the PM on the upper arm of the MMI Mach-Zehnder interferometer coupler, from 0 to 6.5 mA. The large signal gain profile of an SOA is also measured. The SOA has a maximum gain of 9.6 dB when the injection current is above 70 mA, as shown in Fig. 3b.

Single-mode lasing experiment. An experiment to validate the single-mode lasing in the proposed microring laser based on PT symmetry is implemented. By changing the injection currents to the SOAs in the two microring resonators and the injection currents to the tunable couplers, the gain/loss and coupling coefficients can be tuned precisely to satisfy the PT-symmetry condition[18]. As shown in Fig. 4a, an emission spectrum with multiple modes in a single microring resonator is observed when the cavity gain exceeds the loss. Once the PT symmetry is established by tuning the gain/loss and the coupling coefficients in the two ring resonators, single-mode lasing with a wavelength at 1,554.148 nm occurs, as shown in Fig. 4b, where the injection currents to the active components are given in Table 1. The light from the PT-symmetric laser is coupled out of the chip using a lensed fibre and the optical power at the output of the lensed fibre is measured to be −14.0 dBm. Considering that the coupling loss between the lensed fibre and the waveguide is 12.7 dB, the optical power directly from the chip is −1.3 dBm. The presence of the lossy ring serves to suppress the unwanted modes with a side mode suppression ratio exceeding 36 dB, due to the tunable gain, loss and coupling efficiency. The counter propagating modes are also measured and shown in Fig. 4c. It can be seen that the counter propagating mode at the lasing frequency has a power of −60.2 dBm, which is 46.2 dB less than the lasing mode, which is mainly due to the reflection at the output facet. By changing the injection currents to the PMs in the two ring resonators, the lasing wavelength can be continuously tuned. In the experiment, a wavelength tuning range from 1,553.800 to 1,554.020 nm is achieved, as shown in Fig. 5, which is equal to the FSR of the microring resonator. For a ring resonator of a length of 3 mm, the FSR is 0.22 nm. The modal discrimination of the PT-symmetric laser is also measured, which is 13.19 dB (Supplementary Methods). As a comparison, the modal discrimination of a conventional ring laser implemented using the same PIC is also measured, which is 3.26 dB. Thus, an increase in modal discrimination of 9.93 dB is achieved.

Discussion

In the experiment, the total power consumption of the microring laser is 205.1 mW, including 52.6 mW consumed by the output SOAs (SOA2), which can be avoided in a packaged laser without a large fibre coupling loss. In this case, the total power consumption for such a PT-symmetry microring laser can be reduced to 152.5 mW. For real applications, a single SOA with a peak gain of 9.6 dB in a ring resonator is enough to compensate for the total roundtrip loss. As shown in the gain profile of the 400 μm SOA in Fig. 3b, an injection current of ∼27 mA can provide a gain of 4.5 dB, which is large enough to ensure the microring resonator to operate under the same condition, as shown in Table 1. As a result, the total power consumption can be further reduced to 126 mW.

In conclusion, we have proposed and experimentally demonstrated a photonic integrated PT-symmetric single-mode microring laser based on two mutually coupled active microring resonators. Thanks to the tunable gain or loss in the microring

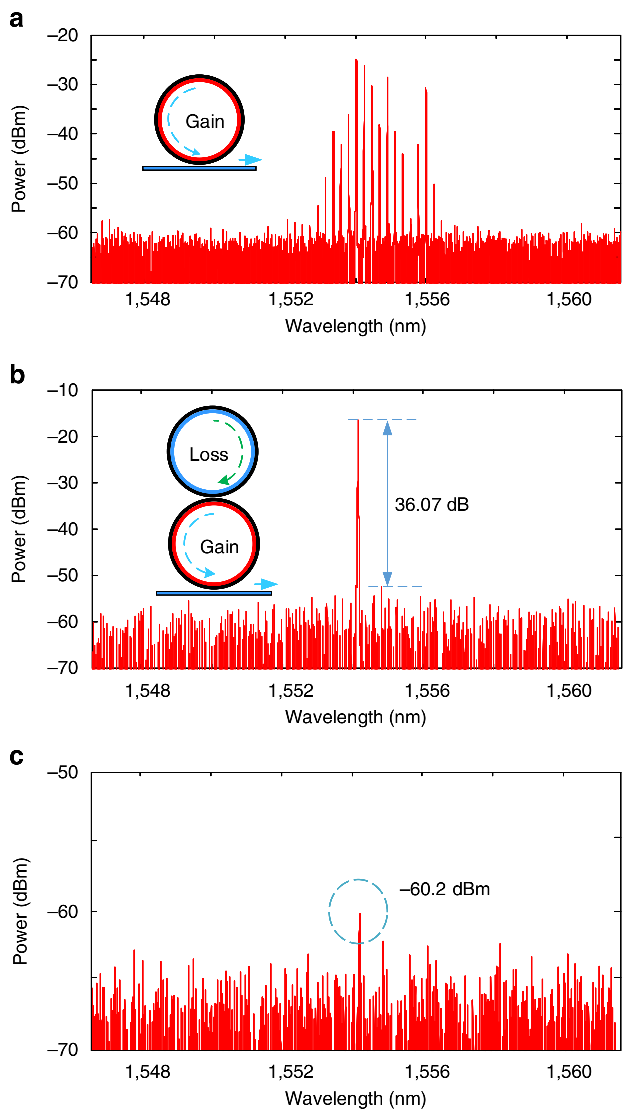

Figure 4 | Experimental results to show mode suppression by breaking the PT-symmetry condition. (**a**) Emission spectrum of a single ring resonator when the two SOAs inside the microring resonator are driven by an injection current of 21 mA each. (**b**) Single-mode spectrum under the PT-symmetry condition. The SOAs in the upper ring resonator are not activated, and the SOAs in the lower ring resonator are driven by an injection current of 21 mA each. The mode suppression ratio is 36.07 dB. (**c**) The optical spectrum at the other output of the laser showing the counter propagating modes and the counter propagating mode at the lasing frequency is marked with a dashed circle.

resonators and the tunable coupling coefficient in the tunable coupler, single-mode operation with a large mode suppression ratio and a continuously tunable wavelength range of 0.22 nm was demonstrated. The two mutually coupled microring resonators in the microring laser were implemented based on InP-InGaAsP with each resonator having two SOAs and a PM incorporated. The incorporation of the SOAs in the ring resonators ensures a precise electrical control of the interplay between gain and loss to achieve PT-symmetry condition and incorporation of the PMs in the ring resonators enables wavelength tuning. By tuning the gain and loss in the two microring resonators to achieve the PT-symmetry condition, a single-mode lasing at 1,554.148 nm with a sidemode suppression ratio exceeding 36 dB was demonstrated. By adjusting the injection currents to the PMs,

Table 1 | The injection currents to the SOAs and PMs.

Component	Injection current	Gain
SOA1	0	0
SOA2	25.000 mA	~3.7 dB
SOA3	21.422 mA	~2.3 dB
SOA4	21.051 mA	~2.2 dB
SOA5	17.513 mA	~0.6 dB
SOA6	17.397 mA	~0.5 dB
PM1	0	N/A
PM2	2.011 mA	N/A
PM3	0	N/A
PM4	0	N/A
PM5	1.282 mA	N/A
PM6	0.103 mA	N/A

NA, not applicable; PM, phase modulator; SOA, semiconductor optical amplifier.

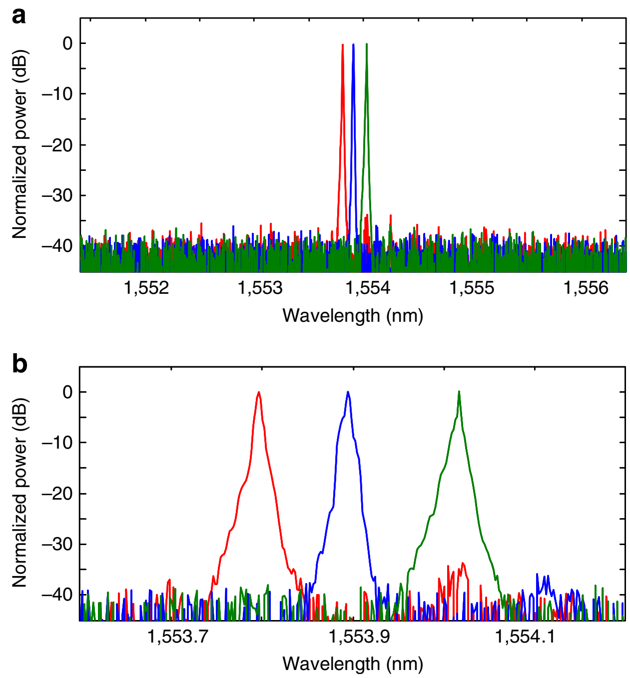

Figure 5 | Experimental results to show tunable single-mode lasing under PT-symmetry condition. (**a**) The wavelength is tuned to three different values by applying three different current pairs to phase modulator PM3 (1, 3 and 5 mA) and PM6 (1.1, 3.1 and 5.2 mA) in the ring resonators. (**b**) A zoom-in view of the wavelength tuning.

the lasing wavelength was continuously tuned from 1,553.800 to 1,554.020 nm with a tuning range of 0.22 nm.

Methods

Device epitaxial structure. The device is fabricated in the InP-InGaAsP material system. An n-doped layer is grown on top of the InP substrate and a waveguide layer is then grown on top of the n-doped layer, which has a thickness of 300 nm, on top of which there is a CTL with a thickness of ~250 nm. For an SOA, there are five QWs grown on top of the CTL, which pushes the QWs away from the waveguide layer to reduce the confinement factor and improve the saturation power. The QW layer is covered by a Zn p-doped layer with a thickness of 1.7 µm. For a passive waveguide, the CTL is covered by the p-doped layer without the QWs. For a PM, the p-doped layer is grown on top of the waveguide layer without the CTL and the QWs. For both the active and passive regions, there is a 150 nm contact layer on top of the p-doped layer and the contact layer is covered by a p-cap layer for the passive waveguides and by a metal layer for the active regions.

SOA gain profile measurement. The gain profile is measured by using a 400 µm standalone SOA with the same design as the SOAs in the ring resonators, and the lensed fibre to waveguide coupling loss and on chip waveguide loss are also measured to calibrate the gain profile. A continuous wave light wave at 1,554.148 nm generated by a tunable laser source is coupled into the standalone SOA by a lensed fibre. The output power of the SOA is measured at different injection currents by an optical spectrum analyser and the measured gain profile is fitted by a quartic polynomial. As the gain profile for a QW SOA is temperature dependent, the internal temperature of a SOA under normal operation is $>60\,^{\circ}C$ without external temperature control; thus, the efficiency of the SOA is reduced due to a high temperature. In addition, the alignment between the lensed fibre and the on-chip waveguide where the measured SOA is located can be shifted without temperature control due to heat accumulation in the measured SOA, which will add loss to the measurement data.

Data availability. All data are available from the corresponding author upon reasonable request.

References

1. Koninck, Y. D., Roelkens, G. & Baets, R. Electrically pumped 1,550 nm single mode III-V-on-silicon laser with resonant grating cavity mirrors. *Laser Photon. Rev.* **9,** L6–L10 (2015).
2. Simon, J. C. Semiconductor laser amplifier for single-mode optical fiber communications. *J. Opt. Commun.* **4,** 51–62 (1983).
3. Boyd, R. W. *Nonlinear Optics* (Academic, 1992).
4. Koyama, F., Kinoshita, S. & Iga, K. Room-temperature continuous wave lasing characteristics of GaAs vertical cavity surface-emitting laser. *Appl. Phys. Lett.* **55,** 221–222 (1989).
5. Ghafouri-Shiraz, H. *Distributed Feedback Laser Diodes and Optical Tunable Filters* (Wiley, 2003).
6. Li, L., Tang, S., Cao, B., Lu, J. & Chen, X. in *Optical Fiber Communication Conference*, M2D.3 (Los Angeles, California, USA, 2015).
7. Hill, M. T. *et al.* Lasing in metallic-coated nanocavities. *Nat. Photonics* **1,** 589–594 (2007).
8. Ma, R. M., Oulton, R. F., Sorger, V. J., Bartal, G. & Zhang, X. Room-temperature sub-diffraction-limited plasmon laser by total internal reflection. *Nat. Mater.* **10,** 110–113 (2011).
9. Oulton, R. F. *et al.* Plasmon lasers at deep subwavelength scale. *Nature* **461,** 629–632 (2009).
10. Liew, S. F., Redding, B., Ge, L., Solomon, G. S. & Cao, H. Active control of emission directionality of semiconductor microdisk lasers. *Appl. Phys. Lett.* **104,** 1–4 (2014).
11. Bender, C. M. & Boettcher, S. Real spectra in non-Hermitian Hamiltonians having PT symmetry. *Phys. Rev. Lett.* **80,** 5243–5246 (1998).
12. Makris, K. G., El-Ganainy, R. & Christodoulides, D. N. Beam dynamics in PT symmetric optical lattices. *Phys. Rev. Lett.* **100,** 103904–103904 (2008).
13. Guo, A. *et al.* Observation of PT-symmetry breaking in complex optical potentials. *Phys. Rev. Lett.* **103,** 093902–093904 (2009).
14. Klaiman, S., Günther, U. & Moiseyev, N. Visualization of branch points in PT-symmetric waveguides. *Phys. Rev. Lett.* **101,** 080402–080404 (2008).
15. Rüter, C. E. *et al.* Observation of parity-time symmetry in optics. *Nat. Phys.* **6,** 192–195 (2010).
16. Peng, B. *et al.* Parity-time-symmetric whispering-gallery microcavities. *Nat. Phys.* **10,** 394–398 (2014).
17. Feng, L., Wong, Z. J., Ma, R. M., Wang, Y. & Zhang, X. Single-mode laser by parity-time symmetry breaking. *Science* **346,** 972–975 (2014).
18. Hodaei, H., Miri, M.-A., Heinrich, M., Christodoulides, D. N. & Khajavikhan, M. Parity-time–symmetric microring lasers. *Science* **346,** 975–978 (2014).
19. Hodaei, H. *et al.* Parity-time-symmetric coupled microring lasers operating around an exceptional point. *Opt. Lett.* **40,** 4955–4958 (2015).
20. Hodaei, H. Single mode lasing in transversely multi-moded PT-symmetric microring resonators. *Laser Photon. Rev.* **10,** 494–499 (2016).
21. Brandstetter, M. *et al.* Reversing the pump-dependence of a laser at an exceptional point. *Nat. Commun.* **5,** 4034 (2014).
22. Norberg, E. J., Guzzon, R. S., Parker, J. S., DenBaars, S. P. & Coldren, L. A. in *37th European Conference and Exhibition on Optical Communication*, 18 (Geneva, Switzerland, 2011).

Author contributions

W.L. analysed the data. W.L., M.L. and J.Y. conceived and designed the experiments, and W.L. performed the experiments. W.L., R.S.G., E.J.N., J.S.P., M.L. and L.A.C. contributed materials and analysis tools. W.L., M.L. and J.Y. jointly wrote the paper.

Additional information

Supplementary Information accompanies this paper at http://www.nature.com/naturecommunications

Competing interests: The authors declare no competing financial interests.

Reprints and permission information is available online at http://npg.nature.com/reprintsandpermissions/

How to cite this article: Liu, W. *et al.* An integrated parity-time symmetric wavelength-tunable single-mode microring laser. *Nat. Commun.* **8,** 15389 doi: 10.1038/ncomms15389 (2017).

Publisher's note: Springer Nature remains neutral with regard to jurisdictional claims in published maps and institutional affiliations.

I. Photonic Integrated Circuits

D. PICs for LIDAR

Research Article

Optics EXPRESS

Sparse aperiodic arrays for optical beam forming and LIDAR

TIN KOMLJENOVIC, ROGER HELKEY, LARRY COLDREN, AND JOHN E. BOWERS

Department of Electrical and Computer Engineering, University of California, Santa Barbara, Santa Barbara, California 93106, USA

*tkomljenovic@ece.ucsb.edu

Abstract: We analyze optical phased arrays with aperiodic pitch and element-to-element spacing greater than one wavelength at channel counts exceeding hundreds of elements. We optimize the spacing between waveguides for highest side-mode suppression providing grating lobe free steering in full visible space while preserving the narrow beamwidth. Optimum waveguide placement strategies are derived and design guidelines for sparse (> 1.5 λ and > 3 λ average element spacing) optical phased arrays are given. Scaling to larger array areas by means of tiling is considered.

OCIS codes: (010.3640) Lidar; (110.5100) Phased-array imaging systems; (130.3120) Integrated optics devices.

References and links

1. S. J. Orfanidis, *Electromagnetic Waves and Antennas* (2016), Chap. 22.
2. W. L. Stutzman and G. A. Thiele, *Antenna Theory and Design*, 3rd ed. (Wiley, 2013), Chap. 8.
3. K. Van Acoleyen, W. Bogaerts, J. Jágerská, N. Le Thomas, R. Houdré, and R. Baets, "Off-chip beam steering with a one-dimensional optical phased array on silicon-on-insulator," Opt. Lett. **34**(9), 1477–1479 (2009).
4. J. K. Doylend, M. J. R. Heck, J. T. Bovington, J. D. Peters, L. A. Coldren, and J. E. Bowers, "Two-dimensional free-space beam steering with an optical phased array on silicon-on-insulator," Opt. Express **19**(22), 21595–21604 (2011).
5. K. Van Acoleyen, K. Komorowska, W. Bogaerts, and R. Baets, "One-dimensional off-chip beam steering and shaping using optical phased arrays on silicon-on-insulators," J. Lightwave Technol. **29**(23), 3500–3505 (2011).
6. J. K. Doylend, M. J. R. Heck, J. T. Bovington, J. D. Peters, M. L. Davenport, L. A. Coldren, and J. E. Bowers, "Hybrid III/V silicon photonic source with integrated 1D free-space beam steering," Opt. Lett. **37**(20), 4257–4259 (2012).
7. D. Kwong, A. Hosseini, J. Covey, Y. Zhang, X. Xu, H. Subbaraman, and R. T. Chen, "On-chip silicon optical phased array for two-dimensional beam steering," Opt. Lett. **39**(4), 941–944 (2014).
8. A. Yaacobi, J. Sun, M. Moresco, G. Leake, D. Coolbaugh, and M. R. Watts, "Integrated phased array for wide-angle beam steering," Opt. Lett. **39**(15), 4575–4578 (2014).
9. J. C. Hulme, J. K. Doylend, M. J. R. Heck, J. D. Peters, M. L. Davenport, J. T. Bovington, L. A. Coldren, and J. E. Bowers, "Fully integrated hybrid silicon two dimensional beam scanner," Opt. Express **23**(5), 5861–5874 (2015).
10. H. Abediasl and H. Hashemi, "Monolithic optical phased-array transceiver in a standard SOI CMOS process," Opt. Express **23**(5), 6509–6519 (2015).
11. F. Aflatouni, B. Abiri, A. Rekhi, and A. Hajimiri, "Nanophotonic projection system," Opt. Express **23**(16), 21012–21022 (2015).
12. H. Nikkhah, K. Van Acoleyen, and R. Baets, "Beam steering for wireless optical links based on an optical phased array in silicon," Ann. Telecommun. **68**(1), 57–62 (2013).
13. J. Sun, E. Hosseini, A. Yaacobi, D. B. Cole, G. Leake, D. Coolbaugh, and M. R. Watts, "Two-dimensional apodized silicon photonic phased arrays," Opt. Lett. **39**(2), 367–370 (2014).
14. J. Sun, E. Timurdogan, A. Yaacobi, E. S. Hosseini, and M. R. Watts, "Large-scale nanophotonic phased array," Nature **493**(7431), 195–199 (2013).
15. J. Sun, E. Timurdogan, A. Yaacobi, Z. Su, E. S. Hosseini, D. B. Cole, and M. R. Watts, "Large-scale silicon photonic circuits for optical phased arrays," IEEE J. Sel. Top. Quantum Electron. **20**(4), 8201115 (2014).
16. K. Van Acoleyen, H. Rogier, and R. Baets, "Two-dimensional optical phased array antenna on silicon-on-insulator," Opt. Express **18**(13), 13655–13660 (2010).
17. W. Guo, P. R. A. Binetti, M. L. Masanovic, L. A. Johansson, and L. A. Coldren, "Large-scale InP photonic integrated circuit packaged with ball grid array for 2D optical beam steering," in *IEEE Photonics Conference* (IEEE, 2013), pp. 651–652.

18. K. Sayyah, O. Efimov, P. Patterson, J. Schaffner, C. White, J.-F. Seurin, G. Xu, and A. Miglo, "Two-dimensional pseudo-random optical phased array based on tandem optical injection locking of vertical cavity surface emitting lasers," Opt. Express **23**(15), 19405–19416 (2015).
19. D. Kwong, A. Hosseini, Y. Zhang, and R. T. Chen, "1× 12 unequally spaced waveguide array for actively tuned optical phased array on a silicon nanomembrane," Appl. Phys. Lett. **99**(5), 051104 (2011).
20. J. K. Doylend, M. J. R. Heck, J. T. Bovington, J. D. Peters, and J. E. Bowers, "Free-space beam steering using silicon waveguide surface gratings," in *IEEE Photonic Society 24th Annual Meeting* (IEEE, 2011), pp. 547–548.
21. D. N. Hutchison, J. Sun, J. K. Doylend, R. Kumar, J. Heck, W. Kim, C. T. Phare, A. Feshali, and H. Rong, "High-resolution aliasing-free optical beam steering," Optica **3**(8), 887–890 (2016).
22. C. V. Poulton, M. J. Byrd, M. Raval, Z. Su, N. Li, E. Timurdogan, D. Coolbaugh, D. Vermeulen, and M. R. Watts, "Large-scale silicon nitride nanophotonic phased arrays at infrared and visible wavelengths," Opt. Lett. **42**(1), 21–24 (2017).
23. W. Song, R. Gatdula, S. Abbaslou, M. Lu, A. Stein, W. Y.-C. Lai, J. Provine, R. F. Pease, D. N. Christodoulides, and W. Jiang, "High-density waveguide superlattices with low crosstalk," Nat. Commun. **6**, 7027 (2015).
24. A. Khavasi, L. Chrostowski, Z. Lu, and R. Bojko, "Significant crosstalk reduction using all-dielectric CMOS-compatible metamaterials," IEEE Photonics Technol. Lett. **28**(24), 2787–2790 (2016).
25. H. Unz, "Linear arrays with arbitrarily distributed elements," IRE Trans. Ant. Prop. **8**(2), 222–223 (1960).
26. M. G. Bray, D. H. Werner, D. W. Boeringer, and D. W. Machuga, "Optimization of thinned aperiodic linear phased arrays using genetic algorithms to reduce grating lobes during scanning," IEEE Trans. Antenn. Propag. **50**(12), 1732–1742 (2002).
27. D. D. King, R. F. Paackard, and R. K. Thomas, "Unequally-spaced, broad-band antenna arrays," IRE Trans. Antennas Propag. **8**(4), 380–384 (1960).
28. J. Kennedy and R. Eberhart, "Particle swarm optimization," in *Proceedings of IEEE International Conference on Neural Networks IV* (IEEE, 1995), pp. 1942–1948.
29. C. V. Poulton, A. Yaccobi, Z. Su, M. J. Byrd, and M. R. Watts, "Optical phased array with small spot size, high steering range and grouped cascaded phase shifters," in *Advanced Photonics 2016* (2016), paper IW1B.2.

1. Introduction

Free-space beam-steering is important for light detection and ranging (LIDAR), free space communications, and has potential applications for holographic displays and biomedical imaging. The beam can be steered mechanically, but an optical phased array (OPA) offers many advantages such as reduced size and weight as well as increased speed due to lack of inertia. Furthermore, OPAs can, for example, be integrated with all the other required circuitry to make a fully-integrated chip-scale LIDAR system.

Phased antenna arrays have extensively been studied in radio frequencies, and there are many book chapters written about them, e.g [1,2]. OPAs, on the other hand, have received less attention, but in recent years, there has been a lot of interest in research and development of OPAs [3–22]. One of the reasons is the use of silicon photonics, with its superior processing and yield, allowing for more complex photonic integrated circuits (PIC) with hundreds or thousands of elements.

There are some key differences between phased antennas in RF and OPAs mainly due to the many orders difference in wavelength. RF arrays typically operate in centimeter wavelength range with a push to millimeter wavelength range, while OPAs operate in micrometer range, most often around 1.5 μm. It is well known that a uniform spaced array has to have the spacing between elements $d < \lambda/2$, where λ is the free-space wavelength, to prevent appearance of grating sidelobes as the main lobe is scanned across the visible region [1,2]. Depending on the scan angle range of the OPA, the limitation can be relaxed a bit, but in all cases $d < \lambda$ holds. This requirement can readily be met in RF, with some consideration due to potential unwanted cross-coupling between antenna elements. In optics the cross-coupling presents more serious challenges, with some suggestions on how to achieve sub-wavelength spacing [23,24], but that is just one of the problems in realizing such a narrow pitch that we turn to in Section 2. Each element also has to have phase control and be electrically contacted for operation, so having a lower number of elements covering the same area makes the driving circuitry simpler. Non-uniform or aperiodic arrays have been studied in 1960s [25], and they make a tradeoff in suppressing the grating lobes for an increase of power in sidelobes. As they cover the same area, the main lobe width is preserved provided that the excitation amplitude has the same taper, while control and circuitry are simplified due to lower number of elements. Such an approach has recently been demonstrated with a larger waveguide count and has allowed for 80° steering in phase direction [21] with over 500 resolvable spots with a small divergence of 0.14°. The array had 128 emitters with average spacing of 7.245 µm at 1.3 µm or 5.57 λ. The positions were randomized using uniformly distributed random numbers and an iterative algorithm to place the waveguides so the array had > 10 dB sidemode suppression ratio (SMSR) at ± 45° deflection. The minimum pitch was set at 5.4 µm and in the final design, the standard deviation of 1.1 µm was reported.

Here our analysis goes several steps further, by first studying non-uniform ordered distributed waveguides and then various randomization approaches. We study the effect of increasing the waveguide count on key performance metrics that include the SMSR, power in the main beam and the main beam full width at half maximum (FWHM), where for randomized approaches, we utilize a global optimization technique. Power in the main beam, as reported in this manuscript, is the integrated power in the direction of the main lobe between first nulls (sometimes called null-to-null beamwidth) divided by the total radiated power of the array.

We show that normal and uniform distributions are not optimal, and also that even better performance can be obtained by using a fully random waveguide placement compared to the offset approach that was typically used to optimize thinned or aperiodic arrays [26].

The OPA design that we study is shown in Fig. 1 and is similar in operation to the ones reported in [9,21] where phase control is used to steer only in one of the axis, while the other axis is steered by wavelength. Such an approach has a distinct advantage compared to a purely phase steered 2D array due to significant reduction in number of controls required. An OPA as shown in Fig. 1 needs only $N + 1$ controls (N phases and 1 wavelength) compared to NxM controls needed for 2D phase array. As we steer the beam using phase only in one axis, our analysis is also simplified as we effectively study 1D phased arrays.

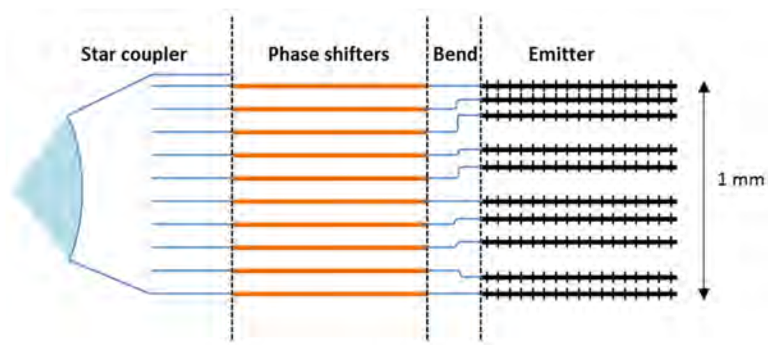

Fig. 1. Optical phase array (OPA) as studied comprises of a star coupler (splitting the input wave into N waveguides), N phase shifters, bend structures to offset the emitter positions and N emitters with non-uniform pitch. For analysis purposes we set the width of the emitter region to 1 mm throughout the manuscript, if not specified differently. This makes it ~645 λ wide at 1.55 µm.

The paper is organized as follows. In Section 2 we analyze a uniform phased array as a metric to compare the aperiodic arrays to. We also address the waveguide crosstalk, and the problem of having phase shifters at small pitch. In Section 3 we describe our method of analysis; briefly the global search algorithm employed and then study various waveguide placement strategies including ordered non-uniform pitch and fully random non-uniform pitch. In Section 4 we compare in detail two most promising placement strategies from previous section and we also address the potential for scaling to larger OPA widths using tiling of basic elements. Finally, we draw conclusions in Section 5.

2. Uniformly spaced arrays

An array of antennas can synthesize any radiation pattern, provided that it has enough elements and that they are spaced by $d < \lambda/2$. The relative displacements of the antenna elements introduce relative phase shifts in the radiation vectors, and fields from individual antennas add constructively or destructively in different directions. This is a direct consequence of the translational phase-shift property of Fourier transforms [1]. By introducing phase control into each element, the array can be steered and the angle can be scanned.

Uniformly-spaced one-dimensional arrays are probably the easiest to analyze with closed expressions derived for the array factor if the excitation is also uniform (in magnitude). In the case $d > \lambda/2$, grating lobes can appear with uniform-spaced arrays. In most cases, including the OPAs, grating lobes are undesirable, which puts severe constraints on OPA design. The angles of other grating lobes are given by

$$\sin\theta_n = \frac{n\lambda}{d} + \sin\theta_0 \tag{1}$$

where θ_n is the angle of the n-th order grating lobe, n is the order of the grating lobe, and θ_0 is the angle of the primary beam (zeroth grating lobe).

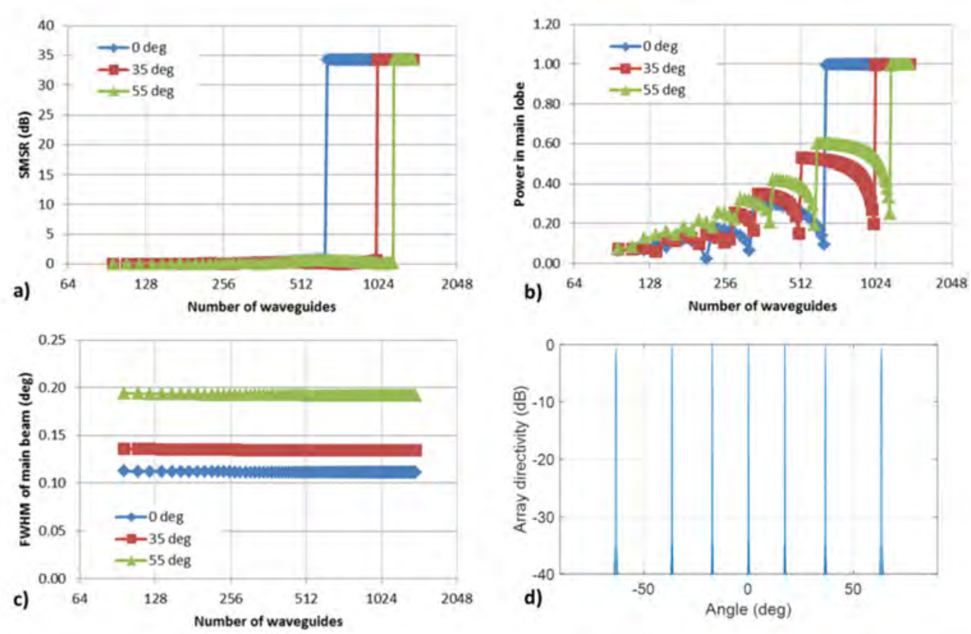

Fig. 2. (a) SMSR as a function of the number of waveguides for 1 mm wide uniformly spaced OPA. The pitch has to be reduced, so all grating lobes are pushed outside the visible region, for SMSR to improve. (b) Power in the main lobe as a function of number of waveguides for the same OPA. Power increases as grating lobe number is reduced (c) FWHM of the main beam as a function of number of waveguides. The FWHM is the same regardless of the number of waveguides, provided that the total size of the array is kept the same. (d) Illustrative far-field for an array with 192 uniformly spaced elements resulting with seven lobes in visible space when looking at broadside.

We plot the SMSR, power and FWHM of the main beam for a uniformly-spaced array 1 mm wide as a function of number of waveguides in Fig. 2. The operating wavelength is set at 1.55 µm. We taper the amplitude of the excitation to −10dB at the ends of the array to suppress the close-in sidelobes that would otherwise limit the SMSR to ~13 dB in a uniformly excited array [1]. This lifts the SMSR limitation to ~35 dB. In all cases, unless specified otherwise, we assume that the elementary emitter has a Gaussian near-field profile with 10 dB taper at ± 250 nm (500 nm total width).

Figure 2(a) shows the SMSR as a function of the number of waveguides, or inversely as the pitch (d) is reduced. For broadside direction (0° in our notation), the grating lobes are suppressed when the waveguide count exceeds 648, or $d \approx 1.54$ µm < λ. But as the same array is steered to 35° or 55° degrees the grating lobes appear as also indicated by Eq. (1) with the right side sine term. To cover ± 35°, ± 55°, or ± 90° with no grating lobes 1018, 1176 or 1291 waveguides are needed corresponding to 0.98 µm, 0.85 µm or 0.774 µm pitch, respectively. Such small spacing is very challenging and we address it in more detail in following section. Figure 2(b) shows the relative power in the main lobe calculated as integrated power in the main lobe (null-to-null beamwidth) divided by the total radiated power. The step increases in power correspond to the reduction of number of grating lobes in visible space. In between these steps, there is a reduction of power in the main lobe due to the broadening of the grating lobes as they are steered closer to the edge of the visible region. This effect can be suppressed with a more directive elementary emitter [1]. Figure 3(c) shows the FWHM of the main lobe, and there is a key takeaway that the FWHM is not dependent on the number of waveguides if they cover the same area. The difference between FWHM for different scan directions is a direct result of reducing the effective area of the emitter array as the beam is scanned from the broadside. Figure 2(d) shows an illustrative far-field for an array with 192 uniformly spaced elements resulting with seven lobes in visible space when looking at broadside.

One could argue that e.g. the 192 waveguide configuration (5.21 µm pitch) can be used to steer the beam in ± 8.5° range as grating lobes are spaced by ~17°, but spurious signals from the grating lobes have to be suppressed for reliable measurements or there will be ambiguity in signal. For that reason, in most practical cases with uniform arrays the pitch has to be reduced to < λ resulting in a number of challenges that have to be addressed such as crosstalk, placement and contacting the phase shifters, etc.

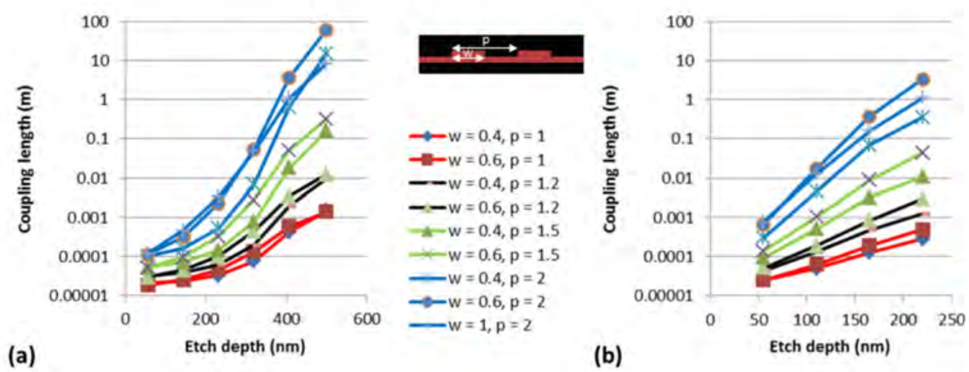

Fig. 3. Coupling length at 1.55 µm calculated by the difference in effective index of refraction between even and odd mode as a function of etch depth for different waveguide widths (w) and waveguide pitch (p). (a) 500 nm thick Si device layer (b) 220 nm thick Si device layer.

2.1 Crosstalk

Optical cross talk is a severe issue with OPAs due to the use of dielectric waveguides where it is hard to tightly confine electromagnetic waves compared to RF frequencies where metals are typically used. Use of high index contrast waveguides such as Si/SiO_2 helps, but obtaining sub-wavelength pitch without crosstalk is still very challenging. We calculate crosstalk in two standard Si photonic platforms: 220 nm thick Si device layer typically used for passive devices and thicker 500 nm Si device layer typically used for heterogeneously integrated silicon photonic devices at 1.55 µm. In both cases we calculate the coupling length corresponding to 100% power transfer between the two straight waveguides. We study a number of pitch (waveguide spacing) values *p* and a few waveguide widths *w*, and plot the coupling length as a function of etch depth, from a very shallow to fully etched. The results are plotted in Fig. 3.

For obtaining a narrow beam in the wavelength steered dimension, one generally wants to have a long and weak grating, so the effective aperture length is large. Due to the requirement to have substantially different phases in neighboring waveguides at certain steer angles, the cross talk has to be minimized. The criterion for the amount of coupling that can be tolerated is somewhat arbitrary, and here we set the requirement for the coupling length to be 10x the grating length. In our considered case of 1 mm long grating, the coupling length has to be at least 1 cm.

From Fig. 3 it is clear that this limits us to 1.5 μm pitch with 220 nm thick silicon and to 1.2 μm pitch with 500 nm thick silicon, and generally requires full etch. In the former case, the pitch requirement allows us to suppress the grating lobes at broadside, but with practically no steering range without grating lobes, while in the latter case we have ~(± 17°) of steering without grating lobes.

There has been an effort to reduce the crosstalk between closely spaced waveguides. One way would be to introduce a phase mismatch in neighboring waveguides [23], but such an approach requires at least two corrections for optimal beam quality. First the pitch of the grating has to be corrected to account for the change in effective index of refraction (wavelength steering direction). Second, the phase has to be adjusted between the waveguides for phase steering direction. It is relatively straightforward to correct for the phase difference at one particular point, but as the emission is continuous along the grating, it is not possible to do so with a small change in feeding waveguides (either their length or their phase velocity). It seems that there have to be multiple transitions between beta values along the length of the grating so that the phase difference between neighboring waveguides does not exceed some predetermined value, making this approach quite complex. Another way of reducing the crosstalk would be the introduction of sub-wavelength periodic structures as in [24], but although the increase in coupling length is substantial, it still does not allow for 1 mm long gratings with negligible coupling and large field of view (FOV). To conclude, although there has been considerable progress, low crosstalk $\lambda/2$ pitch at 1.55 μm with compensated phase difference is still very challenging, so the ability to use larger waveguide spacing for OPAs would simplify the design and manufacturing.

2.2 Phase shifters

An ideal OPA has to have a phase shifter for every waveguide with grating. Due to the complexity of electrically connecting the phase shifters and having large enough separation between the metal and the optical field to reduce the propagation loss, they would usually have much larger pitch than the gratings (e.g. see Fig. 1 in [9] or Fig. 1 in [21]), so in the final chip the grating would occupy relatively small area increasing the cost of the OPA compared to beam width that is predominantly determined by the effective area of the gratings. From that perspective the use of larger pitch sizes would prove beneficial. Another issue with having large emitters with sub-wavelength pitch is the sheer number of phase shifters that have to be controlled increasing the system complexity, power consumption and reducing the yield.

3. Aperiodic arrays

Linear RF arrays with arbitrarily distributed elements were studied in 1960s [25], and the main motivation was that the variable spacing generally allows for fewer elements with similar far field pattern performance. The main advantages of unequally-spaced arrays are [27]: fewer elements for comparable beamwidth and grating lobe replacement by sidelobes of unequal amplitude, which are all less than the main lobe. The reduction in the number of elements allows the arrays to be built at lower cost with lower number of amplifiers and phase shifters.

As the aperiodic array is a quite complex non-linear problem, lack of computational resources in 1960s prevented numerical optimization of such arrays, so most studied arrays had an order where spacing would follow some law: logarithmic, prime number, power spacing, while the minimum pitch would often correspond to $\lambda/2$. The increase in computational power in recent years, allowed for the far-field pattern optimization using iterative search algorithms [21, 26]. Usually global search algorithms have been used, such as genetic algorithm [26] or particle swarm optimization (PSO) [28]. Here, for randomized waveguide placement studied in Section 3.2, we employ the PSO as implemented in Matlab (R2016a) for simplicity. The calculation of non-uniform spaced array pattern (AP) is implemented in matrix notation, which is multithreaded in Matlab and reasonably fast allowing for use of a global optimization algorithm (~50 ms for calculating 192 element far field pattern in 10001 points on a modern PC). As an optimization parameter, we use the SMSR with the beam pointing in given direction.

For a typical optimization run, we used 400 particles and let the optimizer work for 1 hour. Due to the number of degrees of freedom (corresponding to number of waveguides), it is reasonable to expect that the optimizer will not find the optimal result, especially for larger waveguide counts, but with repeated optimizations we generally get less than 1 dB difference in SMSR indicating that we are relatively close to the optimal solution. Optimization of the phase of each emitter could also be implemented, but it is obvious that for the highest power in the main lobe, the phases should be aligned at the direction where the main beam points. A brief study in phase optimization showed that it is possible to improve the SMSR somewhat in certain configurations, but with severe reduction of power in the main beam, which does not seem a worthwhile route for OPAs. For that reason, when steering the non-uniform arrays, we calculate the steering phase using the well-known expression [1] $\psi = kd_i \cos(\varphi)$, where d_i is the distance of the i-th element from the array origin.

For waveguide placement, we consider both the ordered non-uniform spacing and fully random OPAs. In all cases, we impose a minimum pitch that puts some limitations on the waveguide placement. First we turn to the ordered non-uniform spacing OPAs.

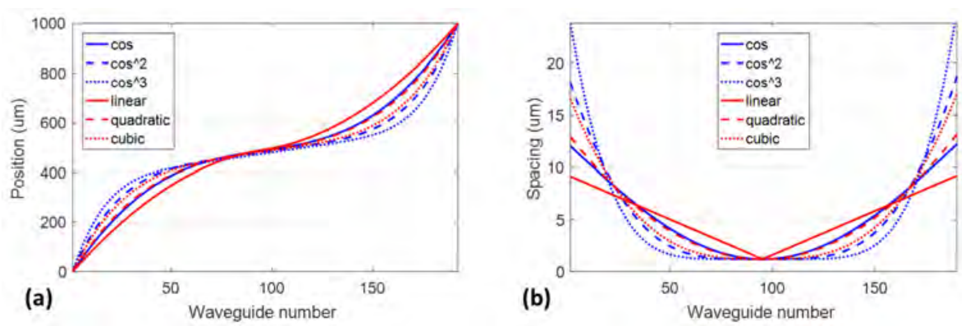

Fig. 4. (a) Position and (b) Spacing for an ordered non-uniform spacing OPAs consisting of 192 waveguides. Shown are linear, quadratic, cubic, cos, cos^2 and cos^3 spacing distribution and waveguide position. The minimum pitch is set at 1.2 μm due to cross-coupling limitations.

3.1 Ordered non-uniform spacing

There are a number of functions that we could use to determine the spacing of the ordered non-uniform spacing OPAs. We plot positions and spacings for six different functions in Fig. 4 as an illustration for the 192 waveguide case with 1.2 μm minimum pitch. We intentionally plot the case with a relatively small number of waveguides as changes between functions are more apparent.

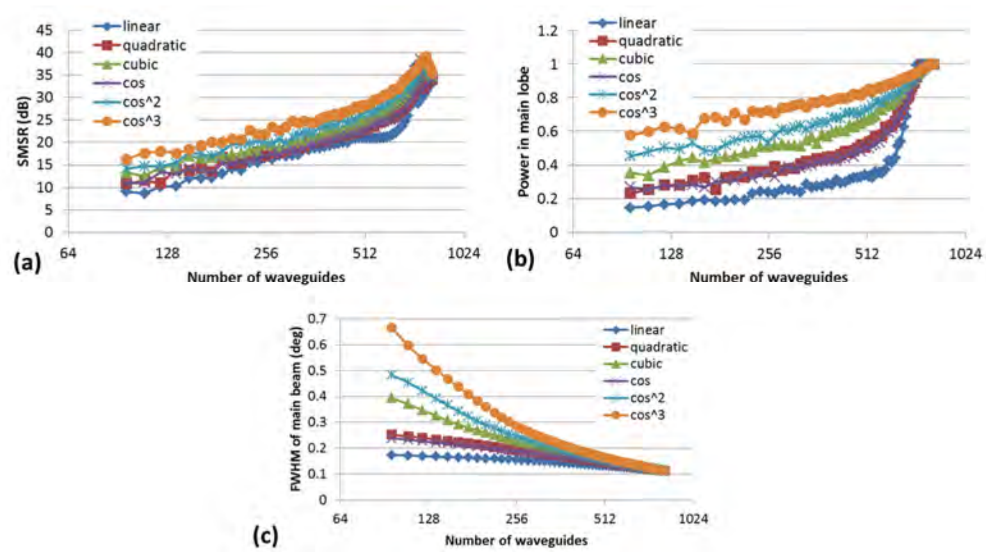

Fig. 5. (a) SMSR at broadside as a function of number of waveguides for 1 mm wide OPA with different spacing distributions. The SMSR generally improves as the number of waveguides is increase. (b) Power in the main lobe at broadside as a function of number of waveguides for the same OPA. Power increases as number of waveguides is increased (c) FWHM of the main beam at broadside as a function of number of waveguides. The FWHM reduces with increase of number of waveguides contrary to the uniform case.

Similar to the uniform pitch case (Fig. 2), we plot the SMSR, power in main lobe and FWHM as a function of the number of waveguides. We limit the number of considered waveguides to 820 due to minimum pitch requirement of 1.2 µm. The results are plotted in Fig. 5. One could conclude, looking at Fig. 5, that the cos^3 spacing distribution is superior due to highest SMSR and power in the main lobe, with the tradeoff being wider main lobe, but that conclusion is valid only at broadside.

Next we study the beam steering performance. Due to constraints placed by the minimum pitch (1.2 µm in this case due to cross-coupling, see Section 2.1) and the total number of waveguides, there is not much difference between some functions (e.g. cos and quadratic), so, due to space consideration, we show results only for linear, quadratic, and cos^3 in more detail as we steer the beam. We study cases with 192 and 480 waveguides, both of which are much smaller than the 1300 waveguides needed for uniform pitch with no grating sidelobes for a 1 mm wide emitter. We plot the SMSR, power in main lobe and FWHM as a function of steering angle in Fig. 6. It is again clear that the more squeezed the waveguides are (e.g. cos^3) we have better SMSR and more power in main lobe, at the expense of the FWHM, but that holds only for smaller steer angles. As we steer more, the SMSR for such squeezed spacings deteriorates rapidly as the large grating lobe that is not strongly suppressed comes into the visible region. A linear change of pitch, on the other hand, has worse SMSR and power in main lobe at broadside, but the performance is largely unaffected by steering the beam, so it is probably preferred for large FOV applications. Non-uniform ordered spacing, as the one considered here, in all cases trades off the FWHM and the quality of the main beam for SMSR. Wider FWHM of the main beam results with more power in the main beam, which helps with range in the case of LIDAR application. At the same time, it influences the number of resolvable spots. The number of resolvable spots with > 10 dB SMSR is much larger with linear and quadratic spacings due to the much larger FOV and narrower lobe compared to cos^3 spacing (approximately 600-700 vs. only 75 in case of 480 waveguides).

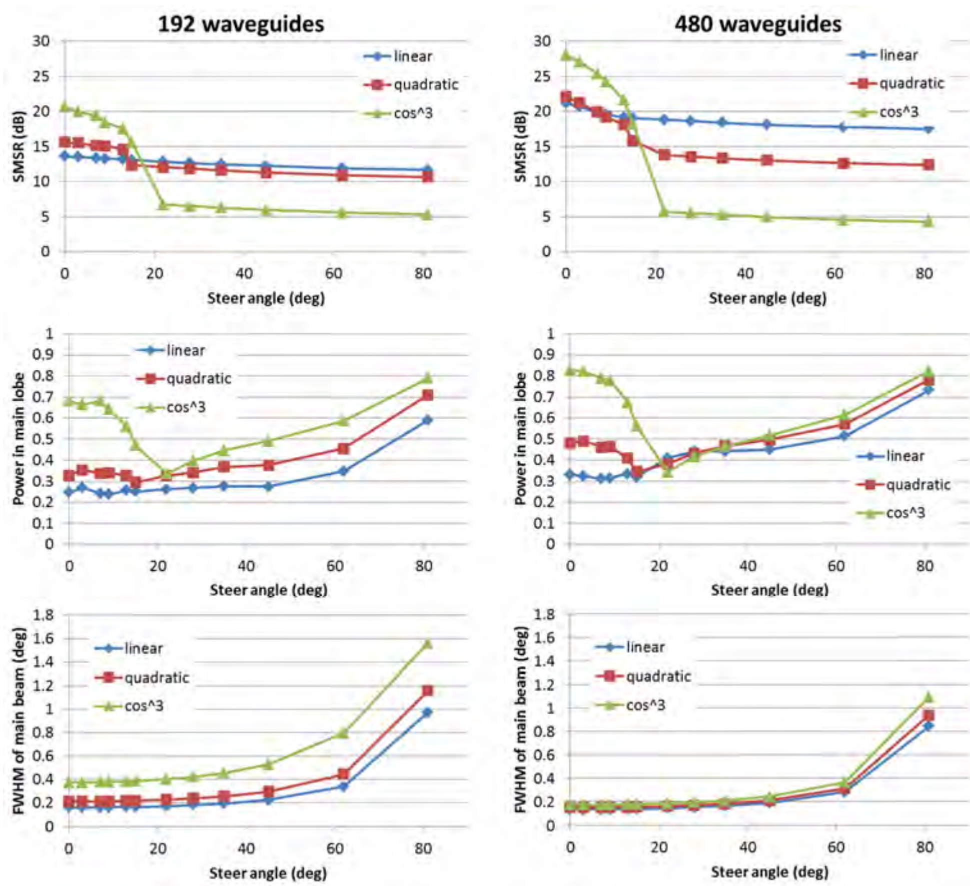

Fig. 6. SMSR, power in main lobe and FWHM of the main lobe as a function of steer angle for ordered non-uniform OPAs with linear, quadratic and cos^3 spacing distributions. (left column) 192 waveguide configuration (right column) 480 waveguide configuration.

Finally, we study the influence of minimum pitch on the OPA performance. Due to space constraints, we show only results for linear and cos^3 non-uniform spacing OPAs as two extreme configurations in Fig. 7. It is clear that for cos^3, a small minimum pitch is required with performance quickly deteriorating as the pitch is increased to ~λ scale, linear pitch is on the contrast largely insensitive to minimum pitch, especially at lower waveguide counts.

Once again we can conclude that linear change in pitch is better if wide FOV is required, while more compressed schemes (quadratic, cubic, cos^3, etc.) can be used for limited FOV if sub-wavelength pitch can be attained as they can offer higher SMSR and higher power in the main lobe. It should be pointed out that linear change in pitch offers decent performance with 192 waveguides even with minimum pitch in 3 µm range (~2 λ) where crosstalk can definitely be neglected.

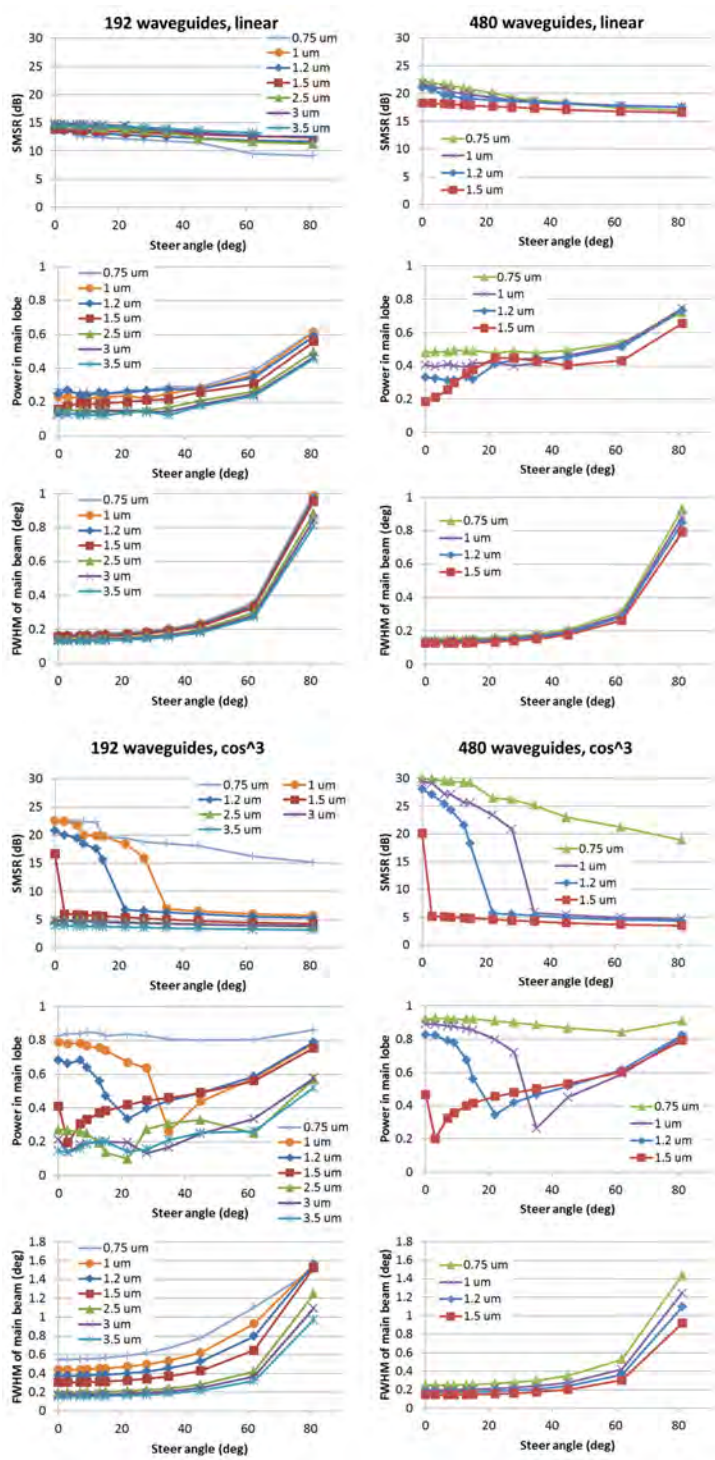

Fig. 7. SMSR, power in main lobe and FWHM of the main lobe as a function of steer angle for ordered non-uniform OPAs with linear and cos^3 spacing distributions for different minimum pitch with 192 and 480 waveguides.

3.2 Randomized non-uniform spacing

We now turn to the analysis of randomized non-uniform spacing using the PSO algorithm to determine optimal spacing. First we compare the randomization approaches, from truly random distributions (both normal and uniformly distributed offsets), PSO optimized offset spacing similar to [26] and fully random PSO distribution. For truly random distributions, we generate a uniform pitch and then a sequence of random numbers with normal or uniform distribution. We then offset the uniform waveguide positions using those generated sequences. As it is a purely random approach sensitive to “roll of dice”, we repeat the process three times and average the result that we plot in Fig. 8. For the PSO optimized offset spacing, we utilize an approach similar to one outlined in [26] where we initially position the waveguides at uniform pitch and then adjust the offsets from the uniform pitch keeping the minimum spacing requirement satisfied using the PSO algorithm. In this case the offset is limited to (average pitch – minimum pitch)/2. Lastly we implement a fully random spacing, in which we skip the generation of the uniform array and add element by element to a location where the distance between the last element is greater than minimum pitch and is less than the distance needed to place all remaining elements at minimum pitch and is further scaled by the random value for that element divided by the sum of the unused part of the random vector. This approach allows us to shuffle the waveguide positions more while still keeping the minimum pitch requirement satisfied. The comparison between all the approaches as a function of number of waveguides is shown in Fig. 8. In Fig. 9 we show histograms with typical offsets from the uniform pitch for the case of 480 waveguides for different waveguide placement strategies. The minimum pitch is 1.2 µm in all cases. The added freedom of the fully random approach allows the optimizer to suppress the sidelobes with 480 and 576 waveguides compared to the offset approach typically used.

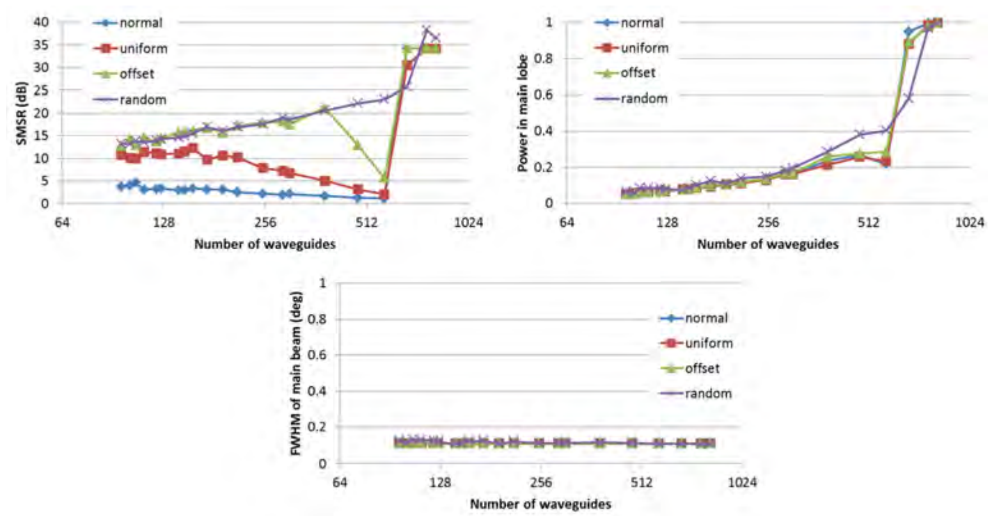

Fig. 8. SMSR, power in main lobe and FWHM of the main lobe as a function of number of waveguides for different randomization approaches of non-uniform OPAs.

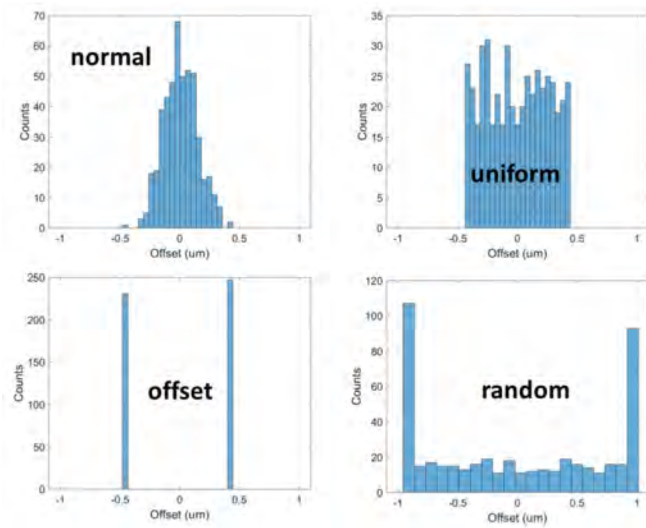

Fig. 9. Histograms showing typical offsets from the uniform pitch for the case of 480 waveguides for 4 considered randomization approaches. Minimum pitch is 1.2 µm in all cases.

Next we study the influence of minimum pitch as a function of number of waveguides for a 1 mm wide emitter using fully random waveguide placement. We consider five different minimum pitch values from sub-wavelength 1.2 µm to 3.5 µm (~2.25 λ) and show the results in Fig. 10. The SMSR generally improves as the number of waveguides is increased, until the minimum pitch limitation prevents the optimizer to arrange the waveguides so that the grating lobes are suppressed.

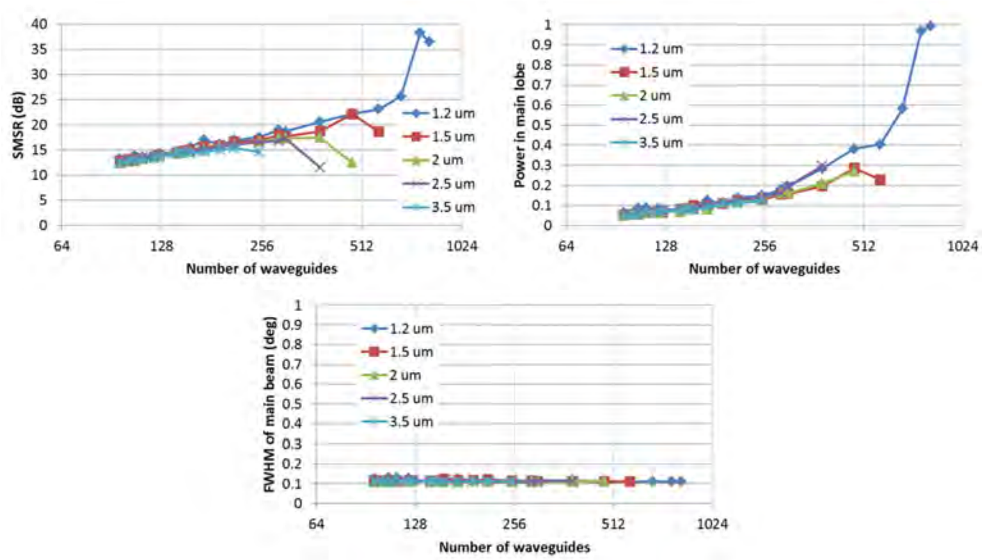

Fig. 10. Minimum pitch influence on SMSR, power in main lobe and FWHM of the main lobe as a function of the number of waveguides. The minimum pitch places a limitation on number of waveguides that can be placed with sufficiently random pitch in 1 mm area to suppress grating lobes. Besides that, there is little influence of minimum pitch on OPA performance.

For 3.5 µm minimum pitch, this happens between 212 and 252 waveguides, while for 2 µm pitch, the transition is around 302 waveguides. This clearly shows that fully random waveguide placement allows for large waveguide separation where crosstalk does not present a problem. Due to randomized placement, the beamwidth is preserved and is equal to approximately 0.11°. It is slightly larger than the diffraction limit due to, already mentioned, the 10 dB excitation taper used to suppress sidelobes.

We select the 2.5 µm pitch, 192 waveguide case to study the steering performance. The array that was optimized at broadside (0° steering) shows relatively large variation in SMSR of ~4 dB when steered between broadside and 81° as shown in Fig. 11. We further compare the steering performance for arrays that were optimized at different angles of 12°, 35° and 65°, and show that a lower variation in performance can be obtained by optimizing the array at larger angles. The array optimized at 65° has variation of less than 1 dB, at the expense of somewhat lower SMSR close to the broadside. The effect on power in main lobe and FWHM is negligible. This shows that the randomized OPAs can be optimized depending on the FOV required.

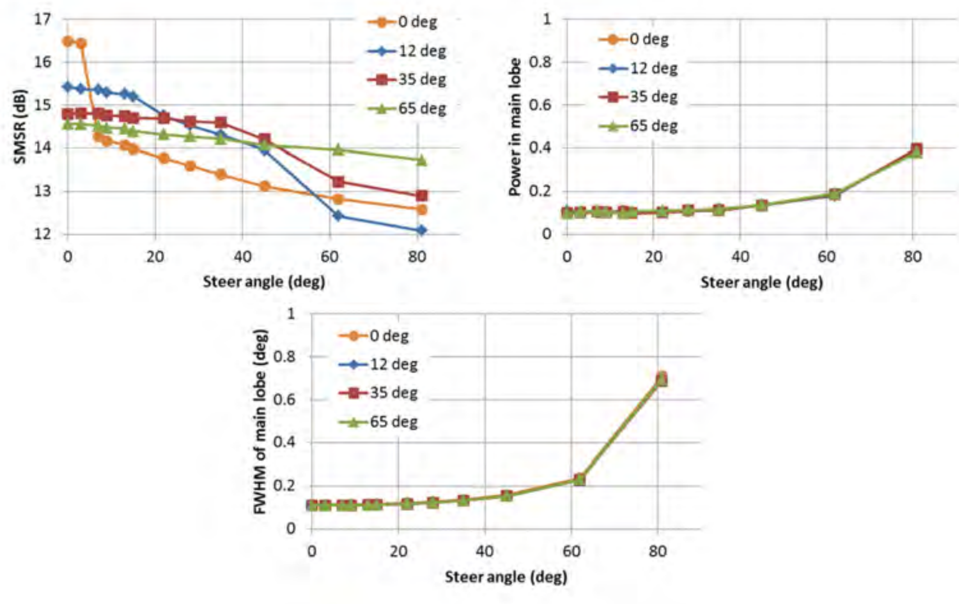

Fig. 11. Beam steering performance of randomized 192 waveguide OPA where the waveguide placement was optimized at broadside (0°) or at an angle (12°, 35° and 65°). Optimization at broadside results with higher SMSR at broadside, but also with larger SMSR variation as the beam is steered. Optimization of waveguide locations at larger angles reduces the SMSR at broadside, but lowers the SMSR variation as the beam is steered. Influence on power in main lobe and FWHM is negligible. The minimum pitch is 2.5 µm.

Due to allowing for larger spacing between the waveguides without sidelobes, randomized spacing, similarly to linearly changing pitch in Section 3.1, allows for wider elementary emitter which can reduce the power in sidelobes or, in other words, increase the relative power in the main beam. This increase in power of the main beam has a tradeoff in reduced scanning angle due to the higher directivity of the elementary emitters. In previous simulations, we have assumed that the elementary emitter has a Gaussian profile with 10 dB taper at ± 250 nm (500 nm total width). Now we show performance when the elementary emitter width is increased to 1 µm and 1.5 µm for the same 192 waveguide case, keeping the same Gaussian approximation. A more rigorous analysis would simulate the mode shape in the waveguide, but we keep the Gaussian approximation due to simplicity and number of degrees of freedom in designing the waveguide (Si device layer thickness, etch depth). The waveguide placement has been optimized for broadside emission. The results are plotted in Fig. 12, and show that by using a wider emitter, it is possible to considerably increase power in the main beam, provided that the required FOV is limited. This allows further optimization of the OPA performance depending on the required FOV.

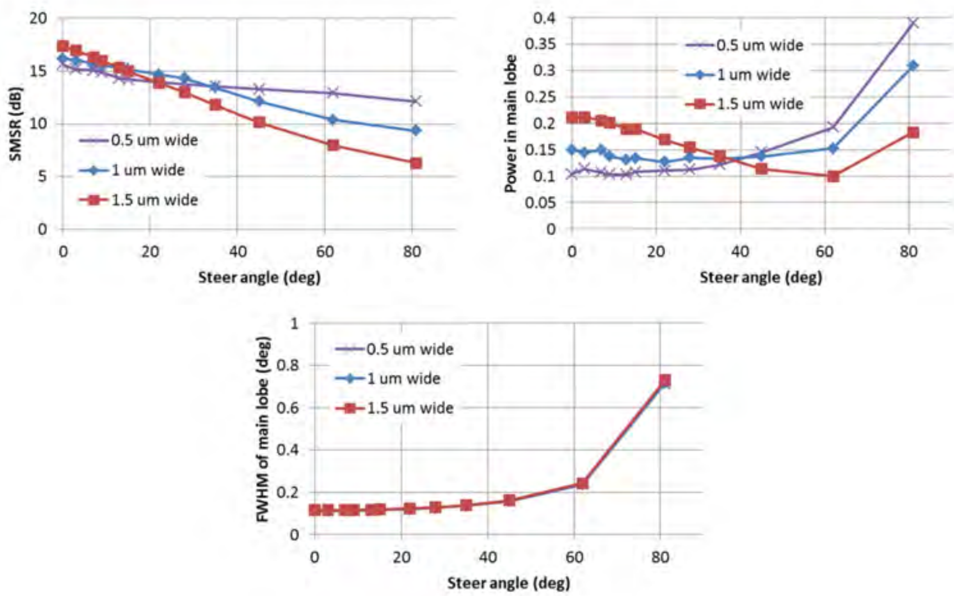

Fig. 12. Beam steering performance of randomized 192 waveguide OPA with 2.5 μm minimum pitch with different widths of elementary emitters. Using wider elementary emitter increases the power in main lobe if OPA FOV is limited.

4. Optimal OPA with reduced number of waveguides

We now directly compare the performance of 192 and 480 waveguide OPAs with linearly varying and fully random pitch. We select these two configurations to show the performance where cross-coupling stops being a critical issue (480 waveguides, average spacing 2.08 μm, minimum spacing 1.2 μm) and with much reduced number of waveguides compared to the uniform pitch with no grating lobes in visible space, which should allow much simpler contacts to the phase shifters and driving circuitry (192 waveguides, average spacing 5.2 μm, minimum pitch 2.5 μm). We show the comparison in Fig. 13.

For the 192 waveguide case, the PSO optimized array, compared to the linear change of pitch, can provide higher SMSR in whole visible space or much more uniform SMSR in the whole visible space (with somewhat lower SMSR very close to broadside) depending on the optimization angle for waveguide placement as addressed in Section 3.2. At the same time, it has a narrower main lobe (0.11° vs. 0.14°) leading to larger number of resolvable spots, but as a downside has lower power in the main lobe. The power is lower due to much higher quality of the beam as shown in Fig. 14.

We also plot the far-field patterns in full visible region for 192 waveguide configuration in Fig. 15, showing comparison between PSO optimized, linear and cubic waveguide placement at broadside and when steered to 65°. This far-field pattern can directly be compared with the far-field pattern of a uniform array with identical number of waveguides shown in Fig. 2(d). In all cases the minimum pitch is 2.5 μm.

The differences between the two approaches are much smaller for the case of 480 waveguides, with the exception of the PSO optimized for broadside, which has higher SMSR at broadside, but much worse SMSR when steered. The linearly changed pitch once again has higher power in main lobe with somewhat wider main lobe (0.13° vs. 0.11°), but with significantly improved quality of the main beam compared to 192 waveguide case.

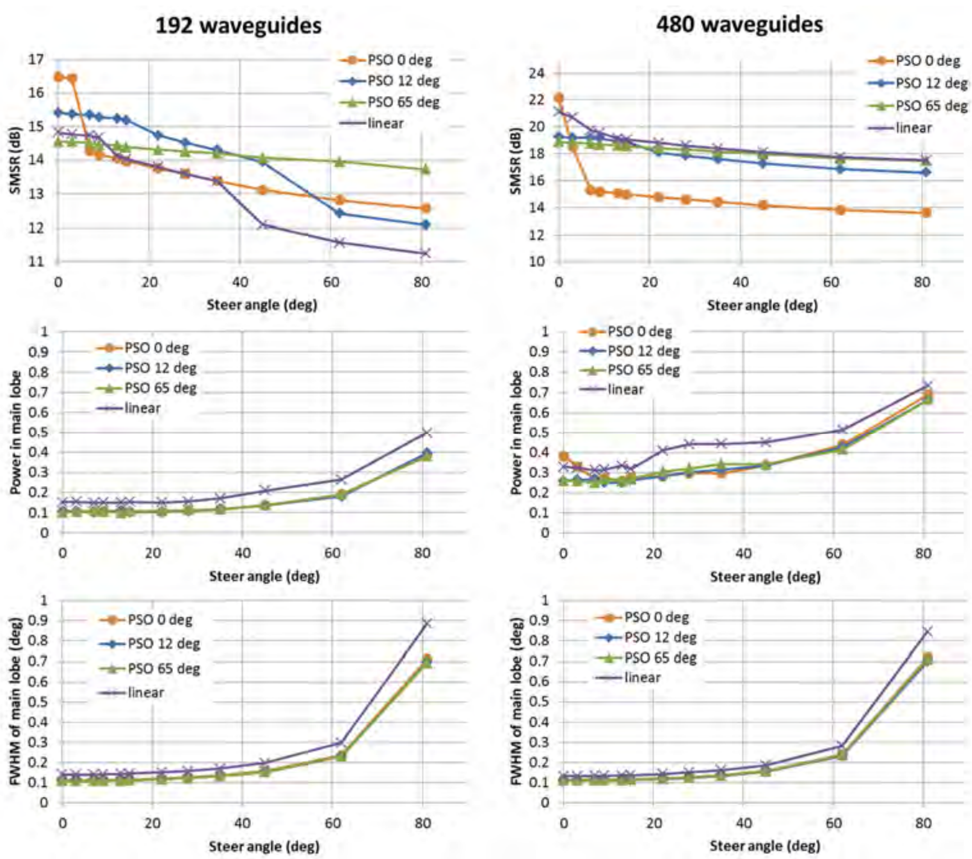

Fig. 13. Direct comparison in beam steering performance of 192 and 480 waveguide OPAs with randomized and linearly changing waveguide spacing. The minimum pitch is 2.5 µm and 1.2 µm for 192 and 480 waveguide case respectively.

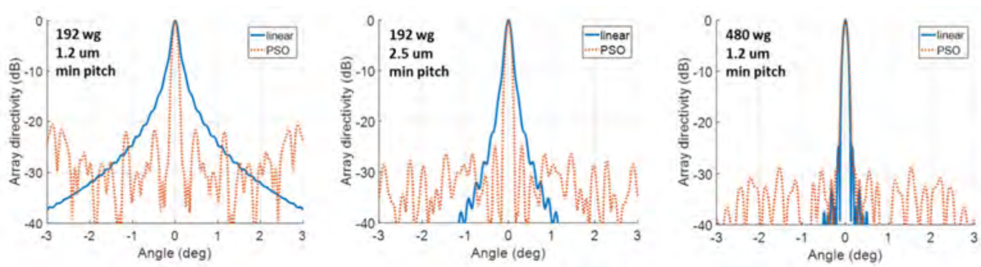

Fig. 14. Quality of the main beam for linearly changing and PSO optimized pitch for 192 waveguide configuration with two minimum pitch spacings (1.2 µm and 2.5 µm) and 480 waveguide configuration (1.2 µm minimum pitch). At lower waveguide counts, the linearly changing pitch sacrifices the quality of the main beam to suppress the sidelobes. The wider main lobe leads to higher ratio of power in the main lobe. At larger waveguide counts, the main beams are almost identical in shape.

Finally, we study the influence of the operating wavelength to the phase steering performance of the OPA. We take the optimized 192 waveguide (PSO) and 480 waveguide (linear chirp) configurations and calculate SMSR in wide wavelength range of 300 nm around 1550 nm, which corresponds to approximately 45° of steering in the wavelength direction. Even in such a large wavelength range, the performance of the OPA is largely insensitive to wavelength with <1.5 dB variation for 192 waveguide case and <4 dB variation for 480 waveguide case (Fig. 16).

As a conclusion, at lower waveguide counts, the PSO optimized spacing is preferred, while at medium waveguide counts, both the PSO optimized and linearly changing pitch offer similar performance levels.

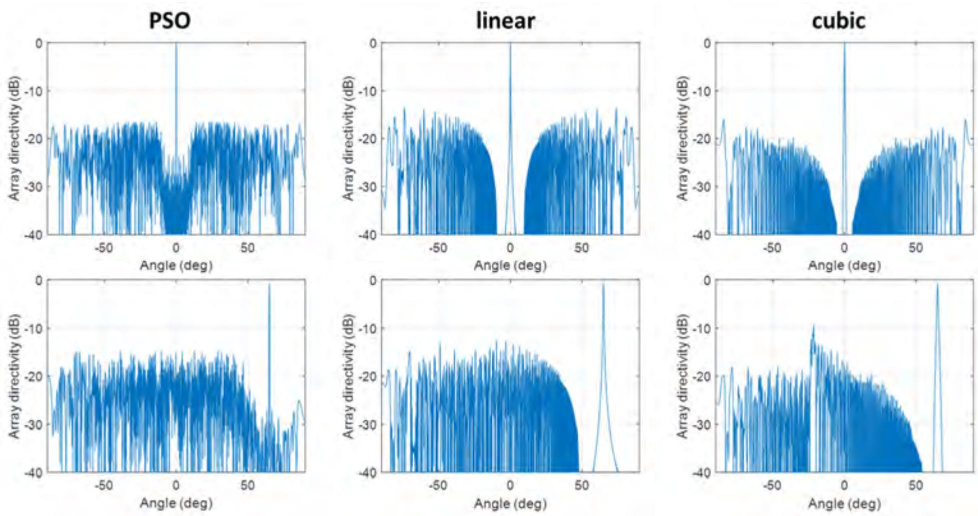

Fig. 15. Illustrative far-field patterns for an array with 192 elements when pointing at broadside (top row) or when steered to 65° (bottom row) for PSO optimized, linear and cubic waveguide placement strategies. In all cases grating lobes are significantly suppressed compared to the uniform array shown in Fig. 2(d).

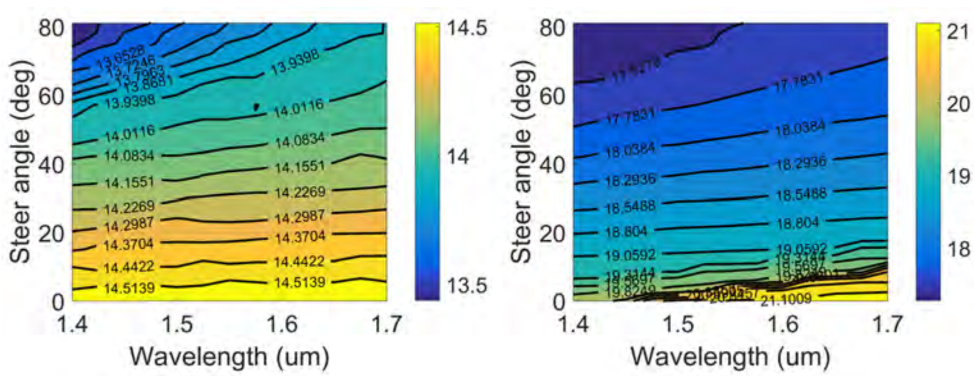

Fig. 16. SMSR as the OPA is steered in both directions using wavelength and phase tuning. (left) 192 waveguides, PSO optimized, 2.5 µm minimum pitch, optimized at 65° (right) 480 waveguides, linearly changing pitch, 1.2 µm minimum pitch

4.1 Scaling to larger areas

Due to the number of elements and the size of the chips considered, it is reasonable to assume that for even larger arrays in cm scale, smaller cells (e.g. 1 mm as considered here) and tiling could be used. This approach is also known as “sub-phased arrays”. Tiling allows for prescreening of individual cells and potentially higher yields of large OPAs. One could envision a number of different cell elements that are optimized to work as a larger array, but that introduces some restrictions and complicates the process. Ideally there would be one basic cell that can then be tiled as needed. Here we study the performance of linearly changing pitch and PSO optimized pitch cells when tiled. We take the 192 waveguide array with 2.5 μm minimum pitch as shown in Section 4 as a unit cell and then stitch them together to increase the size of the emitter area to 5 and 10 mm. We show results in Fig. 17, where we compare them to a larger single cell OPA (10 mm in size, 1920 waveguides, 2.5 μm pitch). Stitched PSO optimized OPAs have the same beam width and power in the main lobe as single cell larger OPAs, but have lower SMSR as waveguide positions are not optimized optimally to suppress grating lobes in all directions. In case of the linear arrays, stitched ones have narrower main lobe resulting with somewhat lower power in the main beam and also have lower SMSR as grating lobes are not suppressed to the extent they are with larger single cell OPAs. As a conclusion, preliminary stitching studies show that larger unit cells can provide improved SMSR compared to smaller ones. In other words, there is a penalty associated with using identical smaller cells when building larger OPA by tiling in terms of SMSR, but depending on the yield, that might be a reasonable tradeoff as power in main lobe and beamwidth are largely unaffected. An alternative approach for increasing the yield of large devices was studied in [29].

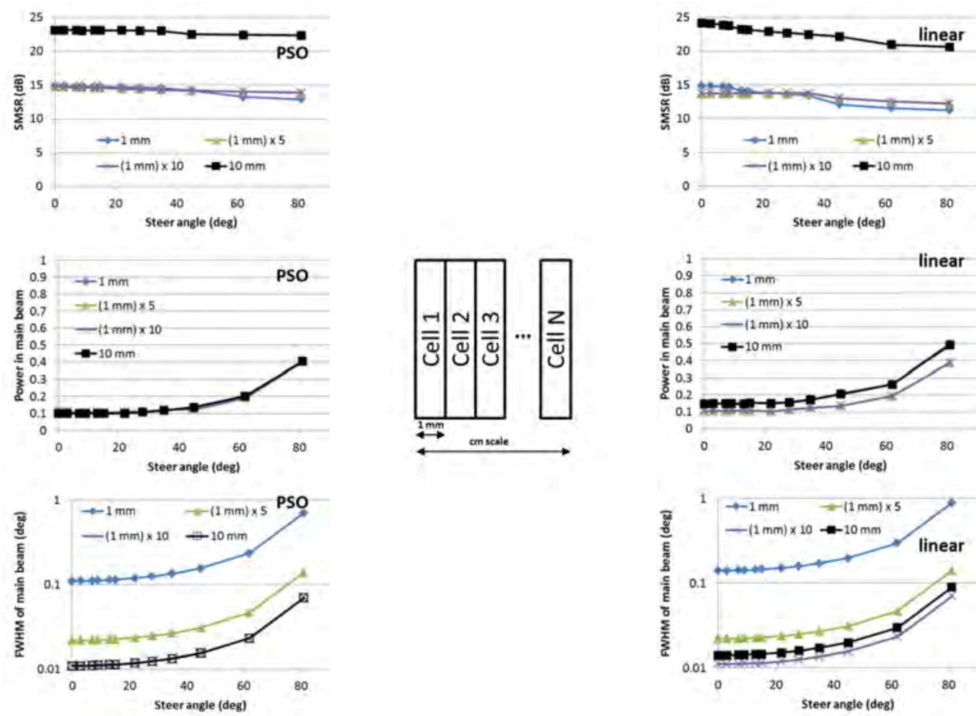

Fig. 17. Performance of stitched 1 mm unit cells with 192 waveguides and 2.5 μm minimum pitch compared to large 10 mm single cell array. (left column) PSO optimized cell (right column) cell with linear change of pitch (middle) inset showing the stitching strategy.

5. Conclusions

We analyze sparse aperiodic arrays for optical phase steering and LIDAR applications and show that, e.g. 192 element array can provide grating lobe free steering in whole visible space (± 90°) with decent > 13.5 dB SMSR using > 3 λ average spacing between elements. This allows for more than six times reduction in number of elements compared to uniformly spaced array, reducing the cost, complexity and improving the yield while keeping the same beam width and same number of resolvable spots in the far-field. Furthermore, the minimum pitch can be larger than > 1.5 λ, removing the cross-coupling issues completely, provided that the optical phased array is realized in a high-index contrast waveguide platform (such as Si/SiO_2).

We show that for best performance, a global search optimization and a fully-random strategy should be utilized, at least at low waveguide densities (> 3 λ average spacing). Furthermore, we demonstrate that for more uniform steer performance, it is beneficial to optimize the array placement at an angle initially.

For medium waveguide densities (~1.5 λ average spacing) ordered non-uniform waveguide spacing can be used due to simplicity and similar performance to the PSO optimized one. In that case, for a wide field of view, a linear change in spacing between the elements seems to be optimal.

Finally, we show ways to improve array performance if a reduced field of view is acceptable and consider stitching multiple smaller cells for scaling to larger emitter areas in order to improve yield.

6. Funding

DARPA MTO (MOABB HR0011-16-C-0106).

Acknowledgments

The authors thank S. J. Ben Yoo from University of California, Davis, and Paul Suni and James R. Colosimo from Lockheed Martin for useful discussions. This research was developed with funding from the Defense Advanced Research Projects Agency (DARPA). The views, opinions and/or findings expressed are those of the author and should not be interpreted as representing the official views or policies of the Department of Defense or the U.S. Government.

II. Low-power Lasers

Coupled-Cavity Lasers for a Low-Power Integrated Coherent Optical Receiver

Shamsul Arafin[1], Gordon Morrison[2], Milan Mashanovitch[2], Leif A. Johansson[2], and Larry A. Coldren[1]
[1]*Department of Electrical and Computer Engineering, University of California, Santa Barbara, CA, 93106, USA.*
[2]*Freedom Photonics LLC, Santa Barbara, CA, 93117, USA*
sarafin@ece.ucsb.edu

Abstract: Compact, tunable, low-power consumption coupled-cavity lasers are designed and experimentally demonstrated. Single-mode operation with an SMSR >24 dB and >11 nm tuning range are achieved, being suitable as on-chip local oscillators in low-power integrated optical coherent receivers.
OCIS codes: (140.3600) Lasers, tunable; (130.3120) Integrated optics devices.

In InP-based integrated coherent optical receivers, tunable lasers are one of the major components which consume most of the electrical power. In order to reduce the power consumption in the PICs, it is currently of significant interest to explore advanced designs of low-power, widely-tunable lasers. Among such designs, Y-branch [1] and simple co-linear coupled-cavity (C-C) lasers were found to be possible ways by which the present and future power requirements might be accommodated. Coupled-cavity design using grating bursts as intercavity coupling elements is proposed here. Although the operating principle as well as some analysis of this kind of laser was reported in the 1980's [2-3], the recent work has been more focused on the low-power consumption and wide tuning-range specifications. Furthermore, due to their potentially short cavities, high fill-factors for the gain regions, and compatibility with PIC fabrication processes, the C-C designs could be more efficient, compared to matured- and low-risk widely tunable lasers, e.g. sampled-grating distributed Bragg reflector (SG-DBR).

A theoretical study of C-C lasers was performed. Figure 1(a) shows an example schematic view of a multi-section C-C laser using an active-passive scheme. It consists of two cavities, denoted as cavity-1 and cavity-2, and each can have active and passive regions isolated by proton implants. In this case, cavity-1 is formed by independent and electrically-isolated active and passive sections whose geometrical lengths are 90 µm and 40 µm, respectively. Similarly, cavity-2 consists of an independent 150-µm-long active section.

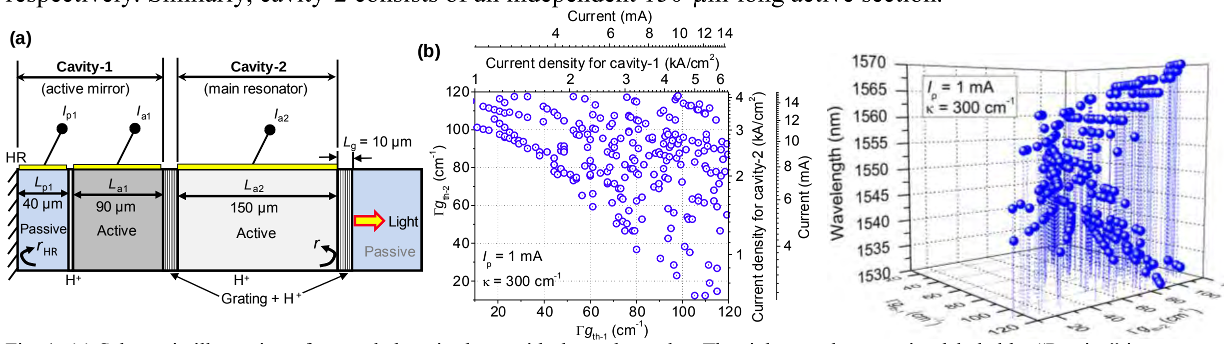

Fig. 1: (a) Schematic illustration of a coupled-cavity laser with three electrodes. The rightmost-long section labeled by "Passive" is not a part of the resonator, (b) 2D plot for modal threshold gain, Γg_{th-1} vs Γg_{th-2} and corresponding current densities for the lasing modes, where phase current is fixed, and (c) 3D trajectories, showing modal threshold gain, Γg_{th-1} vs Γg_{th-2} and corresponding resonant wavelengths as a third dimension. The intra-cavity grating mirror coupling constant, κ was fixed at a relatively weak value of 300 cm^{-1}.

Although the C-C system lases as one resonator, one can gain some intuitive understanding of its operation by thinking of it as two Fabry- Pérot cavities, each with their own mode spacings that interfere to reinforce one mode of the coupled system, as in a Moorea pattern or a Vernier scale. In this example, the mode spacing for cavity-1 and cavity-2 is calculated to be 2.4 nm and 2.1 nm, respectively, resulting a spacing mismatch of 0.3 nm and a possible repeat mode every 16.8 nm. The phase tuning sections enable the modes to be tuned continuously.

The interference or the coupling between cavity-1 and cavity-2 is mainly determined by the reflectivities of the mirrors present in the resonator. In this case, strong reflection ($r_{HR} \approx 0.95$) from the HR coating at the left side and weak reflections ($r_{grating} \approx 0.3$) from each of the gratings in the resonator influences the coupling between these two cavitites. The grating reflection is relatively weak using present design rules (κ = 300 cm^{-1}) and a length (10 µm) that will enable a reasonable tuning range of ~30 nm. The phase section may be longer than necessary to get the needed net π-phase shift. Configurations with shorter phase sections as well as different cavity lengths are being investigated.

The modal threshold gain and the lasing wavelength can be calculated by observing the net transfer function, S_{21}, across the entire device from the HR mirror to the right-most grating. In a numerical calculation, the transmission spectrum of S_{21} for the coupled system will develop a strong maximum at some wavelength, as the gain is increased through electrical pumping. The gain values required for this maximum to reach some large value and its wavelength are the desired threshold values. In other words, the poles of S_{21} for the entire system provide the pair of modal threshold gains for the cavities and the resonant wavelength values $\lambda_{resonant}$. The phase currents are dithered to optimize the modal selectivity with a reasonably good side-mode suppression-ratio (SMSR).

Figure 1(b) gives threshold modal gain pair solutions for wavelengths ranging from 1535 nm to 1575 nm. A 2D plot of the threshold modal gain of cavity-1, Γg_{th-1}, versus the threshold modal gain of cavity-2, Γg_{th-2}, together with the corresponding current and current densities required to reach threshold assuming a fixed phase current in the passive section is shown here. The data is obtained by fixing Γg_{th-1} and solving for Γg_{th-2} and $\lambda_{resonant}$ for each given Γg_{th-1} over a prescribed range of wavelengths. Then, Γg_{th-1} is increased and the process repeated. It should be noted that Γg_{th-1} is determined by the applied current into the gain section of cavity-1, where the confinement factor is Γ= 0.1. Gain parameters are obtained from [4]. 3D trajectories is shown in Fig. 1(c), where wavelength is included as a third dimension, illustrating $\lambda_{resonant}$ that cover the entire range between 1535 nm and 1575 nm for the realistic condition, $\Gamma g_{th} < 120$ cm^{-1}. The missing wavelength values in Fig. 1(c) can be filled out by changing the phase current independently in phase sections of cavity-1 and cavity-2.

Lasers were fabricated in a PIC platform where an offset quantum well (OQW) integration technique was employed [5]. The multi-quantum well (MQW) region acts as the gain medium for the laser device as well as a semiconductor optical amplifier (SOA) that was integrated after the laser. A microscope picture of the fully-processed PIC with a C-C laser and SOA is shown in Fig. 2(a). For testing, devices were mounted on a ceramic carrier and wire bonded, as shown in Fig. 2(a).

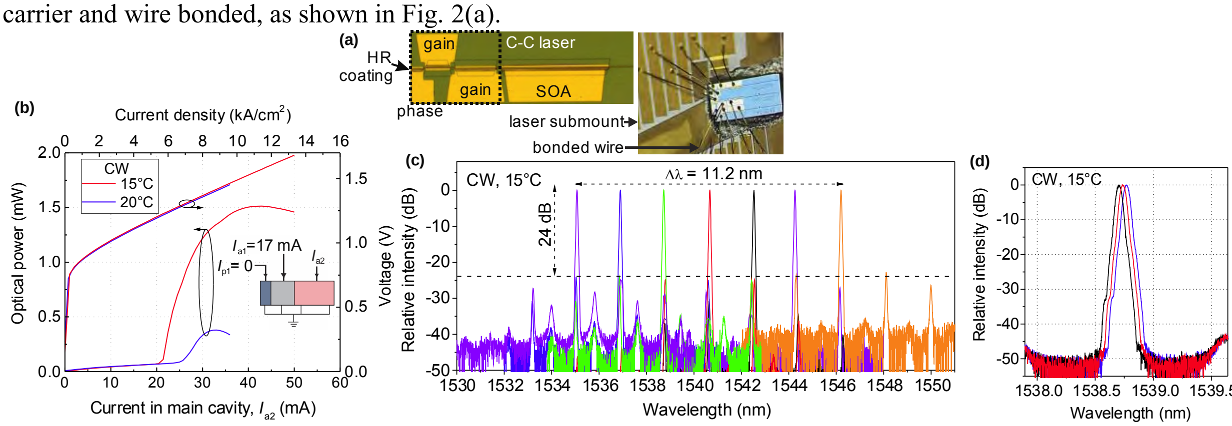

Fig. 2 (a) Microscope image of processed C-C laser with SOA=semiconductor optical amplifier, and microscope image of C-C laser chip mounted on the carrier and wirebonded, (b) measured light-current-voltage characteristics of C-C lasers as a function of temperature, (c) spectra of the laser by varying current in cavity-1 and cavity-2, and (d) fine tuning of the emission wavelength by changing current in the phase section.

Temperature dependent continuous-wave (CW) light-current-voltage (*L-I-V*) characteristics of devices were measured on a Peltier-cooled copper heatsink, as displayed in Fig. 2(b). The device shows CW operation up to room-temperature. Measurements were performed when the current in cavity-1 is fixed to 17 mA and no current in the phase section is applied. On-chip SOA, reverse biased by 2 V, was used as a photodetector with an assumed responsivity of 1 A/W to measure the optical power coming out from the device.

The emission spectra of the C-C device are shown in Fig. 2(c), which was obtained by varying the current in cavity-1 and cavity-2 and keeping the current in the phase section constant. The single-frequency wavelength tuning range of such devices is measured to be 11.2 nm. The device exhibits single-mode operation over this entire operating range with an SMSR >24 dB. Use of higher κ-gratings [6] should enable improved SMSR as well as wider tuning ranges and lower threshold currents. The fine tuning of the emission wavelength (Fig. 2(d)) was measured by varying the phase-section current at a constant current in both cavities, yielding mode-hop-free tuning range of ~0.07 nm. In addition to these static properties of such C-C devices, the potential of such devices in coherent receiver PICs will also be reported at the conference.

[1] J.-O. Wesström, et al., "State of the art performance of widely tunable modulated grating Y-branch lasers," in Proc. OFC, paper TuE2 (2004).
[2] L. B. Allen, H. G. Koenig., and R. R. Rice, "Single Frequency Injection Laser Diodes for Integrated Optics and Fiber Optics Applications", Proc. Soc. Photo. Opt. Eng. **157**, 110-117 (1978).
[3] L. A. Coldren, and T. L. Koch, "Analysis and design of coupled-cavity lasers - Part I: Threshold gain analysis and design guidelines", IEEE J. Quantum Electron. **20**, 659 – 670 (1984).
[4] L. A. Coldren, S. W. Corzine, and M. L. Mashanovich, *Diode Lasers and Photonic Integrated Circuits* (Wiley, New York, 2012), Chap. 4.
[5] J.W. Raring, et al., "Advanced integration schemes for high-functionality/high-performance photonic integrated circuits", Proc. SPIE **6126**, 61260H (2006).
[6] C.H. Chen, et al., "Compact Beam Splitters with Deep Gratings for Miniature Photonic Integrated Circuits: Design and Implementation Aspects", Appl. Opt. **48**, F68-F75 (2009).

Compact Low-Power Consumption Single-Mode Coupled Cavity Lasers

Shamsul Arafin, *Senior Member, IEEE*, Gordon B. Morrison, Milan L. Mashanovitch, *Senior Member, IEEE*, Leif A. Johansson, *Member, IEEE*, and Larry A. Coldren, *Life Fellow, IEEE*

***Abstract*—Ultra-compact, widely-tunable and low-power InP-based four-section coupled-cavity lasers are designed and analyzed. Two Fabry–Pérot cavities of unequal lengths, each containing an amplifier and a phase-tuning section, are coupled together through low-loss Bragg grating. The theoretical analysis of such multisection lasers starts with calculating the poles of a linear transfer function of the entire resonator in order to obtain resonant wavelengths and wavelength-dependent threshold gains. The differential quantum efficiency and the power-current characteristics are then calculated to evaluate the laser performance. The effectiveness of the design procedure is verified by the experimental and proof-of-principle demonstration using simplified three-section lasers. Devices exhibit single-mode operation with a side-mode suppression ratio of over 24 dB and tuning range of 11.2 nm. These telecom-suitable lasers can be used as on-chip local oscillators in low-power integrated optical coherent receivers.**

***Index Terms*—Coupled-cavity, Fabry-Pérot resonators photonic integrated circuits, integrated optoelectronics, tunable lasers.**

I. Introduction

TUNABLE lasers and high-speed photodiodes in coherent photonic integrated circuit (PIC) receivers have always been of great interests for plenty of applications including optical communication [1], microwave photonics [2], sensing [2] and chip-scale frequency synthesis [4]. Given the tunable lasers consume most space and power in PIC receivers, a novel design for low-threshold, high-performance and short-cavity single-mode lasers with a wide tuning range is of utmost importance. Among several types of surface grating-based tunable lasers, sampled-grating distributed Bragg reflector (SG-DBR) [5], Y-branch [6], double-ring resonator [7], ring resonator mirror lasers [8] and grating-coupled sample reflector lasers [9] are some of the commonly used and commercially available ones. These devices, however, are relatively large and consume much electrical power. Considering the class of widely tunable devices based on Vernier effect, for instance, the most compact in-line SG-DBR lasers are 1.5 mm long [10] and consume ∼0.4 W of power [11].

Compared to ring and coupler-based tunable lasers, in-line design is better because it can (i) provide minimal net cavity size by not having rings and couplers, (ii) give high axial fill factor since the device is free from non-tunable passive sections, and (iii) offer the widest mode spacing for a given gain length. Besides, lasers with the ring and passive couplers suffer from additional insertion loss and low mode-suppression ratio due to narrow mode spacing defined by the increased cavity length. Despite these obvious advantages obtained from in-line SG-DBR lasers, their sizes and power requirements are drawbacks for the development of compact and low-power photonic systems.

In the 1980s, a new and novel concept was proposed for simple and in-line lasers with single-mode emission, which are mainly based on coupling two Fabry-Pérot cavities [12]–[15]. Utilizing the same concept, the so-called coupled-cavity (C-C) lasers can be reconsidered to be one of the alternative ways in order to meet up the present and future size and power requirements. Recently, there have been a number of theoretical and experimental studies on C-C lasers reported by the scientific community [16], [17]. Some of the experimental studies report on the use of multimode interference reflector as a coupling element between two cavities [18]–[20]. With an epitaxial-regrowth-free cost-effective approach, devices made by this design had a footprint of 0.5 mm^2 and a power consumption of ∼0.2 W [18].

This work reports an active-passive integrated coupled-cavity design procedure where grating bursts as intercavity coupling elements are used. This study is more focused on the compactness, low-power consumption and wide tuning-range specifications of such devices. Compared to the state-off-the-art results on SG-DBR lasers reported in [10], [11] our proposed C-C laser is 5 times smaller in size, and it consumes 7 times less electrical power for its full operation with the optical output power of 5 mW. Due to potentially short cavities, high fill-factors for the gain regions, and compatibility with simple PIC fabrication processes, the C-C design is more efficient, compared to matured- and low-risk SG-DBR lasers. Therefore, these devices are well-suited for developing next-generation compact, low-power and efficient photonic systems.

This paper is organized as follows: This paper begins with a discussion of the C-C laser design which describes the

Manuscript received February 1, 2017; revised March 26, 2017; accepted May 2, 2017. Date of publication May 10, 2017; date of current version July 19, 2017. This work was supported in part by DARPA-MTO under the DODOS project and in part by the National Science Foundation (NSF) under Grant 1402935. A portion of this work was carried out at the University of California, Santa Barbara Nanofabrication facility, part of the NSF funded NNIN network. *(Corresponding author: Shamsul Arafin.)*

S. Arafin and L. A. Coldren are with the Department of Electrical and Computer Engineering, University of California, Santa Barbara, CA 93106 USA (e-mail: sarafin@ece.ucsb.edu; coldren@ece.ucsb.edu).

G. B. Morrison, M. L. Mashanovitch, and L. A. Johansson are with the Freedom Photonics LLC, Santa Barbara, CA 93117 USA (e-mail: gordon@freedomphotonics.com; mashan@freedomphotonics.com; leif@freedomphotonics.com).

Color versions of one or more of the figures in this paper are available online at http://ieeexplore.ieee.org.

Digital Object Identifier 10.1109/JSTQE.2017.2703161

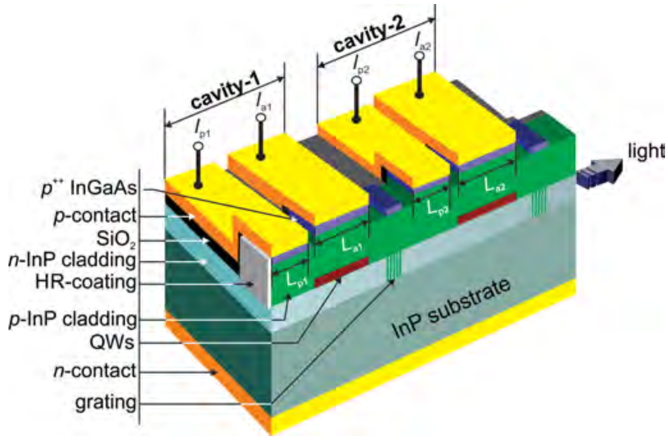

Fig. 1. Schematic cross-sectional view of a C-C laser with four electrodes. L_{p1} and L_{a1} are the passive and active sections lengths of cavity-1, whereas L_{p2} and L_{a2} passive and active sections lengths of cavity-2. The currents I_a and I_p are injected in the active and passive sections of FP cavities, respectively.

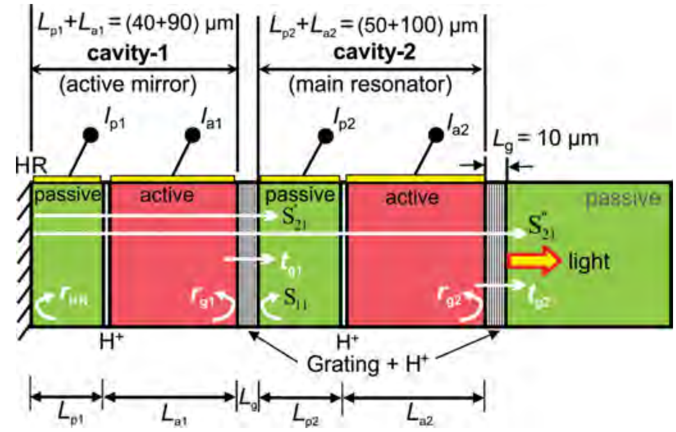

Fig. 2. Simplified schematic illustration of a coupled-cavity laser. The rightmost-long section labelled by "Passive" is not the part of the resonator.

calculation of scattering matrices and how it leads us to find the threshold gains and wavelengths of the modes of the entire coupled system. This section also provides results obtained from the simulation of the differential quantum efficiency, yielding power-current characteristics, and wavelength tuning behavior of the laser. This is then followed by a discussion of the performance improvement concept, power budget estimation and tuning range extension of the device. We then present the processing details of the simplified C-C laser. Finally, the performance characterization of initial experimental devices is reported.

II. Coupled-Cavity Laser Design

Fig. 1 shows a schematic cross-sectional view of a four-section C-C laser which is comprised of two cavities, denoted as cavity-1 and cavity-2. They are in-line coupled via first-order surface grating bursts. Each cavity includes active and passive regions that are electrically isolated by proton implants. Cavity-1 can be referred to as an "active mirror", while cavity-2 as a "main resonator", providing most of the gain. The mode selected by the C-C lasers is nothing but a longitudinal FP mode that has the lowest cavity loss determined by the Vernier effect, resulting from unequal cavity lengths of these two FP cavities. Since the basic operating principle and the mechanism of the mode selectivity in such lasers are well-described in a number of literatures [12], [14] we will immediately move into the theoretical analysis of our proposed compact and low-power single-mode C-C lasers with a unique configuration.

A. Calculation of Scattering Matrices

A theoretical analysis of the C-C lasers requires simultaneous consideration of the gain and loss in the two FP cavities after taking the reflection and transmission at the intercavity coupling interface into account. Scattering matrices were used to perform the numerical analysis of such complex laser structures. The primary objective is to find the resonant longitudinal modes of the coupled system by calculating the corresponding emission wavelengths and their respective gains required to reach threshold. Fig. 2 illustrates a simplified schematic of a representative C-C laser which helps to perform the numerical analysis. In this example, cavity-1 is formed by independent and electrically-isolated 90-μm-long active and 40-μm-long passive sections. The gain of the active section and the phase of the passive section can be independently controlled by currents, denoted by I_a and I_p, respectively. Similarly, cavity-2 consists of independent 100-μm-long active and 50-μm-long passive sections, whose lengths are represented by L_{a2} and L_{p2}. The mode spacings for cavity-1 and cavity-2 are calculated to be 2.4 nm and 2.1 nm, respectively, resulting a spacing mismatch of 0.3 nm and a possible repeat mode every 16.8 nm. The phase tuning sections enable the modes to be tuned continuously.

Prior to obtaining the resonant longitudinal modes of the entire coupled system, it is important to understand how cavity-1 serves as an active mirror modulating the loss of the FP modes via an equivalent mirror. The gain-providing mirror (i.e. cavity-1) can be represented by an effective mirror with complex reflectivity S_{11} which can be written in the form [21]

$$S_{11} = -r_{g1} + \frac{r_{\mathrm{HR}} t_{g1}^2 e^{-2j\tilde{\beta}L_1}}{1 - r_{\mathrm{HR}} r_{g1} e^{-2j\tilde{\beta}L_1}} \tag{1}$$

where r_{g1} and r_{HR} are amplitude reflection coefficients of the grating and the high-reflection mirror coating, respectively, t_{g1} transmission coefficient across the grating interface at cavity-1, $\tilde{\beta}$ complex propagation constant and L_1 the total length of active and passive sections in cavity-1. $\tilde{\beta}$ is defined as

$$\begin{aligned}\tilde{\beta} &= \beta + j\beta_i \\ &= \frac{2\pi\bar{n}}{\lambda} + j\left(\frac{g}{2} - \frac{\alpha_i}{2}\right)\end{aligned} \tag{2}$$

where β is the average propagation constant, $\bar{n}$ the effective refractive index of the mode, g the modal gain and α_i the internal modal loss.

The net reflection coefficient from the grating can be defined by the following approximate sinc-function spectral response:

$$r_{g1} \approx \kappa L_g * \mathrm{sinc}\left(\frac{2\pi L_g \bar{n}}{\lambda} - \frac{2\pi L_g \bar{n}}{1.55}\right) \tag{3}$$

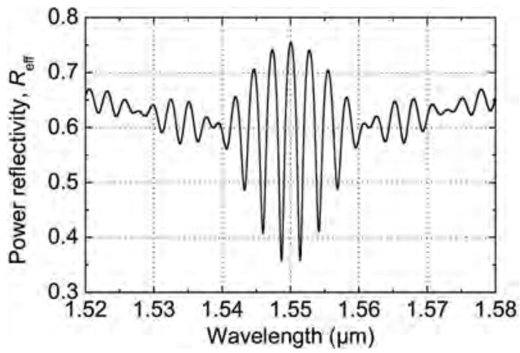

Fig. 3. The effective mirror reflectivity for cavity-2 due to cavity-1, when current applied to cavity-1 and its phase tuning section is 1 mA.

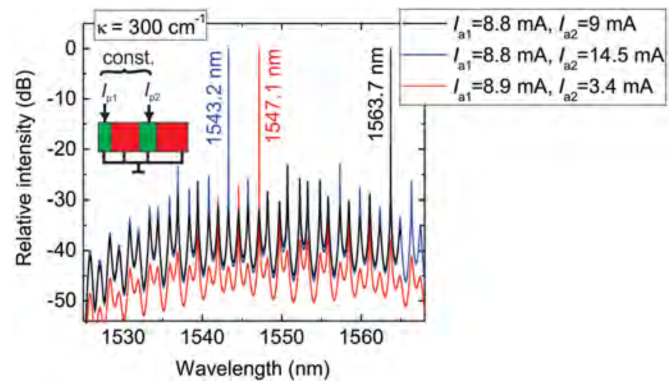

Fig. 4. Example plots of $\mathrm{S}''_{21}(\lambda)$ to obtain "thresholds" for three mode solutions where the phase currents in both cavities are constant.

where L_g is the grating length, κ the reflection per unit length. The grating reflection is relatively weak with $\kappa = 300\,\mathrm{cm}^{-1}$ and $L_g = 10\,\mu$m, but a tuning range of ~30 nm is still possible. The net reflection peak is assumed to be at Bragg wavelength, i.e. 1.55 μm. Note that the reference planes for the gratings are placed at an index down step on their left side in Fig. 2, and they have an integer number of periods. Thus, the reference planes on their right sides are displaced by a half-grating period from the last index down step on that side. Although arbitrary, this selection results in the correct phasing of the two terms in S_{11} shown in (1).

The transmission magnitude through the grating mirror becomes

$$t_{g1} = \sqrt{\left(1 - r_{g1}^2\right) e^{-\alpha_g * L_g}} \tag{4}$$

And its transmission phase is given by its length. For simplicity, the gain function is often approximated by a simple Lorentzian lineshape with a peak at 1550 nm [21],

$$\mathrm{L}(\lambda) = \left(\frac{7 \times 10^{-3}}{4(\lambda - 1.55)^2 + 7 \times 10^{-3}}\right) \tag{5}$$

Experimental material gain g with a number of quantum wells N_{QW} as a function of injected current density J for 1.55 μm lasers is well represented by the g-J relationship

$$g = 583 \times \ln\left(\frac{\eta_i J}{N_{\mathrm{QW}} 81}\right) \mathrm{cm}^{-1} \tag{6}$$

where η_i the current injection efficiency which can be assumed to be 0.8 for initial simulations [21].

Finally, using (2)–(6) in (1) and by applying 1 mA current in both active and passive section of cavity-1, the modulated effective mirror reflectivity $|r_{\mathrm{eff}}|^2$, i.e., what cavity-2 sees due to cavity-1 is plotted as a function of λ in Fig. 3.

Given this basic understanding, we now move on to obtain the threshold gain and resonant wavelengths of the lasing modes. This can be done by finding the net transfer function $\mathrm{S}''_{21}(\lambda)$ of the entire system. The poles of this transmission spectrum indicate the resonant wavelengths of the laser for the particular sets of modal gain values $(\Gamma g_{\mathrm{th}-1}, \Gamma g_{\mathrm{th}-2})$, required to develop a strong maximum of $|\mathrm{S}''_{21}(\lambda)|$ as the gain is increased through electrical pumping. Note that Γ, the transverse-lateral confinement factor, is assumed to be 0.1 in the analysis. This technique is used to determine the pairs of threshold gains of the two active sections for the possible lasing modes.

In order to obtain $\mathrm{S}''_{21}(\lambda)$, we need to find the transmission spectrum $\mathrm{S}'_{21}(\lambda)$ through first grating in cavity-1.

$$\mathrm{S}'_{21}(\lambda) = \frac{t_{\mathrm{HR}} t_{g1} e^{-j\tilde{\beta} L_1}}{1 - r_{\mathrm{HR}} r_{g1} e^{-2j\tilde{\beta} L_1}} \tag{7}$$

Finally, the net transfer function across the entire device from the HR mirror to the right-most grating

$$\mathrm{S}''_{21}(\lambda) = \frac{\mathrm{S}'_{21} t_{g2} e^{-j\tilde{\beta} L_2}}{1 - r_{g2} \mathrm{S}_{11} e^{-2j\tilde{\beta} L_2}} \tag{8}$$

where r_{g2} is the reflection coefficient of the output grating mirror and L_2 the total length of active and passive sections in cavity-2.

Using (1)–(7) in (8), we get a fairly complex equation. By solving it, the poles of $\mathrm{S}''_{21}(\lambda)$ for the mode solutions are obtained, as shown in Fig. 4 for three example cases. The currents in active sections of cavity-1 and cavity-2 are varied, while the currents in phase sections of both cavities are kept constant, to obtain these solutions. As can be seen, a small change in I_{a1} may require a significantly different value of I_{a2}, and this causes a relevant change in the lasing mode wavelength. Dithering the phase currents will help to optimize the modal selectivity even better than the plots in Fig. 4.

Fig. 5(a) gives threshold modal gain pair solutions for wavelengths ranging from 1532 nm to 1568 nm for the device presented in Fig. 2. A 2D plot of the threshold modal gain of cavity-1, $\Gamma g_{\mathrm{th}-1}$, versus the threshold modal gain of cavity-2, $\Gamma g_{\mathrm{th}-2}$ is shown here. The corresponding current and current densities required in each gain section to reach threshold with a fixed phase current in both passive sections is also shown here. The data is obtained by fixing $\Gamma g_{\mathrm{th}-1}$ and solving for $\Gamma g_{\mathrm{th}2}$ and λ for each given $\Gamma g_{\mathrm{th}-1}$ over a prescribed range of wavelengths. $\Gamma g_{\mathrm{th}-1}$ is then increased and the process is repeated. The mode wavelengths and the corresponding threshold gains shown in the upper right corner of Fig. 5(a) are not desirable from a practical point of view, since those wavelengths can be obtained with lower threshold currents, if currents in the two passive sections are tweaked properly.

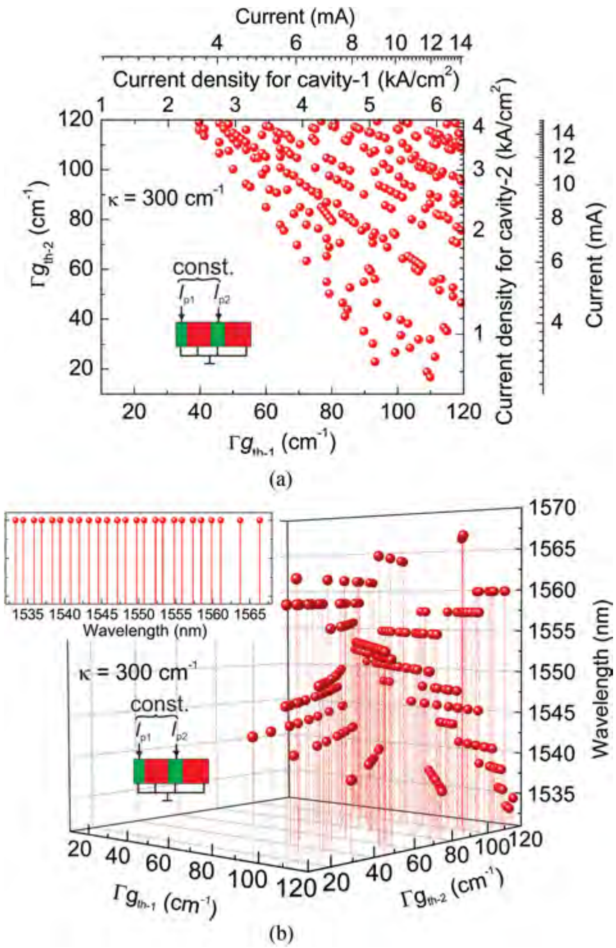

Fig. 5. (a) 2D plot for modal threshold gain, $\Gamma g_{\rm th-1}$ vs $\Gamma g_{\rm th-2}$ and corresponding current densities for the lasing modes, where $\kappa = 300\ \mathrm{cm}^{-1}$ and constant phase current $= 1$ mA, and (b) the corresponding 3D trajectories, showing modal threshold gain, $\Gamma g_{\rm th-1}$ vs $\Gamma g_{\rm th-2}$ and corresponding resonant wavelengths as a third dimension.

Since Fig. 5(a) does not provide information about resonant wavelengths, it is convenient to plot 3D trajectories as shown in Fig. 5(b), where wavelength is included as a third dimension. The inset of Fig. 5(b) illustrates the wavelengths that cover the entire range between 1532 nm and 1568 nm for the realistic condition, $\Gamma g_{\rm th} \leq 120\ \mathrm{cm}^{-1}$.

B. Calculation of Differential Quantum Efficiency

With the threshold modal gain pair solutions for wavelengths ranging from 1532 nm to 1568 nm calculated, we can now determine the differential quantum efficiency η_d of the C-C laser. In such a way, the output characteristics of this complex resonator can also be determined. The differential efficiency can be simply defined as the cavity output modal loss relative to the total modal loss (which is the threshold modal gain), reduced by the injection efficiency. For simplicity, we assume that there is no excess scattering loss caused by the rightmost grating mirror or the leftmost high-reflection coated mirror, so that all output cavity loss is coupled into the output waveguides. Hence, for each wavelength and modal gain pair, η_d is given to a good

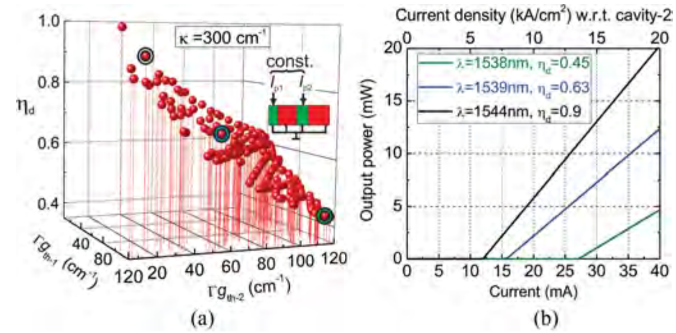

Fig. 6. Output characteristics of C-C lasers, (a) 3D trajectories, showing modal threshold gain, $\Gamma g_{\rm th-1}$ vs $\Gamma g_{\rm th-2}$ and corresponding differential quantum efficiency as a third dimension, and (b) power-current characteristics as a function of differential quantum efficiency. (w.r.t. = with respect to)

approximation by [21, Appendix 5]:

$$\eta_d = \eta_i \frac{\frac{1}{L}\ln\left(\frac{1}{r_{g2}\times r_{\rm HR}}\right)}{\frac{L_{a1}}{L}\Gamma g_{th,1} + \frac{L_{a2}}{L}\Gamma g_{th,2}} \tag{9}$$

where L is the total cavity length including the phase tuning sections and the gratings. For our η_d calculations, η_i and $r_{\rm HR}$ are approximated as 0.8 and 1, respectively. Note that the denominator of (9) is the net cavity modal gain, i.e., the sum of the net modal gains of each cavity, including the axial confinement factors. This could have been more simply written as $[< g_{\rm th,1} > + < g_{\rm th,2} >]$, where the $< >$ denote a 3D averaging of the gain material in each cavity over the entire mode.

Fig. 6(a) displays the threshold modal gain pair solutions for differential efficiencies ranging from 0.45 to 0.9, by applying a fixed phase current in both passive sections of the device. These values represent wavelength solutions across the entire 36 nm tuning range of the laser using a coupling coefficient, $\kappa = 300\ \mathrm{cm}^{-1}$. Given the injection currents applied to each cavity in order to reach threshold, the corresponding resonant wavelengths and the differential efficiency are known, the output optical power-current (*P-I*) characteristics can be calculated from (9) to obtain the following expression,

$$P = \eta_d \frac{hc}{\lambda q}\left(I - (I_{\rm th,1} + I_{\rm th,2})\right) \tag{10}$$

where *h, c, q* are constants; and λ, $I_{\rm th-1}$, $I_{\rm th-2}$ are the values obtained from the solution, representing the resonant emission wavelength, and threshold currents for the cavities, respectively. Finally, *P-I* curves are plotted for three different solutions, differentiated by their resonant wavelength and differential efficiency, as shown in Fig. 6(b). Equations (9) and (10) require that there be some gain in both cavities so that power levels are not drastically different [21, Appendix 5].

C. Quasi-Continuous Tuning

The resonant wavelengths, covering the entire range between 1532 nm and 1568 nm for the realistic condition, $\Gamma g_{\rm th} \leq 120\ \mathrm{cm}^{-1}$ is shown in the inset of Fig. 5(b). It is of great importance to check whether missing wavelength values between adjacent cavity modes in Fig. 7 can be filled out

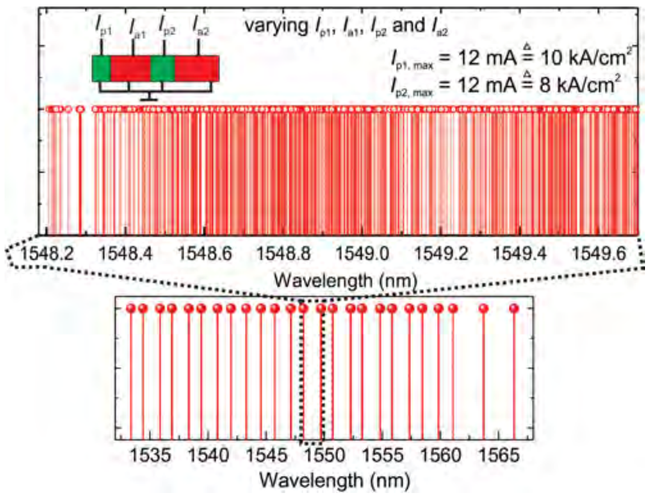

Fig. 7. The lasing modes covering the emission wavelength range between 1532 nm and 1568 nm by fixing the phase currents (bottom). Continuous tuning is possible between any two adjacent cavity-modes by varying the phase currents in both cavities (top).

electronically. To save computation space and time, only the region around 1550 nm, occupying two cavity modes, is simulated. It is found that any wavelength can be obtained by changing the phase current independently in phase sections of cavity-1 and cavity-2, as shown in Fig. 7. However, because of the mode-hoping behavior, the device is expected to exhibit quasi-continuous tuning.

D. Devices With Higher κ

The above theoretical results use a grating with $\kappa = 300\,\mathrm{cm}^{-1}$, which is the value utilized in standard and large-area SGDBR lasers [5]. In spite of showing great potential of C-C lasers, evidenced by the simulated results shown so far, the gratings used have very low-reflectivity mirrors, requiring relatively high threshold current densities for the device, sometimes >10 kA/cm^2. Such unrealistic current densities may prevent such devices even from lasing. Thus, it is of significant interest to consider higher coupling coefficient grating mirrors [22], in order to increase the reflectivity of 10-μm-long grating mirrors and reduce the threshold currents and power dissipations.

In order to confirm such improvements, numerical calculations were performed for the same resonator structure with a higher $\kappa = 600\,\mathrm{cm}^{-1}$ and 900 cm^{-1}. As can be seen in Fig. 8(a), the mode solutions have lower modal gain values, indicating that less current is required to reach threshold compared to the structure with $\kappa = 300\,\mathrm{cm}^{-1}$. The threshold current in a resonators especially with $\kappa = 900\,\mathrm{cm}^{-1}$ is drastically reduced, even as low as ~6 mA for $\eta_d = 0.61$. At the same time, the entire wavelength range between 1532 nm and 1568 nm is covered by these solutions with a more realistic condition, $\Gamma g_{\mathrm{th}} \leq 120\,\mathrm{cm}^{-1}$.

The improved performance is further confirmed through the *P-I* characteristics with different κ for a pair of η_d values, calculated by the threshold modal gain pair solutions. Note that for $\kappa = 900\,\mathrm{cm}^{-1}$, the optical output power as high as 5 mW at $\eta_d = 0.61$ can be achieved for the total injection current of only 15 mA in two active sections (see Fig. 8(b)).

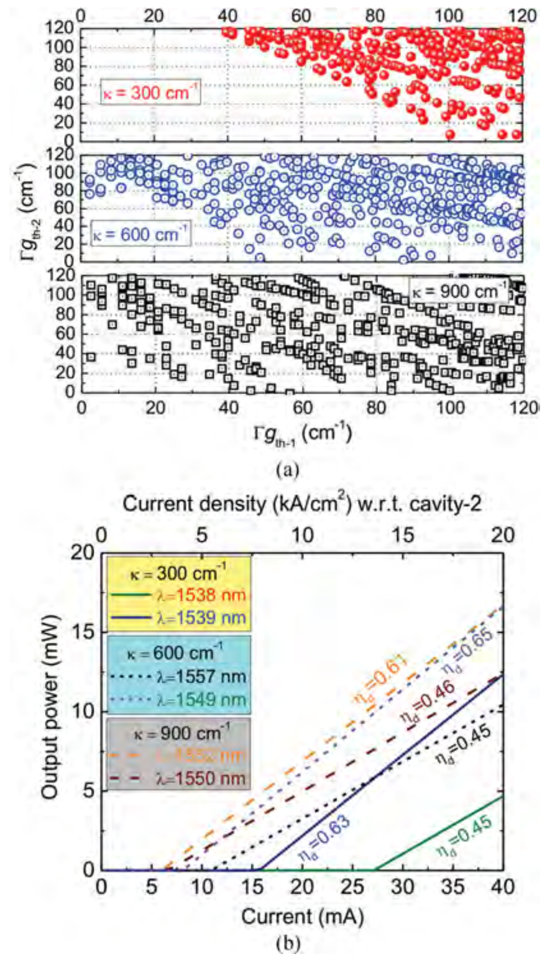

Fig. 8. (a) 2D plot for modal threshold gain, $\Gamma g_{\mathrm{th}-1}$ vs $\Gamma g_{\mathrm{th}-2}$ for lasers with different coupling coefficients. Lasers with the coupling coefficient as high as 900 cm^{-1} obviously require less modal gain to reach threshold, and (b) calculated power-current *(P-I)* characteristics as a function of differential quantum efficiency for grating mirrors of different κ for a grating length of 10 μm.

TABLE I
POWER CONSUMPTION ESTIMATE OF THE C-C LASERS WITH $\kappa = 900\,\mathrm{cm}^{-1}$ FOR 5 mW OUTPUT POWER

Section	Number	Current (mA)	Voltage (V)	Power (mW)
Gain	2	(6 + 10) = 16	1.2, 1.4	21.2
PT	2	(12 + 12) = 24	1.4	33.6
Total		40		**~55**

PT = phase tuner.

E. Power Budget Estimation

Table I presents the total maximum power consumption of the fully-operational C-C laser with $\kappa = 900\,\mathrm{cm}^{-1}$ and optical output power of 5 mW. There are two phase tuning sections integrated in the chip. It should be noted that it is possible to achieve full wavelength tuning using these two phase sections of the laser.

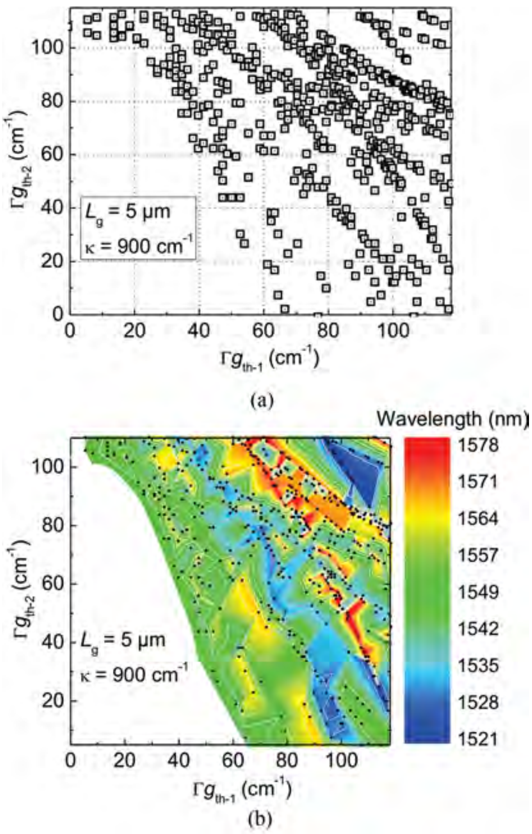

Fig. 9. (a) $\Gamma g_{\mathrm{th}-1}$ vs $\Gamma g_{\mathrm{th}-2}$ for lasers with a grating length of 5 μm and $\kappa = 900$ cm^{-1}, and (b) contour plot of the emission wavelength as a function of the modal gain. The emission wavelength range between 1521 nm and 1578 nm can be covered by the cavity modes where the phase current is fixed in each cavity.

F. Devices With Shorter Grating

Despite this reasonably good performance of C-C lasers with coupling coefficient $\kappa = 900\,\mathrm{cm}^{-1}$, further improvement is still required for the device with wide tuning range as high as 50 nm in order to cover the whole-C band. This is because the grating with a length of 10 μm unfortunately cannot provide such desired wide tuning range. It should be noted that all the simulation results of C-C lasers presented so far used $L_g = 10\,\mu$m. This clearly necessitates of doing the analysis of the device with a grating length as short as 5 μm.

Fig. 9 (a) displays the threshold modal gain pair solutions for $L_g = 5\,\mu$m, by applying a fixed phase current in both passive sections of the structure. Most importantly, this should be technologically achievable with only slight increase in cavity loss in the device. This is reflected by the mode solutions at a bit higher ($\Gamma g_{\mathrm{th}-1}$, $\Gamma g_{\mathrm{th}-2}$) values compared to the case $L_g = 10\,\mu$m. These values represent wavelength solutions across the entire >50 nm tuning range of the laser using a coupling coefficient, $\kappa = 900\,\mathrm{cm}^{-1}$, as presented by the contour plot in Fig. 9(b).

G. Deep Grating

One possible way of increasing the coupling coefficient of such grating mirrors is to use deeply-etched grating, as demonstrated by Chen *et al.* [22], where 50% power reflectivity was obtained experimentally for a grating of length 10 μm.

$$r_g = \tanh(\kappa L_g) \tag{11}$$

Thus, $\kappa = 880\,\mathrm{cm}^{-1}$. Utilizing deeply-etched grating with $\kappa = 880\,\mathrm{cm}^{-1}$ and (11), power reflectivity can be calculated to be 0.5.

For shallow-etch depths, the corrugated grating can be seen as a small perturbation, giving a negligible scattering loss. The loss increases with increased etch depth and importantly, the maximum loss occurs at an etch depth of about half the waveguide thickness. As the etch depth is increased further, the loss starts to roll off. As the grating etch depth penetrates across the entire slab waveguide thickness, a symmetric perturbation is created, thus reducing the scattering loss [23].

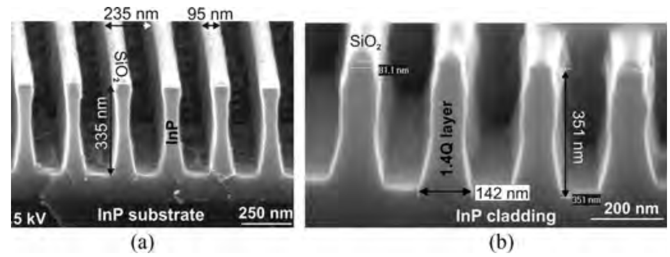

Fig. 10. (a) Holographically patterned deep-grating etched by methane/hydrogen/argon-RIE for (a) InP, and (b) quaternary waveguide layers.

H. Deep Grating Fabrication

There have been experimental efforts in fabricating such high-κ mirrors. Several etching recipes for such deep gratings with high aspect ratio and straight sidewalls were used. While methane-based reactive ion etch (RIE) is a common etching method for InP-based embedded square gratings, the polymer buildup and the photoresist erosion problems generally limit the depth of square gratings beyond 100 nm. However, using our optimized recipe, the grating pattern was successfully transferred to InP and 1.4-quaternary (Q) waveguide layers by methane/hydrogen/argon (MHA) RIE method. Fig. 10(a) and (b) shows examples of the fabricated gratings of InP and 1.4Q layers, respectively, with SiO_2 as the etch mask. A nearly square grating profile of ~350 nm depth, being suitable for the C-C lasers, is produced using an optimized etched recipe. Moreover, the groove opening, clean bottoms and profile straightness are found to be acceptable for $\kappa = 900\,\mathrm{cm}^{-1}$. A layer of 50 nm SiO_2 was deposited on the sample by a plasma enhanced chemical vapor deposition (PECVD) method as the hard mask. Photoresist was then spun on top of this SiO_2 layer. The interference grating patterns are generated by the holographic exposure on the photoresist and are transferred to SiO_2 by a CF_4/CHF_3/O_2 RIE. Finally, semiconductor layers were etched to realize the deep grating.

III. Coupled-Cavity Laser Fabrication

For the sake of simplicity and proof-of-principle demonstration, devices were processed with one phase section and two gain sections. Cavity-1 is formed by 90-μm and 40-μm long gain

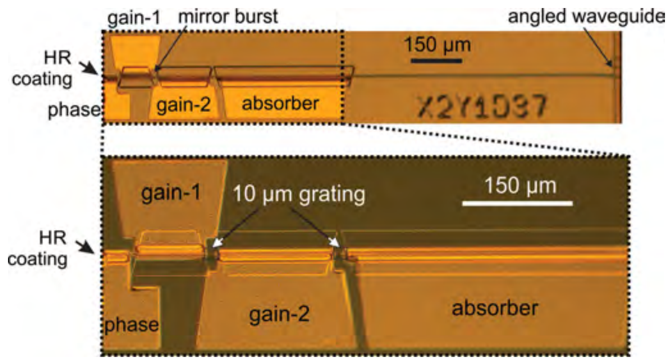

Fig. 11. Microscope image of a fully-processed processed C-C laser followed by an absorber.

and passive sections, respectively, whereas cavity-2 consists of only 100-μm-long active sections. The device is followed by a long absorber section that allows the accurate on-chip static characterization decoupled from facet coupling loss. The absorber may also be forward biased to operate as an integrated booster amplifier. The offset quantum well (OQW) integration platform [24] was chosen for processing C-C lasers. The OQW integration platform has quantum wells offset from the center of the waveguide, with a confinement factor of 10%. The definition of active and passive areas required a wet etch of the top 200-nm-thick InP layer and quantum wells which were selectively removed by the etch-stop layer. This makes the OQW integration platform the simplest way to combine active and passive components on chip. First-order grating mirrors were defined on the device using electron beam lithography. Devices utilized standard shallow grating ($\kappa \sim 300$ cm^{-1}) by etching down to 80 nm in the 1.4Q layer. After grating definition, a blanket p-cladding and p^+-contact layer were regrown. Surface ridge waveguide with a width of 2–3.3 μm was then formed. After that, p-contact vias were opened to allow metallization of p-contact layer. P-side contact metal layers were deposited to allow p-side electrical connection. We implanted the regions between p-side contacts on the PIC to provide electrical isolation. The wafer backside was then thinned down to 140 μm and metallized. After cleaving and anti-reflection (AR) coating of the waveguide facets, devices were singulated, and mounted to a ceramic carrier in order to provide heat-sink and electrical connection for contacting the device. After wirebonding, devices were tested. In the device, the light outcoupling port was accessed by an angled cleaved facet with AR coating to suppress back-reflection. A microscope picture of the fully-processed PIC with a C-C laser followed by an absorber is shown in Fig. 11.

IV. Device Characterization

Temperature dependent continuous-wave (CW) *P-I-V* characteristics of devices were measured on a Peltier-cooled copper heatsink, as shown in Fig. 12. The device shows CW operation up to room-temperature. Measurements were performed when the current in cavity-1 is fixed to 17 mA and no current in the phase section is applied. On-chip absorber, reverse biased by 2 V, was used as a photodetector with an assumed responsivity of 1 A/W to measure the optical power coming out from the device. The maximum off-chip CW output power from the laser to a lensed fiber is 0.4 mW at 15 °C and when the absorber was forward biased to operate as a booster amplifier. In spite of the reasonable series resistance in the device and good diode turn-on voltage, verified by *I-V* characteristics and good material quality of the sample, devices exhibit higher threshold current density compared to the value obtained through numerical simulation. This could be most probably due to grating with $\kappa < 300$ cm^{-1} which introduces high scattering loss. Such a loss was not taken into account in the theoretical analysis.

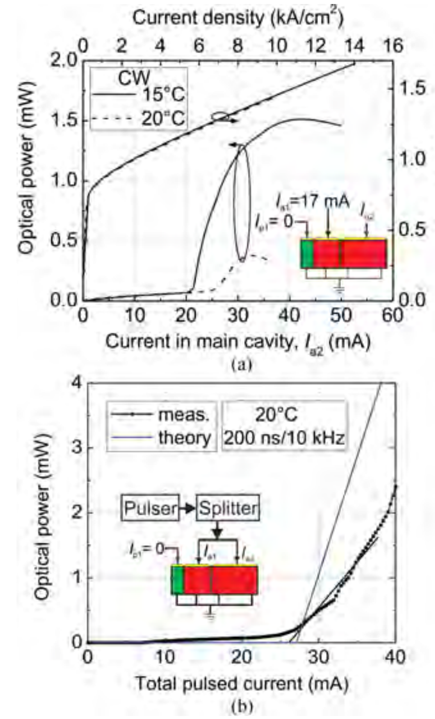

Fig. 12. (a) Temperature dependent *P-I-V* characteristics of the C-C laser. Schematic of the device biasing is shown as inset, and (b) pulsed *P-I* characteristics of the same device, which is superimposed on the plot obtained from the theory.

In order to minimize joule heating effect, pulsed measurement was performed using a pulser with a low duty cycle (e.g. 0.2%). A resistive 50:50 power splitter was used after the pulser to split the pulse current into two paths in order to drive two gain sections of the device. Since the current splitting depends upon the load in these two paths, current probes were connected in each path to know the current going into each gain section. The pulsed and the theoretical *P-I* characteristics, as shown in Fig. 12(b), are superimposed on each other. Device exhibits lasing when the gain-1,2 sections are pumped by 11.9 mA, 14.7 mA, respectively. This operation with modal gain $\Gamma g_{\mathrm{th}-1}$, $\Gamma g_{\mathrm{th}-2}$ can be described by a point (109 cm^{-1}, 115 cm^{-1}) in Fig. 5(a), if one assumes a $\kappa = 300$ cm^{-1}. The threshold currents are in the expected range for the resulting low mirror reflectivities, corresponding to Figs. 6(b) and 8(b) [with solid lines], and the lower differential efficiencies are explained by experimental

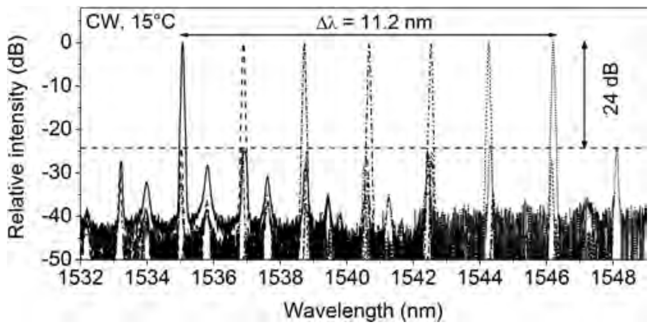

Fig. 13. Spectra of C-C lasers by varying current in cavity-1 and cavity-2, while the phase section current is kept constant.

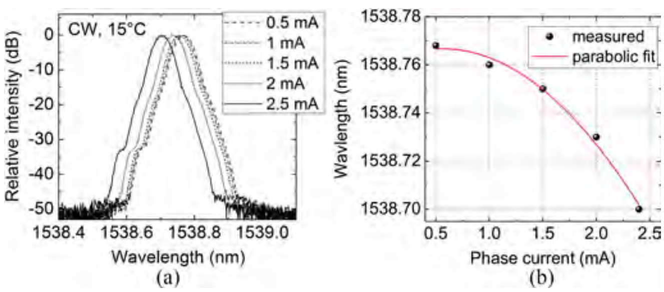

Fig. 14. (a) Fine tuning of the emission wavelength by changing current in the phase section, while the currents in gain sections are constant, and (b) wavelength tuning curve as a function of phase current.

injection efficiencies that are considerably less than unity, which was assumed in the theoretical plots.

The emission spectra of the C-C device are shown in Fig. 13, which was obtained by varying the current in cavity-1 and cavity-2 and keeping the current in the phase section constant. The wavelength tuning range of such devices is measured to be 11.2 nm, whereas the designed repeat mode-spacing of the laser was 16.8 nm. This could be attributed to the low-κ mirrors due to under etched mirrors, resulting in high-threshold devices. This results in device self-heating, which causes early thermal rollover in the device. As can be seen in Fig. 13, the device exhibits single-mode operation with a side-mode suppression ratio (SMSR) of over 24 dB over the entire operating range.

The fine tuning of the emission wavelength was measured by varying the phase-section current at a constant current in both cavities. Fig. 14(a) shows the change of the emission wavelength as a function of phase section, yielding mode-hop-free tuning range around 0.07 nm. However, a mode hop occurs if the phase section is tuned beyond the axial mode spacing within the laser of approximately 1.1 nm, if the other currents are not simultaneously adjusted. The wavelength tuning curve of the phase tuning section follows a square root behavior with respect to injected current, indicating primarily radiative recombination in this region, as can be seen in Fig. 14(b).

V. Conclusion

A comprehensive theoretical analysis of small-size and low-power consumption linear coupled-cavity lasers is proposed in this study. A description of step-by-step design procedures to realize such photonic-integrated circuit compatible devices is also provided here, serving as guidelines for the laser designers to model next-generation single-mode, and widely tunable devices. We have then experimentally demonstrated active-passive integrated C-C lasers with a simple configuration and compared the device results with the theory. The tuning range of these single-mode devices is measured to be 11.2 nm, less than the designed value, but partially explained by relatively low-reflectivity mirrors that require quite high gains and current densities. The relevant works for developing high-performance C-C lasers with short-deep grating to obtain wide tuning ranges as high as 50 nm are in progress and will be presented in future reports. Owing to their advantages of compact size, low-power, simple fabrication technique and full-integrability with standard processes into advanced PIC designs, these lasers should be useful for many diverse applications.

References

[1] V. Houtsma *et al.*, "Manufacturable monolithically integrated InP dual-port coherent receiver for 100G PDM-QPSK applications," in *Proc. Opt. Fiber Commun.*, Los Angeles, CA, 2011, pp. 1–3.

[2] A. Ramaswamy *et al.*, "Integrated coherent receivers for high-linearity microwave photonic links," *J. Lightw. Technol.*, vol. 26, no. 1, pp. 209–216, Jan. 2008.

[3] M. D. Turner, S. Datta, G. W. Kamerman, D. Becker, A. Joshi, and R. Howard, "Ultra-fast coherent optical system for active remote sensing applications," *Proc. SPIE, Laser Radar Technol. Appl. XIII*, vol. 6950, 2008, Art. no. 695008.

[4] S. Arafin *et al.*, "Towards chip-scale optical frequency synthesis based on optical heterodyne phase-locked loop," *Opt. Express*, vol. 25, no. 2, pp. 681–695, 2017.

[5] V. Jayaraman, Z.-M. Chuang, and L. A. Coldren, "Theory, design, and performance of extended tuning range semiconductor lasers with sampled gratings," *IEEE J. Quantum Electron.*, vol. 29, no. 6, pp. 1824–1834, Jun. 2002.

[6] J.-O. Wesstrom, G. Sarlet, S. Hammerfeldt, L. Lundqvist, P. Szabo, and P.-J. Rigole, "State-of-the-art performance of widely tunable modulated grating Y-branch lasers," in *Proc. Opt. Fiber Commun.*, Los Angeles, CA, 2004, p. 389.

[7] S. Matsuo and T. Segawa, "Microring-resonator-based widely tunable lasers," *IEEE J. Sel. Top. Quantum Electron.*, vol. 15, no. 3, pp. 545–554, May/Jun. 2009.

[8] S. Srinivasan, M. Davenport, T. Komljenovic, J. Hulme, D. T. Spencer, and J. E. Bowers, "Coupled-ring-resonator-mirror-based heterogeneous III-V silicon tunable laser," *IEEE Photon. J.*, vol. 7, no. 3, 2015, Art. no. 2700908.

[9] P.-J. Rigole *et al.*, "114-nm Wavelength tuning range of a vertical grating assisted codirectional coupler laser with a super structure grating distributed Bragg reflector," *IEEE Photon. Technol. Lett.*, vol. 7, no. 7, pp. 697–699, Jul. 1995.

[10] M. Lu *et al.*, "Monolithic integration of a high-speed widely tunable optical coherent receiver," *IEEE Photon. Technol. Lett.*, vol. 25, no. 11, pp. 1077–1080, Jun. 2013.

[11] M. Lu, "Integrated optical phase-locked loops," Ph.D. dissertation, Dept. Electr. Comput. Eng., Univ. California, Santa Barbara, CA, USA, 2013.

[12] L. A. Coldren and T. L. Koch, "Analysis and design of coupled-cavity lasers-Part I: threshold gain analysis and design guidelines," *IEEE J. Quantum Electron.*, vol. QE-20, no. 6, pp. 659–670, Jun. 1984.

[13] L. B. Allen, H. G. Koenig, and R. R. Rice, "Single frequency injection laser diodes for integrated optics and fiber optics applications," in *Proc. Soc. Photon. Opt. Eng.*, San Diego, CA, 1978, pp. 110–117.

[14] C. H. Henry and R. F. Kazarinov, "Stabilization of single frequency operation of coupled-cavity lasers," *IEEE J. Quantum Electron.*, vol. QE-20, no. 7, pp. 733–744, Jul. 1984.

[15] R. J. Lang and A. Yariv, "An exact formulation of coupled-mode theory for coupled-cavity lasers," *IEEE J. Quantum Electron.*, vol. 24, no. 1, pp. 66–72, Jan. 1988.

[16] D. Lenstra, "Self-consistent rate-equation theory of coupling in mutually injected semiconductor lasers," *Proc. SPIE, Phys. Simul. Optoelectron. Devices XXV*, vol. 10098 , 2017, Art. no. 100980K.

[17] P. Bardella, W. Chow, and I. Montrosset, "Design and analysis of enhanced modulation response in integrated coupled cavities DBR lasers using photon-photon resonance," *Photonics*, vol. 3, no. 1, 2016, Art. no. 4.

[18] D. D'Agostino, D. Lenstra, H. P. Ambrosius, and M. K. Smit, "Coupled cavity laser based on anti-resonant imaging via multimode interference," *Opt. Lett.*, vol. 40, no. 4, pp. 653–656, 2015.

[19] W. Yao, G. Gilardi, D. D'Agostino, M. K. Smit, and M. J. Wale, "Monolithic tunable coupled-cavity WDM transmitter in a generic foundry platform," *IEEE Photon. Technol. Lett.*, vol. 29, no. 6, pp. 496–499, Mar. 2017.

[20] P. E. Morrissey, N. Kelly, M. Dernaika, L. Caro, H. Yang, and F. H. Peters, "Coupled cavity single-mode laser based on regrowth-free integrated MMI reflectors," *IEEE Photon. Technol. Lett.*, vol. 28, no. 12, pp. 1313–1316, Jun. 2016.

[21] L. A. Coldren, S. W. Corzine, and M. L. Mashanovitch, *Diode Lasers and Photonic Integrated Circuits*, 2nd ed. Hoboken, NJ, USA: Wiley, 2012.

[22] C.-H. Chen, J. Klamkin, L. A. Johansson, and L. A. Coldren, "Design and Implementation of ultra-compact grating-based 2 × 2 beam splitter for miniature photonic integrated circuits," in *Proc. Opt. Fiber Commun.*, Los Angeles, CA, 2008, pp. 1–3.

[23] C.-H. Chen, J. Klamkin, S. C. Nicholes, L. A. Johansson, J. E. Bowers, and L. A. Coldren, "Compact beam splitters with deep gratings for miniature photonic integrated circuits: design and implementation aspects," *Appl. Opt.*, vol. 48, no. 25, pp. F68–F75, 2009.

[24] J. W. Raring *et al.*, "Advanced integration schemes for high-functionality/high-performance photonic integrated circuits," *Proc. SPIE, Photon. Packag. Integr. VI*, vol. 6126, 2006, Art. no. 61260H.

Shamsul Arafin (S'08–M'12–SM'17) received the B.Sc. degree in electrical and electronics engineering from the Bangladesh University of Engineering and Technology, Dhaka, Bangladesh, in 2005, the M.Sc. degree in communication technology from Universität Ulm, Ulm, Germany, in 2008, and the Ph.D. degree from the Technische Universität München, Walter Schottky Institut, Munich, Germany, in 2012. He is currently working as an Assistant Project Scientist with the University of California Santa Barbara (UCSB), Santa Barbara, CA, USA. Prior to joining UCSB, he worked as a Postdoctoral Research Scholar in the Device Research Laboratory, University of California at Los Angeles, CA. Till now, he has authored and coauthored more than 70 papers in leading technical journals and international conferences.

Gordon B. Morrison received the B.A.Sc. degree (Hons.) from the Simon Fraser University, Vancouver, BC, Canada, in 1997, and the Ph.D. degree from McMaster University, Hamilton, ON, Canada, in 2002, both in engineering physics. His doctoral work, under Prof. D. T. Cassidy, focused on modeling and characterization of gain-coupled DFB lasers. From 1998 to 2002, he spent more than a year at Nortel Networks, ON, Canada, as a Graduate Student Researcher. From 2002 to 2003, he was a Post-Doctoral Fellow with McMaster University, where he was involved in development of a model for asymmetric-multiple-quantum-well gain and worked on process development for quantum-well intermixing. In June 2003, he joined the Department of Electrical and Computer Engineering, University of California, Santa Barbara, as a Visiting Assistant Research Engineer in Prof. L. Coldren's group, where he participated in the design, fabrication, and characterization of small footprint DBR EMLs using quantum-well-intermixing technology, and used photocurrent spectroscopy to characterize and optimize photonic integrated circuits. In 2005, he joined ASIP (formally III-V Photonics), Houten, The Netherlands, and in 2006 joined Apogee Photonics (formerly ASIP/T-Networks), Allentown, PA, where he worked on uncooled 1310 EML technology, 40G EA modulators, and monolithically integrated SOA/EA products. Apogee photonics was acquired by CyOptics Inc, Breinigsville PA, and subsequently was acquired by Avago technologies. At CyOptics/Avago, he continued work on EML development while additionally focusing on design, characterization, calibration, and qualification of liquid crystal external cavity tunable lasers for coherent applications. In 2014, he joined Freedom Photonics LLC, Santa Barbara, CA, USA, as the Director of Engineering. He is the author or co-author of more than 30 peer-reviewed journal papers.

Milan L. Mashanovitch (M'99–SM'13) received the Dipl.Ing. degree in electrical engineering from the University of Belgrade, Belgrade, Serbia, in 1998, and the Ph.D. degree in electrical engineering from the University of California, Santa Barbara, CA, USA, in 2004. He co-founded Freedom Photonics LLC, Santa Barbara, CA, USA, in 2005, and he has been in many technical roles related to product development and program management since. In addition to Freedom Photonics, he has worked for the University of California Santa Barbara, both as a Researcher on photonic integrated circuits, and as an Adjunct Professor teaching graduate level classes on semiconductor lasers and photonic ICs. He has co-authored nearly 130 papers, many invited, on photonic integrated circuits and various photonic devices. He is one of the authors of the second edition of the *Diode Lasers and Photonic Integrated Circuits* (Wiley, 2012). He has chaired, serves or has served on technical committees for IEEE Avionics, Fiber Optics and Photonics Conference, IEEE Microwave Photonics Conference, OSA's Integrated Photonics Research Conference, International Semiconductor Laser Conference, and Indium Phosphide and Related Materials Conference.

Leif A. Johansson (M'04) received the Ph.D. degree in engineering from the University College London, London, U.K., in 2002. He has been a Research Scientist with the University of California at Santa Barbara, Santa Barbara, CA, USA, and is the Founder of Freedom Photonics, Santa Barbara, CA, USA. His current research interests include design and characterization of integrated photonic devices for analog and digital applications and analog photonic systems and subsystems.

Larry A. Coldren (S'67–M'72–SM'77–F'82–LF'11) received the Ph.D. degree in electrical engineering from Stanford University, Stanford, CA, USA, in 1972. After 13 years in the research area with Bell Laboratories, he joined the University of California at Santa Barbara (UCSB), Santa Barbara, CA, USA, in 1984. From 2009 to 2011, he served as the the Dean of the College of Engineering. In 1990, he co-founded Optical Concepts, later acquired as Gore Photonics, to develop novel VCSEL technology, and, in 1998, he co-founded Agility Communications, later acquired by JDSU, to develop widely tunable integrated transmitters. At UCSB, he has worked on multiple-section widely tunable lasers and efficient vertical-cavity surface-emitting lasers (VCSELs). More recently, his group has developed high-performance InP-based photonic integrated circuits and high-speed VCSELs. He is currently the Fred Kavli Professor of Optoelectronics and Sensors and holds appointments in the Department of Materials and the Department of Electrical and Computer Engineering, UCSB. He has authored or coauthored more than a thousand journal and conference papers, co-authored eight book chapters, a widely used textbook, and holds 65 patents. He is a Fellow of OSA and IEE, and a member of the National Academy of Engineering. He received the 2004 John Tyndall Award, the 2009 Aron Kressel Award, the 2014 David Sarnoff Award, and the 2015 IPRM Award.